

Joint Editorial Invigorating Hydrological Research through Journal Publications

Nevil Quinn¹, Günter Blöschl², András Bárdossy³, Attilio Castellarin⁴, Martyn Clark⁵,
Christophe Cudennec⁶, Demetris Koutsoyiannis⁷, Upmanu Lall⁸, Lubomir Lichner⁹, Juraj Parajka¹⁰,
Christa D. Peters-Lidard¹¹, Graham Sander¹², Hubert Savenije¹³, Keith Smettem¹⁴, Harry Vereecken¹⁵,
Alberto Viglione¹⁶, Patrick Willems¹⁷, Andy Wood¹⁸, Ross Woods¹⁹, Chong-Yu Xu²⁰, Erwin Zehe²¹

¹ Editor, Hydrology Research

² Past Editor, Water Resources Research; Editor, Hydrology and Earth System Sciences; Co-Editor Journal of Hydrology and Hydromechanics

³ Editor in Chief, Journal of Hydrology

⁴ Co-Editor, Hydrological Sciences Journal; Associate Editor of Water Resources Research

⁵ Editor in Chief, Water Resources Research

⁶ Editor in Chief, Proceedings of the International Association of Hydrological Sciences

⁷ Co-Editor, Hydrological Sciences Journal; Editor, Hydrology and Earth System Sciences (now retired)

⁸ Editor in Chief, Water Security

⁹ Editor in Chief, Journal of Hydrology and Hydromechanics

¹⁰ Associate Editor, Water Resources Research; Co-Editor, Journal of Hydrology and Hydromechanics

¹¹ Chief Editor, Journal of Hydrometeorology

¹² Editor in Chief, Advances in Water Resources

¹³ Editor in Chief, Physics and Chemistry of the Earth

¹⁴ Editor in Chief, Ecohydrology

¹⁵ Editor, Vadose Zone Journal

¹⁶ Associate Editor, Water Resources Research; Associate Editor Hydrological Sciences Journal

¹⁷ Co-Editor in Chief, Journal of Hydrology: Regional Studies

¹⁸ Editor, Journal of Hydrometeorology

¹⁹ Co-Editor, Hydrological Sciences Journal

²⁰ Editor, Hydrology Research

²¹ Chief Executive Editor, Hydrology and Earth System Sciences

Abstract: Editors of several journals in the field of hydrology met during the General Assembly of the European Geosciences Union–EGU in Vienna in April 2017. This event was a follow-up of similar meetings held in 2013 and 2015. These meetings enable the group of editors to review the current status of the journals and the publication process, and to share thoughts on future strategies. Journals were represented at the 2017 meeting by their editors, as shown in the list of authors. The main points on invigorating hydrological research through journal publications are communicated in this joint editorial published in the above journals.

MAIN TEXT

Over the past five years, the Editors of a number of journals in the discipline of hydrology have met informally to discuss challenges and concerns in relation to the rapidly changing publishing landscape. Two of the previous meetings, in Gothenburg in July 2013 and in Prague in June 2015 were followed by Joint Editorials (Blöschl et al., 2014; Koutsoyiannis et al., 2016) published in all participating Journals. A meeting was convened in Vienna in April 2017 (during the General Assembly of the European Geosciences Union – EGU) which was attended by 21 Editors representing 14 journals. Even though the journals are published in quite different settings, the Editors found common cause in a vision of the Editor’s role beyond just that of gatekeeper ensuring high quality publications, to also being critical facilitators of scientific advances. In that enabling spirit, we as Editors, acknowledge the need to anticipate and adapt to the changing publishing landscape. This Editorial communicates our views on the implications for authors, readers, reviewers, institutional assessors and the community of Editors, as discussed during the meeting, and subsequently.

(1) Recent trends in the publication process – quantity, speed and multiple authorships

The previous Joint Editorials have reflected on the increased productivity across the discipline, and more broadly in science, as evidenced by a rise in manuscript submissions. This growth in submissions and publications has continued in recent years at an unflinching rate. Collectively, the 14 journals represented in this Editorial published 46,000 pages in 2017, compared with only 26,000 pages a decade earlier. The main driver of increased submissions has been intensified publication pressure which has given rise to a number of trends of concern that privilege quantity over quality of science: In “Salami-publishing” (Koutsoyiannis et al., 2016; Martin, 2013) authors split a body of work into several papers in order to increase the number of their publications and their citation counts. There is also a tendency to publish work prematurely, where the contribution is incremental rather than significant. Despite the standard use of plagiarism detection tools by most journals, plagiarism still does occur, and ‘recycling’, where authors repackage their own work with minimal extension for a different audience is on the increase. Some of this would be regarded

as self-plagiarism (Martin, 2013). There have been cases of authors submitting the same manuscript simultaneously to multiple journals, and authors immediately submitting a rejected manuscript to another journal without any reflection and revision in response to reviewer evaluations. There are also instances of reviewers (and Editors) attempting to promote their own (or their Journals') citation metrics by requiring authors to cite their list of papers (citation coercion and citation stacking). None of these practices are conducive to advancing the science of hydrology. On the contrary, they contribute to a system overload and a dilution of useful information in the published literature.

Another trend that has become acute recently is that of a push towards speedier publication. New media have created a culture of immediacy for traditional journals (Brossard and Scheufele, 2013), and editors are under pressure to reduce turn-around times, both in relation to time-to-first-decision and the subsequent review process. Most hydrology journals have reduced their turn-around times by at least two months in the last decade, little of which can be attributed to technical and system improvements. A number of journals have introduced a 'fast-track' or 'rapid communication' route in an attempt to report quickly on an extreme event or new technology. These types of papers place a higher burden on reviewers in relation to speed, and additional challenges to editorial teams around review quality, while authors risk compromising quality for expediency. Recent experience has highlighted the additional risks of premature press releases, where a paper is subsequently rejected but broadcasters have already acted on a press-release. Various approaches to providing a 'fast-track' stream are being considered by hydrology journals, with variable success. As a discipline we need to reflect on whether these approaches are consistent with the notion of high quality communication in our journals, or whether other communication forms (newsletters, professional magazines, new media) might be more appropriate. It may well be that different approaches may co-exist within hydrology.

The third, conspicuous trend is that of an increase in the number of authors per paper. In the 1980s, the average number of authors per paper of hydrological journal articles was below 2 while this figure has soared to 4 to 5 in 2017, depending on the journal. While European Research Council (ERC) and other internationally funded research often necessarily involve multiple authorships, this does make an individual's contribution difficult to determine and advantages 'networkers' as much as 'true contributors'. Although long author lists are evidently not negative per-se, as they demonstrate the need for collaboration and integration of specialized knowledge, they may be problematic when used for research assessments. Koutsoyiannis et al. (2016) suggested addressing this issue by normalising citation statistics by the number of authors. There have been similar discussions in other disciplines. In medicine, for example, a new approach to authorship transparency has been formalized through the CRediT (Contributor Roles Taxonomy) initiative (see <http://docs.casrai.org/CRediT> and McNutt et al., 2018). While the discipline reflects on ways of dealing with this challenge, we recommend that, in the interim, multi-authored research papers should include a statement of attribution of contributions, specifying who of the author list contributed in: designing the research, conducting the research, writing the text, editing the text and funding the research. Furthermore, these trends are located within a changing landscape of academic publishing. Research funders and users of research outputs are increasingly demanding open access and publishers are grappling with different models which add additional com-

plexities to the issues of quantity, speed and multiple authorships.

(2) Recognising importance of novel insight

The main purpose of scientific publication consists of communicating new, important findings to peers in order to advance the science. The main role of Editors, together with authors, reviewers and Associate Editors is to maximise the potential towards fostering progress. During the publication process, the degree to which the manuscript contributes to advancing our science is in theory detected by the peer review system. However, as publications become more numerous, models more complex and data sets more extensive, it has sometimes become very difficult to assess the validity of a new theory or model prediction on the basis of the material contained in a manuscript. Most hydrology journals have therefore adopted a policy of open data and open models (e.g., Data Citation Synthesis Group, 2014), to allow peers – at least in principle – to repeat any published study. While the open data/model policies are recognised as being important, there are particular challenges in hydrology as, in some countries, the data (and models) used are often proprietary. Also, publication strategies often involve keeping part of the data for further analyses by the same group. Open data/model policies will certainly need particular attention in the near future, and will likely require a change in the thinking of researchers and data collection agencies. Given the increasing burden that open data and open model policies impose on authors, institutions and journals should seek approaches that facilitate compliance.

A secondary purpose of scientific publication lies in recognising the contributions of individuals and their research institutions. While, traditionally, this was done by attributing seminal achievements to the authors publishing them (e.g. Newton became famous through the power of ideas in his *Principia*), the process has today become more formalised due to the availability of publication data bases and associated metrics. Typical assessment criteria are the number of publications, the citations they receive, and the quality of the journals in which they are published.

The quality of journals, as used in research assessments, is often quantified by journal impact factors (IF). They are a measure of the number of citations to the papers of that journal over a particular period, and have been used to separate reputable journals from low threshold web postings, new media and predatory journals (Beall, 2016). The presumption is that the quality of individual papers can somehow be inferred from the citation count of the journal as a whole. A comparison among six leading hydrology journals over the period 1996 to 2016, published as an editorial in *Water Resources Research* (Clark and Hanson, 2017) concludes that the journal impact factor in a given year does not have much predictive power for journal-level productivity. Impact factors, particularly in smaller journals, were found to vary substantially across years, which can be expected for statistical reasons (small samples). This is not to say that a journal's impact factor is not a useful metric; with many more journals appearing, an impact factor could be helpful, for example, in indicating journal development and maturity. The important point is that assessments of research quality and choices of journals for submitting work to should not be driven by impact factors. Furthermore, a comparison between disciplines suggests that the journal impact factors of hydrology journals are rather low (all journals reviewed have an impact factor less than 5, Clark and Hanson, 2017) in relation to disciplines such as medicine,

chemistry and physics which highlights the problem of using impact factors to compare the quality of work across disciplines (Koutsoyiannis and Kundzewicz, 2007). In hydrology, papers tend to be cited over much longer time periods which, together with the smaller size of the discipline, means that the short 2-year time window for impact factor calculation is a limitation in our discipline. It is also influenced by the fact that impacts of some hydrological publications materialize through application to water-related management, which is not reflected in citations (Cudennec and Hubert, 2008).

It is arguable whether there is any set of metrics that would effectively measure a lasting contribution to academic thought and practice, quite apart from whether these could be gamed by an individual choosing to do so. A general concern therefore emerges from the current practice of assessing and ranking scientific productivity of institutions, journals and individuals by bibliometric indices which could indirectly incentivise academic misconduct (Edwards and Roy, 2017). We also note that the San Francisco Declaration on Research Assessment (DORA) (<http://www.ascb.org/dora/>), urges a focus on the scientific contribution of published papers rather than where the papers were published in an attempt to reduce the misuse of impact factors for research assessment. Similarly, the commendable EU “Open Science” initiative and associated report on next generation responsible metrics (<https://ec.europa.eu/research/openscience/pdf/report.pdf>) should inform our debate and practice. It would stand hydrology in good stead if we, like only a generation ago, assessed research impact (and the performance of individuals and institutions) by the changes in the thinking induced, rather than by citation numbers. This is the (unfortunately not objectively measurable) criterion that would maximise advances in science, suggesting that peer review assessments should be given higher priority in the future.

(3) Role of journals in setting the science agenda

With climate change currently being high on the political agenda and coupled with prevailing publication pressures, it is not surprising that submissions on climate impact studies, often with little novelty or innovation, have become something of a cottage industry. Equally disappointing is the proliferation of model applications with marginal innovation and/or little generality. There is indeed an interesting question of whether societal needs, fundamental ideas or new technologies are the main drivers of scientific progress. Sivapalan and Blöschl (2017) suggested that all three have been and will be important ingredients in hydrology. They also noted that research progress has come about in discrete steps or ‘eras’. For example, the two decades from 1970–1990 focused on hydrological processes involving substantial field work. Later the interest in field work ebbed away because of the high cost/benefit ratio (Blume et al., 2017), and changing societal priorities.

Indeed in the 21st century the human footprint is fast becoming a dominant feature in the hydrological cycle and research across the disciplines is becoming mandatory. Publishing interdisciplinary research, however, still remains challenging. There is a tendency for researchers and their communities to be socialised within their own discipline niches, and communities may become self-reinforcing to the detriment of fresh outside perspectives. Most hydrology journals have already responded strategically to these interdisciplinary publication needs, e.g. by selecting editors and reviewers from a diverse set of disciplines. The strategic response of *Water Resources Research (WRR)* is a potential approach to help mature interdisciplinary thinking. *WRR* encourages didactic

reviews to provide the perspective of other disciplines (i.e. how they undertake research and engage discourse within their field) and also commentary papers that explore why a particular field is struggling and seeks to explore the field from multiple perspectives.

Whether the research is disciplinary or inter/multi-disciplinary, journals play an important role in communicating and setting the trend for the vision of hydrological research, and for fostering innovation in a coherent way. We need to work collectively to ensure that science of the highest quality and innovation content is published in our journals. To do this the hydrological community must redress research investment deficiencies and the publication biases that arise as a result of a lack of funding. Research agendas should not be so narrowly linked to today’s problems, and we need to be bold in setting out the grand challenges of our discipline. For example, the International Association of Hydrological Sciences (IAHS), in collaboration with the Hydrology Divisions of EGU and AGU, have recently called for compiling a list of unsolved scientific problems in hydrology that would invigorate research in the 21st century (<https://iahs.info/IAHS-UPH/>). The initiative has been motivated by David Hilbert’s (1900) unsolved problems which have greatly stimulated focused research in mathematics. The idea is that a similar list of problems could be identified by the hydrological community. For tangible progress to be made the problems should be framed so they:

- ideally relate to observed phenomena and why they happen;
- are universal (i.e. not only apply to one catchment or region); and
- are specific (so there is hope they can be solved).

We commend this initiative and urge colleagues to contribute to shaping progress in hydrology.

SUMMARY AND CONCLUDING REMARKS

Hydrology, a traditionally integrative science with high societal relevance and geographic diversity, is perhaps an optimal place from which to launch the movement to reassert the academic spirit in a time where there is dramatic change in the way people learn, synthesize and interact with each other. Our community stands at the cusp of perhaps the greatest societal revolution in the democratization of access to resources and knowledge, as well as to the largest population the world has ever seen. These societal and technological changes have major effects on the publishing landscape. For hydrological journals there is a unique opportunity to learn through harnessing the energies of the moment to continue to improve our concept of the world and the role water plays in it.

- *Publication quantity, speed and multiple authorships:* Authors, reviewers and Editors are encouraged to prioritise research quality over quantity. Discussions are currently under way to discourage unethical behaviour of authors, reviewers and editorial board members. Measures may involve a system for sharing information on ethical misconduct across hydrology, in addition to reinforcing the guidelines of COPE (Committee of Publication Ethics), to which our journals adhere. Authors are encouraged to make a personal judgement on whether fast-track findings may be more appropriately communicated through scientific journals or other communication forms. Similarly we must emphasise transparency in authorship contributions; multi-authored papers should include a statement of attribution of the individual contributions.

- *Recognising importance of novel insight:* Most hydrology journals have adopted a policy of open data and open models, to allow peers to repeat any published study and fully appreciate the validity and novelty of the material. For these policies to be fully embraced, a change in culture will be required by both researchers and data collection agencies. The issue of research assessment on the basis of impact factors (the “tyranny of metrics”) (Delzon et al., 2016) is symptomatic of a larger problem that we need to address and act on; the core values of transparency and peer review are the foundations of the scientific and social capital of our journals, and these principles, combined with embracing alternate and still-to-emerge media, will ensure that journals remain the trusted and authoritative communications outlets for compelling ideas for, and of, the future. We need to identify ways of ensuring that the value of hydrological journals continues to be recognised; we need to ensure that they are a primary and effective forum for furthering the science and practice of hydrology, and presenting solutions to challenging problems. We also need to ensure the focus of research assessments is on the scientific contributions of individual journal papers rather than on impact factors.

- *Role of journals in setting the science agenda:* Journals play an important contributory role – together with their parent organizations and associated conferences – in communicating and setting the trend for the vision of hydrological research, and for fostering innovation in a coherent way. Research agendas should be forward looking and not be narrowly linked to today’s problems. There is a need for the discipline to work collectively to redress such funding and publication biases that consequently arise. We need to ensure that science of the highest quality and innovative content is published in our journals that facilitates and invigorates hydrological research.

As a hydrological community we are experiencing unprecedented challenges emerging from the rapidly changing science communication landscape. These challenges also represent an opportunity for a renaissance in the scope and societal impact of our discipline. As we engage with new modes of communication, we must remain vigilant to ensure top quality science distinguishes our journals from the mass of unverified online information. The success of new measures for author transparency, for reducing scientometric bias, and for reinvigorating the hydrological science agenda depends on your participation and engagement. To realise this renaissance, we urge all to act in support of the issues raised in this editorial, through activities within journal institutions, professional societies and the broader community of practice.

Acknowledgements. This editorial has benefited from the insightful critique of three reviewers – Dani Or, Murugesu Sivapalan and Ian Littlewood – and we would like to extend our collective thanks to these reviewers for their useful perspectives, comments and additions.

REFERENCES

Beall, J., 2016. Essential information about predatory publishers and journals. *International Higher Education* 86

- (Summer 2016). DOI: 10.6017/ihe.2016.86.9358.
- Blöschl, G., Bárdossy, A., Koutsoyiannis, D., Kundzewicz, Z., Littlewood, I., Montanari, A., Savenije, H., 2014. Joint editorial – On the future of journal publications in hydrology. *Hydrology Research*, 45, DOI: 10.2166/nh.2014.006.
- Blume, T., van Meerveld, I., Weiler, M., 2017. The role of experimental work in hydrological sciences—insights from a community survey. *Hydrological Sciences Journal*, 62, 3, 334–337. DOI: 10.1080/02626667.2016.1230675.
- Brossard, D., Scheufele, D.A., 2013. Science, new media, and the public. *Science*, 339, 6115, 40–41. DOI: 10.1126/science.1232329.
- Clark, M., Hanson, R., 2017. Editorial – The citation impact of hydrology journals. *Water Resources Research*, 53. DOI: 10.1002/2017WR021125.
- Cudennec, C., Hubert, P., 2008. The multi-objective role of HSJ in processing and disseminating hydrological knowledge. *Hydrological Sciences Journal*, 53, 2, 485–487. DOI: 10.1623/hysj.53.2.485.
- Data Citation Synthesis Group, 2014. Joint Declaration of Data Citation Principles. Martone, M. (Ed.). FORCE11, San Diego, CA, USA.
- Delzon, S., Cochard, H., Pfautsch, S., 2016. Indexing the indices: scientific publishing needs to undergo a revolution. *Journal of Plant Hydraulics*, 3, 009. DOI: 10.20870/jph.2016.e009.
- Edwards, M.A., Roy, S., 2017. Academic research in the 21st century: Maintaining scientific integrity in a climate of perverse incentives and hypercompetition. *Environmental Engineering Science*, 34, 1, 51–61. DOI: 10.1089/ees.2016.0223.
- Hilbert, D., 1900. *Mathematische Probleme*. Nachrichten von der Königlichen Gesellschaft der Wissenschaften zu Göttingen – Mathematisch-Physikalische Klasse, 253–297.
- Koutsoyiannis, D., Kundzewicz, Z., 2007. Editorial – Quantifying the impact of hydrological studies. *Hydrological Sciences Journal*, 52, 1, 3–17. DOI: 10.1623/hysj.52.1.3.
- Koutsoyiannis, D., Blöschl, G., Bárdossy, A., Cudennec, C., Hughes, D., Montanari, A., Neuweiler, I., Savenije, H., 2016. Joint editorial – Fostering innovation and improving impact assessment for journal publications in hydrology. *Hydrological Sciences Journal*, 61, 7, 1170–1173. DOI: 10.1002/2016WR018895.
- Martin, B., 2013. Whither research integrity? Plagiarism, Self-plagiarism and coercive citation in an age of research assessment. *Research Policy*, 42, 1005–1014. DOI: 10.1016/j.respol.2013.03.011.
- McNutt, M., Bradford, M., Drazen, J., Hanson, B., Howard, B., Jamieson, K., Kiermer, V., Marcus, E., Pope, B., Scheckman, R., Swaminathan, S., Stang, P., Verma, I., 2018. Transparency in authors’ contributions and responsibilities to promote integrity in scientific publication. *Proceedings of the National Academy of Sciences*, 115, 11, 2557–2560. DOI: 10.1073/pnas.1715374115.
- Sivapalan, M., Blöschl, G., 2017. The growth of hydrological understanding: Technologies, ideas, and societal needs shape the field. *Water Resources Research*, 53, 8137–8146. DOI: 10.1002/2017WR021396.

Recovery of small-scale infiltration and erosion after wildfires

Sierra S. Larson-Nash¹, Peter R. Robichaud^{2*}, Fredrick B. Pierson³, Corey A. Moffet⁴, C. Jason Williams⁵, Kenneth E. Spaeth⁶, Robert E. Brown², Sarah A. Lewis²

¹ Meter Group, 2365 Northeast Hopkins Court, Pullman, WA 99163, USA formally with US Department of Agriculture, Forest Service, Rocky Mountain Research Station. E-mail: sierra.larson-nash@metergoup.com

² US Department of Agriculture, Forest Service, Rocky Mountain Research Station, 1221 S. Main St., Moscow, ID 83843, USA. E-mails: probichaud@fs.fed.us; bbrown02@fs.fed.us; sarahlewis@fs.fed.us

³ US Department of Agriculture, Agricultural Research Service, Northwest Watershed Research Center, 800 E. Park Blvd., Boise, ID 83712, USA. E-mail: fred.pierson@ars.usda.gov

⁴ US Department of Agriculture, Agricultural Research Service, 2000 18th Street, Woodward, OK 73801 USA. E-mail: corey.moffet@ars.usda.gov

⁵ US Department of Agriculture, Agricultural Research Service, Southwest Watershed Research Center, 2000 E. Allen Road, Tucson, AZ 85719 USA, formally with USDA, Agricultural Research Service, Northwest Watershed Research Center. E-mail: jason.williams@ars.usda.gov

⁶ US Department of Agriculture, Natural Resources Conservation Service, Central National Technology Support Center, 501 W. Felix St., FWFC, Building 23, Fort Worth, TX 76115, USA. E-mail: Ken.Spaeth@ftw.usda.gov

* Corresponding author. Tel.: 208 883 2349. E-mail: probichaud@fs.fed.us

Abstract: Wildfires naturally occur worldwide, however the potential disruption to ecosystem services from subsequent post-fire flooding and erosion often necessitates a response from land managers. The impact of high severity wildfire on infiltration and interrill erosion responses was evaluated for five years after the 2003 Hot Creek Fire in Idaho, USA. Relative infiltration from mini-disk tension infiltrometers (MDI) was compared to rainfall simulation measurements on small burned and control plots. Vegetation recovery was slow due to the severity of the fire, with median cover of 6–8% on burned sites after 5 years. Consequently, interrill sediment yields remained significantly higher on the burned sites (329–1200 g m⁻²) compared to the unburned sites (3–35 g m⁻²) in year 5. Total infiltration on the burned plots increased during the study period, yet were persistently lower compared to the control plots. Relative infiltration measurements made at the soil surface, and 1- and 3-cm depths were significantly correlated to non-steady state total infiltration values taken in the first 10 minutes of the hour-long rainfall simulations. Significant correlations were found at the 1-cm ($\rho = 0.4\text{--}0.6$) and 3-cm ($\rho = 0.3\text{--}0.6$) depths (most p -values <0.001), and somewhat weaker correlations at the soil surface ($\rho = 0.2\text{--}0.4$) (p -values <0.05 and up). Soil water repellency is often stronger below the soil surface after severe wildfire, and likely contributes to the reduced infiltration. These results suggest that relative infiltration measurements at shallow depths may be useful to estimate potential infiltration during a short-duration high-intensity storm and could be used as an input for post-fire erosion models.

Keywords: Interrill erosion; Mini-disk infiltrometer; Post-fire erosion; Rainfall simulation; Water repellency.

INTRODUCTION

Wildfires and subsequent post-fire flooding and erosion are natural processes within healthy forest ecosystems worldwide (Agee, 1996; Imeson et al., 1992; Prosser and Williams, 1998; Townsend and Douglas, 2000). However, these processes often threaten life, property and natural resources both inside and outside of the burned area and consequently, a response from land managers is required (Moody et al., 2013; Neary et al., 2005).

Multiple factors contribute to elevated flooding and erosion risk following fire, including loss of water storage in the forest litter and duff, reduction in leaf interception from canopy loss and reduced understory vegetation cover, decreased infiltration and creation or exacerbation of water repellent soil conditions (Shakesby et al., 2000). Many of these factors are closely related to soil burn severity, defined as the effect of fire on ground cover and soil characteristics (e.g., ash depth, organic matter loss, reduced infiltration and altered soil structure) (DeBano et al., 1998; Larsen et al., 2009; Lentile et al., 2006; Parsons et al., 2010; Ryan and Noste, 1985).

Post-fire erosion is often inversely correlated to remaining ground cover that protects the mineral soil (vegetation and

forest litter), which commonly decreases with increasing soil burn severity (Benavides-Solorio and MacDonald, 2005; Cerdà, 1996; Johansen et al., 2001; Parsons et al., 2010; Robichaud et al., 2013a). As ground cover is reestablished, infiltration rate and sediment yield tend to return to pre-fire levels (Cerdà, 1996; Pierson et al., 2008). This recovery process generally takes three to five years (Goetz et al., 2006; Robichaud et al., 2013a; Wine and Cadol, 2016), but recovery times of 5 to 14 years have been measured (DeBano et al., 1996; Robichaud et al., 2013b). The return to pre-fire conditions is affected by many characteristics such as the degree of soil burn severity, soil type, fire location within the watershed, ecosystem, topography, post-fire meteorological conditions and longer-term climate (Cerdà and Robichaud, 2009).

High soil burn severity may also cause or exacerbate water repellency in soils (Doerr et al., 2009a) which varies by inherent soil characteristics, soil moisture, and time since fire. Soil water repellency can develop when surface vegetation and litter are burned and the volatilized organic compounds are released into the soil profile where they condense on soil particles (DeBano, 1971; Ice et al., 2004; Shakesby and Doerr, 2006). Fire-induced soil water repellency is often detected 1- to 3-cm below the soil surface (Doerr et al., 2006; Robichaud, 2000)

and can exhibit high spatial variability (Lewis et al., 2008; Wagenbrenner and Robichaud, 2014). Given that the most apparent hydrological effect of soil water repellency is reduced infiltration, post-fire assessment teams have often used a field test of soil water repellency to estimate the reduction in infiltration.

The availability of the mini-disk tension infiltrometers provides a new opportunity for post-fire assessment teams to make quick field measurements of relative infiltration (relative to the instrument and test time). Both Lewis et al. (2006) and Robichaud et al. (2008) found that water drop penetration time (WDPT) tests and mini-disk infiltrometer measurements (1-min duration, mini-disk infiltrometer) (Decagon Devices, 2016) were closely related and either method would be suitable to predict soil water repellency. However, mini-disk infiltrometer measurements and their relation to small-plot-scale total infiltration (as measured by rainfall simulation) have not been studied.

Soil water repellency also occurs naturally in many different soils and environments (i.e. coarse grained soils in Australia, ash cap soils in Montana, and under vegetation types such as California chaparral and Big Sagebrush) (Doerr et al., 2009b; Hubbert et al., 2006; Huffman et al., 2001; Pierson et al., 2008; Robichaud et al., 2016). Since forest floor cover and naturally occurring, or inherent, water repellent soils often vary spatially on hillslopes, soil water repellency may not always reduce infiltration at the hillslope scale (Barrett and Slaymaker, 1989; Burch et al., 1989; DeBano, 1981; Robichaud et al., 2016). In

the immediate post-fire assessment period, land managers need timely data to make informed decisions about watershed mitigation treatments (Robichaud and Ashmun, 2013). We postulate that the mini-disk infiltrometer will provide information about soil water repellency and infiltration characteristics that will help inform managers in their decision making process.

This study applied a suite of vegetation and soil measurements, and small-plot rainfall simulations to: 1) determine the effects of high soil burn severity wildfire and slope steepness on vegetation and ground cover, soil water repellency, infiltration, runoff, and sediment yield from splash-sheet processes called interrill erosion; 2) determine how these variables change with time after fire; and 3) evaluate the correlations between the mini-disk field infiltrometer measurements at several depths and infiltration rates calculated from the rainfall simulations.

METHODS

Site characteristics

Experimental plots were established at the 2003 Hot Creek Fire, which ignited on 19 July and was contained on 7 August in south central Idaho (Figure 1). Of the 10,000 ha burned, more than 60% of the area was classified as moderate or high soil burn severity and more than half was identified as having water repellent soils (USDA, 2003). These data indicate severe fire conditions and watershed disturbance.

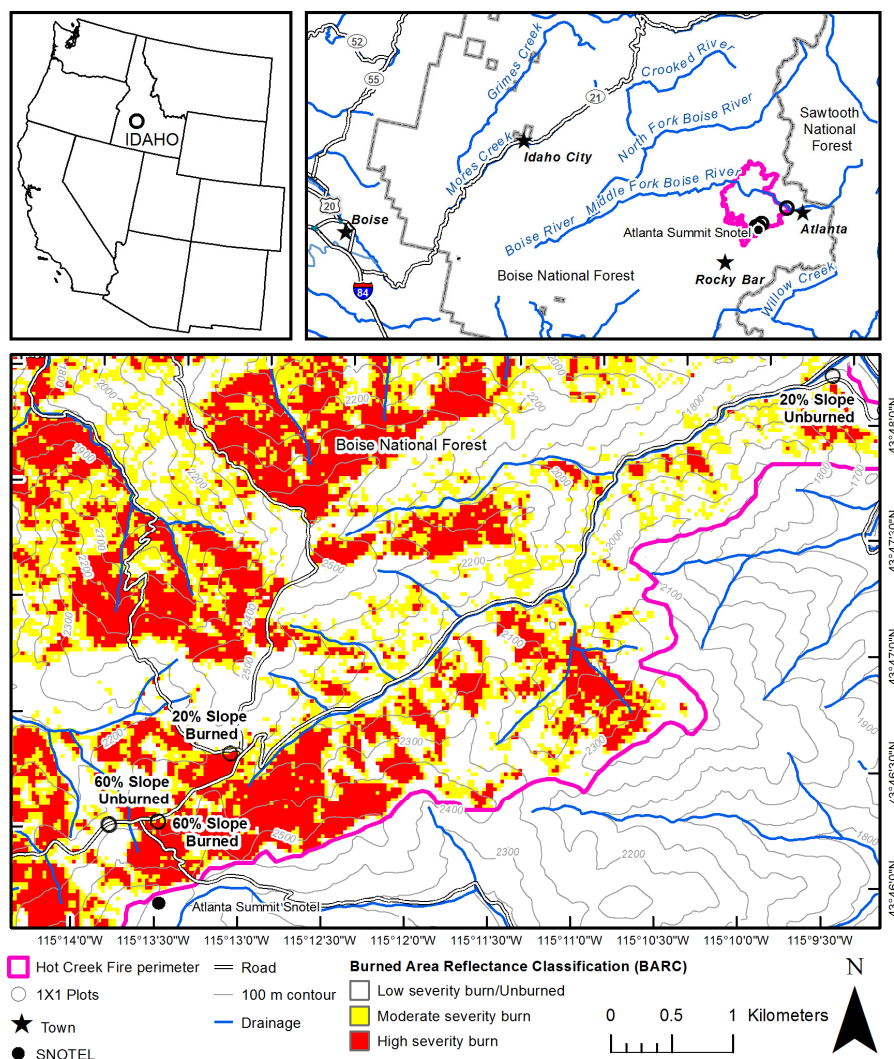


Fig. 1. Site map for Hot Creek Fire study area.

A sandy loam soil (sandy mixed Typic Cryorthent and Typic Xerochrept) with a parent material of Idaho Batholith granite dominated the study area (NRCS, 2010; NRCS, 2011). The pre-fire vegetation was characterized by Douglas-fir (*Pseudotsuga menziesii*) and subalpine fir (*Abies lasiocarpa*) in the overstory with geysers sedge (*Carex geyeri*) and grouse whortleberry (*Vaccinium scoparium*) in the understory (Steele et al., 1981). Mean annual precipitation for the study site averaged 1078 mm (~70% as snow) during the six year study period, as measured at the Atlanta Summit SNOTEL weather station (2310 m elevation) located 2 km from the study areas. Mean maximum temperature in August during the study period was 28°C, and mean minimum January temperature was -17°C. Yearly precipitation ranged from 831 to 1427 mm (NWCC, 2010) (Table 1). The rainfall simulation sites were located within 1 km of each other with elevations ranging between 2000 and 2330 m, except for the 20% slope-unburned site which was 6 km from the other sites at an elevation of 1700 m.

Ten rainfall simulation plots (0.5 m²) were established at each of four sites (40 plots total) that differed by slope (20% and 60%) and surface condition (burned at high severity and unburned control). Measurements of vegetation, ground cover, soil properties, and runoff and sediment yield occurred on each plot within 30 days after the fire (fire year, 2003) prior to any natural rainfall events, and was repeated in late summer of post-fire years one (2004), two (2005) and five (2008) (Table 2). Four plots were excluded in the rainfall simulations in 2008 because of damage to the plot frames: two each on the 20% burned and 60% unburned sites.

Standing dead vegetation, tree stumps, rocks, litter, and live plants by species in each plot were ocularly estimated (Elzinga et al., 1998) two weeks prior to rainfall simulations each year. Calibration and accuracy checks of the ocular ground cover estimates were conducted as described in Pierson et al. (2008). Total ground cover was the summed percent ground cover for each component, and the bare mineral soil was determined by subtracting total ground cover from 100% (Pierson et al., 2008).

Soil gravimetric water content (GWC) was measured in surface (0–2 cm) soil samples taken adjacent to each plot immediately prior to the rainfall simulation. Soil samples were oven dried at 100°C to determine the percent GWC, which is referred to as soil moisture hereafter.

Water repellency and relative infiltration rate were collected prior to rainfall simulation in a location adjacent to each study plot where the soil surface was fairly uniform and undisturbed by trees, animal burrows, etc. Measurement depths were adjusted by year based on findings by Robichaud et al. (2008) and others (e.g., Doerr et al., 2006). These studies have shown that soil water repellency after burning often occurs in the first few centimeters of the soil profile where hydrophobic compounds condense due to cooler temperatures (DeBano, 1981; Doerr et al., 2006). In the year of the fire, measurements were made at the soil surface only, and measurements in the first and second post-fire years were made at the surface and at each centimeter for depths 1–5 cm. In post-fire year five, measurements were made at the surface and at depths 1–5 cm on the burned plots, but only at 1- and 3-cm depths on the unburned plots. To compare coincident measurements between years, we analyzed available data from the surface, 1- and 3-cm depths.

Soil water repellency was measured prior to rainfall simulation using the water drop penetration time (WDPT) test as described in DeBano (1981) and Wilcox et al. (1988). Duff, ash, litter and debris were removed from the soil surface where eight drops of water were placed 5–10 mm apart with a 2-mm diameter nozzle bulb dropper. The time for each drop to pene-

Table 1. Post-fire precipitation at the Atlanta Summit SNOTEL.

Year	Post-fire year	Rainfall simulation date	Annual precipitation (mm)	Deviation from mean annual precipitation (mm)
2003	0	27 Aug 2003	1085	+7
2004	1	2 Aug 2004	1031	-47
2005	2	10 Aug 2005	934	-144
2006	3		1427	+349
2007	4		831	-247
2008	5	9 Sep 2008	1158	+80

trate the soil was recorded to the nearest second up to 5 minutes.

A hand-held tension infiltrometer (Mini Disk Infiltrometer, Meter Group formerly Decagon Devices, Pullman, WA) was used to assess a relative infiltration rate (mL min⁻¹) (Robichaud et al., 2008). The short time used for the test, the small contact area of the infiltration disk (~800 mm²), and the unconfined area of infiltration under the disk makes it difficult to directly compare the infiltration measured in this test to infiltration rates measured over longer times with more controlled conditions and sophisticated equipment—hence the term “relative infiltration rate”. With the mini-disk infiltrometer set to 1-cm of tension, the relative infiltration rate was defined as the amount of water leaving the device in one minute of contact with the soil, and the mean of three repetitions was calculated at each depth. For reference, Robichaud et al. (2008) established that the relative infiltration rate correlated to soil water repellency classes (as measured by the WDPT test) as: a) ≥8 mL min⁻¹ (WDPT 0 to 5 s) = no repellency; b) 3 to <8 mL min⁻¹ (WDPT 6 to 180 s) = weak to moderate repellency; and c) 0 to <3 mL min⁻¹ (WDPT 181 to 300 s) = strong repellency.

Rainfall simulation

The rainfall simulation equipment and procedures used in Robichaud et al. (2016) were nearly identical to this study. Rainfall was applied to each plot at a continuous rainfall intensity of 100 mm h⁻¹ (median = 100.6 mm h⁻¹) for one hour using a US Department of Agriculture Forest Service-modified Purdue-type 90° arc oscillating-nozzle rainfall simulator with specifications from Meyer and Harmon (1979). The application rate was approximately equal to the rainfall intensity of a 10-min rainfall event with a 5- to 10-year return period (Hanson and Pierson, 2001) adjusted for elevation (Bonnin et al., 2006) as well as exceeding the infiltration rate for the unburned forest condition (Robichaud, 2000).

Prior to each simulation, the rainfall was collected in a calibration pan covering the plot and measured with a graduated cylinder. The flow rate to the nozzles was adjusted so that the same per-unit-surface area rainfall rate was applied by repeating the calibration process if the slope-adjusted rainfall rate differed from the target rate by more than 5%. The oscillating nozzle allowed for a more intermittent simulated rainfall similar to natural rainfall with comparable velocity, drop size and intensity (Bertrand and Parr, 1961). A 3-m tall wind skirt was wrapped around the simulator to prevent wind interaction with the rainfall (Meyer and Harmon, 1979).

Each 0.5 m² rainfall simulation plot was delineated by a sheet metal frame with 15-cm tall sides, with 5 cm of each side extended into the soil. A covered tray at the downhill end of the frame captured runoff at the ground surface and routed the runoff into a pipe used for sampling. During the 60-min rainfall simulation, timed runoff samples were collected every minute for the first 16 minutes and every two minutes thereafter. If necessary, sample times were adjusted so that samples would

Table 2. Median values of ground cover, soil moisture, relative infiltration, and water drop penetration time (WDPT) reported by treatment, slope, and calendar year (post-fire year in parenthesis); • = no data. Infiltration and water repellency median values are further divided by depth (cm) of measurement. 95% confidence limits are shown in brackets. Within each column, different letters indicate a significant difference ($\alpha = 0.05$).

Site	Year	Ground cover (%)		Soil moisture ($m^3 m^{-3}$)		Relative infiltration ($ml\ min^{-1}$)			WDPT test (s)								
						Surface	1 cm	3 cm	Surface	1 cm	3 cm						
Unburned 20%	2003 (0)	67 [35–81]	bcd	0.20 [0.13–0.38]	a	7 [5–9]	bcd	•	•	5 [2–27]	cdef	•	•				
	2004 (1)	61 [26–80]	cde	0.12 [0.05–0.18]	abc	4 [1–7]	cde	7 [2–12]	abc	7 [4–14]	abc	90 [16–125]	abcd	15 [2–70]	bcde	0 [0–3]	e
	2005 (2)	58 [9–66]	de	0.14 [0.09–0.20]	ab	1 [0–8]	e	5 [1–9]	c	10 [6–16]	a	270 [90–300]	ab	44 [22–138]	abc	1 [0–25]	de
	2008 (5)	100 [95–100]	a	0.11 [0.05–0.22]	abc	•	•	12 [4–16]	abc	8 [5–13]	ab	•	•	1 [1–7]	de	2 [1–13]	cde
Unburned 60%	2003 (0)	94 [80–97]	ab	0.15 [0.05–0.27]	abc	4 [2–5]	de	•	•	•	•	18 [0–149]	bcde	•	•	•	•
	2004 (1)	88 [70–93]	abcd	0.03 [0.02–0.06]	def	2 [0–19]	cde	3 [2–13]	bc	6 [2–11]	abc	163 [1–300]	abc	75 [1–128]	abcd	5 [1–43]	abcde
	2005 (2)	87 [74–95]	abc	0.04 [0.02–0.06]	def	1 [0–2]	e	6 [2–13]	abc	5 [1–13]	abc	269 [174–300]	a	101 [4–271]	abc	32 [1–205]	abcd
	2008 (5)	95 [85–98]	a	0.04 [0.02–0.09] ^e	def	•	•	12 [7–14]	abc	14 [7–27]	a	•	•	2 [1–41]	cde	1 [1–15]	cde
Burned 20%	2003 (0)	1 [0.05–1]	h	0.07 [0.04–0.10]	bcd	0 [0–1]	e	•	•	•	•	300 [194–300]	a	•	•	•	•
	2004 (1)	1 [0.05–4]	h	0.03 [0.02–0.06]	def	10 [5–14]	abc	4 [0–6]	c	1 [0–4]	c	1 [0–38]	efg	158 [16–300]	ab	263 [10–300]	a
	2005 (2)	2 [0.05–9]	fgh	0.04 [0.03–0.06]	def	12 [7–17]	ab	3 [0–14]	c	2 [0–4]	bc	3 [1–38]	defg	236 [104–300]	a	133 [17–300]	ab
	2008 (5)	6 [3–28]	efg	0.02 [0.01–0.05] ^e	ef	15 [12–19]	a	14 [9–16]	ab	13 [0–16]	a	1 [0–1]	efg	1 [0–6]	de	2 [1–269]	bcde
Burned 60%	2003 (0)	1 [0.5–3]	gh	0.03 [0.02–0.07]	def	1 [0–3]	e	•	•	•	•	224 [153–300]	a	•	•	•	•
	2004 (1)	1 [0.5–3]	gh	0.04 [0.01–0.07]	def	8 [6–13]	abcd	3 [2–7]	c	1 [0–2]	c	1 [0–46]	efg	82 [7–201]	abc	142 [4–269]	ab
	2005 (2)	1 [0–4]	gh	0.05 [0.04–0.08]	cde	17 [11–23]	a	5 [1–8]	c	1 [0–3]	c	0 [0–1]	g	67 [8–205]	abc	38 [5–300]	abc
	2008 (5)	8 [5–20]	ef	0.02 [0.02–0.05]	ef	17 [8–20]	a	15 [11–20]	a	12 [5–16]	a	1 [0–1]	fg	1 [0–2]	e	1 [0–35]	cde

fit in a 1-L bottle. Sediment-laden water samples were weighed in the lab, dried, and re-weighed to obtain the sample runoff volume and the sediment concentration. The weight of any residual sediment in the tray was also dried and included in the total sediment yield for each rainfall simulation.

Total infiltration was calculated by subtracting the total runoff from the total applied rainfall (rainfall rate multiplied by horizontal plot area). The infiltration amount was also calculated for the first 3-, 5-, and 10-minutes of the simulation so that these values could be correlated to mini-disk infiltrometer measurements.

Statistical analysis

Most variables collected reflected non-normal and non-transformable distributions, therefore, nonparametric statistical methods were used (Corder and Foreman, 2009; R Core Team, 2013) by calculating medians (Corder and Foreman, 2009) and the 95% nonparametric (distribution-free) confidence intervals (Hollander and Wolfe, 1999; R Core Team, 2013). It was assumed that unburned plots were spatially close enough to the burned plots to be representative of the burned areas prior to the fire. Significant differences between years, slopes and treatment were analyzed using Kruskal–Wallis comparisons based on rank (Conover, 1999; Corder and Foreman, 2009; R Core Team, 2013). Multiple comparisons were conducted using the post-hoc tests in the Kruskal function in the R package “agricolae” (Conover, 1999; R Core Team, 2013). The Benjamini and Hotchberg false discovery rate correction was used to adjust the p-values to minimize type I errors for multiple comparison tests (Benjamini and Hochberg, 1995). Spearman correlation coeffi-

cients were calculated to determine significant relationships between all variables (Conover, 1999; Corder and Foreman, 2009; R Core Team, 2013). All tests were considered significant at $\alpha = 0.05$. A ratio of infiltration on the burned sites to infiltration on the unburned sites was calculated for both the relative infiltration values as measured by the mini-disk infiltrometer and the actual infiltration values from the rainfall simulation for each year.

RESULTS

Site characteristics

Nearly 100% of the ground cover was consumed on severely burned portions of the Hot Creek Fire, and consequently, vegetation recovery was slow on the burned plots during the five years of monitoring. By post-fire year five, median ground cover on the burned sites was 7% compared to 95–100% on the unburned sites (Table 2). Ground cover varied on the unburned plots in the first three years of the study, and was slightly lower on the 20% unburned plots (60–70%) compared to the 60% unburned plots (~90%) (Table 2).

Soil moisture in the fire year was lower on the burned sites (0.03–0.07, Table 2) compared to the unburned sites (0.15–0.20). After the first year, soil moisture was consistently greater on the 20% slope unburned site (0.11–0.14) than all other sites (0.02–0.05), likely due to nearby ground water seeps. The lack of cover and a possible increase in soil water evaporation may have also contributed to low soil moisture on the burned sites. Varying degrees and depths of soil water repellency as well as reduced relative infiltration were found on both the burned and unburned sites in the first two post-fire years (Table 2).

Table 3. Spearman correlation coefficients between relative infiltration values (mL min^{-1}) and WDPT values (s) are shown for surface, 1-cm and 3-cm depths using data from all years—all treatments and using data from all years—burned sites only. Correlations are all negative because as infiltration decreases, WDPT values increase. $p < 0.0001$ for all values.

Depth (cm)	All years—all treatments		All years—burned only	
	<i>n</i>	ρ	<i>n</i>	ρ
Surface	138	-0.83	78	-0.69
1	122	-0.68	61	-0.77
3	120	-0.78	60	-0.84

Relative infiltration rate was significantly correlated ($p < 0.0001$) with WDPT measurements at all depths and over all years and treatments ($\rho = -0.77$ to -0.84 , Table 3).

In the fire year (2003), the mineral soil surface was strongly water repellent (WDPT > 180 s, relative infiltration rate < 3 mL min^{-1}) on burned sites, but was wettable to only slightly water repellent on unburned sites (WDPT < 60 s, relative infiltration rate > 3 mL min^{-1}). On burned plots in post-fire years one and two (2004 and 2005), soil water repellency and reduced infiltration was moderate to strong at soil depths of 1- and 3-cm and absent at the mineral soil surface when surface measurements were taken (Table 2). In contrast, water repellency and relative infiltration rate on unburned soils in post-fire years one and two generally exhibited moderate to strong repellency at the mineral surface, slight to moderate repellency at 1-cm depth and wettable to slightly repellent conditions at 3-cm depth (Table 2). No repellency or reduced infiltration was measured at any of the sites or depths in the fifth post-fire year (2008).

The differences between the 20% and 60% slope sites (both burned and unburned) were varied and unpredictable. Through the first two post-fire years, ground cover was lower on the 20% slope unburned site than the 60% slope unburned site, despite having statistically higher soil moisture in post-fire years 1 and 2 (but not the year of the fire). In the final year of our study, soil moisture was still higher on the 20% slope unburned site than the 60% slope unburned site, and both sites had nearly 100% ground cover (Table 2).

Soil water repellency and relative infiltration were similar on the 20% and 60% slope unburned sites at comparable depths over all years. Total infiltration was significantly greater for the unburned 20% slope plots than the unburned 60% slope plots through the first post-fire year. These differences in cover and soil properties suggest some inherent site differences between the two unburned sites, which highlights the importance of spatial scale when measuring or predicting watershed characteristics.

Rainfall simulation

The fire significantly decreased total infiltration on the 20% burned plots (Table 4). The infiltration rates for simulated rainfall on 20% slope burned plots were one third that for unburned conditions through two post-fire years (2003–2005; Figure 2). In contrast, burning did not significantly reduce infiltration rate or total infiltration on 60% slope plots (Table 4, Figure 2). By the fifth post-fire year (2008), median total infiltration ranged from 62–83 mm on all plots, with the exception of 20% slope burned plots (27 mm).

Interrill erosion sediment yield from burned rainfall simulation plots increased after fire by at least 10 to 100 times on both 60% and 20% slopes, respectively, compared to their unburned counterparts (Table 4). Through the first post-fire year, sediment yield from 20% slope burned plots (1900–2214

Table 4. Median values of total infiltration (mm) and total sediment (g m^{-2}) from rainfall simulations reported by treatment, slope, and calendar year (post-fire year in parenthesis). Each value is calculated from $n = 10$ samples, unless indicated otherwise. Within each column and variable, different letters indicate a significant difference ($\alpha = 0.05$). 95% confidence limits are shown in brackets.

Site	Year	Total infiltration (mm)	Total sediment (g m^{-2})	
Unburned 20%	2003 (0)	61 [49–97]	abc	8 [2–34] ef
	2004 (1)	67 [55–91]	ab	7 [5–17] ef
	2005 (2)	70 [49–98]	ab	5 [0.4–11] f
	2008 (5)	83 [69–97]	a	3 [2–11] f
Unburned 60%	2003 (0)	35 [28–44]	de	57 [23–139] d
	2004 (1)	42 [37–49]	cde	40 [16–93] d
	2005 (2)	45 [36–70]	bcd	39 [15–162] d
	2008 (5) ^a	73 [70–91]	a	35 [25–147] de
Burned 20%	2003 (0)	20 [13–26]	g	1900 [1307–2249] ab
	2004 (1)	18 [15–24]	g	2214 [1725–2656] ab
	2005 (2)	19 [15–31]	fg	1698 [1305–2306] ab
	2008 (5) ^a	27 [23–59]	efg	329 [182–902] cd
Burned 60%	2003 (0)	33 [32–36]	de	2151 [1726–2586] ab
	2004 (1)	33 [32–36]	def	2356 [1957–2996] a
	2005 (2)	33 [31–40]	def	2532 [1910–3193] a
	2008 (5)	62 [48–83]	abc	1200 [372–2152] bc

^aOnly 8 values were used in calculations.

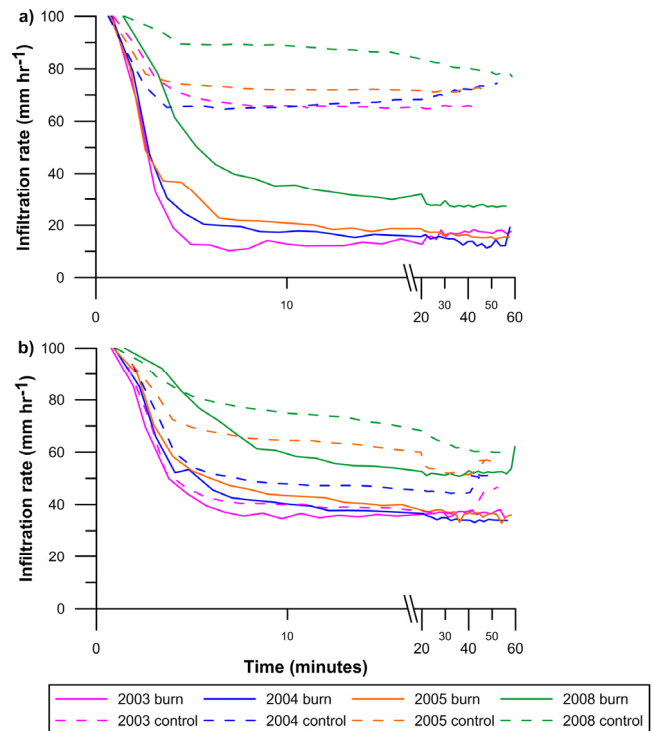


Fig. 2. Infiltration rate versus time for the rainfall simulator experiments on burned and control sites on a) 20% slope plots and b) 60% slope plots, in the year of the fire (2003), post-fire year 1 (2004), post-fire year 2 (2005), and post-fire year 5 (2008).

g m^{-1}) and 60% slope burned plots (2151–2356 g m^{-1}) was similar. However, by post-fire year five (2008), there was one-quarter less sediment on the 20% slope burned plots (329 g m^{-1}) than the 60% slope burned plots (1200 g m^{-1}). Over all years and plots ($n = 156$), slope had a low, yet significant positive correlation to sediment yield ($\rho = 0.26$; $p = 0.001$).

Over the study period, sediment yields on the burned sites decreased as ground cover returned and soils stabilized. Total sediment was correlated to ground cover over all years and plots at $\rho = -0.73$ ($p < 0.0001$). Although sediment decreased

Table 5. Correlation coefficients (ρ) between relative infiltration values as measured at the surface, 1-cm and 3-cm depths and total infiltration values as measured at 3-, 5-, and 10-min in the rainfall simulation and final infiltration (60 min). Correlations for data from all years–all treatments and for data from all years–burned sites only are shown.

Depth (cm)	All years – all treatments				All years – burned only			
	3 min	5 min	10 min	60 min	3 min	5 min	10 min	60 min
Surface	0.20*	0.15	0.10	–0.11	0.33*	0.33*	0.39*	0.31*
1	0.40**	0.48**	0.49**	0.32*	0.51*	0.60**	0.60**	0.48*
3	0.30*	0.50**	0.52**	0.57**	0.28*	0.42*	0.46*	0.37*

* $p < 0.05$
 ** $p < 0.001$

during the study, the decrease was statistically significant only between post-fire year two and post-fire year five (Table 4) when sediment decreased by 80% on the 20% burned site and by half on the 60% burned site. By post-fire year five, sediment produced on the burned sites ($329\text{--}1200\text{ g m}^{-1}$) was still orders of magnitude greater than unburned sites ($3\text{--}35\text{ g m}^{-1}$, Table 4). Sediment yields were similar within a slope class on unburned sites in all years (Table 4); however, there was significantly less sediment on the 20% slope plots than on the 60% slope plots in every year regardless of burn.

In the year of the fire alone, relative infiltration (measurements made with a mini-disk infiltrometer) taken at the soil surface were significantly correlated to total infiltration from the rainfall simulation when all treatments were pooled ($\rho = 0.67$; $p < 0.0001$) (data not shown). As relative infiltration increased, total infiltration increased. When all years were considered, relative infiltration measurements taken at 1- or 3-cm depth were more indicative of total infiltration than those taken at the soil surface (Table 5). In general, greater relative infiltration values below the soil surface indicated an increase in total infiltration over all years and plots.

The ratio analysis comparing relative infiltration at 1- and 3-cm depths to total infiltration indicated similarly trending values over time (Figure 3). In the year of the fire there was much less infiltration on the burned 20% slope plots compared to the control plots (ratio = 0.3) (Figure 3a), while infiltration was nearly equivalent on the 60% slope plots (ratio = 0.97). In 2004 and 2005 infiltration was lower on all burned plots than on control plots, which were measured both by rainfall simulation and the mini-disk infiltrometer measurements (Figure 3). In the fifth post-fire year (2008), mini-disk infiltrometer relative infiltration measurements suggest recovery to pre-fire (unburned) levels, while rainfall simulation showed continued reduced infiltration on the burned plots, particularly on the 20% slope site.

To evaluate our ability to associate relative infiltration as measured by the mini-disk infiltrometer with non-steady state infiltration amounts, we calculated correlations at 3-, 5-, and 10-min into the hour-long rainfall simulations. The strongest relationships were found between the 1-cm relative infiltration measures at 5- or 10-min into the rainfall simulation on the burned plots ($\rho = 0.6$; $p < 0.0001$, Table 5). Slightly weaker yet significant correlations ($\rho = 0.4\text{--}0.5$; $p < 0.001$) were found at the 3-cm depth at the same time periods. When all treatments were pooled, relative infiltration rate measurements taken at 1- and 3-cm depth were also significantly correlated ($\rho = 0.3\text{--}0.5$) with total infiltration (Table 5).

DISCUSSION

Trends in site recovery

One of the most startling impacts of the Hot Creek Fire was the extremely slow recovery of vegetation in the high severity burned areas included in this study. Generally, most burned areas in western US mountain regions exhibit significant vege-

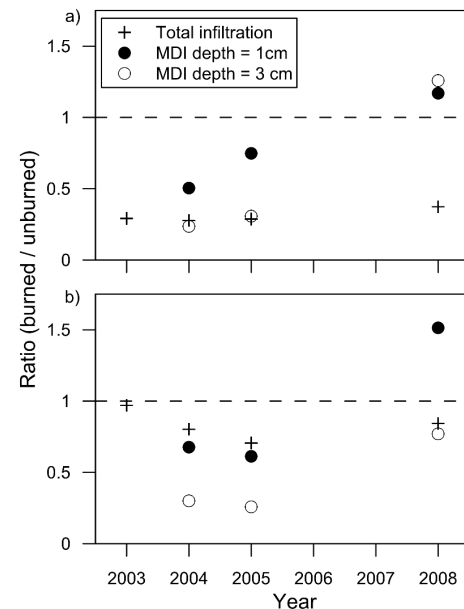


Fig. 3. Ratio of burned to unburned (control) infiltration values for total infiltration from the rainfall simulation and for relative infiltration measured with the mini-disk infiltrometer (MDI) on a) 20% slope plots, and b) 60% slope plots. 2003 was the year of the fire, post-fire year 1 (2004), post-fire year 2 (2005), and post-fire year 5 (2008). Values below the dashed line indicate less infiltration on the burned plots compared to the unburned plots; ratios increase over time as infiltration returns to unburned levels.

tation recovery by post-fire year five, although they can take up to 13 years or more to fully return to pre-fire levels (DeBano et al., 1996; Goetz et al., 2006; Robichaud et al., 2013a). Given that 60–70% natural ground cover is needed to effectively decrease erosion (Benavides-Solorio and MacDonald, 2005; Pannkuk and Robichaud, 2003; Wine et al., 2012), the less than 10% median ground cover in post-fire year 5 on the burned sites in our study (compared to 95–100% on the unburned sites) provided little protection from erosion. Slow vegetative recovery is usually attributed to low rainfall; however, annual and growing season (April through September) precipitation over monitoring years was not largely different from the mean precipitation prior to the fire (Table 1). The extremely slow recovery of vegetation observed in this study is more likely due to unusually high soil burn severity, and the subsequent loss of soil and surface cover due to wind- and water-driven erosion. It is probable that the fire intensity and severity of the Hot Creek Fire sterilized the soil, and possibly the seed bank, thus limiting various regeneration strategies of plant growth in the area (Graham, 2015; Mataix-Solera et al., 2009; Ryan, 2002). The sites most likely experienced intense crown and ground fire due to pre-heated dry fuels resulting in soil temperatures that exceeded 120°C . Such intense soil heating generally kills viable seeds and underground rhizomes from which post-fire vegetative

regrowth normally occurs (Ryan, 2002). It is also possible that the strong soil water repellency reported immediately after the fire and through post-fire year two also decreased the vegetative survival by decreasing infiltration especially in the summer as the soil dries and water repellency is enhanced (Madsen et al., 2012).

In the year of the fire, there was significantly higher soil water repellency on the soil surface of the burned sites than the unburned sites. Although we did not sample water repellency or relative infiltration below the soil surface in the year of the fire, we likely would have measured strong water repellency and reduced infiltration deeper into the soil profile (Doerr et al., 2000) as we did in subsequent years of the study (Table 2). At the scale of our measurements, soil water repellency contributed to reduced infiltration rates (DeBano, 1971; Doerr et al., 2009b). This reduced infiltration combined with loss of soil structure and ground cover from the high severity fire led to greater interrill erosion and subsequent greater sediment yields on the burned plots throughout the study period.

The unburned sites exhibited natural, or inherent, water repellency intermittently throughout the study period, particularly on the soil surface (Doerr et al., 2009a), where water repellency was sometimes greater on the unburned than on the burned sites (Table 2). Inherent soil water repellency is characteristic of the ash cap soils in the study area (Doerr et al., 2009a; Kawamoto et al., 2007; Robichaud et al., 2016). In a previous study on the Hot Creek Fire, moderate levels of water repellency were measured through post-fire recovery year five (Robichaud et al., 2013a). While we did not measure any soil water repellency in the fifth year on the plots in this study, we attribute this inconsistency to site differences (e.g., aspect, soil moisture, soil organic matter).

The high severity burned sites exhibited significantly less vegetation and lower relative infiltration, somewhat lower total infiltration, and increased sediment yield compared to the unburned sites; however all values trended toward unburned site values over time. Measurements of soil water repellency, relative infiltration rate and ground cover were aggregately good indicators of infiltration and interrill sediment yields. It was difficult to separate the effects of any one factor, as they are not independent and tend to confound one another. This is consistent with previous post-fire studies that have shown high correlations among these factors (Benavides-Solorio and MacDonald, 2001; Robichaud et al., 2013a; Shakesby et al., 1993) and was also consistent with previous studies where ground cover was the predominate indicator of infiltration and runoff on recovering burned sites (Benavides-Solorio and MacDonald, 2005; Johansen et al., 2001; Larsen et al., 2009; Robichaud et al., 2013a). Vieira et al. (2015) found stronger relationships between burn severity and sediment yields than with runoff, which is consistent with what we measured. The measured sediment yields were likely lower than typical hillslope erosion rates after fire as suggested by Williams et al. (2016), who states that runoff contributes to the formation of concentrated-flow paths that would increase sediment yields above those measured in this study, where the concentrated-flow processes were not active.

The ratio of infiltration on burned to unburned sites was consistent with other literature and indicated a recovery trend towards pre-fire conditions (Figure 3). In the first and second post-fire years (2004, 2005), the ratio of total infiltration values was closer to relative infiltration measured at 1-cm on the 60% slope plots (~0.6), and at 3-cm on the 20% slope plots (0.25). Martin and Moody (2001) reported a ratio of about 0.4 on burned mountainous sites in New Mexico and Colorado in the

first four months after wildfire. On burned oak sites in Spain, Imeson et al. (1992) measured infiltration ratios of 0.3 to 0.5 for up to two years following fire, and Arend (1941) measured infiltration in the Missouri Ozarks (oak forests) which had a burned to unburned ratio of 0.6. By the fifth post-fire year (2008), the ratio of total and relative infiltration values at both depths were mostly greater than 1.0, indicating a return to pre-fire (unburned) infiltration values at all sites. Interestingly, infiltration values measured by the MDI (but not the rainfall simulation) indicated greater infiltration on the burned sites compared to the unburned sites. This may be in part due to the destruction of the inherent soil water repellency due to the burning of the surface soil organic layers. The meta-analysis by Ebel and Martin (2017) reported upwards of 20 years for organic matter to recover to pre-fire levels in soil. The ability to estimate the difference in infiltration between burned and unburned sites with a mini-disk infiltrometer test is an important benefit for quick assessment of post-fire conditions.

Slope effects

On the burned areas, we observed varied microtopography of the soil surface between the 20% and 60% slope sites (Figures 4a, b). Large numbers of burned roots and displaced rocks created macropores on the 60% slope site that were not observed on the 20% slope site. These macropores could have increased infiltration by providing pathways for water to penetrate reducing overland flow, and subsequently decreased sediment yield by allowing places for sediment deposition within the plot. Cerdà and García-Fayos (1997) cited soil cracks and heterogeneous surfaces to be the controlling factors on infiltration, runoff, and sediment yields on sloped plots. Imeson et al. (1992) made similar observations, that on comparable slopes within their study “hydrological processes are structured by interactions with vegetation.” Small plots are particularly prone to microtopographic- or point-differences because they do not have the benefit of the equalizing properties of an entire hillslope or watershed (Larsen et al., 2009). The burned 60% slope plots had greater infiltration as compared to the 20% burned plots, but the 60% burned plots also had greater sediment yields compared to the burned 20% slope site, especially in post-fire years two and five. This may indicate that the soil on the burned 60% site was more erodible than the soil on the burned 20% site or that the greater influence of gravity on the burned 60% slope site increased erosion as compared to the burned 20% site (Scott et al., 2009).

The use of relative infiltration measurements

Relative infiltration rates, as measured by the mini-disk infiltrometer at 1- and 3-cm were significantly correlated with the total infiltration measurements made during the first ten minutes (non-steady state) of the rainfall simulations (Table 5). This early period of the 60-min 100 mm h⁻¹ rainfall simulation (Figure 2) provides a reasonable facsimile of the short-duration, high-intensity convective rain storms (i.e., not long enough to reach steady-state infiltration) that are fairly typical in the Rocky Mountains and often cause the most runoff and erosion in post-fire environments (Robichaud et al., 2016; Wondzell and King, 2003). Thus, knowing the potential infiltration rate for such a rainstorm would allow for more accurate post-fire erosion modeling. From the data analyzed in this study, it seems reasonable that mini-disk measurements of relative infiltration could be transformed into total infiltration values, or at the very least, a ratio of infiltration reduction that could then be



Fig. 4. Example plots from a) the burned 20% site, and b) the burned 60% site. The metal plot frames delineate the 0.5 m² plot area from which the runoff and sediment samples were taken. Black ovals on b) show the rocks and stumps on site which can indicate macropores and increased ponding, while arrows highlight the rougher soil surface texture which slows surface flow and may increase infiltration.

used within various prediction models, such as the Erosion Risk Management Tool (ERMiT; Robichaud et al., 2007). Modeling post-fire erosion is most beneficial to land managers for determining downstream impacts and where erosion mitigation treatments are most likely needed (Elliott, 2013; Moody et al., 2013).

CONCLUSION

The Hot Creek Fire study area experienced a slow and incomplete return to pre-fire vegetation cover and infiltration conditions during our five-year study. Ground cover was remarkably low on all burned sites through post-fire year five; consequently, runoff and interrill erosion were elevated in all years on the burned sites compared to the unburned sites. Differences in site microtopography and burn characteristics between the burned 20% and 60% slope sites affected soil structure and composition, resulting in less infiltration and more runoff on the sites with low slopes than sites with steeper slopes. Over all burned sites, total infiltration rate decreased and sediment yield increased immediately after the fire and

gradually trended toward unburned conditions in the years following the fire.

Relative infiltration rate measured with the mini-disk infiltrometer was significantly correlated to total infiltration and particularly non-steady state infiltration amounts. We conclude these relative measurements taken at shallow depths (1- to 3-cm) below the soil surface could be used to describe potential infiltration of a burned site during short-duration high-intensity storms and used in post-fire erosion models. Modelling post-fire soil conditions and the resulting potential for increased runoff and sediment is an important task for land managers after wildfires.

Acknowledgements. This study was funded in part by the US Department of Interior and US Department of Agriculture Joint Fire Sciences Program. The authors would like to acknowledge the contributions of field crews from the US Department of Agriculture, Forest Service, Rocky Mountain Research Station and Agricultural Research Service, Northwest Research Center and logistical support from the Boise National Forest. Additional special thanks to Joseph Wagenbrenner for assistance in statistical analysis, and Louise Ashmun for providing critical comments on earlier drafts of the manuscript. We also thank two anonymous reviewers who provided comments that greatly improved the clarity of the manuscript.

REFERENCES

- Agee, J.K., 1996. *Fire Ecology of the Pacific Northwest Forests*. Island Press, Washington DC, USA, 505 p.
- Arend, J.L., 1941. Infiltration rates of forest soils in the Missouri Ozarks as affected by burning and litter removal. *J. Forest.*, 39, 726–728.
- Barrett, G., Slaymaker, O., 1989. Identification, characterization, and hydrological implications of water repellency in mountain soils, Southern British Columbia. *Catena*, 16, 4, 477–489. DOI: 10.1016/0341-8162(89)90029-5.
- Benavides-Solorio, J.D., Macdonald, L.H., 2001. Post-fire runoff and erosion from simulated rainfall on small plots, Colorado Front Range. *Hydrol. Process.*, 15, 2931–2952. DOI: 10.1002/hyp.383.
- Benavides-Solorio, J.D., Macdonald, L.H., 2005. Measurement and prediction of post-fire erosion at the hillslope scale, Colorado Front Range. *Int. J. Wildland Fire*, 14, 4, 457–474. DOI: 10.1071/WF05042.
- Benjamini, Y., Hochberg, Y., 1995. Controlling the false discovery rate: a practical and powerful approach to multiple testing. *J. Roy. Stat. Soc. Series B Methodology*, 57, 1, 289–300.
- Bertrand, A.R., Parr, J.F., 1961. Design and operation of the Purdue sprinkling infiltrometer. *Research Bulletin No. 723*. U.S. Department of Agriculture, Purdue University Agricultural Experiment Station, Lafayette, Indiana, USA.
- Bonnin, G.M., Martin, D., Lin, B., Parzybok, T., Yekta, M., Riley, D., 2006. *Precipitation frequency atlas of the United States*. NOAA Atlas 14, Volume 1, Version 4. NOAA National Weather Service, Silver Spring, Maryland, USA.
- Burch, G.J., Moore, I.D., Burns, J., 1989. Soil hydrophobic effects on infiltration and catchment runoff. *Hydrol. Process.*, 3, 3, 211–222. DOI: 10.1002/hyp.3360030302.
- Cerdà, A., 1996. Seasonal variability of infiltration rates under contrasting slope conditions in southeast Spain. *Geoderma*, 69, 3–4, 217–232. DOI: 10.1016/0016-7061(95)00062-3.
- Cerdà, A., García-Fayos, P., 1997. The influence of slope angle on sediment, water and seed losses on badland landscapes. *Geomorphology*, 18, 77–90. DOI: 10.1016/S0169-555X(96)00019-0.
- Cerdà, A., Robichaud, P.R., 2009. Fire effects on soil infiltration. In: Cerdà, A., Robichaud, P.R. (Eds.): *Fire Effects on Soils and*

- Restoration Strategies. Science Publishers, Enfield, New Hampshire, USA, pp. 81–103.
- Conover, W.J., 1999. *Practical Nonparametric Statistics*. 3rd ed. John Wiley & Sons Inc., New York, New York, USA, 816 p.
- Corder, G.W., Foreman, D.I., 2009. *Nonparametric Statistics for Non-Statisticians: A Step-by-Step Approach*. John Wiley & Sons, Inc., Hoboken, New Jersey, USA, 264 p.
- DeBano, L.F., 1971. The effect of hydrophobic substances on water movement in soil during infiltration. *Soil Sci. Soc. Am. Proc.*, 35, 2, 340–343.
- DeBano, L.F., 1981. Water repellent soils: a state-of-the-art. General Technical Report PSW-46. US Department of Agriculture, Forest Service, Pacific Southwest Forest and Range Experiment Station, Berkeley, California, USA, 21 p.
- DeBano, L.F., Ffolliott, P.F., Baker, M.B., 1996. Fire severity effects on water resources. In: Ffolliott, P.F., DeBano, L.F., Baker, Jr., M.B., Gottfried, G.J., Solis-Garza, G., Edminster, C.B., Neary, D.G., Allen, L.S., Hamre, R.H. (Eds.): *Proc. Symp. Effects of fire on Madren province ecosystems*. General Technical Report RM-GTR-289. US Department of Agriculture, Forest Service, Rocky Mountain Forest and Range Experiment Station, Ft. Collins, Colorado, USA, pp. 77–84.
- DeBano, L.F., Ffolliott, P.F., Neary, D.G., 1998. *Fire's Effects on Ecosystems*. John Wiley and Sons, Inc., New York, New York, USA, 352 p.
- Decagon Devices, Inc. 2016. Mini disk infiltrometer manual, Ver. September 2, 2016. Decagon Devices Inc., Pullman, WA. Available at: http://manuals.decagon.com/Manuals/10564_Mini%20Disk%20Infiltrometer_Web.pdf (accessed 2 February 2017).
- Doerr, S.H., Shakesby, R.A., Walsh, R.P.D., 2000. Soil water repellency: its causes, characteristics and hydro-geomorphological significance. *Earth-Sci. Rev.*, 51, 33–65. DOI: 10.1016/S0012-8252(00)00011-8.
- Doerr, S.H., Shakesby, R.A., Blake, W.H., Chafer, C.J., Humphreys, G.S., Walbrink, P.J., 2006. Effects of differing wildfire severities on soil wettability and implications for hydrological response. *J. Hydrol.*, 319, 1, 295–311. DOI: 10.1016/j.jhydrol.2005.06.038.
- Doerr, S.H., Woods, S.W., Martin, D.A., Casimiro, M., 2009a. 'Natural background' soil water repellency in conifer forests of the north-western USA: Its prediction and relationship to wildfire occurrence. *J. Hydrol.*, 371, 1–4, 12–21. DOI: 10.1016/j.jhydrol.2009.03.011.
- Doerr, S.H., Shakesby, R.A., MacDonald, L.H., 2009b. Soil water repellency: a key factor in post-fire erosion. In: Cerdà, A., Robichaud, P.R. (Eds.): *Fire Effects on Soils and Restoration Strategies*. Science Publishers, Enfield, New Hampshire, USA, pp. 197–224.
- Ebel, B.A., Martin, D.A., 2017. Meta-analysis of field-saturated hydraulic conductivity recovery following wildland fire: Applications for hydrologic model parameterization and resilience assessment. *Hydrol. Process.*, 31, 3682–3696. DOI: 10.1002/hyp.11288.
- Elliot, W.J., 2013. Erosion processes and prediction with WEPP technology in forests in the north-western US. *T. ASABE*, 56, 2, 563–579. DOI: 10.13031/2013.42680.
- Elzinga, C.L., Salzer, D.W., Willoghby, J.W., 1998. *Measuring and monitoring plant populations*. Technical Reference 1730-1. Bureau of Land Management, US Department of the Interior, Denver, Colorado.
- Goetz, S.J., Fiske, G.J., Bunn, A.G., 2006. Using satellite time-series data sets to analyze fire disturbance and forest recovery across Canada. *Remote Sens. Environ.*, 101, 3, 352–365. DOI: 10.1016/j.rse.2006.01.011.
- Graham, R., 2015. Personal communication.
- Hanson, C.L., Pierson, F.B., 2001. Characteristics of extreme precipitation and associated streamflow in the Reynolds Creek Experimental Watershed, Idaho. In: *Proceedings of the 12th Symposium on Global Climate Change*. American Meteorological Society, Boston, MA, pp. J2.13–J2.16.
- Hollander, M., Wolfe, D.A., 1999. *Nonparametric Statistical Methods*. 2nd ed. John Wiley & Sons, Inc., New York, New York, 816 p.
- Hubbert, K.R., Preisler, H.K., Wohlgemuth, P.M., Graham, R.C., Narog, M.G., 2006. Prescribed burning effects on soil physical properties and soil water repellency in a steep chaparral watershed, Southern California, USA. *Geoderma*, 130, 3–4, 284–298. DOI: 10.1016/j.geoderma.2005.02.001.
- Huffman, E.L., MacDonald, L.H., Stednick, J.D., 2001. Strength and persistence of fire-induced soil hydrophobicity under ponderosa and lodgepole pine, Colorado Front Range. *Hydrol. Process.*, 15, 15, 2877–2892. DOI: 10.1002/hyp.379.
- Ice, G.G., Neary, D.G., Adams, P.W., 2004. Effects of wildfire on soils and watershed processes. *J. Forest.*, 102, 6, 15–20.
- Imeson, A.C., Verstraten, J.M., van Mulligan, E.J., Sevink, J., 1992. The effects of fire and water repellency on infiltration and runoff under Mediterranean type forest. *Catena*, 19, 3–4, 345–361. DOI: 10.1016/0341-8162(92)90008-Y.
- Johansen, M.P., Hakonson, T.E., Breshears, D.D., 2001. Post-fire runoff and erosion from rainfall simulation: contrasting forests with shrublands and grasslands. *Hydrol. Process.*, 15, 15, 2953–2965. DOI: 10.1002/hyp.384.
- Kawamoto, K., Moldrup, P., Komatsu, T., de Jonge, L.W., Oda, M., 2007. Water repellency of aggregate size fractions of volcanic ash soil. *Soil Sci. Soc. Am. J.*, 71, 6, 1658–1666. DOI: 10.2136/sssaj2006.0284.
- Larsen, I.J., MacDonald, L.H., Brown, E., Rough, D., Welsh, M.J., Pietraszek, J.H., Libohova, Z., de Dios Benavides-Solorio, J., Schaffrath, K., 2009. Causes of post-fire runoff and erosion: Water repellency, cover, or soil sealing? *Soil Sci. Soc. Am. J.*, 73, 1393–1407. DOI: 10.2136/sssaj2007.0432.
- Lentile, L.B., Holden, Z.A., Smith, A.M.S., Falkowski, M.J., Hudak, A.T., Morgan, P., Lewis, S.A., Gessler, P.E., Benson, N.C., 2006. Remote sensing techniques to assess active fire characteristics and post-fire effects. *Int. J. Wildland Fire*, 15, 319–345. DOI: 10.1029/2006JG000230.
- Lewis, S.A., Wu, J.Q., Robichaud, P.R., 2006. Assessing burn severity and comparing soil water repellency, Hayman Fire, Colorado. *Hydrol. Process.*, 20, 1, 1–16. DOI: 10.1002/hyp.5880.
- Lewis, S.A., Robichaud, P.R., Frazier, B.E., Wu, J.Q., Laes, D.Y.M., 2008. Using hyperspectral imagery to predict post-wildfire soil water repellency. *Geomorphology*, 95, 192–205. DOI: 10.1016/j.geomorph.2007.06.002.
- Madsen, M.D., Petersen, S.L., Fernelius, K.J., Roundy, B.A., Taylor, A.G., Hopkins, B.G., 2012. Influence of soil water repellency on seedling emergence and plant survival in a burned semi-arid woodland. *Arid Land Res. Manag.*, 26, 3, 236–249. DOI: 10.1080/15324982.2012.680655.
- Martin, D.A., Moody, J.A., 2001. Comparison of soil infiltration rates in burned and unburned mountainous watersheds. *Hydrol. Process.*, 15, 2893–2903. DOI: 10.1002/hyp.380.
- Mataix-Solera, J., Guerrero, C., García-Orenes, F., Bárcenas-Moreno, G., Torres, M.P., 2009. Forest fire effects on soil microbiology. In: Cerdà, A., Robichaud, P.R. (Eds.): *Fire Effects on Soils and Restoration Strategies*. Science Publishers, Enfield, New Hampshire, USA, pp. 133–175.
- Meyer, L.D., Harmon, W.C., 1979. Multiple-intensity rainfall simulator for erosion research on row sideslopes. *T. Am. Soc. Civ. Eng.*, 22, 100–108.
- Moody, J.A., Shakesby, R.A., Robichaud, P.R., Cannon, S.H., Martin, D.A., 2013. Current research issues related to post-wildfire runoff and erosion processes. *Earth-Sci. Rev.*, 122, 10–37. DOI: 10.1016/j.earscirev.2013.03.004.
- Natural Resources Conservation Service (NRCS), 2010. *Keys to soil taxonomy* 11th ed. US Department of Agriculture, Natural Resources Conservation Service, Washington, DC.

- Natural Resources Conservation Service (NRCS), 2011. Official soil series descriptions. US Department of Agriculture, Natural Resources Conservation Service, Washington, DC. Available online [<https://soilseries.sc.egov.usda.gov/osdname.asp>] (accessed 15 June 2016)
- National Water and Climate Center (NWCC), 2010. Atlanta Summit SNOTEL data. Available online [<http://www.wcc.nrcs.usda.gov/snow/>] (accessed 25 November 2016).
- Neary, D.G., Ryan, K.D., DeBano, L.F., Landsberg, J.D., Brown, J.K., 2005. Chapter 1: Introduction. In: Neary, D.G., Ryan, K.D., DeBano, L.F. (Eds.): *Wildland Fire in Ecosystems: Effects of Fire on Soil and Water*. General Technical Report, RMRS-GTR-42, vol. 4. U.S. Department of Agriculture, Forest Service, Rocky Mountain Research Station, Ogden, UT, USA. pp. 1–17.
- Pannkuk, C.D., Robichaud, P.R., 2003. Effectiveness of needle cast at reducing erosion after forest fires. *Water Resour. Res.*, 39, 12, 1333–1344. DOI: 10.1029/2003WR002318.
- Parsons, A., Robichaud, P.R., Lewis, S.A., Napper, C., Clark, J.T., 2010. Field guide for mapping post-fire soil burn severity. General Technical Report RMRS-GTR-243. US Department of Agriculture, Forest Service, Rocky Mountain Research Station, Ft. Collins, Colorado, USA, 49 p.
- Pierson, F.B., Robichaud, P.R., Moffett, C.A., Spaeth, K.E., Hardegree, S.P., Clark, P.E., Williams, C.J., 2008. Fire effects on rangeland hydrology and erosion in a steep sagebrush-dominated landscape. *Hydrol. Process.*, 22, 16, 2916–2929. DOI: 10.1002/hyp.6904.
- Prosser, I.P., Williams, L., 1998. The effect of wildfire on runoff and erosion in native Eucalypt forest. *Hydrol. Process.*, 12, 2, 251–265. DOI: 10.1002/(SICI)1099-1085(199802)12:2<251:AID-HYP574>3.0.CO;2-4.
- R Core Team, 2013. R: A Language and Environment for Statistical Computing. R Foundation for Statistical Computing, Vienna, Austria.
- Robichaud, P.R., 2000. Fire effects on infiltration rates after prescribed fire in Northern Rocky Mountain forests. USA. *J. Hydrol.*, 231–232, 220–229. DOI: 10.1016/S0022-1694(00)00196-7.
- Robichaud, P.R.; Ashmun, L.E., 2013. Tools to aid post-wildfire assessment and erosion-mitigation treatment decisions. *Int. J. Wildland Fire*, 22, 1, 95–105. DOI: 10.1071/WF11162.
- Robichaud, P.R., Elliott, W.J., Pierson, F.B., Hall, D.E., Moffett, D.E., Ashmun, L.E., 2007. Erosion Risk Management Tool (ERMiT) user manual (version 2006.01.18). General Technical Report RMRS-GTR-188. US Department of Agriculture, Forest Service, Rocky Mountain Research Station, Ft. Collins, Colorado, USA, 24 p.
- Robichaud, P.R., Lewis, S.A., Ashmun, L.E., 2008. New procedure for sampling infiltration to assess post-fire soil water repellency. Research Note RMRS-RN-33. US Department of Agriculture, Forest Service, Rocky Mountain Research Station, Ft. Collins, Colorado, USA, 85 p.
- Robichaud, P.R., Lewis, S.A., Wagenbrenner, J.W., Ashmun, L.E., Brown, R.E., 2013a. Post-fire mulching for runoff and erosion mitigation: Part I: Effectiveness at reducing hillslope erosion rates. *Catena*, 105, 75–92. DOI: 10.1016/j.catena.2012.11.015.
- Robichaud, P.R., Wagenbrenner, J.W., Lewis, S.A., Ashmun, L.E., Brown, R.E., Wohlgemuth, P.M., 2013b. Post-fire mulching for runoff and erosion mitigation. Part II. Effectiveness in reducing runoff and sediment yields from small catchments. *Catena*, 105, 93–111. DOI: 10.1016/j.catena.2012.11.016.
- Robichaud, P.R., Wagenbrenner, J.W., Pierson, F.B., Spaeth, K.E., Ashmun, L.E., Moffet, C.A., 2016. Infiltration and interrill erosion rates after a wildfire in western Montana, USA. *Catena*, 142, 77–88. DOI: 10.1016/j.catena.2016.01.027.
- Ryan, K.C., 2002. Dynamic interactions between forest structure and fire behavior in boreal ecosystems. *Silva Fenn.*, 36, 1, 13–39.
- Ryan, K.C., Noste, N.V., 1985. Evaluating prescribed fires, General Technical Report INT-GTR-182. In: Lotan, J.E., Kilgore, B.M., Fischer, W.C., Mutch, R.W. (Eds.): *Proc. Symposium and Workshop on Wilderness Fire*. US Department of Agriculture, Forest Service, Intermountain Forest and Range Experimental Station, Ogden, Utah, USA, pp. 230–238.
- Scott, D.F., Curran, M.P., Robichaud, P.R., Wagenbrenner, J.W., 2009. Soil erosion after forest fire. In: Cerda, A., Robichaud, P.R. (Eds.): *Fire Effects on Soils and Restoration Strategies*. Science Publishers, Enfield, New Hampshire, USA, pp. 178–195.
- Shakesby, R.A., Coelho, C.D.A., Ferreira, A.D., Terry, J.P., Walsh, R.P.D., 1993. Wildfire impacts on soil erosion and hydrology in wet Mediterranean forest, Portugal. *Int. J. Wildland Fire*, 3, 2, 95–110. DOI: 10.1071/WF9930095.
- Shakesby, R.A., Doerr, S.H., Walsh, R.P.D., 2000. The erosional impact of soil hydrophobicity: current problems and future research directions. *J. Hydrol.*, 231–232, 178–191. DOI: 10.1016/S0022-1694(00)00193-1.
- Shakesby, R.A., Doerr, S.H., 2006. Wildfire as a hydrological and geomorphological agent. *Earth-Sci. Rev.*, 74, 3–4, 269–307. DOI: 10.1016/j.earscirev.2005.10.006.
- Steele, R., Pfister, R.D., Ryker, R.A., Kittams, J.A., 1981. Forest habitat types of central Idaho. General Technical Report INT-114. US Department of Agriculture, Forest Service, Intermountain Forest and Range Experiment Station, Ogden, Utah.
- Townsend, S.A., Douglas, M.M., 2000. The effect of three fire regimes on stream quality, water yield and export coefficients in a tropical savanna (northern Australia). *J. Hydrol.*, 229, 3, 118–137. DOI: 10.1016/S0022-1694(00)00165-7.
- USDA Forest Service, 2003. Hot Creek Fire Burned Area Report. Available at https://forest.moscowfl.wsu.edu/BAERTOOLS/baerdb/2500-8/2500-8_Hot%20Creek%20Fire_Boise.pdf (accessed 2 February 2017)
- Vieira, D.C.S., Fernández, C., Vega, J.A., Keizer, J.J., 2015. Does soil burn severity affect the post-fire runoff and interrill erosion response? A review based on meta-analysis of field rainfall simulation data. *J. Hydrol.*, 523, 452–464. DOI: 10.1016/j.jhydrol.2015.01.071.
- Wagenbrenner, J.W., Robichaud, P.R., 2014. Post-fire bedload sediment delivery across spatial scales in the interior western United States. *Earth Surf. Proc. Land.*, 39, 7, 865–876. DOI: 10.1002/esp.3488.
- Wilcox, B.P., Wood, M.K., Tromble, J.M., 1988. Factors influencing infiltrability of semiarid mountain slopes. *J. Range Manag.*, 41, 3, 197–206.
- Williams, C.J., Pierson, F.B., Robichaud, P.R., Al-Hamdan, O.Z., Boll, J., Strand, E.K., 2016. Structural and functional connectivity as a driver of hillslope erosion following disturbance. *Int. J. Wildland Fire*, 25, 3, 306–321. DOI: 10.1071/WF14114.
- Wine, M.L., Zou, C.B., Bradford, J.A., Gunter, S.A., 2012. Runoff and sediment responses to grazing native and introduced species on highly erodible Southern Great Plains soil. *J. Hydrol.*, 450–451, 336–341. DOI: 10.1016/j.jhydrol.2012.05.012.
- Wine, M.L., Cadol, D., 2016. Hydrologic effects of large southwestern USA wildfires significantly increase regional water supply: Fact or fiction? *Environ. Res. Lett.*, 11, 085006. DOI: 10.1088/1748-9326/11/8/085006.
- Wondzell, S.M., King, J.G., 2003. Postfire erosional processes in the Pacific Northwest and Rocky Mountain regions. *Forest Ecol. Manag.*, 178, 1–2, 75–87. DOI: 10.1016/S0378-1127(03)00054-9.

Received 21 August 2017
Accepted 2 November 2017

Note: Colour version of Figures can be found in the web version of this article.

Natural colloid mobilization and leaching in wettable and water repellent soil under saturated condition

Nasrollah Sepehrnia^{1,2*}, Olga Fishkis¹, Bernd Huwe¹, Jörg Bachmann³

¹ Soil Physics Group, Building Geo II, University of Bayreuth, Germany.

² Department of Soil Science, College of Agriculture, Isfahan University of Technology, Isfahan, 84156-83111, Iran.

³ Institute of Soil Science, Leibniz Universität Hannover, Herrenhäuser Str. 2, D-30419 Hannover, Germany.

* Corresponding author. Tel.: +983133913471. Fax: +983133913471. E-mail: n.sepehrnia@ag.iut.ac.ir

Abstract: The coupled transport of pollutants that are adsorbed to colloidal particles has always been a major topic for environmental sciences due to many unfavorable effects on soils and groundwater. This laboratory column study was conducted under saturated moisture conditions to compare the hydrophobic character of the suspended and mobilized colloids in the percolates released from a wettable subsoil and a water repellent topsoil. Both soils with different organic matter content were analyzed for wettability changes before and after leaching using sessile drop contact angles as well as water and ethanol sorptivity curves, summarized as repellency index. Hydrophobicity of the effluent suspensions was assessed using the C18 adsorption method. Water repellency level of the repellent soil decreased after leaching but remained on a lower level of water repellency, while, the wettable soil remained wettable. The leached colloids from the repellent soil were predominantly hydrophilic and the percentage of the hydrophobic colloid fraction in the effluent did not systematically changed with time. Total colloid release depended on soil carbon stock but not on soil wettability. Our results suggest that due to the respective character of transported colloids a similar co-transport mechanism for pollutants may occur which does not depend explicitly on soil wettability of the releasing horizon, but could be more affected by total SOM content. Further studies with a wider range of soils are necessary to determine if the dominant hydrophilic character of leached colloids is typical. Due to the mostly hydrophilic colloid character we conclude also that changes in wettability status, i.e. of wettable subsoil horizons due to the leachate, may not necessarily occur very fast, even when the overlying topsoil is a repellent soil horizon with a high organic matter content.

Keywords: Soil water repellency; Hydrophobic colloids; C18; Sessile drop; Repellency index.

INTRODUCTION

Colloids (i.e. particles with effective diameters of around 10 nm to 10 μ m) in natural subsurface environments may have various organic and inorganic sources: i.e. silicate clays, sesquioxides (Fe- and Al- oxyhydroxides), mineral precipitates, humic materials, microemulsions of non-aqueous phase liquids and microorganisms including viruses and bacteria (Bradford and Torkzaban, 2008; McCarthy and Zachara, 1989). Colloid translocation by convective water flux in soil and sediments is an important environmental issue for the co-transport of organic and inorganic contaminants (Lazouskaya and Jin, 2008; Sepehrnia et al., 2014; Tufenkji et al., 2004) whereby mobile organic or inorganic colloids can serve as effective shuttles. Pollutant transport (i.e. heavy metals, radionuclides, pesticides, phosphorus, and pathogens) in natural environments may be accelerated by the complexation with mobile colloids (so-called colloid-facilitated contaminant transport) as shown by many others (Amrhein et al., 1993; Carstens et al., 2017; Guo and Chorover, 2003; Karathanasis, 1999; Motoshita et al., 2003; Totsche et al., 2006; Tufenkji et al., 2004). The extent to which these various colloid fractions are mobile in porous media affects also the mobility of associated contaminants.

Among various factors (McCarthy and McKay, 2004; Chen and Flury, 2005; Sen and Khilar, 2006), soil water repellency, or in extreme cases soil hydrophobicity, is an often overseen but important property that may principally affect colloid transport (Baumann and Niessner, 2006). In most studies using laboratory-scale columns under well-controlled conditions colloid transport is focused on injection of colloids to the wettable or nonwettable porous media to analyze chemical, physi-

cal and/or physicochemical interactions between pore wall and colloid (Goebel et al., 2013; Lazouskaya and Jin, 2008; Ochiai et al., 2006; Wang and Yoon, 2005). In these studies, either the transport of natural colloids (i.e. extracted water dispersible soil colloids) or of artificial model colloids (i.e. hydrophilic/hydrophobic carboxylic tubes) is conducted to identify main mechanisms that govern transport and retention of colloids through porous media (Auset and Keller, 2004; Crist et al., 2004; Keller and Auset, 2007; Keller and Sirivithayapakorn, 2004). Some results indicated that the transport of colloids in natural environments are affected by the respective properties of the organic matter components such as dissolved organic matter (DOM) or dissolved organic carbon (DOC) (Larsen et al., 1992; Nanny and Ratasuk, 2002; Wood et al., 2011). Therefore, a growing research effort aimed to develop an understanding of the impact of hydrophilic or hydrophobic organic components in leachates through different methods (Dilling and Kaiser, 2002; Egeberg and Alberts, 2002; Ghernaout, 2014; Lindroos et al., 2002; Nanny and Ratasuk, 2002).

Given that hydrophilicity is the inverse of hydrophobicity (Brown and Peake, 2003) it still remains unknown what the respective effects of wettable and water repellent soils on the specific colloidal translocation processes like mobilization, transport, retention (Goebel et al., 2013) and colloidal flocculation and stabilization processes (van Oss, 1995) are. Ritsema and Dekker (1998) found by using 3D-visualizations of water content and water repellency pattern that the dissolution of hydrophobic substances proceeded along flow paths which were formed by instability-driven fingered flow which rendered the soil within the pathways more wettable than the surrounding soil. In contrast, Dymov et al. (2015, 2017) concluded that

transport of hydrophobic components in water solutions might be the reason for an increase of subsoil water repellency.

To analyze such phenomena listed above, a method is needed to characterize the hydrophilicity/hydrophobicity character to the organic colloids. Determination of hydrophobic colloids in leachates using the C18-method (Octadecyl: micro-particles; 40 μm diameter) is relatively new (Klitzke and Lang, 2007). Therefore, the current knowledge about mobilization and transport of natural colloids detached from repellent or wettable soil material in context with the hydrophilic or hydrophobic character of the mobile colloids is very limited.

Generally, the topsoil is potentially more influenced by higher rates of hydrophobic organic matter input (Fishkis et al., 2015; Fröberg et al., 2003; Goebel et al., 2005, 2011). One of our hypotheses is therefore that the colloids released from a repellent topsoil are in average more hydrophobic than those detached from the underlying wettable subsoil. We further suppose that the relative amount of the hydrophilic colloids will increase with leaching duration because colloids are easier detached as the functional group arrangements associated with wettable surfaces changed during leaching, i.e. due to swelling (Diehl, 2013; Urbanek et al., 2007).

Summarizing, at present information regarding the hydrophobicity/hydrophilicity status of the suspended colloids in leachates drained to the subsurface media is scarce. Therefore, following the findings and conclusions published by Fishkis et al. (2015) and Dymov et al. (2015, 2017), we have the following hypothesis: i) the total amount of colloids that can be released from the soil matrix depends on soil wettability (either hydrophobic or hydrophilic), ii) colloids released from a repellent topsoil are more hydrophobic than those detached from the respective underlying wettable subsoil, because, topsoil is more influenced by higher rate of hydrophobic organic matters (Bachmann et al., 2016; Fishkis et al., 2015; Fröberg et al., 2003; Goebel et al., 2005, 2011), iii) the relative amount of the hydrophobic colloids is increased by time and depended on soil carbon stock and wettability, and iv) the leached colloids may contribute differently to changes of subsoil wettability by time due to the specific hydrophilic or hydrophobic character of the colloids which is determined by the emitting soil horizon. The objectives of this study are correspondingly focused on the wetting properties of the soil and leachates:

- i) Comparison of the hydrophobicity status of the suspended colloids in leachates from a repellent topsoil and the respective underlying wettable subsoil under saturated conditions,
- ii) Evaluation of the relative amount of hydrophobic colloids from the wettable and repellent soils with leaching time, and,
- iii) Investigation of soil water repellency persistency in term of repellency index (*RI*) and contact angle (*CA*) changes before and after leaching.

MATERIAL AND METHODS

Soil sampling and soil properties

The studied spruce forest soils are classified as Stagnic Podzol ($\text{O}_e\text{-O}_e\text{-O}_a\text{-AE}_h\text{-B}_s\text{-B}_w\text{-B}_{gd}$) ($50^\circ 7' 39.64''$ N; $11^\circ 51' 18.51''$ E) and located in the Fichtel Mountains in southeast Germany.

Table 1. Physical and chemical properties of the studied soils.

Property soil	Depth (cm)	Texture ^a	pH _{H2O}	pH _{CaCl2}	C _{org} (%)	DOC (mg L ⁻¹)
Repellent	0–4	Sandy loam	4.30	3.40	11.00	20.00
Wettable	26–55	Sandy loam	4.60	3.60	1.30	2.40

^a Estimated in the field by hand texture according to Fishkis et al (2015). C_{org}: organic carbon, DOC: Dissolved organic carbon.

This site was already studied by Fishkis et al. (2015). Bulk soil from the top (0–4 cm) and from subsoil horizons (26–55 cm) were gathered as repellent and wettable soil, respectively. Prior studies using contact angle measurement showed that surface horizons ($\text{O}_e\text{-O}_a\text{-AE}_h$) of this location were hydrophobic, while, the deeper subsoil horizons ($\text{B}_w\text{-B}_{gd}$) were hydrophilic (Fishkis et al., 2015). Three undisturbed soil cores (5 cm diameter, 5 cm height) were taken from the mentioned depths to determine field bulk density of the soil layers. The samples were gently passed through a 3.60 mm sieve with minimum disturbance to prevent destruction of hydrophobic particle surfaces by abrasion. Sieved samples were then air-dried in the lab.

Organic carbon (C_{org}), dissolved organic carbon (DOC), pH, and soil texture were analyzed according to Fishkis et al (2015) (Table 1). The C_{org} and DOC content were measured by dynamic flash combustion (Thermo Quest, Flash EA, Wigan, United Kingdom) and by high temperature analyzer (Elementar, high-TOC, Germany), respectively. Porosity ($P=1\text{-BD/PD}$, BD and PD are bulk and particle densities, respectively) was calculated and pore volume (PV) was considered as saturated water filled pore volume (Klute and Dirksen, 1986; Kirkham, 2005) established during the column experiments. The K_s , saturated hydraulic conductivity, was measured by the constant-head procedure through an infiltration experiment and calculated by Darcy's equation (Klute and Dirksen, 1986).

Column preparation and leaching set-up

Six PVC columns (7 cm diameter, 17 cm height) were packed for each soil sample to field bulk density. A rigid coarse plastic membrane (i.e. 0.5 mm in diameter) was also used to stabilize the soil materials. The soil columns were saturated via capillary rise by submerging the wettable and repellent soil columns into tap water for 24 and 48 h, respectively. Water ponding was subsequently observed on the top of the columns. Because the studied soils were not aggregated the presence of larger amounts of poorly accessible soil volume inside aggregates (immobile water volume fraction) could be excluded. Accordingly, it was assumed that the columns were saturated under these initial conditions and during the following percolation experiment. The upper and the lower boundary condition of the columns were constant pressure head and seepage face, respectively. Chloride (Cl^-) was used as the conservative chemical tracer. A volume of 10 mM NaCl solution (equal to 0.1 PV of the hydrophobic soil) was poured on top of the soil columns while they were saturated. Then a saturated flow condition (zero pressure at the contact plane of soil and infiltrometer) was applied at the top of the soil columns using a disc infiltrometer. Effluent was sampled at periodic intervals (i.e. in steps of 0.1 PV before 0.5 PV, and in steps of 0.25 PV leachate for the rest of the experiment) from the bottom outlet of the columns. Soil columns were leached based on K_s and pore volume PV. The duration of leaching experiments (i.e. 2 and 2.5 h for repellent and wettable soil, respectively) was considered as time equivalent to account for eight PVs. Totally, 35 samples were taken for each column run to analyze the hydrophobicity of the colloidal suspensions.

Measurement of soil and suspension hydrophobicity

The status of water repellency of both soils was tested before and after the leaching experiments applying the sessile drop method (Bachmann et al., 2000) and the soil water repellency index, RI , method (Tillman et al., 1989). Soil samples were oven-dried at 40°C before the measurements.

To evaluate RI , the cumulative liquid infiltration rate I of water and ethanol were measured for the time interval < 180 s with a microinfiltrometer (Sepehrnia et al., 2016, 2017). The infiltrometer was placed on top of the samples and the results were plotted against $t^{0.5}$. Three replicate soil cores (5 cm height, 5 cm diameter) were prepared for each soil with the same bulk density which was used for the column experiments. The infiltration process were conducted with a negative pressure equivalent of $h_0 = -2$ cm water column. The sorptivity for water (S_w) and ethanol (S_e) infiltration were calculated using the equation $S(h_0) = I / t^{0.5}$ (Philip, 1957). RI as a measure of the extent of soil water repellency (Tillman et al., 1989) was calculated from equation (1):

$$RI = 1.95 S_e(-2 \text{ cm}) / S_w(-2 \text{ cm}) \quad (1)$$

A soil is classified as being water repellent if $RI > 1.95$.

The sessile drop method was performed using a CCD-equipped contact angle microscope (OCA 15, Data Physics, Filderstadt, Germany). The initial contact angle was evaluated by placing a water drop of 1 μL on the soil cores used later for RI measurements (Fishkis et al., 2015). After termination of mechanical perturbations of the droplet ($t > 30$ ms after contact with sample surface), the CA was measured at both intersections of the drop contour line with the horizontal solid surface baseline by automated drop shape analysis using the software SCA15 (DataPhysics, Filderstadt, Germany) (Bachmann et al., 2000). Three drops were measured for one soil core. A soil was classified as water repellent if $CA > 90^\circ$, subcritical-repellent if $0^\circ < CA < 90^\circ$, and water wettable if $CA = 0$ (Bachmann et al., 2007).

Hydrophobicity of the effluent was assessed using the C18-method proposed by Klitzke and Lang (2007). In this separation method, a defined hydrophobic solid surface (Octadecyl: micro-particles; 40 μm diameter) is used instead of a non-polar organic solvent to attach hydrophobic colloids to the granular particles which removes them from the effluent liquid. The suspensions were filtered immediately after sampling over a 15 μm Nylon mesh (VWR International, GmbH, Germany) prior to turbidity measurements (T_1) using a spectrophotometer (LAMBDA 1050 UV/Vis/NIR, Perkin Elmer). The emission

wavelength of 420 nm was chosen to maximize the average of turbidity. The detector was centered at 90° to the incident light path (Brown and Peake, 2003; EPA, 1993). Thirty milligrams of C18 microparticles (VWR International, GmbH, Germany) and 10 mL of suspension were mixed in a glass tube allowing for hydrophobic colloids to sorb onto the hydrophobic surface of the microparticles. The tube was attached to a horizontal shaker for 2 h at 100 rpm. After the shaking period, C18 particles were separated using the 15 μm nylon mesh and the turbidity of the filtered suspensions was determined (T_2). The suspension hydrophobicity index (HI) for all particles $< 15 \mu\text{m}$ is then calculated according to the equation 2.

$$HI = \frac{T_1 - T_2}{T_1} \quad (2)$$

Statistical analysis

The experiment was performed using a complete randomized design with three replications for contact angle (CA) and repellency index (RI) as dependent and the studied soils (repellent and wettable) as independent variables. A further similar complete randomized test was done for effluent concentrations C/C_0 to compare the first seven effluent samples (pore volumes 0.1 PV to 1.0 PV) for differences between the wettable and the water repellent soil in the initial phase of the experiment. Statistical analyses were done using SAS (Statistical Analysis System) and the mean comparisons were performed by the LSD test (SAS Institute, 2004).

RESULTS AND DISCUSSION

Basic soil properties are given in Table 1. Basic parameters of the columns are presented in Table 2. Repellent soil had significantly higher total and dissolved organic carbon content (C_{org} and DOC), saturated water content (θ_s), porosity (P), and saturated hydraulic conductivity (K_s) compared to wettable soil.

Contact angle (CA) and repellency index (RI) data before and after the percolation experiment of the wettable and repellent soil are summarized in Table 3. CA and RI of the repellent soil material were strongly affected ($p < 0.001$) by the percolation experiment, i.e. CA dropped from 107° to 71° , while the CA of the wettable soil was stable with 0° before and after leaching. Similarly, RI of the water repellent soil decreased significantly ($p < 0.05$) after leaching from $140 (\pm 13)$ to $57 (\pm 11)$ and, in agreement to CA results, RI of the wettable soil was < 1.95 and remained unchanged (Table 3). For the repellent soil the comparison of CA and RI values before and

Table 2. Physical properties of the soil columns during leaching under saturated flow condition.

Property soil	θ_s	BD	PD	P	V_t	PV	K_s
	($\text{cm}^3 \text{cm}^{-3}$)						
Repellent	0.72	0.51	2.20	77.00	654	471	0.90
Wettable	0.51	1.25	2.65	53.00	654	334	0.50

Table 3. Mean and standard error of contact angle (CA) and repellency index (RI) of the studied soils before and after leaching ($n = 6$)^a.

Property soil	CA		RI	
	before	after	before	after
Repellent	107 (± 13) ^{***}	71 (± 18) ^{***}	140 (± 13) ^{***}	57 (± 11) ^{***}
Wettable	0.00 ^{***}	0.00 ^{***}	1.84 (± 0.20) ^{***}	1.67 (± 0.26) ^{***}

^a denotes the number of replicates for the columns of each soil in the leaching experiment. CA: Contact angle, RI : repellency index. ^{***} denotes the properties which are significantly different between soils on significance level 0.001.

after leaching suggested on one hand that measurable portions of hydrophobic material could have been removed and transported with the percolation solution (Ritsema and Dekker, 1998). On the other hand, non-polar functional groups that are responsible for measured repellency on the particle surfaces may have been oriented away due to conformational changes of the functional groups, i.e. from the solid surface into deeper layers of the interphase after contact with water (Diehl, 2013). The latter effect was similarly observed for technical polymers (Ferguson and Whiteside, 1992) as well as for column capillary rise experiments made with a water repellent sandy soil (Reszkowska et al., 2014). Fishkis et al. (2015) also found the negative relations between the soil water repellency level (as quantified by CA) as function of water content (ranged from $pF = -\infty$ to $pF = 4.2$). They found that the CA was affected significantly by saturation history (wetting and drying cycles); so that at a given water content, the CA was significantly larger during drying than during rewetting. These observations are in line with the changes in persistency of water repellency as found in this study by CA and *RI* before and after leaching.

Cl⁻ tracer breakthrough curve characteristics

To compare the water flow characteristics in both soils, mean breakthrough curves (BTCs) of Cl⁻ are presented in Fig. 1. The BTC for the wettable soil was characterized by a concentration peak in C/C_0 at 1 PV which is typical for homogeneous media and suggests that preferential flow did not occur in the packed columns (Guo and Chorover, 2003). The repellent soil BTC showed a tendentially earlier peak maximum with higher Cl⁻ concentrations in the 0.1 PV to 0.75 PVs ($p < 0.05$) interval. Faster movement of Cl⁻ could principally occur due to higher local pore water velocities (i.e. preferential flow on the pore scale, Jarvis et al. (2008)). It could also be supported by a lower retention capacity of the repellent soil to hold Cl⁻ ions due to a lower specific surface charge, which is indirectly indicated by the higher CA (Bachmann et al., 2007; Deurer and Bachmann, 2007; Raats, 1973; Ritsema and Dekker, 1994, 1998). The decreasing slopes after the maximum concentration of the BTCs of both soils were approximately similar in shape and overlapping regarding the respective values of the standard deviation. This trend continued for the rest of the experiment.

Leaching and hydrophobic character of the organic colloids

Effluent turbidity of unfiltered, filtered, and C18-treated effluent samples as a function of the out-flux water volume is presented in Fig. 2. For the entire leaching experiment, significantly higher turbidity was observed in the unfiltered samples of the repellent soil (Fig. 2a) compared with the effluent of the wettable soil (Fig. 2b). These data suggest that the repellent soil, higher in SOC content, released a higher total amount of mobilized colloids during the leaching process. The peak at 0.5 PV in the effluent turbidity of the wettable soil has a height of 1.2 AU (absorbance units). It shows a much stronger pronounced characteristic corresponding to a short-time event compared with the more or less monotonically decreasing turbidity with time observed for water repellent soil. In average, as mentioned, the turbidity of the repellent soil was on a much higher level, indicated by the maximum absorbance of 1.75 at 0.5 PV. The turbidity of the wettable soil effluent sharply decreased after 0.5 PV and, on average, the values remained below 0.25 AU for the rest of the experiment. However, in addition to the first turbidity peak, the unfiltered effluent of the

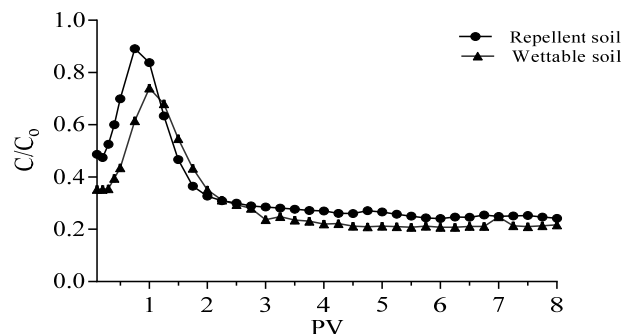


Fig. 1. Breakthrough curves of the inert tracer chloride (Cl⁻) passing through the repellent and wettable soils. Depicted are mean values of six replicate soil columns with a mean standard error of ± 0.18 (wettable) and ± 0.13 (repellent columns).

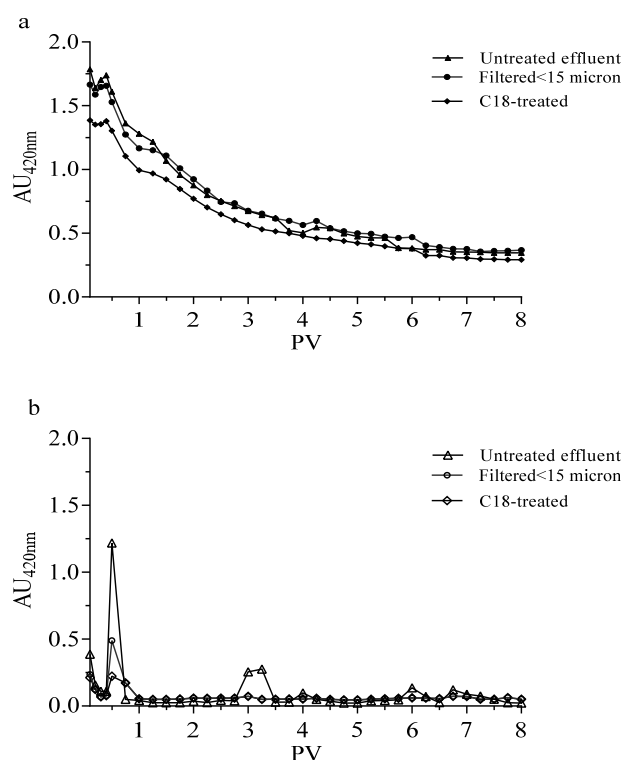


Fig. 2. Variations of turbidity as absorbance with water as reference (baseline set to zero for water) for the effluents of repellent (a) and wettable (b) soils. Depicted are mean values of six replicate soil columns with a mean standard errors of ± 0.50 , ± 0.40 and ± 0.37 in Fig. 2a, and ± 0.2 , ± 0.1 and ± 0.04 in Fig 2b for untreated, filtered (<15micron), and C18 effluents, respectively.

wettable soil columns showed some fluctuations in turbidity when approaching the end of sampling with increased values at 3 PV, 4 PV, 6 PV, and 6.75 PV (Fig. 2b). This could indicate sudden events of separation and removal of dispersible colloids i.e. caused by spontaneous destruction of soil bulk aggregates or smaller components detached from particle coatings as reported by Laegdsmand et al. (2005). The effluent turbidity of the repellent soil decreased much slower than for the wettable soil and reached a stable plateau of 0.5 AU after 7 to 8 PV (Fig. 2a).

The differences between the leachates for the wettable and repellent soils (Fig. 2a) may be caused by larger source of readily available organic colloids on the particle surfaces of the

repellent soil particles. A second mechanism could also be a higher release rate of recaptured colloids on the repellent soil surfaces along the columns due to lower adsorption energies. However, if the leachate data (Fig. 2) are compared with the studies of Deb and Shukla (2011), Flury and Qiu (2008), Laegdsmand et al. (2005) it is confirmed that higher total DOM leaching resulted from a larger source of available colloids due to the higher total OM content in the repellent soil (Table 1). Further, Laegdsmand et al. (2005) investigated the leaching of dispersible colloids and DOM from columns (4 cm diameter and 6 cm height) packed with natural soil aggregates (2–4 mm) and observed that colloid leaching increased also for aggregated systems with increasing organic matter content.

More specifically, analyzing the contribution of colloids to turbidity, the plots related to the filtered effluents (excluding particles larger than 15 μm) also showed higher mobilization of colloids from the repellent soil compared to the wettable soil. Generally, differences between the turbidities of untreated effluents and filtered effluents of the repellent and wettable soils were almost negligible which suggest that the transported particles were predominantly colloids < 15 μm in size (Fig. 2b), supporting the assumption of predominantly colloidal transport. The filtered effluents showed somewhat higher values in some points of the repellent soils compared to the unfiltered effluents which might fell into the experimental error (± 0.06) during absorbance measurements.

Generally, the high turbidity values are probably caused by colloidal species including a mixture of hydrophobic, hydrophilic, and amphiphilic components as stated by Mainwaring et al. (2013) or Tschapek and Wasowki (1976). The presence of hydrophobic colloids in the effluent of wettable soil suspensions was detected only at 0.1 PV and 0.5 PV with a hydrophobicity index (H) of 9.5% (± 9.9) and 54% (± 19), respectively. Thus, a large part of the increased turbidity found at 0.5 PV (Fig. 2b) is apparently related to the temporary mobilization of hydrophobic organic colloids leached from the bulk soil. Such a high value (54%) for the wettable soil was never reached for the repellent soil. This suggests the preferential release of hydrophobic components, probably occluded in organic matter before the release, from particle surfaces, which are in average characterized as hydrophilic by the CA and RI values. Total turbidity of the suspensions was significantly increased at these selected sampling points. Dymov et al. (2015) also found that the hydrophobic property (in term of CA) for the upper mineral horizons of four studied soils were largely determined by the contents of free and occluded organic matter fractions. On the other hand, the data of 3, 4, 6 and 6.75 PVs for wettable soil (Fig. 2b) do not indicate an increased H because no differences were observed for the turbidities at these PVs. This shows that probably no relevant amounts of hydrophobic colloids were mobilized after 1 PV and that an increase of total turbidity is not necessarily an evidence for a higher amount of hydrophobicity of the suspension components for the wettable soil. Dymov et al. (2017) investigated the polycyclic aromatic hydrocarbons concentrations (PAHs) and water repellency (in term of CA) in burnt and unburnt soil horizons ($\text{O}_i\text{-O}_{\text{ea}}\text{-E-Bs}$) of lichen pine forests. They attributed the increase of soil water repellency (i.e., CA) to the high amount of PAHs accumulated in fractions of free and occluded organic matter. Dymov et al. (2017) also observed a gradual increase of the CA values in E and B horizons. They suggested that this could be associated partly with the composition of the horizon-specific SOM composition, but also partly due to the migration of hydrophobic components from upper soil layers with soil water transport. If the results including the CA (Table 1) and the amount of hydrophobic

colloids for the wettable soil are compared with Dymov et al. (2015, 2017) and Laegdsmand et al. (2005), it might be assumed that the hydrophobic components in the leachate samples at 0.1 PV and 0.5 PV are likely originated from the release of larger occluded colloidal organic matter particles which were originally covered with a hydrophilic coating before the detachment from the solid interface. Experimental evidence also suggests that hydrophilic and hydrophobic components are packed side-by-side on the particle surface forming a chemically composite surface on the molecular scale (Tschapek, 1976). Woche et al. (2017) showed by X-ray photoelectron spectroscopy (XPS) that always polar and non-polar functional groups are present on solid surfaces of soil organic matter, no matter if the soil is water repellent or exhibit complete wettability. Only the ratio of non-polar to polar functional groups in the interface increased with increasing water repellency level of the samples, which is not reflected by conventional bulk analysis of the respective soils. Therefore, depending on the respective binding strength of the organic matter subunits, components usually in the size of colloids, with a net dominance of either hydrophilic or hydrophobic character can potentially be released from both types of soils as confirmed by this study.

The absolute hydrophobicity on the leachate components showed a continuous release of hydrophobic colloids for the repellent soil with a maximum value of 30% at 0.2 PV (Fig. 3). Absolute reduction with a significant negative slope ($R^2 = 0.77^{***}$) was greater than the relative hydrophobicity reduction with a positive and gentle slope ($R^2 = 0.18^*$, Fig. 3). Data of Fig. 3 were also separated into two parts to find any trend in time for H characteristics during leaching. These data, however, demonstrated that the gradient was not significantly different for the 5 PVs to 8 PVs intervals ($R^2 = 0.13^{\text{ns}}$) compared to the 0.1 PV to 5 PVs ($R^2 = 0.05^{\text{ns}}$). In conclusion, the absolute and relative changes of the suspension hydrophobicity demonstrated that during the entire process the suspended colloids leached from the repellent soil were mostly hydrophilic.

Many studies focused on the wettability of leachates through chemical fractionation of DOM (Crow et al., 2009; Dilling and Kaiser, 2002; Fröberg et al., 2003; Lindroos et al., 2002). Wandruszka et al. (1997) have shown that aqueous solutions of soil humic acids respond also to the addition of cations by forming intramolecular and intermolecular microaggregates or compact structures with relatively hydrophobic interiors and hydrophilic surfaces. Lindroos et al. (2002) found that the groundwater mainly consisted of hydrophilic neutral compounds. Crow et al. (2009) investigated chemical structures of the leached materials, but did not investigated the hydrophobicity status of the colloids itself. They reported that the respective soil horizon determines in the predominant molecular components of the leachates, i.e. hydrophobic and hydrophilic acid groups dominated in leachates from Oe-horizons compared to the Oi- or Oa-horizons.

The relation between colloid release, DOC, and SOC content was thus assessed for both soils of this study. The absolute amount of SOM and DOC were higher in the repellent soil compared to the wettable soil (Table 1). The DOC/SOM ratio for the wettable and repellent soils, however, was quite close on the same level; i.e., 2.70 and 2.60, respectively. This indicates that the release of colloids is proportional to the existing carbon stock in the soil and could be independent from soil wettability. Laegdsmand et al. (2005) also found a significant greater DOM leaching from the soil with 3.5% OM compared to one with 2.5%, while the DOM/SOM ratio was also similar for the two soils.

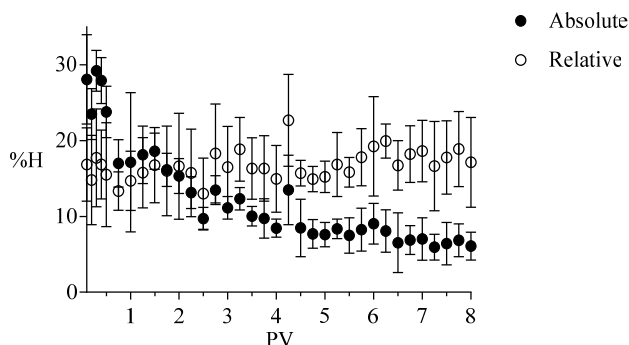


Fig. 3. Absolute hydrophobicity in the effluent during leaching for the repellent soil (i.e. T_1-T_2 in equation 2, data points are represented by filled circles). Linear regression: $HI (\%) = -2.41PV + 22$, $R^2 = 0.77^{***}$, (line not shown). Corresponding relative hydrophobicity index (HI) values ($(T_1-T_2)/T_1$ of suspended particles are represented by open circles ($HI (\%) = 0.31PV + 15.5$, $R^2 = 0.18^*$). Error bars are standard deviation of six replications in column experiments (* and *** denote the significant status of the hydrophobicity as function of PV on significance level 0.05 and 0.001, respectively).

The leachate hydrophobicity (Fig. 3) and the persistency of matrix water repellency (i.e., $CA = 71^\circ$) showed that the repellent soil did not quickly rendered wettable (Table 3). This suggests, in line with the predominant release of hydrophilic colloids, that much of the hydrophobic components remained at the interfaces of the solid particles. Urbanek et al. (2007) found also varying ratios of hydrophilic (C = O) and hydrophobic functional group (C–H) components at the solid particle interface as well as in the interior of aggregates which was affected by the respective land-uses system. In a recent paper, Woche et al. (2017) suggested the elemental surface O/C ratio as a general parameter linking surface wettability (in term of CA) and surface elemental composition of soil particle interfaces. This analytical approach might, on one hand, close the gap between the specific surface chemistry of the solid particles and its wetting properties in a dynamic context. On the other hand, corresponding analytical tools may help to unravel the relation between chemically altered surfaces, i.e. after detachment of organic components, and the amount and nature of released DOM components as has been done in this study.

CONCLUSION

This study showed that natural hydrophobic colloids could be mobilized from bulk soil and transported through the wettable and the repellent soils. The major fraction of the leached colloids was hydrophilic and independently from the respective wettability status of the soils. The total amount of the leached colloids were higher for the repellent soil due to the higher SOC content, whereas the normalized values (ratio between DOC/SOC) were quite similar compared with the wettable soil. Leaching of the smaller fraction of hydrophobic colloids was continuously observed in the effluent samples of the repellent soil. For the wettable soil the hydrophobic colloid contribution was not assessable except for two samples, whereby one of these effluent samples showed the highest fraction of hydrophobic components.

The RI and CA values did not change after leaching for the wettable soil while a significant reduction was found for the repellent soil. We conclude that these results have some out-

comes: A certain amount of natural hydrophobic colloids will, on one hand, potentially be released from wettable soil horizons and are mobile in the soil matrix. On the other hand, hydrophobic soil horizons release always predominantly hydrophilic colloids. This supports the assumption, that pollutants, i.e. preferentially bound either to hydrophilic or hydrophobic organic compounds, can principally be released and transported over longer distances, no matter what the wettability state of the respective soil horizons is. Regarding the impact of the released colloids on deeper layers, the mostly wettable subsoils will continuously receive also a smaller fraction of hydrophobic colloids. As observed for many subsoils (Woche et al., 2005), the wettability of the majority of subsoil horizons may not be necessarily influenced intensively by this DOM influx, i.e. originated from an overlaying repellent soil horizon, due to the majority of hydrophilic colloids. However, regarding the wide spectrum of soils and soil forming processes much more research is needed to obtain a comprehensive view regarding the relation between DOM release, transport, hydrophobic character of colloids and the specific interaction regarding soil wettability. So far, some hypotheses can be suggested: 1) Hydrophilic colloids are predominantly released from the repellent soil because of their higher affinity to water, 2) Hydrophobic soil horizons may also release a certain amount of hydrophobic colloids, 3) Hydrophilic colloids (probably organic matter-associated) dominate composition in the leachates because during the wetting process hydrophobic leached materials may also become hydrophilic as stressed by Deb and Shukla (2016) for the hydrophobic contaminants, 4) Therefore, detachment and release of natural hydrophilic compounds might be rated as more effective for the co-transport of contaminants in environments for most soils which are considered as non-hydrophobic, 5) Hydrophobic soils, however, will need definitely more attention in further investigations.

Acknowledgements. We thank Andreas Kolb and Michael Wachten for their helps with preparing staff and soil sampling, and the German Academic Exchange Service (DAAD) for partial financial support of this project. We appreciate the valuable manuscript reviews provided by Professor Mark Coyne from the University of Kentucky, USA.

REFERENCES

- Amrhein, C., Mosher, P.A., Strong, J.E., 1993. Colloid-assisted transport of trace metals in roadside soils receiving deicing salts. *Soil. Sci. Soc. Am. J.*, 57, 1212–1217.
- Auset, M., Keller, A.A., 2004. Pore-scale processes that control dispersion of colloids in saturated porous media. *Water Resour. Res.*, 40, W03503. DOI: 10.1029/2003WR002800.
- Baumann, T., Niessner, N., 2006. Micromodel study on repartitioning phenomena of a strongly hydrophobic fluorophore at a colloid/1-octanol interface, *Water Resour. Res.*, 42, W12S04.
- Bachmann, J., Ellies, A., Hartge, K.H., 2000. Development and application of a new sessile drop contact angle method to assess soil water repellency. *J. Hydrol.*, 231–232, 66–75.
- Bachmann, J., Deurer, M., Arye, G., 2007. Modeling water movement in heterogeneous water-repellent soil: 1. Development of a contact angle-dependent water-retention model. *Vadose Zone J.*, 6, 436–445.
- Bachmann, J., Krüger, J., Goebel, M.-O., Heinze, S., 2016. Occurrence and spatial pattern of water repellency in a beech forest subsoil. *J. Hydrol. Hydromech.*, 64, 100–110.

- Bradford, S.A., Torkzaban, S., 2008. Colloid transport and retention in unsaturated porous Media: A review of interface-, collector-, and pore-scale processes and models. *Vadose Zone J.*, 7, 667–681.
- Brown, J.N., Peake, B.M., 2003. Determination of colloiddally-associated polycyclic aromatic hydrocarbons (PAHs) in fresh water using C18 solid phase extraction disks. *Anal. Chim. Acta.*, 486, 159–169.
- Carstens, J.F., Bachmann, J., Neuweiler, I., 2017. Effects of flow interruption on transport and retention of iron oxide colloids in quartz sand. *Colloids and Surfaces A: Physicochem. Eng. Aspects.*, 520, 532–543.
- Chen, G., Flury, M., 2005. Retention of mineral colloids in unsaturated media as related to their surface properties. *Colloids Surf. A: Physicochem. Eng. Aspects.*, 256, 207–216.
- Crist, J.T., McCarthy, J.F., Zevi, Y., Baveye, P., Throop, J.A., Steenhuis, T.S., 2004. Pore-scale visualization of colloid transport and retention in partly saturated porous media. *Vadose Zone J.*, 3, 444–450.
- Crow, S.E., Lajtha, K., Richard, D., Bowden, R.D., Yano, Y., Brant, J.B., Caldwell, B.A., Sulzman, E.W., 2009. Increased coniferous needle inputs accelerate decomposition of soil carbon in an old-growth forest. *For Ecol Manage.*, 258, 2224–2232.
- Deb, S.K., Shukla, M.K., 2011. A review of dissolved organic matter transport processes affecting soil and environmental quality. *Journal of Environmental and Analytical Toxicology*, 1, 106. DOI: 10.4172/2161-0525.1000106.
- Diehl, D., 2013. Soil water repellency: Dynamics of heterogeneous surfaces. *Colloids and Surfaces A: Physicochem. Eng. Aspects*, 432, 8–18.
- Dilling, J., Kaiser, K., 2002. Estimation of the hydrophobic fraction of dissolved organic matter in water samples using UV photometry. *Water Res.*, 36, 5037–5044.
- Deurer, M., Bachmann, J., 2007. Modelling water movement in heterogeneous water-repellent soil: 2: Numerical simulation. *Vadose Zone J.*, 6, 446–457.
- Dymov, A.A., Milanovskii, E.Y., Kholodov, V.A., 2015. Composition and hydrophobic properties of organic matter in the densimetric fractions of soils from the Subpolar Urals. *Eurasian Soil Sci.*, 48, 1212–1221.
- Dymov, A.A., Gabov, D.N., Milanovskii, E.Y., 2017. ¹³C-NMR, PAHs, WSOC and water repellence of fire-affected soils (Albic Podzols) in lichen pine forests, Russia. *Environ. Earth Sci.*, 76, 275. DOI: 10.1007/s12665-017-6600-2.
- Egeberg, P.K., Alberts, J.J., 2002. Determination of hydrophobicity of NOM by RP-HPLC, and the effect of pH and ionic strength. *Water Res.*, 36, 4997–5004.
- EPA (Environmental Protection Agency), 1993. Turbidity (Nephelometric). Method #180.1 Approved for NPDES (Editorial Revision 1974, 1978).
- Ferguson, G.S., Whiteside, G.M., 1992. Thermal reconstruction of the functionalized interface of polyethylene carboxylic acid and its derivatives. In: Schrader, M. E., Loeb, G. (Eds.): *Modern Approaches to Wettability: Theory and Applications*. Plenum Press, New York, pp. 143–177.
- Fishkis, O., Wachten, M., Hable, R., 2015. Assessment of soil water repellency as a function of soil moisture with mixed modelling. *Eur. J. Soil Sci.*, 66, 910–920.
- Flury, M., Qiu, H.X., 2008. Modeling colloid-facilitated contaminant transport in the vadose zone. *Vadose Zone J.*, 7, 682–697.
- Fröberg, M., Berggren, D., Bergkvist, B., Bryant, C., Knicker, H., 2003. Contributions of Oi, Oe and Oa horizons to dissolved organic matter in forest floor leachates. *Geoderma*, 113, 311–322.
- Ghernaout, D., 2014. The hydrophilic/hydrophobic ratio vs. dissolved organics removal by coagulation – A review. *Journal of King Saud University - Science*, 26, 169–180.
- Goebel, M.-O., Bachmann, J., Woche, S.K., Fischer, W.R., 2005. Soil wettability, aggregate stability, and the decomposition of soil organic matter. *Geoderma*, 128, 80–93.
- Goebel, M.-O., Bachmann, J., Reichstein, M., Janssens, I.A., Guggenberger, G., 2011. Soil water repellency and its implications for organic matter decomposition – is there a link to extreme climatic events? *Glob. Change. Biol.* 17, 2640–2656.
- Goebel, M., Woche, S.K., Abraham, P.M., Schaumann, G.E., Bachmann, J., 2013. Water repellency enhances the deposition of negatively charged hydrophilic colloids in a water-saturated sand matrix. *Colloids and Surfaces A.*, 431, 150–160.
- Guo, M., Chorover, J., 2003. Transport and fractionation of dissolved organic matter in soil columns. *Soil Sci.*, 168, 2, 108–118.
- Jarvis, N., Etana, A., Stagnitti, F., 2008. Water repellency, near-saturated infiltration and preferential solute transport in a macroporous clay soil. *Geoderma*, 143, 223–230.
- Karathanasis, A.D., 1999. Subsurface migration of copper and zinc mediated by soil colloids. *Soil Sci. Soc. Am. J.*, 63, 830–838.
- Keller, A.A., Auset, M., 2007. A review of visualization techniques of biocolloid transport processes at the pore scale under saturated and unsaturated conditions. *Adv. Water Resour.*, 30, 6–7, 1392–1407.
- Keller, A.A., Sirivithayapakorn, S., 2004. Transport of colloids in unsaturated porous media: Explaining large-scale behavior based on pore-scale mechanisms. *Water Resour. Res.*, 40, W12403. DOI: 10.1029/2004WR003315.
- Kirkham, M.B., 2005. *Principles of Soil and Plant Water Relations*. Elsevier Academic Press.
- Klitzke, S., Lang, F., 2007. A method for the determination of hydrophobicity of suspended soil colloids. *Colloids and Surfaces A: Physicochem. Eng. Aspects.*, 303, 249–252.
- Klute, A., Dirksen, C., 1986. Hydraulic conductivity and diffusivity: laboratory methods. In: Klute, A. (Ed.): *Methods of Soil Analysis. Part 1. Physical and Mineralogical Methods*. 2nd ed. ASA/SSSA Monograph 9(1), Madison, WI, pp. 687–732.
- Laegdsmand, M., de Jonge, L.W., Moldrup, P., 2005. Leaching of colloids and dissolved organic matter from packed with natural soil aggregates. *Soil Sci.*, 170, 13–27.
- Larsen, T., Christensen, T.H., Pfeffer, F.M., Enfield, C.G., 1992. Landfill leachate effects of sorption of organic micropollutants onto aquifer materials. *J. Contam Hydrol.*, 9, 307–324.
- Lazouskaya, V., Jin, Y., 2008. Colloid retention at air–water interface in a capillary channel. *Colloids and Surfaces A: Physicochem. Eng. Aspects*, 325, 141–151.
- Lindroos, A.-J., Kitunen, K., Deromeb, J., Helmisaari, H.S., 2002. Changes in dissolved organic carbon during artificial recharge of groundwater in a forested esker in Southern Finland. *Water Res.*, 36, 4951–4958.
- Mainwaring, K., Hallin, I.L., Douglas, P., Doerr, S.H., Morley, C.P., 2013. The role of naturally occurring organic compounds in causing soil water repellency. *European Journal of Soil Science*, 64, 667–680.

- McCarthy, J.F., McKay, L.D., 2004. Colloid transport in the subsurface: past, present, and future challenges. *Vadose Zone J.*, 3, 326–337.
- McCarthy, J.F., Zachara, J.M., 1989. Subsurface transport of contaminants. *Environ. Sci. Technol.*, 23, 496–502.
- Motoshita, M., Komatsu, T., Moldrup, P., de Jonge, L.W., Ozaki, N., Fukushima, T., 2003. Soil constituent facilitated transport of phosphorus from a high-P surface soil. *Soils Found.*, 43, 105–114.
- Nanny, M.A., Ratasuk, N., 2002. Characterization and comparison of hydrophobic neutral and hydrophobic acid dissolved organic carbon isolated from three municipal landfill leachates. *Water Res.*, 36, 1572–1584.
- Ochiai, N., Kraft, E.L., Selker, J.S., 2006. Methods for colloid transport visualization in pore networks. *Water Resour. Res.*, 42, W12S06.
- Philip, J.R., 1957. The theory of infiltration: 1. The infiltration equation and its solution. *Soil Sci.*, 83, 345–357.
- Raats, P.A.C., 1973. Unstable wetting fronts in uniform and non-uniform soils. *Soil Sci. Soc. Am. Proc.*, 37, 681–685.
- Reszkowska, A., Bachmann, J., Lamparter, A., Diamantopoulos, E., Durner, W., 2014. The effect of temperature-induced soil water repellency on transient capillary pressure–water content relations during capillary rise. *Eur. J. Soil Sci.*, 65, 369–376.
- Ritsema, C.J., Dekker, L.W., 1994. How water moves in water repellent sandy soil. 2. Dynamics of fingered flow. *Water Resour. Res.*, 30, 2519–2531.
- Ritsema, C.J., Dekker, L.W., 1998. Modeling and field evidence of finger formation and finger recurrence in a water repellent sandy soil. *Water Resour. Res.*, 34, 555–567.
- SAS Institute, 2004. SAS User's Guide: Statistics. Ver. 9. SAS Institute Inc., Cary, N.C.
- Sen, T.K., Khilar, K.C., 2006. Review on subsurface colloids and colloid-associated contaminant transport in saturated porous media. *Adv. Colloid Interface Sci.*, 119, 71–96.
- Sepehrnia, N., Mahboubi, A.A., Mosaddeghi, M.R., Safari Sinejani, A.A., Khodakaramian, G., 2014. *Escherichia coli* transport through intact gypsiferous and calcareous soils during saturated and unsaturated flows. *Geoderma*, 217–218, 83–89.
- Sepehrnia, N., Hajabbasi, M.A., Afyuni, M., Lichner, L., 2016. Extent and persistence of water repellency in two Iranian soils. *Biologia*, 71, 10, 1137–1143.
- Sepehrnia, N., Hajabbasi, M.A., Afyuni, M., Lichner, L., 2017. Soil water repellency changes with depth and relationship to physical properties within wettable and repellent soil profiles. *J. Hydrol. Hydromech.*, 65, 2017, 1, 99–104.
- Tillman, R.W., Scotter, D.R., Wallis, M.G., Clothier, B.E., 1989. Water-repellency and its measurement by using intrinsic sorptivity. *Aust. J. Soil Res.*, 27, 637–644.
- Tschapek, M., Wasowski, C., 1976. Adsorption of aliphatic alcohols by soil minerals as a method of evaluating their hydrophobic sites. *Soil Sci.*, 27, 175–182.
- Totsche, K.U., Jann, S., Kogel-Knabner, I., 2006. Single event-driven export of polycyclic aromatic hydrocarbons and suspended matter from coal tar-contaminated soil. *Vadose Zone J.*, 6, 233–243.
- Tufenkji, N., Miller, G.F., Ryan, J.N., Harvey, R.W., Elimelech, M., 2004. Transport of *Cryptosporidium* oocysts in porous media: Role of straining and physicochemical alteration. *Environ. Sci. Technol.*, 38, 5932–5938.
- Urbanek, E., Hallett, P., Feeney, D., Horn, R., 2007. Water repellency and distribution of hydrophilic and hydrophobic compounds in soil aggregates from different tillage systems. *Geoderma*, 140, 147–155.
- Van Oss, C.J., 1995. Hydrophobicity of biosurfaces—origin, quantitative determination and interaction energies. *Biointerfaces.*, 5, 91–110.
- Wandruszka, R., Ragle, C., Engebretson, R., 1997. The role of selected cations in the formation of pseudomicelles in aqueous humic acid. *Talanta*, 44, 805–809.
- Wang, L., Yoon, R.H., 2005. Hydrophobic forces in thin aqueous films and their role in film thinning. *Colloids and Surfaces A - Physicochem. Eng. Aspects*, 263, 267–274.
- Woche, S.K., Goebel, M.-O., Horton, R., Van Der Ploeg, J., Bachmann, J., 2005. Contact angle of soil as affected by depth, texture, and land management. *Eur. J. Soil Sci.*, 56, 239–251.
- Woche, S.K., Goebel, M.-O., Mikutta, R., Schurig, Ch., Kaestner, M., Guggenberger, G., Bachmann, J., 2017. Soil wettability can be explained by the chemical composition of particle interfaces - An XPS study. *Sci. Rep.*, 7, 42877. DOI: 10.1038/srep42877.
- Wood, C.M., Al-Reasia, H.A., Smith, D.S., 2011. The two faces of DOC. *Aquat. Toxicol.*, 105S, 3–8.

Received 8 December 2016

Accepted 3 October 2017

Encounter probability analysis of irrigation water and reference crop evapotranspiration in irrigation district

Jinping Zhang^{*}, Jiayi Li, Xixi Shi

Institute of Water Resources and Environment, Zhengzhou University, High-tech District, No. 100 Science Road, Zhengzhou City, 450001, Henan Province, China.

^{*} Corresponding author. Tel.: +86-371-60119629. Fax: +86-372-7132666. E-mail: iwhrzhy@sohu.com

Abstract: Based on the data series of the annual reference crop evapotranspiration (ET_0) and the amount of irrigation water (IR) from 1970 to 2013 in the Luhun irrigation district, the joint probability distribution of ET_0 and IR is established using the Gumbel-Hougaard copula function. Subsequently, the joint probability, the conditional joint probability, and the conditional return period of rich-poor encounter situations of ET_0 and IR are analysed. The results show that: (1) For the joint probabilities of rich-poor encounter situations of ET_0 and IR , the asynchronous encounter probability is slightly larger than the synchronous encounter probability. (2) When IR is in rich state or ET_0 is in poor state, the conditional joint probability is larger, and the conditional return period is smaller. (3) For a certain design frequency of ET_0 , if the design frequency decreases, the conditional joint probability of the amount of irrigation water will decrease, therefore the encounter probability of them will decrease. (4) For a certain design frequency of the amount of irrigation water, if the design frequency decreases, the conditional joint probability of ET_0 will increase, thus the encounter probability of them will increase.

Keywords: Luhun irrigation district; Copula function; Reference crop evapotranspiration; Amount of irrigation water; Encounter probability.

INTRODUCTION

The amount of irrigation water (IR) is the main factor in irrigation planning and operation management in an irrigation district (Wang et al., 2015; Zhang et al., 2017) and represents the artificial water supply. Reference crop evapotranspiration (ET_0) is an important parameter for calculating the water demand of crops. Moreover, it is the basic data in irrigation planning (Abolfazl et al., 2017; Kong et al., 2013; Li et al., 2007; Liu et al., 2007; Luo et al., 2008; Ni et al., 2006). Irrigation water is affected by precipitation, evaporation, temperature, crop species, and management level (Li et al., 2017; Wang et al., 2015), whereas ET_0 is influenced by meteorological factors and the geographical environment (Fan et al., 2012; Li et al., 2017; Wang et al., 2015). Some scholars have carried out research on the statistical characteristics and evolution laws of these two variables, respectively (Bai et al., 2004; Feng et al., 2011; Huang et al., 2008; Lan et al., 2014; Matin et al., 2016; Ren et al., 2007; Tong and Guo, 2013; Yan et al., 2007). These two variables change randomly, but there is a certain relationship between them. However, the correlation between ET_0 and IR has been considered in univariate analysis all the time. Thus, it is difficult to reflect the practical characteristics of ET_0 and the changes of IR . ET_0 and IR are two mutually influenced hydrological variables, referring to the natural water demand and the artificial water supply in an irrigation district, respectively. Hence, their joint distribution can show the joint statistical characteristics of the natural water demand and the artificial water supply, facilitating the assessment of water shortage risk. However, the characteristics of the joint distribution of these two factors involving their correlation have not been sufficiently studied. Moreover, a study on water supply and demand of ET_0 and (IR) has not yet been conducted. Therefore, it is necessary to explore the joint probability, the conditional joint probability as well as the conditional return period of ET_0 and IR to evaluate the water supply and demand in an irrigation district.

In this study, based on the data series of the annual ET_0 and IR in the Luhun irrigation district of Henan province in China from 1970 to 2013, a two-dimensional joint probability distribution model of ET_0 and IR is constructed using the Gumbel-Hougaard copula. This model can be applied to quantitatively analyse the joint probability, the conditional joint probability, and the conditional return period of annual ET_0 and IR in various rich-poor encounter situations. Then, the water shortage risk under the artificial water supply condition is studied.

METHODS

Copula functions are used for establishing the joint distribution of multiple random variables, and the marginal distributions of the variates are uniformly distributed on $[0, 1]$. The Sklar theorem (Song, 2012) is the theoretical basis of a copula function, and its two-dimensional form is expressed as follows: It is assumed that there are two continuous random variables X and Y . Let $F_X(x)$ and $F_Y(y)$ be their marginal distribution functions, and $G(x, y)$ be their joint distribution function. If $F_X(x)$ and $F_Y(y)$ are continuous, there is a unique copula function $C_\theta(u, v)$ defined by:

$$G(x, y) = C_\theta(F_X(x), F_Y(y)), \forall x, y \quad (1)$$

where $C_\theta(u, v)$ is called the copula function, θ is an undetermined parameter.

In hydrology and water resources, three types of symmetrical Archimedean cluster copula functions that contain only one parameter are widely used (Song, 2012). The correlation measure τ is the Kendall rank correlation coefficient (Davis and Chen, 2007), which describes the nonlinear correlation

Table 1. Three types of common copula functions currently used in hydrological research.

Archimedean copula	$C_\theta(u, v)$	Parameter value	Relation between τ and θ
Frank	$-\frac{1}{\theta} \ln \left[1 + \frac{(e^{-\theta u} - 1)(e^{-\theta v} - 1)}{e^{-\theta} - 1} \right]$	$\theta \in R$	$\tau = 1 - \frac{4}{\theta} \left[-\frac{1}{\theta} \int_0^1 \frac{t}{\exp(t) - 1} dt - 1 \right]$
Clayton	$(u^{-\theta} + v^{-\theta} - 1)^{-1/\theta}$	$\theta > 0$	$\tau = \frac{\theta}{\theta + 2}$
Gumbel-Hougaard	$\exp \left[-\left((-\ln u)^\theta + (-\ln v)^\theta \right)^{1/\theta} \right]$	$\theta \geq 1$	$\tau = 1 - \frac{1}{\theta}$

between the variables and has a corresponding relationship with the parameters of the copula function, as shown in Table 1. Based on this, after determining the relationship between the marginal distribution function and the measurement variables, the copula joint distribution functions of the two variables can be obtained by Table 1. Using Kolmogorov-Smirnov (K-S) inspection for performing fitting test and the ordinary least squares (OLS) for evaluating goodness-of-fit, the most suitable copula functions to describe the correlation of the variables are chosen.

PRACTICAL APPLICATION
Research area

The Luhun irrigation district, with a total irrigation area of 1838.48 km², is the fourth largest irrigation district in the western Henan province in China. Henan Province is the most populous agricultural province in China. The Luhun irrigation district is located in a hilly area and crosses the Yellow River and the Huai River. The Gross Domestic Product of the Luhun irrigation district is moderate. However, agricultural development lags behind partly because there are three poverty-stricken counties. The irrigation areas are mainly located on both sides of the Yi River (the second tributary of the Yellow River), south of the Luo River and north of the Ru River. The irrigation water in the Luhun irrigation district is from the Luhun reservoir, which is on the upper reaches of the Yi River, and the annual amount of irrigation water is approximately 1.82 × 10⁸ m³. The irrigation district has a continental monsoon climate, and its annual average rainfall is only 611.02 mm. However, evaporation attains 1034.32 mm, which is due to meteorological drought. Recently, owing to the decrease of the Yi River’s runoff, the water storage capacity of the Luhun reservoir has been severely reduced, which greatly influences irrigation activities.

The data series in the Luhun irrigation district involves daily meteorological data and the annual amount of irrigation water from 1970 to 2013. The irrigation water of the Luhun Irrigation District comes from the Luhun Reservoir located on the upper reaches of the Yi River and represents the artificial water supply. The Penman-Monteith formula recommended by FAO in 1998 was used to calculate the annual ET₀ from 1970 to 2013, as shown in Fig. 1.

Joint probability distribution model of ET₀ and IR

According to the data series of annual ET₀ (mm) and IR (10⁸ m³) in the Luhun irrigation district from 1970 to 2013, the joint probability distribution model was constructed using a copula function. The model expression is given by Eq. (2), and the specific modelling process can be found in Zhang et al.

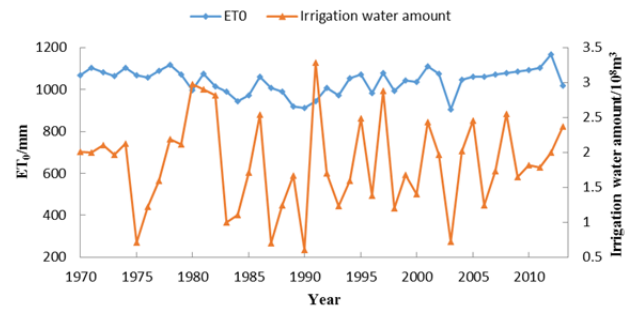


Fig. 1. Data series of ET₀ and IR in the Luhun irrigation district.

(2017). X and Y represent the frequency of ET₀ and IR, respectively. It assumed that u and v are the marginal distribution of annual ET₀ and IR, respectively. Let $F(x, y)$ be their joint probability distribution. The expression of $F(x, y)$ based on the Gumbel–Hougaard copula function is:

$$F(x, y) = \exp \left[-\left((-\ln u)^{1.4205} + (-\ln v)^{1.4205} \right)^{1/1.4205} \right] \quad (2)$$

Application analysis

Joint probability analysis of rich–poor encounter situations

The data series of the annual ET₀ and IR in the Luhun irrigation district from 1970 to 2013 obey the GEV and normal distribution, respectively (Zhang et al., 2017). Frequency analysis is commonly used to classify the annual average flow series. Frequency less than 37.5% corresponds to the ‘rich’ state, and frequency more than 62.5% to the ‘poor’ state. Frequency between 37.5% and 62.5% is the ‘normal’ state.

Thus, the values $pf = 37.5\%$ and $pk = 62.5\%$ are used for classifying a state as ‘rich’ and ‘poor’ of the annual ET₀ and IR in the Luhun irrigation district, respectively. Then, the established two-dimensional copula joint distribution model is used to analyse various rich–poor encounter situations.

The numerical division of the annual ET₀ and IR according to the frequency distribution curve is shown in Table 2.

Table 2. Classification standards of rich–poor states between ET₀ and IR.

Variables	Frequency	
	37.5%	62.5%
ET ₀ (mm)	1071.9	1035.1
Irrigation water (10 ⁸ m ³)	2.05	1.61

The frequency method is used to classify the rich-poor encounter situations of the annual ET_0 and IR into nine types that are further classified as synchronous and asynchronous as follows:

$$\text{Rich-rich: } p_1 = P(X \geq x_{pf}, Y \geq y_{pf});$$

$$\text{Rich-normal: } p_2 = P(X \geq x_{pf}, y_{pk} < Y < y_{pf});$$

$$\text{Rich-poor: } p_3 = P(X \geq x_{pf}, Y \leq y_{pk});$$

$$\text{Normal-rich: } p_4 = P(x_{pk} < X < x_{pf}, Y \geq y_{pf});$$

$$\text{Normal-normal: } p_5 = P(x_{pk} < X < x_{pf}, y_{pk} < Y < y_{pf});$$

$$\text{Normal-poor: } p_6 = P(x_{pk} < X < x_{pf}, Y \leq y_{pk});$$

$$\text{Poor-rich: } p_7 = P(X \leq x_{pk}, Y \geq y_{pf});$$

$$\text{Poor-normal: } p_8 = P(X \leq x_{pk}, y_{pk} < Y < y_{pf});$$

$$\text{Poor-poor: } p_9 = P(X \leq x_{pk}, Y \leq y_{pk}).$$

After the calculation, the results of the rich-poor encounter analysis of the annual ET_0 and IR in the Lulun irrigation district are shown in Table 3.

Table 3 shows the following:

(1) The encounter probability of 'Rich-rich' is the highest among these nine situations, which is up to 21.45%.

(2) Among the synchronous probabilities of ET_0 and IR , there are few differences between the probabilities of 'rich-rich' and 'poor-poor' (21.45% and 20.14%, respectively), and 'Normal-normal' is the lowest (7.91%).

(3) Among the asynchronous probabilities of ET_0 and IR , the encounter probability of 'Rich-normal' (or 'Normal-rich') is the lowest among these nine situations, which is 7.89%; the encounter probability of 'Rich-poor' (or 'Poor-rich') is 8.16%; the encounter probability of 'Normal-poor' (or 'Poor-normal') is 9.20%. There are few differences among these six types of asynchronous probabilities.

(4) In total, the asynchronous probabilities of ET_0 and IR are higher than synchronous probabilities, which are 50.50% and 49.50%, respectively, but their differences are not significant.

Encounter probability analysis of conditional joint probability (CJP) and conditional return period (CRP) in rich and poor state

When ET_0 is in rich state $X \geq x_{pf}$, normal state $x_{pk} \leq X \leq x_{pf}$, or poor state $X \leq x_{pk}$, the CJP and the corresponding CRP of IR not exceeding a given value are given by Eq. (3) and Eq. (4), respectively.

$$\begin{cases} F_{Y_i|x_f}(X, Y_i) = P(Y_i \leq y | X \geq x_{pf}) = \frac{F_Y(y) - F(x_{pf}, y)}{1 - F_X(x_{pf})} \\ F_{Y_i|x_p}(X, Y_i) = P(Y_i \leq y | x_{pk} \leq X \leq x_{pf}) = \frac{F(x_{pf}, y) - F(x_{pk}, y)}{F_X(x_{pf}) - F_X(x_{pk})} \\ F_{Y_i|x_k}(X, Y_i) = P(Y_i \leq y | X \leq x_{pk}) = \frac{F(x_{pk}, y)}{F_X(x_{pk})} \end{cases} \quad (3)$$

$$\begin{aligned} T_{Y_i|x_f}(X, Y_i) &= \frac{1}{F_{Y_i|x_f}(X, Y_i)}, T_{Y_i|x_p}(X, Y_i) = \\ &= \frac{1}{F_{Y_i|x_p}(X, Y_i)}, T_{Y_i|x_k}(X, Y_i) = \frac{1}{F_{Y_i|x_k}(X, Y_i)} \end{aligned} \quad (4)$$

where $F_{Y|x}(\bullet)$ represents the CJP of IR and $T_{Y|x}(\bullet)$ represents its corresponding CRP.

When IR is in rich state $Y \geq y_{pf}$, normal state $y_{pk} \leq Y \leq y_{pf}$, or poor state $Y \leq y_{pk}$, the CJP and the corresponding CRP of ET_0 exceeding a given value are given by Eq. (5) and Eq. (6), respectively.

$$\begin{cases} F_{X_i|y_f}(X_i, Y) = P(X_i \geq x | Y \geq y_{pf}) = \\ = \frac{1 - F_Y(y_{pf}) - F_X(x) + F(x, y_{pf})}{1 - F_Y(y_{pf})} \\ F_{X_i|y_p}(X_i, Y) = P(X_i \geq x | y_{pk} \leq Y \leq y_{pf}) = \\ = \frac{F_Y(y_{pf}) - F_Y(y_{pk}) - F(x, y_{pf}) + F(x, y_{pk})}{F_Y(y_{pf}) - F_Y(y_{pk})} \\ F_{X_i|y_k}(X_i, Y) = P(X_i \geq x | Y \leq y_{pk}) = \\ = \frac{F_Y(y_{pk}) - F(x, y_{pk})}{F_Y(y_{pk})} \end{cases} \quad (5)$$

$$\begin{aligned} T_{X_i|y_f}(X_i, Y) &= \frac{1}{F_{X_i|y_f}(X_i, Y)}, \\ T_{X_i|y_p}(X_i, Y) &= \frac{1}{F_{X_i|y_p}(X_i, Y)} \\ T_{X_i|y_k}(X_i, Y) &= \frac{1}{F_{X_i|y_k}(X_i, Y)} \end{aligned} \quad (6)$$

where $F_{X|y}(\bullet)$ represents the CJP of ET_0 , and $T_{X|y}(\bullet)$ represents its corresponding CRP.

Table 3. Encounter probabilities (%) of synchronous-asynchronous encounter between ET_0 and IR .

Synchronous probabilities				Asynchronous probabilities						
Rich-rich	Normal-normal	Poor-poor	Total	Rich-normal	Rich-poor	Normal-poor	Normal-rich	Poor-rich	Poor-normal	Total
21.45	7.91	20.14	49.50	7.89	8.16	9.20	7.89	8.16	9.20	50.50

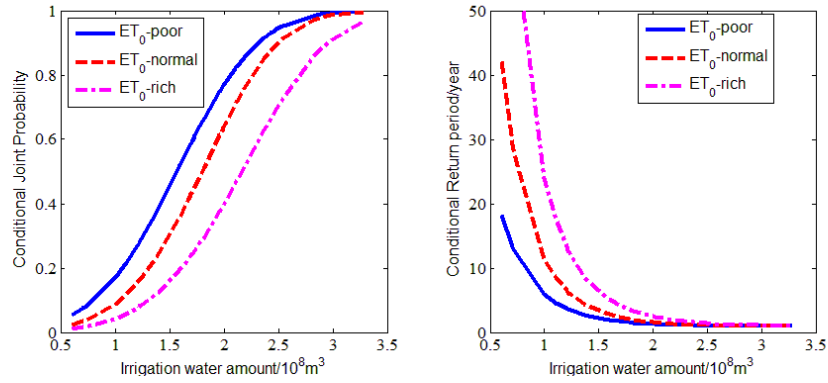


Fig. 2. CJP and CRP of IR not exceeding a given value.

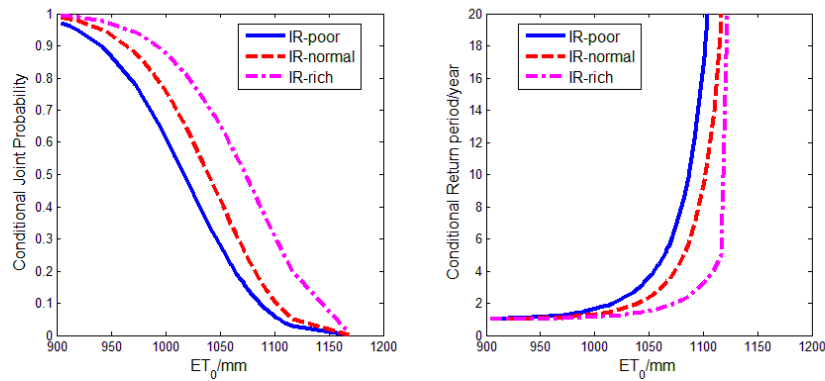


Fig. 3. CJP and CRP of ET_0 exceeding a given value.

Fig. 2 shows the values of CJP and CRP of IR not exceeding a given value when ET_0 is in rich, normal, and poor state. The results are as follows:

(1) When IR increases, the CJP of IR increases, whereas the CRP of IR decreases.

(2) When ET_0 is in rich state ($ET_0 \geq 1071.9$ mm), the CJP of IR is minimum, whereas the CRP of IR is maximum. By contrast, when ET_0 is in poor state ($ET_0 \leq 1035.1$ mm), the CJP and the CRP of IR exhibit the inverse results: the CJP is maximum, whereas the CRP is minimum.

(3) When ET_0 is in rich state ($ET_0 \geq 1071.9$ mm), the CJP when IR is less than 1.0×10^8 , 2.0×10^8 , and 3.0×10^8 m^3 are approximately 0.04, 0.40, and 0.91, respectively. The corresponding values of the CRP are approximately 23.87, 2.51, and 1.10 years.

(4) When ET_0 is in normal state (1035.1 mm $< ET_0 < 1071.9$ mm), the CJP when IR is less than 1.0×10^8 , 2.0×10^8 , and 3.0×10^8 m^3 are approximately 0.09, 0.63, and 0.98, respectively. The corresponding values of the CRP are approximately 11.3, 1.54, and 1.02 years.

(5) When ET_0 is in poor state ($ET_0 \leq 1035.1$ mm), the CJP when IR is less than 1.0×10^8 , 2.0×10^8 , and 3.0×10^8 m^3 are approximately 0.17, 0.77, and 0.99, respectively. The corresponding values of the CRP are approximately 5.86, 1.23, and 1.01 years.

From (3) and (4), it can be concluded that when ET_0 is in rich and normal state and IR is in normal and poor state, the probabilities that the artificial water supply cannot meet water demand are small. However, from (5) we can know that when ET_0 is in poor state and IR is in rich state, the probability is up to 0.99, which means that there may be a phenomenon of wasting water resources in the irrigation district. This information may facilitate irrigation regulation.

Fig. 3 shows the value of CJP and CRP of ET_0 exceeding a given value when IR is in rich, normal, and poor state. The results are as follows:

(1) When ET_0 increases, the CJP of ET_0 decreases, whereas the CRP of ET_0 increases.

(2) When IR is in rich state ($IR \geq 2.05 \times 10^8$ m^3), the CJP of ET_0 is maximum, whereas the CRP of ET_0 is minimum; by contrast, when IR is in poor state ($IR \leq 1.61 \times 10^8$ m^3), the CJP and CRP of ET_0 exhibit the inverse results: the CJP is minimum, whereas the CRP is maximum.

(3) When IR is in rich state ($IR \geq 2.05 \times 10^8$ m^3), the CJP when ET_0 is greater than 950 mm, 1050 mm and 1150 mm are approximately 0.97, 0.65, and 0.08, respectively. The corresponding values of the CRP are approximately 1, 1.48, and 12.5 years.

(4) When IR is in normal state (1.61×10^8 $m^3 < IR < 2.05 \times 10^8$ m^3), the CJP when ET_0 is greater than 950 mm, 1050 mm and 1150 mm are approximately 0.93, 0.43, and 0.04, respectively. The corresponding values of the CRP are approximately 1.02, 2.23, and 25 years.

(5) When IR is in poor state ($IR \leq 1.61 \times 10^8$ m^3), the CJP when ET_0 is greater than 950 mm, 1050 mm and 1150 mm are approximately 0.87, 0.28, and 0.02, respectively. The corresponding values of the CRP are approximately 1.15, 3.57, and 50 years.

From (4) and (5), it can be concluded that when IR is in normal and poor state and ET_0 is in rich and normal state the probabilities that the artificial water supply cannot meet water demand are small, which means that it is less likely to be uncoordinated of water supply and demand. However, from (3) we can know that when IR is in rich state and ET_0 is in poor state

the probability is up to 0.97, which means that water using may be not reasonable in the irrigation district. Thus, the water supply cannot meet demand in the low frequency and long return period.

Analysis of the CJP and CRP with a certain design frequency

The smaller CJP and longer CRP of either *IR* or ET_0 indicates that the artificial water supply can mostly satisfy the water demand, but when the extremely water supply–demand situations occur, whether water supply–demand is coordinated is very important. Thus, the CJP and CRP of *IR* (or ET_0) with a certain design frequency of ET_0 (or *IR*) need to be considered as follows:

Condition I:

$$\begin{cases} P(Y \leq y | X \geq x) = \frac{F_Y(y) - F(x, y)}{1 - F_X(x)} \\ T(Y \leq y | X \geq x) = \frac{1}{P(Y \leq y | X \geq x)} \end{cases} \quad (7)$$

where $P(Y \leq y | X \geq x)$ is the CJP of *IR* in poor state not exceeding a certain design frequency when ET_0 in rich state exceeds a specific frequency, and $T(Y \leq y | X \geq x)$ is the corresponding CRP.

Condition II:

$$\begin{cases} P(X \geq x | Y \leq y) = \frac{F_Y(y) - F(x, y)}{F_Y(y)} \\ T(X \geq x | Y \leq y) = \frac{1}{P(X \geq x | Y \leq y)} \end{cases} \quad (8)$$

where $P(X \geq x | Y \leq y)$ is the CJP of ET_0 in rich state exceeding a certain design frequency when *IR* in poor state does not exceed a specific frequency, and $T(X \geq x | Y \leq y)$ is the corresponding CRP.

These two types of CJP and CRP reflect the probability of unbalanced phenomenon of artificial water supply and demand, and reveal the corresponding water resources utilization. The results of the CJP and the CRP are shown in Tables 4 and 5, respectively.

Table 4 shows that when the frequency of ET_0 in rich state exceeds a certain design frequency, the CJP of *IR* decreases as the design frequency of ET_0 decreases, and the encounter probability of these two variables decreases. The results are as follows:

(1) When the frequency of ET_0 in rich state exceeds a certain design frequency, the probability of *IR* being in extremely poor state without exceeding the design frequency of 95% is less than 0.015, and the CRP is considerably long (the minimum is 66.67 years, the maximum is 200 years). Thus, in such an extreme situation, irrigation water cannot meet demand within 66.67–200 years. Therefore, the probability of unbalanced phenomenon of water supply and demand in irrigation district is low.

(2) When the frequency of ET_0 in rich state exceeds a certain design frequency, the probability of *IR* being in poorer state without exceeding the design frequency of 90% and 75% is less than 0.13 (respectively, 0.015–0.040, 0.046–0.126), and the CRP is longer (respectively, 25.00–66.67 years, 7.94–21.74 years).

(3) When the frequency of ET_0 in rich state exceeds a certain design frequency, the probability of *IR* being in poor state without exceeding the design frequency of 62.5% is less than 0.20. In addition, the maximum CRP is 13.89 years, and the minimum is 5.13 years.

Thus, it can be concluded from Table 4 that the probability of severe water shortage is low when the frequency of water demand exceeds a certain design frequency in the irrigation district.

Table 5 shows that when *IR* in poor state does not exceed a certain design frequency, the CJP of ET_0 increases as the design frequency of *IR* decreases, and the encounter probability of these two variables increases. The results are as follows:

(1) When the frequency of *IR* in poor state does not exceed the design frequency, the probability of ET_0 in extremely rich state exceeding the design frequency of 5% is less than 0.033, and the CRP is considerably long (the minimum is 30.30 years, the maximum is 47.62 years).

(2) When the frequency of *IR* does not exceed the design frequency, the probability of ET_0 in richer state exceeding the design frequency of 25% and 10% is less than 0.122, and the CRP is longer (respectively, 8.20–12.20 years, 18.52–29.41 years).

(3) When the frequency of *IR* does not exceed the design frequency, the probability of ET_0 in rich state exceeding the design frequency of 37.5% is less than 0.161, and the average CRP is 7.78 years.

Table 4. CJP I and CRP I of *IR* when ET_0 in rich state exceeds a certain design frequency.

		<i>IR</i> (10^8 m^3)						<i>IR</i> (10^8 m^3)							
		0.7	1.0	1.4	1.6										
CJP I	ET_0 (mm)	P%	95	90	75	62.5	CRP I	ET_0 (mm)	P%	95	90	75	62.5		
		1071.9	37.5	0.015	0.040	0.126		0.195		1071.9	37.5	66.67	25.00	7.94	5.13
		1079.2	25	0.012	0.033	0.100		0.156		1079.2	25	83.33	30.30	10.00	6.41
		1102.7	10	0.007	0.020	0.063		0.099		1102.7	10	142.86	50.00	15.87	10.10
		1113.2	5	0.005	0.015	0.046		0.072		1113.2	5	200.00	66.67	21.74	13.89

Table 5. CJP II and CRP II of ET_0 when *IR* in poor state does not exceed a certain design frequency.

		ET_0 (mm)						ET_0 (mm)							
		1071.9	1079.2	1102.7	1113.2										
CJP II	<i>IR</i> (10^8 m^3)	P%	37.5	25	10	5	CRP II	<i>IR</i> (10^8 m^3)	P%	37.5	25	10	5		
		0.7	95	0.107	0.082	0.034		0.021		0.7	95	9.35	12.20	29.41	47.62
		1.0	90	0.117	0.090	0.038		0.024		1.0	90	8.55	11.11	26.32	41.67
		1.4	75	0.143	0.107	0.047		0.029		1.4	75	6.99	9.35	21.28	34.48
		1.6	62.5	0.161	0.122	0.054		0.033		1.6	62.5	6.21	8.20	18.52	30.30

From the analysis of Table 4 and 5, the CRP of IR in poor state without exceeding the design frequency when the frequency of ET_0 in rich state exceeds a certain design frequency, and the CRP of ET_0 in rich state exceeding the design frequency when the frequency of IR in poor state does not exceed the design frequency are considerably long, which means that the probability of the extremely water supply–demand occurring in the irrigation water system is very low. At the same time, the analysis indicates that water supply and demand in the irrigation district is relatively coordinated.

CONCLUSION

Using Gumbel-Hougaard copula function, the joint distribution model of the amount of irrigation water and reference crop evapotranspiration was constructed. The frequency of rich–poor encounter situations, the CJP, and the CRP of the amount of irrigation water and reference crop evapotranspiration were analysed to study the unbalanced phenomena in artificial water supply and demand conditions. The following conclusions can be concluded:

(1) The asynchronous frequency was found to be slightly larger than the synchronous frequency in the Lulun irrigation district. Thus, water supply and demand of irrigation district may be in high risk of incoordination, but the probability of extremely uncoordinated artificial water supply and demand (rich IR , poor ET_0 or rich ET_0 , poor IR) is not high.

(2) Using the established joint probability distribution of ET_0 and IR for a specific ET_0 or IR , the encounter probability of artificial water supply and demand was estimated. Similarly, the probability of water shortage exceeding ET_0 or not exceeding IR was also obtained. Thus, the water supply and demand, and utilization of water resources in irrigation district could be described and evaluated quantitatively.

(3) Regardless of the design frequency of reference crop evapotranspiration or the amount of irrigation water, severe water supply–demand issues would not occur in the irrigation district. This is of great significance for the development of the irrigation system, the optimal allocation of regional water resources, and other practical problems in the irrigation district.

Acknowledgements. This research is supported by Outstanding Young Talent Research Fund of Zhengzhou University (Grant No.1521323002), Program for Innovative Talents (in Science and Technology) of University of Henan Province (Grant No.18HASTIT014), State Key Laboratory of Hydraulic Engineering Simulation and Safety, Tianjin University (Grant No. HESS-1717).

REFERENCES

- Abolfazl, M., Mohammad, G.S., Ayed-Hosseini, S., Yousof, M., Mohammad, B., 2017. Sensitivity analysis of monthly reference crop evapotranspiration trends in Iran: a qualitative approach. *Theoretical and Applied Climatology*, 128, 857–873.
- Bai, C.Y., Zhao, Y.X., Feng, X., 2004. Grey relation analysis on change trend of Irrigation water capacity. *Yellow River*, 26, 7, 33–34.
- Davis, M.K., Chen, G., 2007. Graphing Kendall's. *Comput. Stat. Data. An.*, 51, 5, 2375–2378.
- Fan, W.B., Wu, P.T., Han, Z.Q., 2012. Influencing factors analysis of reference crop evapotranspiration and modification of Hargreaves method in Manas River basin. *Transactions of the Chinese Society of Agricultural Engineering*, 28, 8, 19–24.
- Feng, X.M., Liu, G.Q., Zhou, L., 2011. Application of Markov chain in prediction for irrigation water consumption. *Journal of Water Resources and Architectural Engineering*, 9, 2, 98–101.
- Huang, X.F., Shao, D.G., Dai, T., 2008. Analysis on chaotic evolution characteristic of irrigation water. *Journal of Irrigation and Drainage*, 27, 3, 56–59.
- Kong, F.D., Chen, T.T., Zou, L., 2013. Complexity analysis of reference crop evapotranspiration spatio-temporal variation in Liaoning Province. *Journal of Shenyang Agricultural University*, 44, 6, 805–811.
- Lan, J., Tan, Q.H., Dong, Q.J., 2014. Selection of forecasting models for irrigation water consumption based on nonstationarity measure. *Engineering Journal of Wuhan University*, 47, 6, 721–725.
- Li, L., Chi, D.C., Zhang, Z.L., 2007. Analysis of the change characteristics and effect factors of reference evapotranspiration in Taizi River basin. *Transactions of the Chinese Society of Agricultural Engineering*, 23, 9, 34–38.
- Li, X.L., Tong, L., Niu, J., Kang, S.Z., Du, T.S., Li, S.E., Ding, R.S., 2017. Spatio-temporal distribution of irrigation water productivity and its driving factors for cereal crops in Hexi Corridor, Northwest China. *Agricultural Water Management*, 179, 55–63.
- Liu, B.J., Shao, D.G., Shen, X.P., 2007. Study on spatial fractal features of reference crop evapotranspiration. *Journal of Hydraulic Engineering*, 38, 3, 337–341.
- Luo, Y.F., Jiao, X.Y., Peng, S.Z., 2008. Long-term trend of reference evapotranspiration in Liuyankou irrigation system and its impacts on irrigation water requirements. *Chinese Agricultural Science Bulletin*, 24, 9, 480–484.
- Matin, A., Mehdi, K., Mina, E.J., 2016. Developing equations for estimating reference evapotranspiration in Australia. *Water Resources Management*, 30, 11, 3815–3828.
- Ni, G.H., Li, X.H., Cong, Z.T., 2006. Temporal and spatial characteristics of reference evapotranspiration in China. *Transactions of the CSAE*, 22, 5, 1–4.
- Ren, Y.D., Cui, Y.L., Jiang, W., 2007. Long-term variation of reference evapotranspiration and the mechanism analysis. *Journal of Irrigation and Drainage*, 26, 4, 8–10.
- Song, S.B., 2012. Copula Function and its Application in Hydrology. Science Press, Beijing, China, pp. 55–116.
- Tong, F.F., Guo, P., 2013. Forecast method of irrigation water considering uncertain runoff. *Transactions of the Chinese Society of Agricultural Engineering*, 29, 7, 66–75.
- Wang, Z., Han, N.N., Chen, J., 2015. Stochastic simulation method is used to determine the frequency curve of irrigation water. *Science and Technology Innovation Herald*, 12, 12, 52–54.
- Yan, B.W., Guo, S.L., Xiao, Y., 2007. Synchronous-asynchronous encounter probability of rich-poor precipitation between water source area and water receiving areas in the middle route of South-to-North water transfer project. *Journal of Hydraulic Engineering*, 38, 10, 1178–1185.
- Zhang, J.P., Lin X.M., Zhao, Y., 2017. The joint distribution of reference crop evapotranspiration and irrigation water in the irrigation district. *Water Science & Technology: Water Supply*, in press.

Received 25 September 2017

Accepted 22 December 2017

Note: Colour version of Figures can be found in the web version of this article.

Improving the positional accuracy of drainage networks extracted from Global Digital Elevation Models using OpenStreetMap data

Elisabete S.V. Monteiro^{1*}, Cidália C. Fonte², João L.M.P. de Lima³

¹ UDI-Research Unit for Inland Development - Polytechnic Institute of Guarda / Institute for Systems Engineering and Computers at Coimbra, Av. Dr. Francisco Sá Carneiro, 50 6300-559, Guarda, Portugal. E-mail: emonteiro@ipg.pt

² Department of Mathematics University of Coimbra / Institute for Systems Engineering and Computers at Coimbra, Apartado 3008, EC Santa Cruz, 3001-501, Coimbra, Portugal. E-mail: cfonte@mat.uc.pt

³ Department of Civil Engineering of University of Coimbra / MARE - Marine Environmental Sciences Centre, Faculty of Sciences and Technology, University of Coimbra, Rua Luís Reis Santos, Pólo II University of Coimbra, 3030-788 Coimbra, Portugal. E-mail: plima@dec.uc.pt

* Corresponding author. E-mail: emonteiro@ipg.pt

Abstract: Drainage networks allow the extraction of topographic parameters that are useful for basins characterization and necessary for hydrologic modelling. One way to obtain drainage networks is by their extraction from Digital Elevation Models (DEMs). However, it is common that no freely available DEMs at regional or national level exist. One way to overcome this situation is to use the available free Global Digital Elevation Models (GDEMs). However, these datasets have relatively low spatial resolutions, 30 and 90 meters for ASTER and SRTM, respectively, and it has been shown that their accuracy is relatively low in several regions (e.g., Kääb, 2005; Mukul et al., 2017). In this study a methodology is presented to improve the positional accuracy of the drainage networks extracted from the GDEMs using crowdsourced data available in the collaborative project OpenStreetMap (OSM). In this approach only free and global datasets are used, enabling its application to any location of the world. The methodology uses elevation points derived from the GDEMs and the water lines extracted from the collaborative project OSM to generate new DEMs, from which new water lines are obtained. The methodology is applied to two study areas and the positional accuracy of the used data and the obtained results are assessed using reference data.

Keywords: Drainage networks; GDEMs; OpenStreetMap; Positional accuracy.

INTRODUCTION

Drainage networks are necessary for many hydrologic studies, namely the morphometric basin characterization and hydrologic modelling. They are represented accurately in topographic maps, but those may not be available freely in digital form. Another way to obtain them is by extraction from Digital Elevation Models (DEMs). These models can be generated using photogrammetric methods, laser scanning surveys, or radar data and interferometry and may be produced by national mapping agencies or companies. These products in most cases are not available for free use. On the other hand, there are Global Digital Elevation Models (GDEMs) freely accessible with no costs, which cover almost the entire surface of the Earth. However, the GDEMs have errors due to several factors, such as limited spatial resolution (Florinsky and Kuryakova, 2000; Lacroix et al., 2002), terrain characteristics (Fisher, 1998; Kyriakidis et al., 1999; Toutin, 2002), or due to the techniques used in data acquisition and raw data processing (e.g., Elkhachy, 2017). If used to generate drainage networks, the errors in the DEMs are propagated to the drainage networks and also to the parameters derived from them. Therefore, these networks are not as accurate as the ones represented in detailed topographic maps or derived from regional or national DEMs. However, if changes are made to the GDEMs that improve their accuracy, this may also cause an improvement of the topographic parameters and drainage networks extracted from them.

The improvement of DEMs accuracy may be achieved through the combination of DEMs constructed by data acquired with different techniques, namely stereo imaging and interferometry (e.g., Roth et al., 2002) or even, proposed more recent-

ly, using data acquired by unmanned aerial systems or terrestrial sensors (e.g., Petrasova et al., 2017). However, these data may be difficult and expensive to obtain. This raises the attention to the currently available Volunteered Geographic Information (Goodchild, 2007), which is obtained by volunteers that collect many types of features, such as, photographs, geotags, geo-names or routes of the Earth surface, acting like sensors. Among the large number of projects that allow citizens to create geographic information, OpenStreetMap (OSM) is one of the most well-known (Goodchild, 2007; Haklay, 2010; Neis and Zielstra, 2014). This initiative allows citizens to create vector data representing different types of geographic features, such as buildings, forests, roads or rivers. Even though large amounts of data related to water bodies and water lines are available, few references are found about the use of these data for the improvement of the GDEMs. Schellekens et al. (2014) developed a study that allows the extraction of information from OSM for hydrological and hydraulic models. Using OSM data, the authors created gridded maps with fraction of paved and unpaved area and of open water in each cell. One of the features used corresponds to the “rivers” represented in OSM, also used in the present study. Another study developed by Monteiro et al. (2015) assessed the positional accuracy of the drainage networks derived from the SRTM and ASTER DEMs and compared them with the positional accuracy of drainage networks extracted from OSM. The results showed that the OSM watercourses had a higher positional accuracy than the drainage networks obtained from the ASTER and the SRTM GDEMs. The fact that the drainage networks available in OSM presented better positional accuracy than the ones derived from the GDEMs, even though they may not be complete, motivated

the current study, which aims to analyse whether the inclusion of OSM watercourses and elevation points extracted from the GDEMs enables the creation of improved DEMs from which drainage networks with higher positional accuracy can be extracted. The developed process is semi-automatic and uses only free geographic data, enabling the identification of drainage networks in regions where high accurate networks are not available or are not freely accessible.

The proposed methodology requires: 1) the extraction of water lines from OSM that represent natural drainage networks; 2) the extraction of elevation points from the GDEMs; 3) generating a new DEM using an interpolation method that creates hydrologically correct DEMs; and 4) extract the drainage networks from the resulting DEMs. To assess if the methodology improved the accuracy of the obtained drainage networks, the study areas used to test the methodology were chosen in regions where authoritative reference data was available. This enabled the assessment of the positional accuracy of the OSM water lines, and of the drainage networks extracted from the original and the transformed DEMs.

This paper is organized in six sections. In the first one an introduction of the theme and the framing is presented. The datasets used in the study are explained in section "DATASETS". Section "METHODOLOGY" is dedicated to the explanation of the proposed methodology. The study areas are presented and characterized in Section "STUDY AREAS". The results are shown and analysed in section "RESULTS" and finally, in section "DISCUSSION AND CONCLUSIONS", some discussion and conclusions are presented, referring the advantages and limitations of this methodology and future work.

DATASETS

Three different datasets were used in this study: 1) Two GDEMs, namely ASTER and SRTM; 2) data extracted from OSM corresponding to waterways; and 3) the rivers of Great Britain available in Ordnance Survey, which were used as reference data.

The GDEMs

The GDEMs ASTER and SRTM are free elevation datasets available in grid format, where the attribute of each cell is the elevation, with spatial resolutions of 30 and 90 metres, respectively. The grid format is appropriate to implement hydrologic tools (e.g., Zhang and Montgomery, 1994), hence their frequent use in hydrologic applications, such as in the morphometric characterization of basins or flood simulations (Arun et al., 2005; Freeman, 1991; Vieux, 1993).

These datasets are georeferenced with the World Geodetic Coordinate System 1984 (WGS-84) and are generated from satellite images. They have some advantages over the use of local or regional DEMs as they cover large regions of the Earth's surface and are accessible at no cost for the users. The ASTER GDEM is acquired by photogrammetric methods (Greve, 1996), while the SRTM GDEM is collected using Interferometric Synthetic Aperture Radar (InSAR) technology (Hanssen, 2001). These datasets have some limitations, such as their resolution, which restricts their use in applications where high accuracy is required, as their errors will propagate to the GDEM-derived attributes/products (e.g., Kenward et al., 2000; Rodriguez et al., 2006). Thus, the accuracy assessment of the GDEMs is an issue well covered in literature. Several studies have been made to assess the accuracy of the GDEMs in different regions of the world (e.g., Cook et al., 2012; Eckert et al.,

2005; Mukherjee et al., 2013; Varga and Bašić, 2013; Weydahl et al., 2007; Yadav and Indu, 2016) and also the accuracy of the topographic parameters extracted from them (Ebenezer, 2015; Lin et al., 2005; Liu et al., 2015; Monteiro et al., 2015; Mukherjee et al., 2013; O'Callaghan and Mark, 1984; Tarboton et al., 1991). These studies enable to conclude that the vertical accuracy of DEMs is affected by morphologic terrain characteristics (Holmes et al., 2000), by the land use and land cover, but also by the techniques used for data acquisition and processing. The radar technology, used in SRTM, has some advantages over optical techniques (Massonet and Feigl, 1998), including the fact that it uses an active system that includes the self-transmitting and receiving electromagnetic waves. Therefore, the images acquisition is independent of natural illumination conditions (Forkuor and Maathuis, 2012). Another advantage is that the SRTM images are not affected by clouds. However, the SRTM, as the ASTER, is also not able to penetrate the vegetation (Das et al., 2016; Sefercik, 2012).

OSM data

OSM is a collaborative project that creates and distributes free geographic data of and for the world. This project is designed to create and provide free spatial datasets based on volunteered efforts (e.g., Al-Bakri and Fairbairn, 2010). The OSM database is a collection of vector objects that consist of point, line and polygon features (Fonte et al., 2016). The OSM community is composed of over 3,000,000 registered users (http://www.openstreetmap.org/stats/data_stats.html), from all around the world, collecting and updating geographic information, which is immediately visible to all other users. OSM data are structured by tags (formed by a "key" and a "value") that represent objects on Earth, including roads, rivers, buildings, etc. A list of OSM tags is available in the OSM Wiki webpage at http://wiki.openstreetmap.org/wiki/Map_Features. However, volunteers may choose to use other tags.

The coverage and consistency of OSM data varies widely among different geographic areas (Bossard et al., 2000; Heymann, 1994), with urban zones having usually the highest coverage (Neis and Zipf, 2012). The quality assessment can be performed by comparing OSM data with authoritative geographic databases with higher accuracy, used as reference data. Several researchers have analysed the quality of OSM data using this methodology (e.g., Haklay, 2010; Zielstra and Zipf, 2010). Other approaches have however also been used, such as shape similarity with existing data as an indicator of quality (e.g., Mooney et al., 2010). In general terms, what is evidenced in the literature on the quality of OSM data is that the quality is quite heterogeneous across the globe and in some areas it even exceeds the quality of proprietary data (Brovelli et al., 2016). In the present study, the quality of OSM data is assessed by comparing the water lines position with the corresponding position in the Ordnance Survey data.

Reference data

The reference data used was downloaded from the Ordnance Survey web page (www.ordnancesurvey.co.uk), which is the British National Mapping Agency. This institution has some cartographic products available for free download in their web page, such as roads, names of places and rivers. The data used in this work was the drainage network of Great Britain, which is formed by 144,000 km of watercourses, including freshwater rivers, tidal estuaries and canals. These data are available in GML 3.2 and ESRI Shapefile formats, at scales ranging from

1/15,000 to 1/30,000, and are in the British National Grid Projected Reference System. The attributes of these data are: watercourse name; watercourse type and direction of water flow. This drainage network was used in this study as reference to assess the positional accuracy of OSM watercourses and the positional accuracy of the drainage networks extracted from the original and rebuilt DEMs.

METHODOLOGY

The methodology used in the work presented in this article was applied considering the following steps: 1) The extraction of drainage networks from the original GDEMs and the analysis of their positional accuracy; 2) The extraction from OSM of the waterways that correspond to natural drainage networks and the assessment of their positional accuracy; 3) The creation of new DEMs applying an interpolation method that uses data extracted from the original GDEMs and OSM watercourses; and 4) Extraction of new drainage networks from the rebuilt DEMs and the assessment of their positional accuracy. The methodology flowchart is shown in Figure 1.

Drainage networks extraction from the DEMs

For the extraction of the drainage networks the popular D8 flow algorithm was applied (e.g., Jenson and Domingue, 1988; Lin et al., 2008; Mark, 1984; Martz and Garbrecht, 1998; O’Callaghan and Mark, 1984; Tarboton, 1997). This method enables the extraction of drainage networks from grid elevation data. To correct the DEMs of possible artificial depressions (sinks) and peaks the “Fill” tool available in ArcGIS software was used (Planchon and Darboux, 2002; Tarboton et al., 1991). The matrix of flow direction was generated, where each cell gives the direction of water flow. Then, the flow accumulation matrix was computed, where the value of each pixel is the total number of pixels that drains to itself. To generate the watercourses a critical level (CL) needs to be defined. This threshold limit enables to establish if a pixel belongs or not to the drainage network. The pixels that have values of flow accumulation lower than the CL value do not belong to the network while the ones with higher values form the stream network. Therefore, lower threshold values generate more branched networks, as more pixels will be included in the network.

To choose the CL appropriate values for the drainage networks extracted from the ASTER and SRTM DEMs two factors were considered. One was the spatial resolution of the DEMs and the other was to obtain drainage networks with a

total length similar to the total length of the reference drainage network. To this aim, firstly the appropriate value for the SRTM DEM was selected having into consideration the total length of the reference network. Then, taking into account that one pixel of SRTM DEM corresponds to nine pixels of the ASTER DEM, the threshold value chosen for ASTER was nine times larger than that defined for SRTM. For the rebuilt DEMs derived from ASTER the threshold values were the same as the ones used for the original ASTER, and the same was done for the rebuilt DEMs derived from SRTM.

Extraction of waterways from OSM

To extract the waterways from OSM, an analysis of the tags available in OSM was performed. The tag with key “waterway” is used to describe different types of waterways, such as rivers, streams, drains and canals. As for this study only waterways corresponding to natural watercourses should be used, only the lines corresponding to the values “river” and “stream” were considered.

Creation of the rebuilt DEMs

The reconstruction of the DEMs was performed applying the ANNUEM interpolation method that uses altimetry (elevation points), and lines (streams). This interpolation method, developed by Hutchinson et al. (2011), generates a surface hydrologically correct and is implemented in the ArcGIS tool “Topo to raster”. The method was applied using the elevation points extracted from the GDEMs, which were obtained from the original GDEMs by converting them to the vector data model, extracting an elevation point corresponding to the centre of each raster cell. The linear features used corresponding to the streams were the ones extracted from OSM. The boundary of the study areas was also used to limit the obtained DEMs.

Assessment of the positional accuracy of the drainage networks

The horizontal position of the drainage networks extracted from the original GDEMs, the ones extracted from the rebuilt DEMs, and the ones extracted from OSM was compared to the horizontal position of the reference drainage network.

To calculate the horizontal distance between each set of the lines and the reference lines, a set of steps was performed. First, it was necessary to determine which lines of the drainage net-

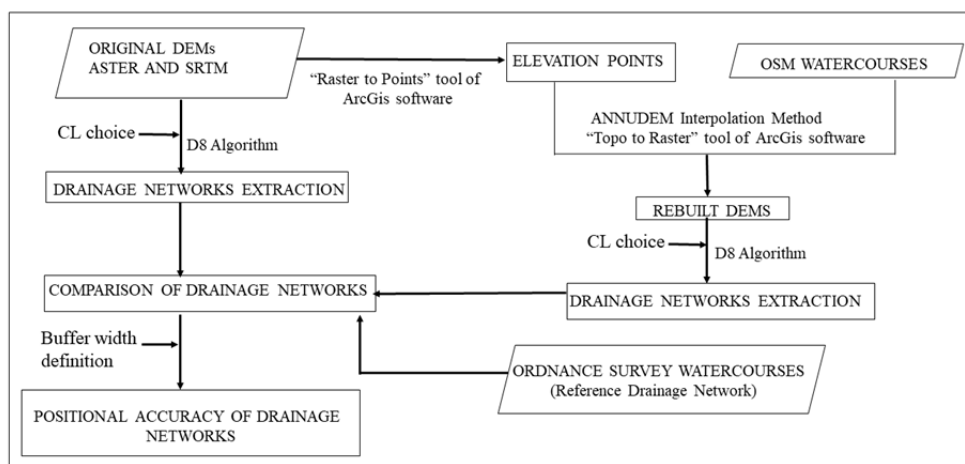


Fig. 1. Methodology flowchart.

work under analysis correspond to the reference lines. For this, a buffer was generated around each reference line, in order to identify the set of lines under study that are inside this buffer and that may be considered as corresponding waterways. The selection of a suitable buffer width is dependent on the dimension of the area and the relative positioning of the corresponding lines. Once this step is completed, to compute the distance between the identified corresponding lines two steps were used: 1) the tool “Feature Vertices to Points” of ArcGIS software was used to transform the selected lines into points (for example, the middle points or end-points of line segments forming the drainage network may be used); 2) the ArcGIS tool “Near” was used to compute the horizontal distance between the points of the waterway under analysis and the reference line. This tool computes the shortest distance between a point and a line.

This computation was only done for the points that are inside the buffers created around the reference drainage network. Then, for each drainage network, the mean M and the standard deviation σ of the obtained distances D_i (Figure 2) were calculated using equations (1) and (2), where n is the number of points considered for the waterway under analysis. The total length of the drainage networks L was also computed and compared.

$$M = \frac{\sum_{i=1}^n D_i}{n} \tag{1}$$

$$\sigma = \sqrt{\frac{\sum_{i=1}^n (D_i - M)^2}{n}} \tag{2}$$

STUDY AREAS

The methodology was applied to two regions located in distinct parts of the United Kingdom. Study Area 1 (SA1) corresponds to a drainage basin (in Scotland) with an area of 42 km² generated using the tool “Basin” of ArcGIS software applied to both ASTER and SRTM GDEMs, which produced slightly

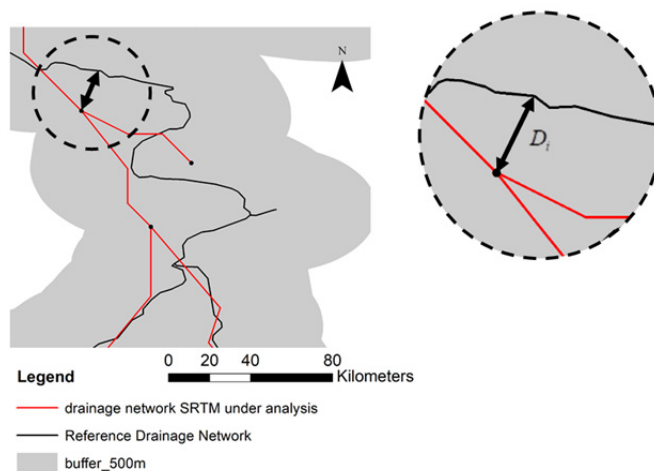


Fig. 2. Distance from a point of the drainage network derived from the DEM to the reference drainage network as computed with the tool “Near” of ArcGIS software.

different basins for the same region due to the differences in the DEMs. Study Area 2 (SA2) corresponds to a 13,899 km² rectangular area located in England (Figure 3). The SA1 region has a maximum altitude of 683 m and a minimum of 16 m, while the maximum and minimum altitude of SA2 is 212 m and 2 m, respectively. Both areas have different characteristics in terms of relief and dimension.

The location of the study areas and the ASTER and SRTM DEMs for each are shown in Figure 3.

The reference data (the drainage network of Ordnance Survey) obtained for each study area, are presented in Figure 4.

The OSM watercourses were downloaded in the shapefile format from Geofabrik in September 8th, 2015. These datasets are presented in Figure 5a) and 5b), respectively, for study areas SA1 and SA2. In terms of connectivity, it can be seen that the network obtained for SA2 shows several disconnected watercourses, while all watercourses are totally connected in SA1.

For the extraction of the drainage networks from the original and the rebuilt DEMs the appropriate critical levels had to be

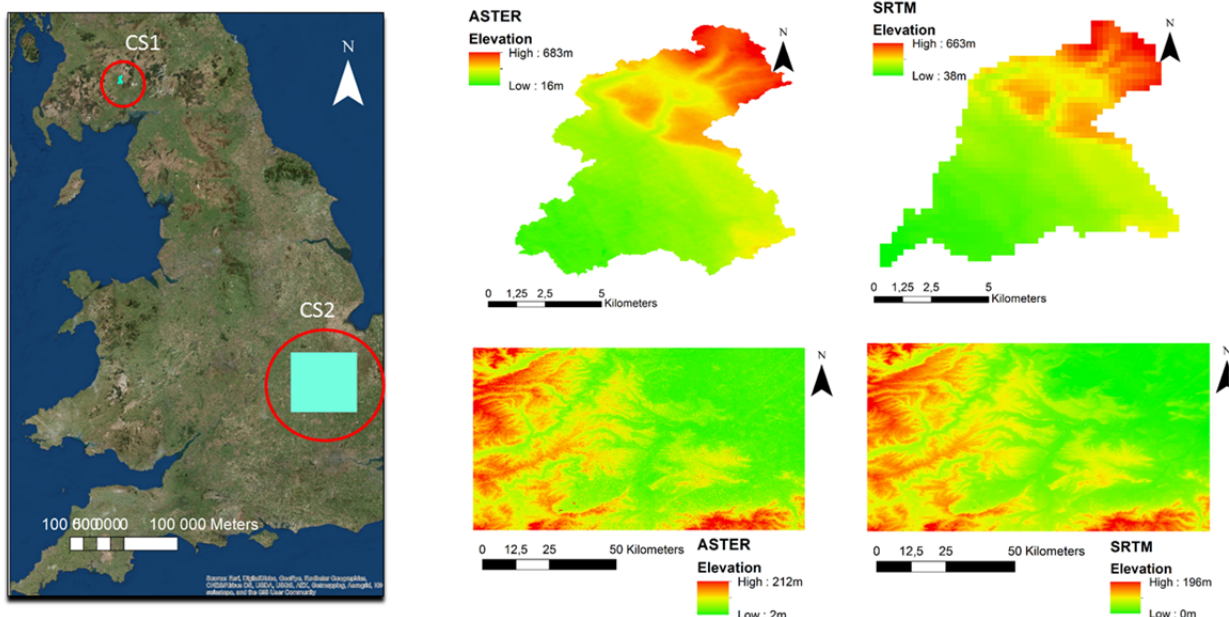


Fig. 3. Location and DEMs of both study areas, SA1 in North and SA2 in South of United Kingdom.

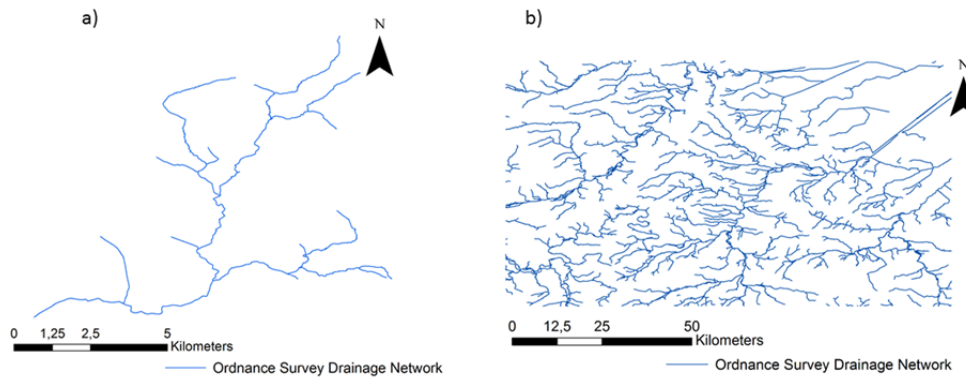


Fig. 4. Drainage networks of the Ordnance Survey for study area 1 (SA1) (a) and for study area 2 (SA2) (b).

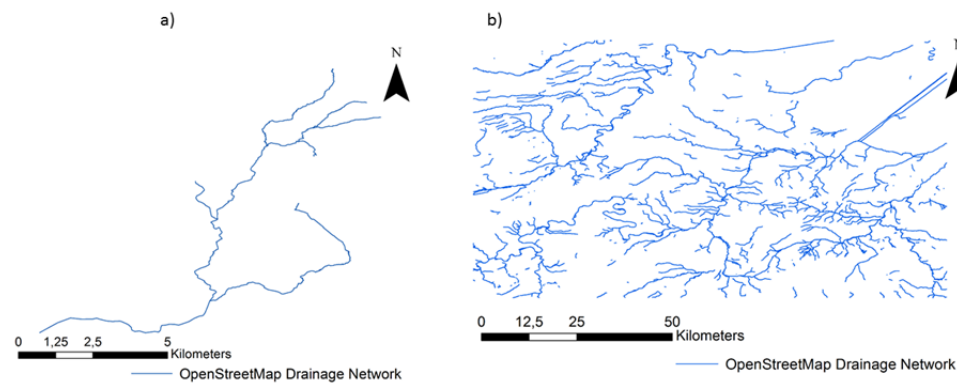


Fig. 5. OSM watercourses available for both study areas - SA1 (a) and SA2 (b).

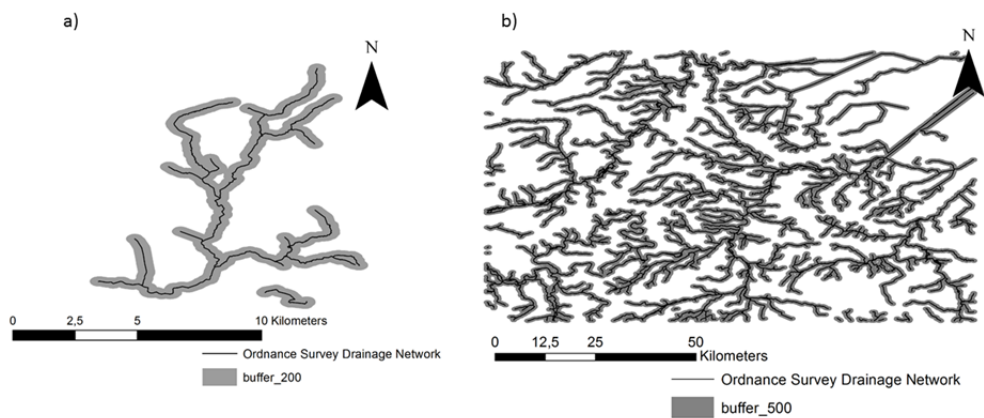


Fig. 6. a) A 200 m buffer around the reference drainage network in SA1; b) A 500 m buffer around the reference drainage network in SA2.

determined. Some tests were made to determine the appropriate *CL* for each SA. For SA1 the critical levels of 14 and 126 pixels were used, respectively, for SRTM and ASTER DEMs, derived as explained in section “Drainage networks extraction from the DEMs”. For SA2 the values used were 445 and 4,000 pixels, respectively for the SRTM and ASTER DEMs. The horizontal distances between each drainage network and the reference drainage network was calculated for the parts of the network inside the buffer created as describe in section “Assessment of the positional accuracy of the drainage networks”. The appropriate width of the buffers to consider was determined by visually analysis. This resulted in the use of 200 and 500 m for SA1 and SA2, respectively (Figure 6).

To compute the positional accuracy of the different drainage networks all data georeferenced in the World Geodetic System 1984 (WGS-84) was projected to the same projected Reference System (The British National Grid Reference System).

RESULTS

The drainage networks derived from the original and rebuilt DEMs ASTER and SRTM in both study areas are shown in Figure 7.

A visual analysis shows that for SA1 (Figure 7 a) and b)) the drainage network derived from the rebuilt SRTM DEM is more branched than the drainage network derived from the original DEM. The opposite situation occurs for the networks extracted from the ASTER models (original and rebuilt). Some changes in the horizontal position of the drainage network can also be seen. For the study area SA2 (Figure 7 c) and d)), the drainage network derived from the rebuilt ASTER DEM presents a higher similarity with the network extracted from the original ASTER DEM, namely in zones of lower altitude in the Northeast region of this study area.

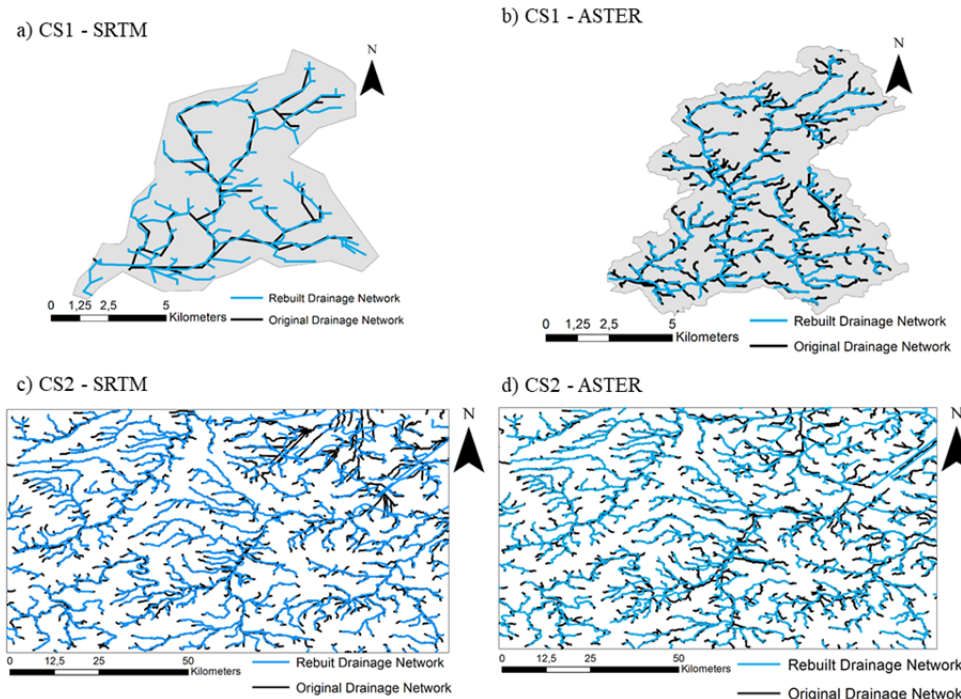


Fig. 7. Drainage networks extracted from the original and rebuilt SRTM DEMs, using the same critical levels a) for SA1 and c) for SA2; and from the original and rebuilt ASTER DEMs b) for SA1 and d) for SA2.

Some topographic parameters derived from the drainage networks were analysed and discussed. The parameters the order of the basin (O), the orders included in basin (O_i), the number of segments of i order (Ns_i) and the segments length of i order (L_i) and are shown in Table 1 for SA1 for the original and the rebuilt GDEMs. Table 2 show the results for the same parameters for SA2 for the original and rebuilt GDEMs.

In SA1 study area the order of the basin derived from SRTM DEM increased with the DEMs transformation presenting the values of $O = 3$ and $O = 5$, for the basins derived from original and rebuilt DEM, respectively. Also the number of segments and the segments length of each order show an increasing with the values of 34 and 140 numbers of segments for original and rebuilt SRTM DEM, respectively. For the basin derived from ASTER DEM the order maintains the value ($O = 5$), while the number of segments shows a decreasing from 330 to 140, as well as the segments length. In the SA2 the order of the basin varies with the same tendency of the SA1, for both DEMs with $O = 4$ and $O = 5$, for basins derived from original and rebuilt SRTM DEM, respectively. The basins derived from original and rebuilt DEM present the same order, $O = 5$. The number of segments decreased for basins extracted from both DEMs with the values of 1,150 and 772 for SRTM and the values of 1,281 and 776 for ASTER. The segments length also shows a decreasing for both DEMs. The analysis of OSM drainage networks positional accuracy was performed for each study area to assess whether OSM watercourses showed better positional accuracy than the drainage networks derived from the original GDEMs, as this assumption should be fulfilled to apply this methodology. Table 3 shows the mean (M) and standard deviation (σ) of the horizontal distances between the points of OSM watercourses and the reference drainage network. This table also shows the mean (M) and the standard deviation (σ) of the horizontal distances between the reference drainage network and the points of the drainage network obtained from the original ASTER and SRTM DEMs for both study areas.

Table 1. Basin order (O), number and length of segments for stream order O_i of the hydrographic network extracted from the original and rebuilt GDEMs for study area 1 (SA1).

SA1			
GDEMs	ORIGINAL		
	O_i	Number of segments	Length (km)
SRTM ($O=3$)	1	18	21.2
	2	10	11.4
	3	6	5.9
Total=		34	38.5
ASTER ($O=5$)	1	170	62.5
	2	68	24.4
	3	51	17.3
	4	35	11.9
	5	6	1.7
Total =		330	117.8

SA1			
GDEMs	REBUILT		
	O_i	Number of segments	Length (km)
SRTM ($O=5$)	1	73	30.6
	2	34	18.9
	3	16	10.3
	4	9	4.5
	5	8	5.4
Total =		140	69.7
ASTER ($O=5$)	1	111	34.9
	2	44	25.3
	3	34	9.2
	4	12	5.0
	5	10	1.7
Total =		211	76.1

It can be observed that the positional accuracy obtained for the OSM watercourses in both study areas is better than the positional accuracy obtained for the drainage networks derived from the original GDEMs, and therefore the above mentioned requirement is fulfilled.

Table 2. Basin order (O), number and length of segments for stream order O_i of the hydrographic network extracted from the original and rebuilt GDEMs for study area 2 (SA2).

SA2			
GDEMs	ORIGINAL		
	O_i	Number of segments	Length (km)
SRTM ($O=4$)	1	603	1,436.7
	2	299	665.5
	3	173	330.5
	4	75	149.0
Total =		1,150	2,581.7
ASTER ($O=5$)	1	637	1,484.4
	2	316	721.7
	3	163	312.3
	4	59	204.4
Total =		1,218	2,627.5

SA2			
GDEMs	REBUILT		
	O_i	Number of segments	Length (km)
SRTM ($O=5$)	1	401	1,117.1
	2	202	523.1
	3	73	213.2
	4	63	215.4
Total =		772	2,138.3
ASTER ($O=5$)	1	407	1,206.7
	2	213	605.3
	3	62	157.4
	4	64	214.8
Total =		776	2,265.1

Table 4 shows the mean and the standard deviation of the horizontal distances between the reference drainage network and the points of the drainage networks derived from the original (M_O and σ_O) and the rebuilt DEMs (M_R and σ_R), for both study areas. The differences between the obtained these values for the networks obtained from the original are rebuilt DEMs are also shown.

The results show that the mean and the standard deviation of the distance between the DEM extracted drainage networks and the reference lines decreases with the transformation in both study areas and for both DEMs, which corresponds to an im-

Table 4. Mean and standard deviation of the horizontal distances between the reference drainage network and the drainage networks obtained from the original and the rebuilt DEMs for study areas SA1 and SA2, as well as the differences between the values obtained for the original and rebuilt DEMs.

Study area	DEM	CL (pixels)	Buffer width (m)	Original GDEM		Rebuilt GDEM		Differences	
				M_O (m)	σ_O (m)	M_R (m)	σ_R (m)	$M_O - M_R$ (m)	$\sigma_O - \sigma_R$ (m)
SA1	SRTM	14	200	45.4	47.0	27.2	42.5	18.2	4.5
	ASTER	126	200	38.7	55.4	27.8	49.4	10.9	6.0
SA2	SRTM	445	500	92.8	116.6	54.4	89.5	38.4	27.1
	ASTER	4,000	500	104.9	127.8	56.0	102.0	48.9	25.8

Table 5. Total length of the Ordnance Survey drainage network (L_{OS}), of the drainage network extracted from the original DEMs (L_O) and of the one extracted from the rebuilt GDEMs (L_R), as well as the differences between the obtained values.

Study area	L_{OS} (km)	DEM used	CL (pixels)	L_O (km)	L_R (km)	$L_O - L_R$ (km)	$L_{OS} - L_O$ (km)	$L_{OS} - L_R$ (km)
SA1	38.8	SRTM	14	38.5	69.7	-31.2	0.3	-30.9
		ASTER	126	117.8	76.1	41.7	-79.0	-37.3
SA2	2,733.8	SRTM	445	2,581.7	2,138.3	443.4	152.1	595.5
		ASTER	4,000	2,722.8	2,261.5	461.3	11.0	472.3

Table 3. Mean and standard deviation of the horizontal distances between the reference drainage network (from Ordnance Survey) and the OSM watercourses, as well as the drainage networks obtained from the original DEMs, for study areas SA1 and SA2.

Study area	Data set	CL (pixels)	Buffer width (m)	Original GDEM	
				M (m)	σ (m)
SA1	OSM	---	200	10.5	28.0
	SRTM	14	200	45.4	47.0
	ASTER	126	200	38.7	55.4
SA2	OSM	---	500	20.7	57.3
	SRTM	445	500	92.8	116.6
	ASTER	4,000	500	104.9	127.8

provement of their positional accuracy. The results show a larger improvement in the mean distance for SRTM in SA1 (18.2 m for SRTM and 10.9 m for ASTER) and for ASTER in SA2 (48.9 m for ASTER and 38.4 m for SRTM). However, the opposite is observed for standard deviation, even though the values are very similar, in both cases with differences smaller than 1.5 m.

The topographic parameter total length of the drainage network (L) was analysed. Table 5 shows, for both study areas, the results obtained for the total length of the Ordnance Survey drainage network (reference data), the total length of the drainage networks obtained from the original and rebuilt DEMs and the differences between the obtained values.

It can be seen that using the same critical levels for the rebuilt DEMs that were used for the original models, the differences of total length obtained in SA1 between the reference drainage network (L_{OS}) and the drainage networks derived from the rebuilt DEMs (L_R) is -30.9 and -37.3 km for ASTER and SRTM, respectively. This shows that the drainage network obtained with the rebuilt DEMs is larger than the one available in Ordnance Survey and that this difference increased for SRTM, in relation to the difference between the reference drainage network and the drainage networks derived from the original DEMs ($L_{OS} - L_O$ is 0.3 km). However, for ASTER this difference decreased for the rebuilt DEM ($L_{OS} - L_O$ is -79 km, while $L_{OS} - L_R$ is -37.3 km). In SA2 the differences between the reference drainage network (L_{OS}) and the drainage networks derived from the rebuilt DEMs (L_R) are 595.5 and 472.3 km, respectively for the SRTM and ASTER DEMs. The difference between the drainage network obtained from the original and the rebuilt DEMs was also in both cases of the order of 400 km,

and in both cases the length of the drainage network decreased when obtained from the rebuilt DEM.

These differences were obtained considering the same *CL* that was used for the original DEMs. However, the choice of the *CL* to use in for each DEM may also be defined for each DEM, and therefore the length of the drainage network will change with this value and can be adjusted according to the needs. To illustrate this, different critical values were used for each DEM, so that drainage networks with similar characteristics could be obtained. This was done first taking into account the same factors and procedures that were used for original DEMs, that is, choose the *CL* that produces drainage networks derived from SRTM with total length next to the total length of reference drainage network. After that, use a *CL* nine times greater than the one used for SRTM DEM to extract the drainage networks from ASTER. Also independent values were used for ASTER, to analyse the differences. The *CL* used and the obtained results are shown in Table 6 and the obtained drainage networks can be seen in Figure 8, for both study areas.

In SA1, a *CL* of 55 pixels was used for SRTM, generating a drainage network with a total length of 39.0 km, presenting a difference of length of only -0.2 km in relation to the reference network. Using a *CL* nine times greater for ASTER model (*CL* = 495 pixels) the drainage network extracted have a total length of 31.3 km, presenting a difference of 7.5 km in relation to the reference network. Choosing an independent value for the DEM rebuilt from ASTER of 250 pixels, a drainage network with a length of 38.9 km is obtained, corresponding to a difference of -0.1 km in relation to the reference one. For SA2 the *CL* of 255 pixels used for the DEM rebuilt from SRTM produced a drainage network with a total length of 2,752.4 km, presenting a difference of -18.6 km in relation to the reference drainage network. Using a *CL* nine times greater for DEM rebuilt from ASTER (2,295 pixels), a drainage network with a total length of 2,925.7 km is obtained, which corresponds to a difference of -191.9 km. If an independent *CL* of 2,650 pixels was used, produce a drainage network with a total length of 2,732.1 km is obtained, which corresponds to a difference of

Table 6. Total length of the Ordnance Survey drainage network (L_{OS}) and of the drainage networks extracted from the rebuilt DEMs (L_R) considering *CL* that provide drainage networks with characteristics similar to the reference drainage network, as well as the differences between the obtained values.

Study area	L_{OS} (km)	DEM used	<i>CL</i> (pixels)	L_R (km)	$L_{OS} - L_R$ (km)
SA1	38.8	SRTM	55	39.0	-0.2
		ASTER	495	31.3	7.5
		ASTER	250	38.9	-0.1
SA2	2,733.8	SRTM	255	2,752.4	-18.6
		ASTER	2,295	2,925.7	-191.9
		ASTER	2,650	2,732.1	1.7

1.7 km. The drainage networks shown in Figure 8 show that when *CL* are chosen that provide networks with similar length the networks obtained from the rebuilt DEMs are in fact very similar to the reference drainage networks.

DISCUSSION AND CONCLUSIONS

The aim of the current work was to determine whether the watercourses available in OSM data could contribute to the creation of DEMs, generated using the ASTER and SRTM GDEMs, which enable the extraction of drainage networks with higher positional accuracy. The methodology uses only free geographic dataset and shows that the combination of OSM watercourses with ASTER and SRTM GDEMs generates DEMs that allow the extraction of more accurate drainage networks.

The study was applied to two areas located in the United Kingdom with different characteristics in terms of relief, dimension, coverage and completeness of OSM watercourses, which are some factors that may influence the accuracy of drainage networks. Authoritative data (from Ordnance Survey) was used as reference to assess the positional accuracy of the data used and results obtained.

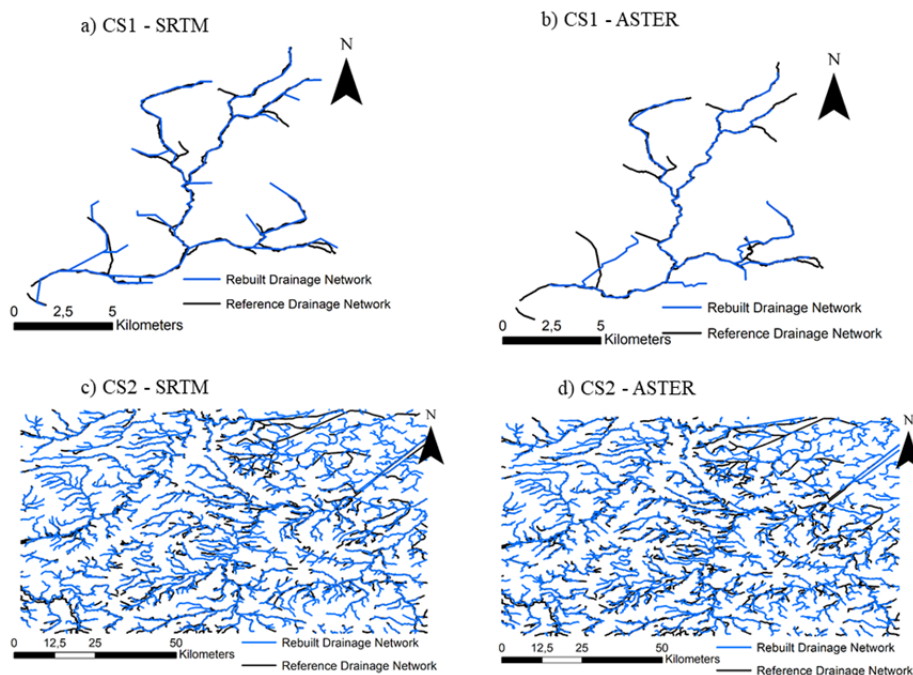


Fig. 8. Reference drainage networks and drainage networks extracted from the rebuilt DEMs, choosing the critical levels that approximate the length of the network under analysis to the reference network, for SRTM DEMs a) for SA1 and c) for SA2; and the rebuilt ASTER DEMs b) for SA1 and d) for SA2.

The results show that the positional accuracy of the drainage networks improved for both study areas and also for the data extracted from the SRTM and ASTER GDEMs, which proves the usefulness of the methodology. It can also be stressed that the positional accuracy improvement for both study areas is always higher for the data extracted from the SRTM DEM. That is, the data derived from this DEM takes more advantage of the transformation than those extracted from the ASTER DEM. The similarity of the obtained drainage networks with the reference network depends upon the *CL* parameter considered when extracting them from the DEMs, and therefore this value should be chosen independently for each DEM. This parameter also influences the topographic parameters derived from the drainage networks, such as the basin order as well as the number of segments and the segments length obtained for each stream order.

This methodology may be of particular interest for regions where there are no detailed and accurate topographic maps available, as the data sets used are free and available worldwide. It can also be useful when large areas are to be considered, covering more than one country, which would require merging detailed data from different institutions.

A fundamental aspect related to the application of this methodology is the positional accuracy of the OSM waterways. If mistakes are present in OSM data this will have negative impacts in the results. Therefore, the development of methods that enable the identification of erroneous data are particularly useful. Another limitation of the procedure is the coverage and completeness of OSM data, although the trend is that the volume of OSM data increases with an impressed speed (Haklay, 2010), and the waterways are one of the features that start to be inserted by the volunteers. Even if the completeness of OSM data in relation to the waterways is relatively low, the available waterways will likely still be useful, however this needs to be further investigated.

Future work will include the analysis of the impact of this transformation not only on the positional accuracy of the drainage network but also on other types of parameters extracted from the drainage network, such as bifurcation ratio and drainage density (Strahler, 1964), as well as the analysis of potential influence of the region's relief. Further investigations may analyse the variation of positional accuracy of those drainage networks in sub-areas of the global study area. An analysis of the accuracy of the rebuilt DEMs will be performed to ascertain whether they are also more accurate than the original DEMs.

Acknowledgements. This work has been supported by the Portuguese Foundation for Science and Technology (FCT) under project grant UID/MULTI/00308 / 2013.

REFERENCES

- Al-Bakri, M., Fairbairn, D., 2010. Assessing the accuracy of 'Crowdsourced' data and its integration with official spatial data sets. In: Proc. Symp. Accuracy 2010. Leicester, UK, pp. 317–320.
- Arun, P.S., Jana, R., Nathawat, M.S., 2005. A rule base physiographic characterization of drought prone watershed applying remote sensing and GIS. *Journal of the Indian Society of Remote Sensing*, 32, 189–201.
- Bossard, M., Feranec, J. and Otahel, J., 2000. CORINE Land Cover Technical Guide: Addendum 2000. European Environment Agency, Copenhagen.
- Brovelli, M.A., Minghini, M., Molinari, E., Zamboni, G., 2016. Positional accuracy assessment of the OpenStreetMap buildings layer through automatic homologous pairs detection: The methodology and a case study. *The International Archives of the Photogrammetry*. In: Proc. XXIII ISPRS Congress Remote Sensing and Spatial Information Sciences, vol. XLI-B2, , 12–19 July, Prague, Czech Republic.
- Cook, A.J., Murray, T., Luckman, A., Vaughan, D.G., Barrand, N.E., 2012. A new 100-m digital elevation model of the Antarctic Peninsula derived from ASTER Global DEM: Methods and accuracy assessment. *Earth System Science Data*, 4, 129–142.
- Das, S., Patel, P.P., Sengupta, S., 2016. Evaluation of Different Digital Elevation Models for Analysing Drainage Morphometric Parameters in a Mountainous Terrain: A Case Study of the Supin-Upper Tons Basin, Indian Himalayas. *Springer Plus*, 38 p. DOI: 10.1186/s40064-016-3207-0.
- Ebenezer, S.S., 2015. GIS Based Automated Drainage Extraction for the Analysis of Basin Morphometry in Vaniyar Sub-Basin, South India. *International Association of Scientific Innovation and Research (IASIR)*, pp. 31–34.
- Eckert, S., Kellenberger, T., Itten, K., 2005. Accuracy assessment of automatically derived Digital Elevation Models from ASTER data in mountainous terrain. *International Journal of Remote Sensing*, 9, 1943–1957.
- Elkhrachy, I., 2017. Vertical accuracy assessment for SRTM and ASTER Digital Elevation Models: A case study of Najran City, Saudi Arabia. *Ain Shams Eng J.* <http://dx.doi.org/10.1016/j.asej.2017.01.007>.
- Fisher, P., 1998. Improved modelling of elevation error with geostatistics. *GeoInformatica*, 2, 215–233.
- Florinsky, I.V., Kuryakova, G.A., 2000. Determination of grid size for digital terrain modelling in landscape investigations – Exemplified by soil moisture distribution at a micro-scale. *International Journal of Geographical Information Science*, 8, 815–832.
- Fonte, C.C., Minghini, M., Antoniou, V., See, L., Patriarca, J., Brovelli, M.A., Milcinski, G., 2016. An Automated Methodology for Converting OSM Data into a Land Use/Cover Map. In: *Proceedings of the 6th International Conference on Cartography & GIS, Albena (Bulgaria)*, June 13–17, 2016, Bulgarian Cartographic Association, 1, pp. 462–473. ISSN 1314-0604.
- Forkuor, G., Maathuis, B., 2012. Comparison of SRTM and ASTER Derived Digital Elevation models over two regions in Ghana – Implications for hydrological and environmental modelling. In: Piacentini T. (Ed.): *Studies on environmental and applied geomorphology*. InTech, pp. 219–240.
- Freeman, T.G., 1991. Calculating catchment area with divergent flow based on a regular grid. *Computers and Geosciences*, 17, 413–422.
- Goodchild, M.F., 2007. Citizens as sensors: the world of volunteered geography. *GeoJournal*, 4, 211–221.
- Greve, C. (Ed.), 1996. *Digital Photogrammetry – Addendum to the Manual of Photogrammetry*. Publication of the American Society of Photogrammetry and Remote Sensing.
- Haklay, M., 2010. How good is the volunteered geographic information? A comparative study of OpenStreetMap and Ordnance Survey datasets. *Environment and Planning B: Planning and Design*, 37, 682–703.
- Hanssen, R.F., 2001. *Radar Interferometry: Data Interpretation and Error Analysis*. Kluwer Academic Publishers, Dordrecht.
- Heymann, Y., 1994. Commission of the European Communities, Directorate-General for Environment, N.S., C.P. CORINE Land Cover: Technical Guide. European Guide. European Commission. Directorate-General. Environment, Nuclear Safety and Civil Protection, Luxembourg.
- Holmes, K.W., Chadwick, O.A., Kyriakidis, P.C., 2000. Errors in USGS 30-meter Digital Elevation Model and its impact on terrain modelling. *Journal of Hydrology*, 233, 154–173.
- Hutchinson, M.F., Xu, T., Stein, J.A., 2011. Recent progress in the ANNUDEM elevation gridding procedure. In: Hengel, T., Evans, I.S., Wilson, J.P., Gould, M. (Eds.): *Geomorphometry 2011*, pp. 19–22.

- Jenson, S.K., Domingue, J.O., 1988. Extracting topographic structure from digital elevation data for Geographic Information System analysis. *Photogrammetry Engineering and Remote Sensing*, 54, 1593–1600.
- Kääb, A., 2005. Combination of SRTM3 and repeat ASTER data for deriving alpine glacier flow velocities in the Himalaya. *Remote Sensing Environment*, 4, 463–474.
- Kenward, T., Lettenmaier, D.P., Wood, E.F., Fielding, E., 2000. Effects of Digital Elevation Model accuracy on hydrologic predictions. *Remote Sensing and Environment*, 3, 432–444.
- Kyriakidis, P.C., Shortridge, A.M., Goodchild, M.F., 1999. Geostatistics for conflation and accuracy assessment of Digital Elevation Models. *International Journal of Geographical Information Science*, 7, 677–707.
- Lacroix, M.P., Martz, L.W., Kite, G.W., Garbrecht, J., 2002. Using digital terrain analysis modelling techniques for the parametrization of a hydrologic model. *Environmental Modelling Software*, 17, 127–136.
- Lin, W.T., Chou, W.C., Lin, C.Y., Huang, P.H., Tsai, J.S., 2005. Automated suitable drainage network extraction from Digital Elevation Models in Taiwan's upstream watersheds. *Hydrological Processes*, 20, 2, 289–306. DOI: 10.1002/hyp.5911.
- Lin, W.T., Chou, W.C., Lin, C.Y., Huang, P.H., Tsai, J.S., 2008. WinBasin: using improved algorithms and the GIS technic for automated watershed modelling analysis from Digital Elevation Models. *International Journal of Geographical Information Science*, 22, 47–69.
- Liu, T., Yan, H., Zhai, L., 2015. Extract relevant features from DEM groundwater potential mapping. *The International Archives of the Photogrammetry, Remote Sensing and Spatial Information Sciences*, XL-7/W4, International Workshop on Image and Data Fusion, USA, pp. 113–119.
- Mark, D.M., 1984. Automated detection of drainage networks from Digital Elevation Models. *Cartographica*, 21, 168–178.
- Martz, L.W., Garbrecht, J., 1998. The treatment of flat areas and depressions in automated drainage analysis of Raster Digital Elevation Models. *Hydrological Processes*, 12, 843–855.
- Massonet, D., Feigl, K.L., 1998. Radar interferometry and its applications to changes in the Earth's surface. *Reviews of Geophysics*, 36, 441–500.
- Monteiro, E.V., Fonte, C.C., de Lima, J.L.M.P., 2015. Assessing positional accuracy of drainage networks extracted from ASTER, SRTM and OpenStreetMap. In: *Proceedings of AGILE 2015*, Lisbon, Portugal, June 9–12, 5 p.
- Mooney, P., Corcoran, P., Winstanley, A.C., 2010. Towards quality metrics for OpenStreetMap. In: *SIGSPATIAL GIS'10*, pp. 514–517.
- Mukherjee, S., Joshi, P.K., Mukherjee, S., Gosh, A., Garg, R.D., Mukhopadhyay, A., 2013. Evaluation of vertical accuracy of open source Digital Elevation Model (DEM). *International Journal of Applied Earth Observation and Geoinformation*, 21, 205–217.
- Mukul, M., Srivastava, V., Jade, S., Mukul, M., 2017. Uncertainties in the Shuttle Radar Topography Mission (SRTM) heights: Insights from the Indian Himalaya and Peninsula. *Scientific Reports*, DOI: 10.1038/srep41672, www.nature.com/scientificreports, 10 p.
- Neis, P., Zipf, A., 2012. Analysing the contributor activity of a volunteered geographic information project – The case of OpenStreetMap. *ISPRS International Journal of Geo-Information*, 1, 146–165.
- Neis, P., Zielstra, D., 2014. Recent developments and future trends in volunteered geographic information research: The case of OpenStreetMap. *Future Internet* 2014, 1, 76–106. DOI: 10.3390/fi6010076.
- O'Callaghan, J.F., Mark, D.M., 1984. The extraction of drainage networks from Digital Elevation Data. *Computer Vision, Graphics, and Image Processing*, 28, 323–344.
- Petrasova, A., Mitasova, H., Petras, V., Jeziorka, J., 2017. Fusion of high-resolution DEMs for water flow modelling. *Open Geospatial Data, Software and Standards*. DOI: 10.1186/s40965-017-0019-2.
- Planchon, O., Darboux, F., 2002. A fast, simple and versatile algorithm to fill the depressions of Digital Elevation Models. *Catena*, 2, 159–176.
- Rodriguez, E., Morris, C., Belz, J., 2006. A global assessment of SRTM performance. *Photogrammetric Engineering and Remote Sensing*, 72, 249–260.
- Roth, A., Knopfle, W., Strunz, G., Lehner, M., Reinartz, P., 2002. Towards a global elevation product: Combination of multi-source Digital Elevation Models. In: *Proceedings of Symposium on Geospatial Theory, Processing and Applications*, Ottawa 2002, 5 p.
- Schellekens, J., Broolsma, R.J., Dahm, R.J., Donchyts, G.V., Winesemius, H.C., 2014. Rapid setup of hydrological and hydraulic models using OpenStreetMap and the SRTM derived Digital Elevation Model. *Environmental Modelling & Software*, 61, 98–105.
- Sefercik, U.G., 2012. Performance estimation of ASTER Global DEM depending upon the terrain inclination. *Journal of Indian Society of Remote Sensing*, 4, 565–576.
- Strahler, A.N., 1964. Quantitative geomorphology of drainage basins and channel networks. In: Chow, V.T. (Ed.): *Handbook of Applied Hydrology*, pp. 4–39.
- Tarboton, D.G., Bras, R.L., Rodriguez-Iturbe, I., 1991. On the extraction of channel networks from Digital Elevation Data. *Hydrologic Processes*, 5, 81–100.
- Tarboton, D.G., 1997. A new method for the determination of flow directions and upslope areas in Grid Digital Elevation Models. *Water Resources*, 2, 309–319.
- Toutin, T., 2002. Impact of terrain slope and aspect on radargrammetric DEM accuracy. *ISPRS Journal of Photogrammetry and Remote Sensing*, 57, 228–240.
- Varga, M., Bašić, T., 2013. Quality assessment and comparison of Global Digital Elevation Models on the territory of Republic of Croatia. *Cartography and Geoinformation*, 20, 4–17.
- Vieux, B.E., 1993. DEM aggregation and smoothing effects on surface runoff modelling. *Journal of Computing in Civil Engineering*, 3, 310–338.
- Weydahl, D.J., Sagstuen, J., Dick, O.B., Ronning, H., 2007. SRTM DEM accuracy over vegetated areas in Norway. *International Journal of Remote Sensing*, 16, 3513–3527.
- Yadav, S., Indu, J., 2016. Estimation of vertical accuracy of Digital Elevation Models over complex of Indian Subcontinent. *IGARSS*, 978-1-5090-3332-4/16, IEEE, 6036-6039.
- Zhang, W., Montgomery, D.R., 1994. Digital Elevation Model grid size, landscape representation, and hydrologic simulation. *Water Resources Research*, 30, 1019–1028.
- Zielstra, D., Zipf, A., 2010. OpenStreetMap quality research in Germany. In: *Sixth International Conference on Geographic Information Science*, pp. 15–17.

Received 4 September 2017
Accepted 30 November 2017

Note: Colour version of Figures can be found in the web version of this article.

The Wavelets show it – the transit time of water varies in time

Milan Onderka*, Vladimír Chudoba

Comenius University, Faculty of Mathematics, Physics and Informatics, Department of Astronomy, Physics of the Earth and Meteorology, Mlynská dolina, SK-842 48 Bratislava, Slovakia.

* Corresponding author. E-mail: milan.onderka@fmph.uniba.sk

Abstract: The ways how water from rain or melting snow flows over and beneath the Earth's surface affects the timing and intensity at which the same water leaves a catchment. Several mathematical techniques have been proposed to quantify the transit times of water by e.g. convolving the input-output tracer signals, or constructing frequency response functions. The primary assumption of these techniques is that the transit time is regarded time-invariant, i.e. it does not vary with temporarily changing e.g. soil saturation, evaporation, storage volume, climate or land use. This raises questions about how the variability of water transit time can be detected, visualized and analyzed. In this paper we present a case study to show that the transit time is a temporarily dynamic variable. Using a real-world example from the Lower Hafren catchment, Wales, UK, and applying the Continuous Wavelet Transform we show that the transit time distributions are time-variant and change with streamflow. We define the Instantaneous Transit Time Distributions as a basis for the Master Transit Time Distribution. We show that during periods of elevated runoff the transit times are exponentially distributed. A bell-shaped distribution of travel times was observed during times of lower runoff. This finding is consistent with previous investigations based on mechanistic and conceptual modeling in the study area according to which the diversity of water flow-paths during wet periods is attributable to contributing areas that shrink and expand depending on the duration of rainfall. The presented approach makes no assumptions about the shape of the transit time distribution. The mean travel time estimated from the Master Transit Time Distribution was ~54.3 weeks.

Keywords: Transit time distribution; Tracer; Chloride; Continuous wavelet transform; Non-stationary.

INTRODUCTION

The transit time of water became an important descriptor of catchment functioning due to its potential to affect many chemical and biological processes and also because it can reveal new phenomena in the process of runoff generation (Duffy et al., 1985; Heidebüchel et al., 2012; Kirchner, 2016; Kirchner et al., 2000, 2001; White, 1987). The distribution of water transit times improves our understanding of how catchments response to changes in land use, how fast a contaminant will decay, and how promptly a catchment will respond to altered management practices (Duffy et al., 1985; McGuire et al., 2002). Basically, every catchment can be characterized by its water transit time distributions (TTD) that reflect the diversity of flowpaths connecting each point on the landscape with a stream outlet (Benettin et al., 2015a, 2015b; Botter et al., 2011; Davies et al., 2013; Harman, 2015; Heidebüchel et al., 2012; Hrachovitz et al., 2010; Kirchner et al., 2001, 2000; McGuire and McDonnell, 2006; Tekleab et al., 2014). Some authors relate physiographic characteristics of catchments to the mean of water transit times (Dunn et al., 2007; Gomez and Wilson, 2013; Hrachovitz et al., 2010; Onderka et al., 2012; McGuire et al., 2005). As the mean transit time is only a central tendency measure, it cannot reveal much about the underlying distribution of all transit times, as it is the shape of the distribution of transit times that reflects the heterogeneity of flow paths and velocities (Hrachovitz et al., 2010; Kirchner et al., 2001, 2000; McGuire and McDonnell, 2006). A common assumption in estimating the transit time distribution is that the hydrologic conditions in a catchment under investigation are constant (Harman, 2015; Heidebüchel et al., 2012; Maloszewski and Zuber, 1983). However, this assumption is in most cases unjustified (Harman, 2015; Heidebüchel et al., 2012; Maloszewski and Zuber, 1983; McMillan et al., 2012; van der Velde et al., 2012; van der Velde

et al., 2015), as the steady state approximation is applicable only when the dynamic part of the investigated system is small in comparison with the total volume of the catchment storage. Maloszewski and Zuber (1983) stated that a catchment can be considered as a steady state system when changes in flow rates are short in comparison with the duration of changes in tracer concentration. Other plausible mechanisms explaining the non-stationary nature of TTDs include e.g. activation of various flowpaths during the runoff generation (Heidebüchel et al., 2012), freezing/thawing of soil water, accumulation of snowpack and its subsequent snowmelt, and infiltration excess overland flow during extreme rainfall events and evaporation. Both time and frequency domains became popular for studying transit time distributions (Hrachovitz et al., 2009; Kirchner et al., 2000, 2001; Maloszewski and Zuber, 1983; McDonnell et al., 2010; McGuire and McDonnell, 2006; McGuire et al., 2002, 2005; Soulsby et al., 2014, 2015). However, in the time domain representation of a signal it is recognized that information about the frequency content of the signal is hidden. On the other hand, in the frequency domain analysis, the information about the temporal evolution of a signal gets obscured (Torrence and Compo, 1998). Unfortunately, the Fourier analysis does not allow us to examine the temporal variations in TTD. To overcome this problem, we use the Continuous Wavelet Transform (CWT). The key advantage of the CWT over the conventional Fourier methods or integral convolution is its ability to detect changes in the individual frequency components of a signal in time (Farge, 1992; Torrence and Compo, 1998). Our hypothesis is that by using CWT we can: 1) estimate the distribution of transit times in the lower Hafren catchment; and 2) quantify and visualize the non-stationary nature of transit times in contrast to the results from previous studies in the area (Kirchner et al., 2000, 2001).

MATERIALS AND METHODS

Sources of data: To test our approach on real-world data we used the publically available datasets from the Plynlimon research catchments (Benettin et al., 2015a, 2015b; Kirchner et al., 2001; Neal, 1997; Neal et al., 2011, 2013), which are the most thoroughly investigated experimental catchments worldwide. The Plynlimon research catchments lie within the headwaters of the River Severn and the River Wye in the uplands of mid-Wales, UK. The Centre of Ecology and Hydrology, UK, made this database available to scientific research such as this one. These catchments were described in detail in Neal (1997) so we restrict the description of the dataset and the catchment only within necessary limits. More details can be found in Neal et al. (2011). Data from a headwater catchment (the Lower Hafren) were used in this study. The publically available dataset from the Plynlimon research catchment contain two sets: raw data, and edited data. In our analyses we used the edited data, where any problematic data values have been corrected or excluded. The edited data include only those measurements in which we have a high degree of confidence (<https://data.gov.uk/dataset/plynlimon-research-catchment-hydrochemistry>). The datasets we used include time-series of rainfall, runoff and chloride concentrations measured in bulk

precipitation and stream water with a weekly sampling frequency. The catchment has a temperate maritime climate with precipitation primarily arriving from the Atlantic Ocean, with sea-salt chloride inputs fluctuating substantially (Benettin et al., 2015a, 2015b; Kirchner et al., 2000; Neal, 1997). We assume that rainfall is the dominant input of chloride to the catchment. The catchment area is about 3.5 km², and consists of about 60% forest and 40% moorland overlying Lower Paleozoic mudstone and shale with some glacial drift (Harman et al., 2015). Chloride concentrations measured in precipitation and in stream-water were chosen to represent the non-reactive tracer. Bulk precipitation was collected at Carreg Wen near the edge of the catchment in continuously open containers. No substantial anthropogenic sources of chloride are expected, making chloride an effective non-reactive chemical tracer originating mostly from rainfall (Benettin et al., 2015a, 2015b; Harman, 2015; Kirchner et al., 2000, 2001).

Signal analyses: First, the mass fluxes of chloride in rainfall and stream water were calculated. The observed time series of rainfall, runoff and chloride concentrations are shown in Fig. 1.

As rainfall is sampled in collectors, i.e. the amount of water collected is an integrated sample of precipitated water since the last read-out. The mass fluxes of chloride in rainfall were calculated by multiplying the amount of water collected over a

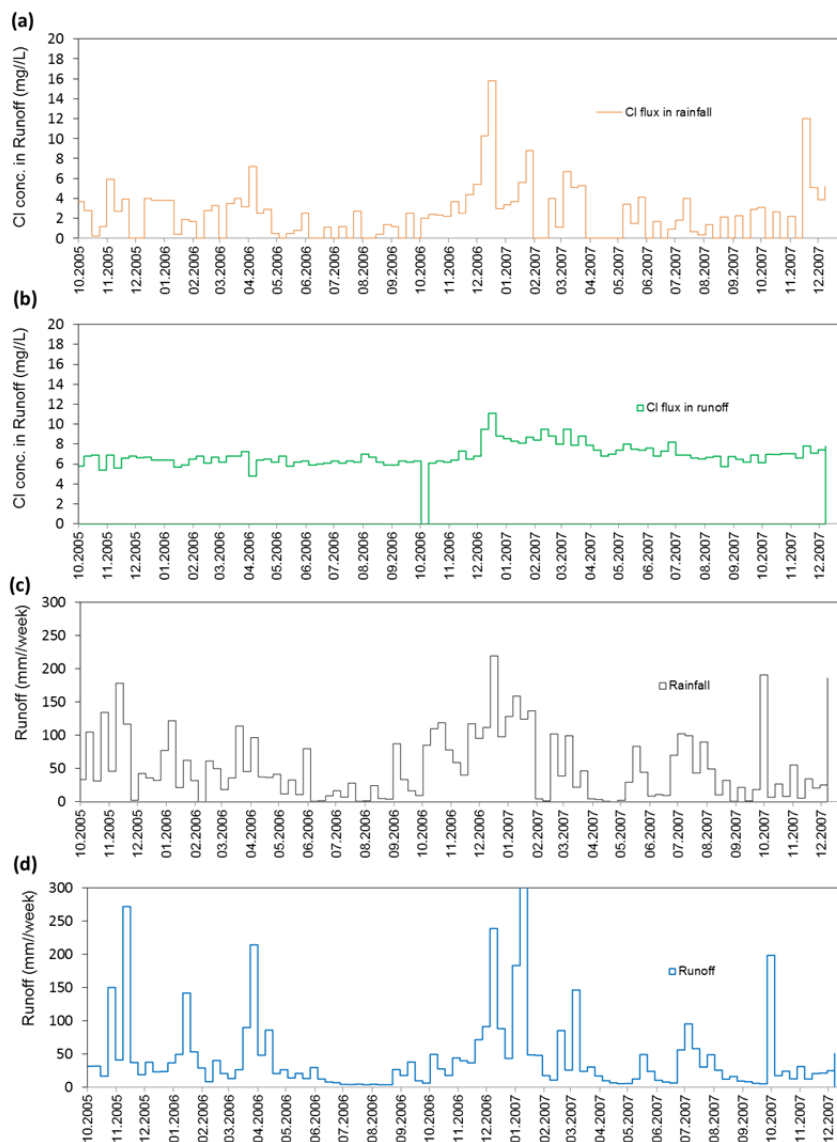


Fig. 1. Chloride concentrations in rainfall (a) and runoff (b). Weekly precipitation totals (c) and weekly runoff (d).

week and the concentration of chloride detected in the rainfall sample at the time of read-out. Chloride mass fluxes in runoff were calculated by multiplying the discharge at the ‘Lower Hafren’ gauging station and the concentration of chloride in the grab sample taken at a weekly sampling interval. Both time series of chloride fluxes were resampled to a common temporal resolution of 7 days.

The Continuous Wavelet Transform

Several attempts have been made recently to apply wavelet analysis to hydrometric and hydrochemical problems. For example, Weigand et al. (2017) applied CWT to relate temporal and spatial changes in dissolved organic carbon and nitrate concentrations. Another example is the paper of Onderka et al. (2013) where the authors used the CWT to estimate seepage velocities of water in stream sediments. Generally, two forms of wavelet transforms exist: the discrete wavelet transform, which gives a compact data presentation and is mostly used for the reduction and compression of noise, and its counterpart CWT (Weigand et al., 2017), which is more appropriate for the extraction of features, especially of complex time series containing noise. Since we seek a solution for the time-varying problem of TTD, we use the Continuous Wavelet Transform. A concise description of the wavelet analysis can be found e.g. in Farge (1992) or Torrence and Compo (1998). However, for the sake of clarity, we restrict ourselves here only to the description of CWT and its properties that are essential for the estimation of TTD. The main difference between the Fourier Transform and the Continuous Wavelet Transform is that wavelets are localized in both time and frequency. One can think of the difference also in terms of the Heisenberg Uncertainty principle, according to which, each wavelet reveals information about the temporal extent of the signal as well as about the frequency spectrum of the signal. The continuous wavelet transform (CWT) of a time series is essentially its convolution with the local basis functions, called ‘wavelets’ (Farge, 1992; Torrence and Compo, 1998). The wavelets can be stretched and translated to provide flexible resolution in both frequency and time (Torrence and Compo, 1998). The Continuous Wavelet Transform for a discrete sequence of measurements x_n (e.g. tracer mass flux in our case) with equidistant spacing δt is defined as the convolution product of x_n with a dilated and translated wavelet $\psi(\eta)$ to balance the resolution between the time domain and frequency domain depending on a non-dimensional time parameter η as:

$$W_n^X(s) = \sum_n^{N-1} x_n \psi^* \left[\frac{(n' - n)\delta t}{s} \right] \quad (1)$$

where W^X is the wavelet power, n is the time index, s is the wavelet scale, δt is the sampling period, N is the number of observations in the time series, and the asterisk indicates the complex conjugate. Since the above equation leads to complex wavelet coefficients (containing real and imaginary parts), the wavelet power spectrum $|W_n(s)|^2$ is a convenient way to describe the fluctuations of the variance of a signal at different times and frequencies. The Morlet wavelet is defined as:

$$\psi_0(\eta) = \pi^{-1/4} e^{j\omega_0\eta} e^{-\eta^2/2} \quad (2)$$

where ω_0 is the non-dimensional frequency ($\omega_0 = 6$), as defined in Torrence and Compo (1998). A bias occurs at the beginning and at the end of the wavelet power spectrum because the wavelet is not completely localized in time (Grinsted et al.,

2004; Torrence and Compo, 1998). A cone of influence (COI) has been proposed to ignore the edge effects. The COI is an area in which the wavelet power caused by the poorly localized wavelet near the beginning and end of a time-series has dropped to e^{-2} of the wavelet power at the edge. Our wavelet analysis was implemented in the package of Matlab codes provided by Aslak Grinsted (<https://github.com/grinsted/wavelet-coherence>) and the Torrence & Compo codes (<http://paos.colorado.edu/research/wavelets/>). We used the Matlab workspace to further to process and analyze the variables (wavelet coherence power, phase, etc.).

Since we are interested in quantifying the relative time-lags between two wavelet traces, we use the cross-wavelet power to calculate the wavelet phase-difference. The time-frequency dependencies between the two time series of chloride can be analyzed by the cross-wavelet transform (XWT) of the two time series x_t and y_t as:

$$W_{xy} = W^X W^{Y*} \quad (3)$$

where W^X and W^Y denote the wavelet transforms of x_t and y_t , respectively. The asterisk indicates the complex conjugate of the series y_t . Then the phase-difference $\Delta\phi_{xy}$ between the two time series at any point in time is defined as:

$$\Delta\phi_{xy} = \arctan \left(\frac{I(W_{xy})}{R(W_{xy})} \right) \quad (4)$$

where I and R in Eq. 4 refer to the imaginary and real parts of the WXT. Taking the inverse tangent of the ratio of the imaginary and real parts of the XWT we obtain a phase difference between the two series anywhere between $-\pi$ and $+\pi$ (radians). A phase-difference of zero indicates that the two series are in perfect phase, i.e. moving together without any time-lag. If $\Delta\phi_{xy}$ is constrained by zero and $\pi/2$, it is said that the time series y_t leads x_t ; and if $\Delta\phi_{xy}$ is constrained by $-\pi/2$ and zero, then the time series x_t leads the time series y_t . After calculating the phase differences for all time scales (s) at all times (t) we can define the ‘instantaneous’ time-lag $\Delta T_{xy}(s, t)$ between the two series, i.e. a time-lag calculated for every scale and for every point in time as:

$$\Delta T_{xy}(s, t) = \frac{\phi_{xy}(s, t)}{\omega(t)} \quad (5)$$

where $\omega(t)$ is the angular frequency corresponding to the wavelet scale s .

Since the CWT can be also used as a bandpass filter, the original signal can be reconstructed from the wavelet coefficients on a scale by scale basis. We used the procedure described in Torrence and Compo (1998) to decompose the original signal for all scales separately. The full reconstructed original signal is the sum of the individual decomposed components. Decomposing the signal into its frequency components makes it possible to analyze the contribution of the individual frequency components of the signal (κ_i) to the total signal (y_{total}) by:

$$\kappa_i(s, t) = \frac{y_{si}}{\sum_{i=m}^{i=n} y_{si}} \quad (6)$$

where y_{si} is the i -th frequency component ($i \in \langle n, m \rangle$) of the full signal y_{total} , n is the indexed beginning of the time-series and m is the indexed end of the time series, s refers to the scale, and

finally $y_{total} = \sum_{i=n}^{i=m} y_{si}$ is the full original signal.

The extent to which the chloride fluxes in runoff lag the rainfall fluxes of chloride was investigated scale by scale by analyzing the phases derived from cross-wavelet spectra. First, we derived the phase differences from the calculated cross-wavelet spectra by applying Eq. 4 to the wavelet coefficients (Eq. 1). As we are interested in time-lags rather than the phase differences, the phases were transformed to time-lags by Eq. 5.

To get a sense of how each frequency contributes to the overall signal variance, the basic filtering property of wavelets can be used. In this way the relative contribution of the individual frequencies to the whole signal is determined (Eq. 6). Now as we know to what extent the individual frequency components contribute to the total signal at time t_i we can construct empirical distribution functions for the time-lags that are defined for each sampling time t_i . According to the law of mass conservation, the total mass that leaves the catchment has to equal the total tracer mass at the input (rainfall in our case); hence an instantaneous pulse of tracer can be translated into an output signal by convolving the input signal with a time-dependent transfer function $g(t, \tau)$

$$g(t, \tau) = \frac{c_{out}(t, \tau) Q_{out}(t, \tau)}{\int_{\tau} c_{out}(t, \tau) Q_{out}(t, \tau) dt} \quad (7)$$

where t is the time of leaving and τ is the time of entry; $c_{out}(t, \tau)$ is the output tracer concentration, and $Q_{out}(t, \tau)$ is the outflow volumetric flowrate. Note that the area under the integral in Eq. 7 has to equal to 1.0:

$$\int_{\tau} g(t, \tau) dt = 1 \quad (8)$$

Two-parameter Weibull distribution

The Weibull distribution is a very flexible distribution model with two parameters, the β shape parameter, λ scale parameter, allowing the distribution to take on a broad range of shapes (Eq. 9):

$$f(t) = \frac{\beta}{\lambda} \left(\frac{x}{\lambda}\right)^{\beta-1} \exp\left(-\left(\frac{x}{\lambda}\right)^{\beta}\right) \quad (9)$$

where β is the shape parameter and λ is the scale parameter of the distribution function. A special case is when the Weibull distributions equals one ($\beta = 1$), i.e. when the Weibull distribution reduces to the exponential distribution. For $\beta < 1$, the Weibull distribution decreases as a sharp exponential, while for $\beta > 1$ the distribution becomes bell-shaped with long tails. We choose the Weibull distribution function due to its known flexibility in fitting empirical data; however, one could also consider the Gamma Function which has similar properties as the Weibull, and which has also been previously used in transit time modeling (e.g. Kirchner et al., 2000), or the Beta distribution as used in van der Velde et al. (2012). The median and mean values of the estimated transit times were calculated from the fitted Weibull distributions as: $TTD_{mean} = \lambda \Gamma\{1+(1/\beta)\}$ and $TTD_{median} = \lambda \{\ln(2)\}^{1/\beta}$.

Instantaneous Transit Time Distributions

The previously defined time-lags $\Delta T_{xy}(s, t)$ in (Eq. 5) and the individual frequency contributions $\kappa_i(s, t)$ in (Eq. 6) are used to estimate the transit time distributions for each point in time t individually. Recalling that the TTD is essentially the time-dependent transfer function $g(t, \tau)$, (see Eq. 7), then by sorting the individual frequency contributions $\kappa_i(s, t)$ according to the time-lags $\Delta T_{xy}(s, t)$ in an ascending order one obtains an empirical form of the transfer function $g(t, \tau)$. We can now fit the Weibull distribution function (Eq. 9) to $g(t, \tau)$ to obtain Instantaneous Transit Time Distributions (ITTDs). Each Instantaneous Transit time Distribution is defined by its scale $\lambda(t)$ and shape $\beta(t)$ Weibull parameters.

Master Transit Time Distribution

To generalize the Instantaneous Transit Time Distributions defined above and to obtain a more integrated view on the distribution of transit times, the Master Transit Time Distribution (MTTD) can now be introduced. Our motivation to define the MTTD is that it merges all the ITTDs into a single distribution. The MTTD is defined here as the mean of all instantaneous transit time distributions. The rationale behind using the MTTD is that it can be thought of as a surrogate of a transit time distribution that could be derived from Fourier power spectra, as described e.g. in McGuire and McDonnell (2006). Moreover, the Master Transit time distribution allows us to compare our results estimates of the transit times with other authors who used the Fourier transform (Kirchner et al., 2001).

RESULTS

As expected, the chloride fluxes in runoff exhibit a smaller portion of high frequency components compared to the rainfall signal (Fig. 1a, b). This phenomenon has been already explained in Kirchner et al. (2000), i.e. the short-lived pulses of rainfall water are translated to the catchment outlet slowly, causing the input trace of water to stretch in time. Therefore the chloride fluxes at the catchment output fluctuate less than those at the input. We further looked at the cross-wavelet spectra of chloride fluxes in rainfall (Fig. 2) to see a strong and

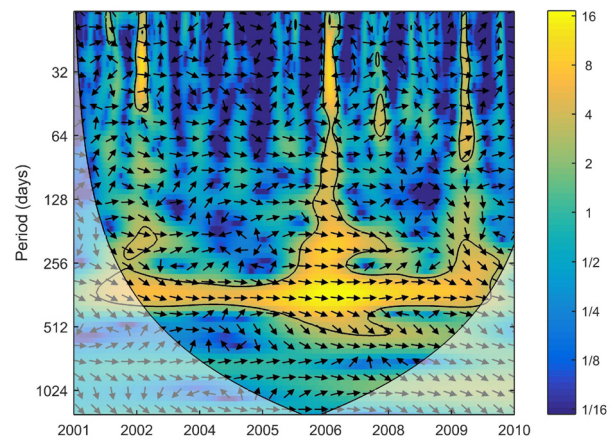


Fig. 2. The cross-wavelet power spectrum of chloride fluxes in rainfall and runoff. The contour level depicts the 95% significance level (tested against red noise). The colorbar placed on the right represents the squared power of the cross-wavelet transform. The phase arrows show the relative phasing of two time series. The arrow can be interpreted as a lead/lag.

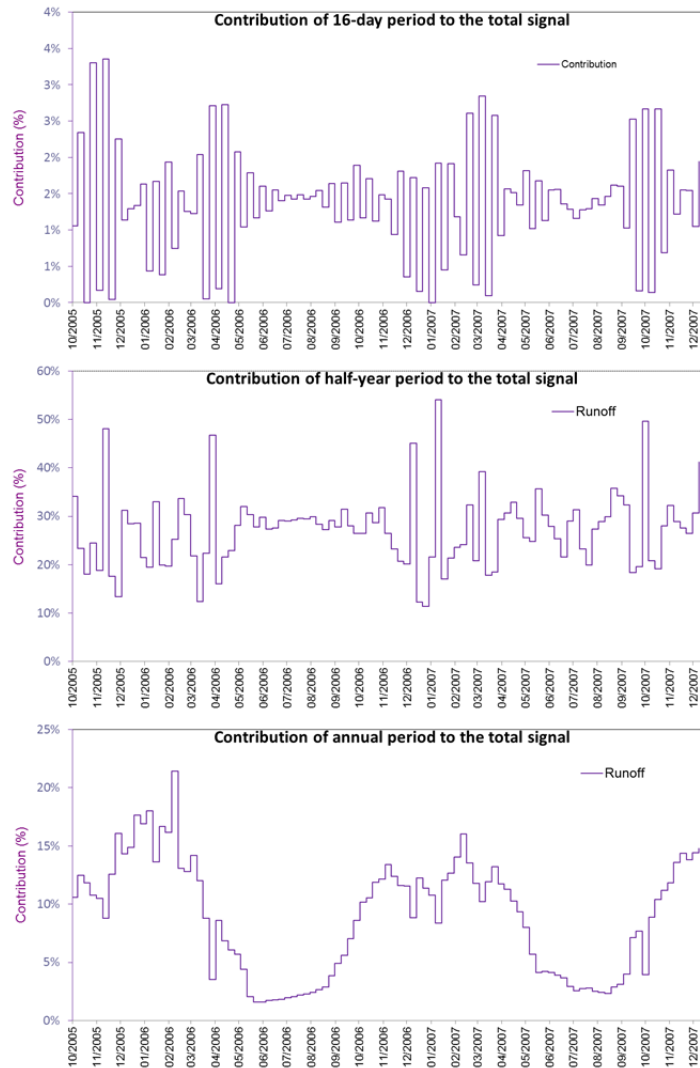


Fig. 3. Contribution of three (arbitrarily chosen) frequency contents (y_i) to the total signal (y_{total}) calculated from Eq. 6. (Upper plot) contribution of the 16-day signal; (Middle plot) contribution of the semi-annual period (6-months period) to the total signal; and (Bottom plot) contribution of the annual signal (12-month period) component.

statistically significant coherency between the rainfall and runoff signals with an annual periodicity, which is visible in the spectrogram as a high-energy region near the period of ~ 50 weeks (Fig. 2). The phase relationship is indicated by the orientation of the arrows (with in-phase pointing right, anti-phase pointing left). Since the phase-arrows point only in one dominant direction (to the right) at the annual period, we can say that the two series are phase-locked at periods around 365 days. Generally, the extent to which a certain frequency component contributes to the overall signal variance is visualized in Fig. 2 on the color bar. The annual frequencies located at period between 250 and 450 days (enclosed within the contour) are contain more energy and are red in color. The contribution of the reconstructed chloride fluxes in runoff to the total signal indicate (Fig. 3c) that this annual component contributes to the overall variance of the runoff fluxes of chloride by up to some 30%.

The β parameter of the Weibull distribution defines the overall shape of the distribution. We plotted the estimated β parameters versus time and runoff (Fig. 6). By tracking the effect of runoff on the shape of the ITTDs, one can see that during and briefly after periods of high runoff episodes the β shape parameter drops below 1.0, which indicates that the ITTD can change its shape dramatically from a bell-shape to an exponential.

After constructing the Instantaneous Transit Time Distributions for each time t_i , the Master Transit Time Distribution was calculated and plotted in Fig. 4. The MTTD is the defined as the mean of all ITTDs. The mean transit time calculated from the MTTD is 54.73 weeks, and the median is 40.79 weeks. This implies that 50% of water that has fallen on the catchment leaves the catchment via its stream outlet within 40.79 weeks (~ 285 days). Finally, the mean and median values were calculated also for the ITTDs. Fig. 5 shows how the means and medians evolve in time.

DISCUSSION

Over the last 10 years, there was considerable progress in time-dynamic formulations of transit time distributions (Benettin, 2015a, 2015b; Botter et al., 2011; Harman, 2015; Heidbüchel et al., 2012; Hrachovitz et al., 2015; van der Velde et al., 2012). In spite of recent progress in studying the transport processes and pathways that vary over time and are site-specific (Herman et al., 2015), hydrological processes underlying observed water quality response patterns, such as the emergence of near-chemostatic conditions (Hrachowitz et al., 2015) are still not completely understood. While the notion of time-variant transit times is not entirely new (Benettin, 2015a,

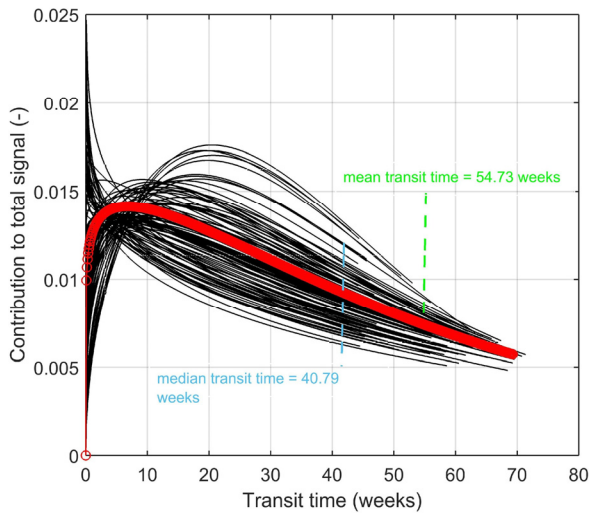


Fig. 4. Master Transit Time Distribution (red line) and the individual Instantaneous Transit Time Distributions – ITTDs (black curves). The mean transit time (calculated from the mean of all instantaneous transit time distributions ITTDs) is 54.73 weeks, with the median located at 40.79 weeks. The Weibull distribution parameters for the Master Transit Time Distribution: α scale parameter = 56.82, and the shape parameter $\beta = 1.106$.

2015b; Botter et al., 2011; Harman, 2015; Heidebüchel et al., 2012; Hrachovitz et al., 2015; Klaus et al., 2015; van der Velde et al., 2012), our approach is novel in that it is data-driven and capable of dealing with non-stationarities. This is the first time the Continuous Wavelet Transform is applied to estimate TTD.

Our analyses revealed that the mean of all transit times (Fig.

5) is 54.73 weeks (1.07 years), which is a slightly longer mean transit time than the 0.82 ± 0.02 years estimated by Kirchner et al. (2001) who applied the 2-parameter Gamma distribution on the Fourier power spectra of chloride data from the same catchment. However, it should also be noted that the difference in the mean transit time compared to static formulations may be small. The actual difference in the mean transit time may partially arise from the fact that Kirchner et al. (2001) analyzed an older period of record (1983–1997), while in this paper the results represent the period 2001–2012. Our results show that the transit time distribution is a dynamic catchment characteristic and that a single distribution function can be insufficient to describe the functioning of a catchment. Our observations agree with the most recent studies of other authors in terms that the assumption of a static TTD is not generally valid and that a predetermined distribution such as the gamma or exponential distributions that are often used to describe the TTD (Klaus et al., 2015). By means of the continuous wavelet transform and an example from the Lower Hafren catchment we showed that the TTD indeed varies with time. The Lower Hafren catchment has been extensively studied in the past, which made it possible to cross-check the results with already published studies. This paper shows that the instantaneous distribution of transit times may change abruptly depending on the wetness conditions.

Therefore a conclusion can be made that applying a distribution function with fixed parameters to the entire time series cannot adequately describe the behavior of the catchment. Fig. 4 illustrates that the family of the individual instantaneous distribution functions spreads over a wide interval. We merged the individual instantaneous distribution functions into a single empirical curve defining the ‘mean’ empirical distribution function – ‘Master Transit Time Distribution’. From the

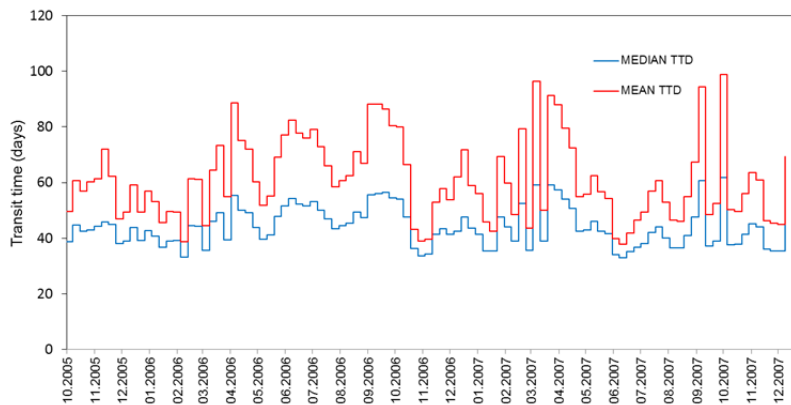


Fig. 5. Means and medians of the instantaneous transit time distributions (period 10/2005–12/2007).

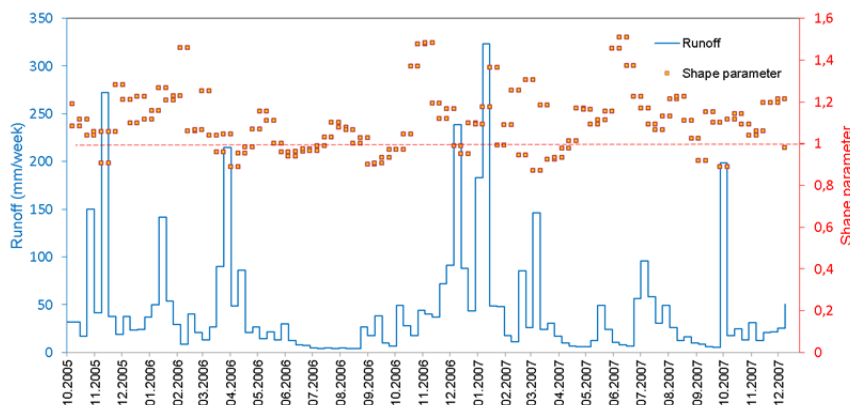


Fig. 6. Weibull shape β parameter plotted along with the runoff (period 10/2005–12/2007).

MTTD presented in Fig. 4 it is evident that it takes ‘on average’ ~54.3 weeks for rainwater to leave the catchment and pass the stream gauge at Lower Hafren. The MTTD has a long tail with the shape parameter $\beta = 1.106$. This feature is observed in many catchments worldwide (Harman, 2015; Heidbüchel et al., 2012; Hrachovitz et al., 2010; Kirchner, 2016; Kirchner et al., 2000, 2001; McGuire and McDonnell, 2006; Tekleab et al., 2014). The long tail implies that a particle of water that landed on the catchment today will continue to affect the streamflow in small proportions for a long time. As water acts as the carrier, or solvent, for many chemical substances, the transit time distribution inherently affects chemical reactions, and thus affecting the water quality of groundwater surface waters with ultimate consequences for ecological functioning.

We showed that periods of elevated runoff are accompanied with an exponentially distributed transit times ($\beta < 1$). This may indicate a change in the diversity of water flow-paths and velocities during wet periods because contributing areas have been previously shown to shrink and expand depending on the duration of rainfall. Indeed, mechanistic and conceptual modeling in the Upper Hafren catchment by Benettin et al. (2015a, 2015b) showed that the storages involved in solute mixing affect the dynamics of travel time distributions and that most of the high-frequency fluctuations in the measured chloride concentration of stream water can be explained by the sharp transition between groundwater flows and faster flows originating from shallower storage layers driven by the inter-seasonal variability of atmospheric inputs.

CONCLUSIONS

The wavelet analysis as a technique is described and applied in this paper to shed light into the temporal aspects of transit time distributions. We showed that the continuous wavelet transform has the potential to remarkably increase our ability to visualize and analyze the temporal aspects of transit times. Decomposition of time series locally in both frequency and time provide a new view on temporal variability of TTD. It was not the goal of this paper to provide mechanistic explanations why TTD varies temporarily in the Lower Hafren catchment; nevertheless, we believe that the findings of this study have the potential to open a completely new avenue of research. The presented methodology has demonstrated the ability of wavelets to map the time-variant nature of water transit times. Advances in our understanding of the time-variant nature of water transit times are highly dependent in the development of novel methodologies that allow for the evaluation of such non-stationarities. However, such methodological advances should also aim at improving our understanding of the processes and mechanisms behind such catchment dynamics. Otherwise, new methodological tools will only be mere mathematical representations. In this paper we concentrated on the technical aspects of using the wavelets in the estimation of transit times. Physics-based models and conceptual models require detailed knowledge about hillslope or catchment properties such as hydraulic conductivity of the soil for their use. Such detailed data is rarely obtainable and available. The conceptual models need some assumption on the mixing within the modelled catchment. The presented wavelet-based approach does not require such detailed information about the physical aspects of the investigated catchment. Our approach makes no assumptions about the shape of the transit time distribution. The advantage of such an approach is that detailed catchment property information is not needed which makes the approach relatively easy to apply over various hydrological scales. The wavelet

analysis has the potential to become a practical diagnostic tool in studying the temporal evolution of hydrological processes under naturally time-variant conditions.

Acknowledgement. All real-world data (Plynlimon research catchment hydrochemistry) used and analyzed in this paper were downloaded from the web of the Centre for Ecology & Hydrology (Environmental Information Data Centre). This resource is made available under the terms of the Open Government Licence: <http://eidc.ceh.ac.uk/administration-folder/tools/ceh-standard-licence-texts/ceh-open-government-licence/plain>. The data are owned by NERC - Centre for Ecology & Hydrology; © Database Right/Copyright NERC - (CEH).

REFERENCES

- Benettin, P., Bailey, S.W., Campbell, J.L., Green, M.B., Rinaldo, A., Likens, G.E., McGuire, K.J., Botter, G., 2015a. Linking water age and solute dynamics in stream-flow at the Hubbard Brook Experimental Forest, NH, USA. *Water Resources Research*, 51(11), 9256–9272. <http://doi.org/10.1002/2015WR017552>
- Benettin, P., Kirchner, J.W., Rinaldo, A., Botter, G., 2015b. Modeling chloride transport using travel time distributions at Plynlimon, Wales. *Water Resources Research*, 51(5), 3259–3276. <http://doi.org/10.1002/2014WR016600>
- Botter, G., Bertuzzo, E., Rinaldo, A., 2011. Catchment residence and travel time distributions: The master equation. *Geophysical Research Letters*, 38(11). <http://doi.org/10.1029/2011GL047666>
- Davies, J., Beven, K., Rodhe, A., Nyberg, L., Bishop, K., 2013. Integrated modeling of flow and residence times at the catchment scale with multiple interacting pathways. *Water Resour. Res.*, 49, 4738–4750. <http://doi.org/10.1002/wrcr.20377>
- Duffy, C.J., Gelhar, L.W., 1985. Frequency domain approach to water quality modeling in groundwater: theory. *Water Resources Research*, 21, 1175–1184.
- Dunn, S.M., McDonnell, J.J., Vaché, K.B., 2007. Factors influencing the residence time of catchment waters: A virtual experiment approach. *Water Resources Research*, 43, W06408. DOI: 10.1029/2006WR005393.
- Farge, M., 1992. Wavelet transforms and their applications to turbulence. *Annu. Rev. Fluid Mech.*, 24, 395–457.
- Gomez, J.D., Wilson, J.L., 2013. Age distributions and dynamically changing hydrologic systems: Exploring topography-driven flow. *Water Resour. Res.*, 49, 1503–1522. DOI: 10.1002/wrcr.20127.
- Grinsted, A., Moore, J.C., Jevrejeva, S., 2004. Application of the cross wavelet transform and wavelet coherence to geophysical time series. *Nonlinear Processes in Geophysics, European Geosciences Union EGU*, 11 5/6, 561–566.
- Harman, C.J., 2015. Time-variable transit time distributions and transport: Theory and application to storage-dependent transport of chloride in a watershed. *Water Resour. Res.*, 51, 1–30. DOI: 10.1002/2014WR015707.
- Harman, C., Kim, M., 2014. An efficient tracer test for time-variable transit time distributions in periodic hydrodynamic systems. *Geophysical Research Letters*, 41(5), 1567–1575. <http://doi.org/10.1002/2013GL058980>
- Heidbüchel, I., Troch, P.A., Lyon, S.W., Weiler, M., 2012. The master transit time distribution of variable flow systems. *Water Resour. Res.*, 48, W06520. DOI: 10.1029/2011WR011293.
- Hrachowitz, M., Soulsby, C., Tetzlaff, D., Dawson, J.J.C., Dunn, 2009. Using long-term data sets to understand transit

- times in contrasting headwater catchments. *Journal of Hydrology*, 367, 3, 237–248.
- Hrachowitz, M., Soulsby, C., Tetzlaff, D., Speed, M., 2010. Catchment transit times and landscape controls – does scale matter? *Hydrological Processes*, 24, 117–125.
- Hrachowitz, M., Fovet, O., Ruiz, L., Savenije, H.H.G., 2015. Transit time distributions, legacy contamination and variability in biogeochemical 1/f scaling: how are hydrological response dynamics linked to water quality at the catchment scale? *Hydrological Processes*, 29, 25, 5241–5256. <http://doi.org/10.1002/hyp.10546>
- Kirchner, J.W., Feng, X., Neal, C., 2000. Fractal stream chemistry and its implications for contaminant transport in catchments. *Nature*, 403, 524–527.
- Kirchner, J.W., Feng, X., Neal, C., 2001. Catchment-scale advection and dispersion as a mechanism for fractal scaling in stream tracer concentrations. *Journal of Hydrology*, 254, 82–101.
- Kirchner, J.W., 2016. Aggregation in environmental systems – Part 1: Seasonal tracer cycles quantify young water fractions, but not mean transit times, in spatially heterogeneous catchments. *Hydrol. Earth Syst. Sci.*, 20, 279–297.
- Klaus, J., Chun, K.P., McGuire, K.J., McDonnell, J.J., 2015. Temporal dynamics of catchment transit times from stable isotope data. *Water Resources Research*, 516, 4208–4223. <http://doi.org/10.1002/2014WR016247>
- Maloszewski, P., Zuber, A., 1983. Interpretation of artificial and environmental tracers in fissured rocks with a porous matrix. Report No. 1221/AP, Inst. Nucl. Phys., Krakow, Poland.
- McDonnell, J. J., McGuire, K., Aggarwal, P., Beven, K. J., Biondi, D., Destouni, G., Dunn, S., James, A., Kirchner, J., Kraft, P., Lyon, S., Maloszewski, P., Newman, B., Pfister, L., Rinaldo, A., Rodhe, A., Sayama, T., Seibert, J., Solomon, K., Soulsby, C., Stewart, M., Tetzlaff, D., Tobin, C., Troch, P., Weiler, M., Western, A., Worman, A., Wrede, S. 2010. How old is streamwater?: Open questions in catchment transit time conceptualization, modelling and analysis. *Hydrological Processes*, 24, 12, 1745–1754.
- McGuire, K.J., McDonnell, J.J., 2006. A review and evaluation of catchment transit time modeling. *Journal of Hydrology*, 330, 543–563.
- McGuire, K.J., DeWalle, D.R., Gburek, W.J., 2002. Evaluation of mean residence time in subsurface waters using oxygen-18 fluctuations during drought conditions in the mid-Appalachians. *Journal of Hydrology*, 261, 132–149.
- McGuire, K.J., McDonnell, J.J., Weiler, M., Kendall, C., McGlynn, B.L., Welker, J.M., Seibert, J., 2005. The role of topography on catchment-scale water residence time. *Water Resources Research*, 41, 5. DOI: 10.1029/2004WR003657.
- McMillan, H., Tetzlaff, D., Clark, M., Soulsby, C., 2012. Do time-variable tracers aid the evaluation of hydrological model structure? A multi model approach. *Water Resources Research*, 485. <http://doi.org/10.1029/2011WR011688>
- Neal, C., 1997. A view of water quality from the Plynlimon watershed. *Hydrology and Earth Systems Sciences*, 13, 743–753.
- Neal, C., Reynolds, B., Norris, D., Kirchner, J.W., Neal, M., Rowland, P., Wickham, H., Harman, S., Armstrong, L., Sleep, D., Lawlor, A., Woods, C., Williams, B., Fry, M., Newton, G., Wright, D., 2011. Three decades of water quality measurements from the Upper Severn experimental catchments at Plynlimon, Wales: an openly accessible data resource for research, modelling, environmental management and education. *Hydrological Processes*, 25, 3818–3830. DOI: 10.1002/hyp.8191.
- Neal, C., Kirchner, J., Reynolds, B., 2013. Plynlimon research catchment hydrochemistry. NERC Environmental Information Data Centre 10.5285/44095e17-43b0-45d4-a781-aab4f72da025
- Onderka, M., Wrede, S., Rodný, M., Pfister, L., Hoffmann, L., Krein, A., 2012. Hydrogeologic and landscape controls of dissolved inorganic nitrogen DIN and dissolved silica DSi fluxes in heterogeneous catchments. *Journal of Hydrology*, 450–451, 36–47.
- Onderka, M., Banzhaf, S., Scheytt, T.J., Krein, A., 2013. Seepage velocities derived from thermal records using wavelet analysis. *Journal of Hydrology*, 479, 64–74
- Soulsby, C., Birkel, C., Tetzlaff, D., 2014. Assessing urbanization impacts on catchment transit times. *Geophysical Research Letters*, 412, 442–448. <http://doi.org/10.1002/2013GL058716>
- Soulsby, C., Birkel, C., Geris, J., Dick, J., Tunaley, C., Tetzlaff, D., 2015. Stream water age distributions controlled by storage dynamics and nonlinear hydrologic connectivity: Modeling with high-resolution isotope data. *Water Resources Research*, 519, 7759–7776. <http://doi.org/10.1002/2015WR017888>
- Tekleab, S., Wenninger, J., Uhlenbrook, S., 2014. Characterisation of stable isotopes to identify residence times and runoff components in two meso-scale catchments in the Abay/Upper Blue Nile basin, Ethiopia. *Hydrol. Earth Syst. Sci.*, 18, 2415–2431.
- Torrence, C., Compo, G.P., 1998. A Practical Guide to Wavelet Analysis. *Bull. Amer. Meteor. Soc.*, 79, pp. 61–78.
- van der Velde, Y., Torfs, P.J.J.F., van der Zee, S.E.A.T.M., Uijlenhoet, R., 2012. Quantifying catchment-scale mixing and its effect on time-varying travel time distributions. *Water Resources Research*, 48, 6. DOI: 10.1029/2011WR011310.
- van der Velde, Y., Heidbüchel, I., Lyon, S.W., Nyberg, L., Rodhe, A., Bishop, K., Troch, P.A., 2015. Consequences of mixing assumptions for time-variable travel time distributions. *Hydrological Processes*, 29, 16, 3460–3474. <http://doi.org/10.1002/hyp.10372>
- Weigand, S., Bol, R., Reichert, B., Graf, A., Wiekenkamp, I., Stockinger, M., Luecke, A., Tappe, W., Bogena, H., Puetz, P., Amelung, W., Vereecken, H., 2017. Spatiotemporal analysis of dissolved organic carbon and nitrate in waters of a forested catchment using wavelet analysis. *Vadose Zone Journal*. DOI: 10.2136/vzj2016.09.0077.
- White, R.E., 1987. A transfer function model for the prediction of nitrate leaching under field conditions. *Journal of Hydrology*, 92, 207–222.

Received 19 May 2017
Accepted 26 September 2017

Note: Colour version of Figures can be found in the web version of this article.

Conceptual model building inspired by field-mapped runoff generation mechanisms

Alberto Viglione^{1*}, Magdalena Rogger¹, Herbert Pirkl², Juraj Parajka¹, Günter Blöschl¹

¹ Institute for Hydraulic Engineering and Water Resources Management, Vienna University of Technology, Karlsplatz 13, 1040 Vienna, Austria.

² Technical Office for Geology Dr. Herbert Pirkl, Plenergasse 5/27, 1180 Vienna, Austria.

* Corresponding author. Tel.: +43-1-58801-22317. Fax: +43-1-58801-22399. E-mail: viglione@hydro.tuwien.ac.at

Abstract: Since the beginning of hydrological research hydrologists have developed models that reflect their perception about how the catchments work and make use of the available information in the most efficient way. In this paper we develop hydrologic models based on field-mapped runoff generation mechanisms as identified by a geologist. For four different catchments in Austria, we identify four different lumped model structures and constrain their parameters based on the field-mapped information. In order to understand the usefulness of geologic information, we test their capability to predict river discharge in different cases: (i) without calibration and (ii) using the standard split-sample calibration/validation procedure. All models are compared against each other. Results show that, when no calibration is involved, using the right model structure for the catchment of interest is valuable. A-priori information on model parameters does not always improve the results but allows for more realistic model parameters. When all parameters are calibrated to the discharge data, the different model structures do not matter, i.e., the differences can largely be compensated by the choice of parameters. When parameters are constrained based on field-mapped runoff generation mechanisms, the results are not better but more consistent between different calibration periods. Models selected by runoff generation mechanisms are expected to be more robust and more suitable for extrapolation to conditions outside the calibration range than models that are purely based on parameter calibration to runoff data.

Keywords: Rainfall-runoff; Catchment geology; Hydrologic models; Runoff response times; A-priori information.

INTRODUCTION

Several strategies have been developed in recent years to cope with the diversity of hydrological processes in hydrological modelling. One avenue has been to develop models that include all the relevant processes in as much detail as possible, i.e. using the equations derived in laboratory studies for processes such as infiltration, subsurface flow etc. The epitome of this group of models is the SHE model (Abbott et al., 1986). The rationale is that one universal model should represent all processes based on universal concepts of physics. However, because of their detail, these models tend to be highly complex involving a large number of parameters and model structural elements. It may then be very difficult to identify the parameters and the suitability of the model structure at the catchment scale because of the diversity of the hydrological environment and measurement constraints (e.g. Beven, 2001; Blöschl, 2006; Savenije, 2009).

An alternative has hence been to propose simple models with a structure that is tailor made to the processes occurring in a particular catchment (e.g., Fenicia et al., 2011; Hrachowitz et al., 2014; Van den Bos et al., 2006). These models were developed in a way to strike a balance between model complexity and data availability, by keeping models as simple as possible, but complex enough to explain the dynamics of the data. While the universal models of the first group can be compared to a Swiss multi tool Army knife, the models of the second group can be compared to speciality tools – for each purpose a dedicated tool. The models, typically, consist of a combination of reservoirs and threshold functions. The models can differ in terms of the way they represent dominant catchment scale processes. Bai et al. (2009), for example, tested eight model variants with different hypotheses on the mechanisms of soil

moisture accounting at the catchment scale. The complexities of the models and their related hypothesis on the model structure provided an indication of the dominant controls on catchment response at the inter-annual, intra-annual, monthly, and daily time scales. The models can also differ in terms of the way they represent dominant local runoff generation processes. For example, Hellebrand et al. (2011) identified Hortonian overland flow, saturation overland flow, subsurface stormflow and deep percolation by a classification scheme (Müller et al., 2009). They then represented each of these runoff generation processes by a combination of reservoirs.

Several studies compared model performance and model development strategies for different landscape characteristics (e.g., Hogue et al., 2006; Nijzink et al., 2016; Rosero et al., 2010; Samuel et al., 2008). The studies indicated differences in the signatures, the controls, and the need to adapt model structures and parameters to the particular vegetation and hydroclimatic conditions when moving from one catchment to another. Winter (2001), Wolock et al. (2004) and Savenije (2010) highlighted the role of the geomorphological landscape characteristics. Winter (2001) suggested that hydrological landscapes are multiples or variations of fundamental hydrological landscape units and defined fundamental hydrological landscape units on the basis of land-surface form, geology and climate. By describing actual landscapes in terms of land-surface slope, hydraulic properties of soils and geology, and the difference between precipitation and evapotranspiration, the hydrological system of actual landscapes can then be conceptualised in a uniform way. Savenije (2010) argued that plateaus, hillslopes and wetlands are associated with different flow pathways, so the model structures for these units should also differ. This is particularly important in water-limited landscapes (Caylor et al., 2006). Wagener et al. (2007) and Gutknecht et al. (2008)

summarised the storage and transport characteristics of a landscape by the notion of “catchment functions”. It is interesting that regionalisation studies (e.g., Blöschl et al., 2013; Merz and Blöschl, 2009) provided similar evidence of contrasting controls on runoff for wet and dry regions and for different geographic regions. Differences were also evident from theoretical studies that explored the sensitivity of the dynamic water balance to its controls at catchment scale (e.g., Milly and Dunne, 2002).

Geology usually has a marginal role in the identification of model structures, mainly because of the lack of information, although, for example, Rogger et al. (2012b) and He et al. (2015) have demonstrated the value of geologic information for hydrological processes. In a comparative hydrology study, Gaál et al. (2012) have also shown that geology is, together with climate, an even stronger control than catchment area in determining flood timescales through soil characteristics. The aim of this work is to understand how useful geologic information can be for the derivation of model structure for different catchments (from high alpine to lowland). To this purpose a detailed modelling exercise is performed for four different catchments in Austria, where detailed geological information is available. Model structures and parameters are first derived mainly based on this information and then cross validated against each other. We therefore focus on the information that can be obtained from runoff generation mapped in the field (i.e. resulting from a combination of soils maps, geology maps and in-situ surveys performed by a expert geologist). Our hypothesis is that using this information may be an advantage over the usual procedure of using soil type, texture, geological units because it is a procedure more geared towards hydrology.

STUDY SITES AND DATA

The four study sites belong to the set of catchments described in Gaál et al. (2012), who analysed the hydrographs of 396 Austrian catchments as a function of climatic controls such as storm type and catchment controls such as soils, soil moisture, geology and land form. They identified 13 hot spot regions with distinct runoff characteristics. Four catchments of four of these hot spots regions are chosen for this study because of the availability of field-mapped geologic information: one high alpine catchment, the Gail, two alpine/midland catchments, the Dornbirnerach and Wimitzbach, and one lowland catchment, the Perschling. An overview over the location of the catchment is given in Figure 1.

The Dornbirnerach is the westernmost catchment, located in Vorarlberg. It is an alpine catchment with elevations ranging from 485 m to 1804 m characterised by very steep slopes. The catchment is mainly forested with some grassland and a few pastures in the higher elevations. It has a size of about 51 km².

The highest catchment in the study is the Gail which is located in Eastern Tyrol at the Southern border of Austria. It has a size of 146 km² and elevations ranging from 1094 m to 2622 m.

The catchment is characterised by forest and grassland areas on the hillslopes, while the alluvial soils in the valley bottom are used as pastures. The side valleys are steep in the north and shallower in the south. The third catchment is the Wimitzbach, a midland catchment located in Carinthia with elevations ranging from 529 m to 1309 m. Most of the catchment is forested with a few agricultural areas in the mid and lower parts close to the gauging station. The catchment has a size of about 106 km². The only lowland catchment in the study is the Perschling which is located in Lower Austria. The elevation ranges from 230 m to 640 m and a size of 55 km². The catchment is dominated by forested areas in the southern parts and agricultural areas in the northern parts. An overview over the most important catchment characteristics is given in Table 1.

To obtain hourly rainfall inputs at the catchment scale, daily precipitation of stations belonging to the network of the Austrian Hydrografische Dienst are interpolated using the classical Thiessen polygon technique. The result is then time-downscaled to hourly values using the timepatterns obtained by averaging the timepattern values at sites equipped with tipping bucket rain gauges (as in Merz et al., 2006). Hourly mean basin air temperature is obtained from linear regression between hourly measurements at climate stations and their elevation (i.e., lapse rate method). In the first step, climate stations with hourly air temperature observations are identified in radius 50 km around the runoff gauge. In the second step, linear regression is estimated between hourly air temperature and elevation of climate stations. Finally, the mean basin air temperature is estimated from linear regressions by using mean elevation of each basin. Hourly mean basin potential evaporation (EP, in mm) is estimated by modified Blaney-Criddle method as in Parajka et al. (2003) and Nester et al. (2012), e.g. as a function of air temperature and the sun shine duration index that was estimated from 1 km digital elevation model at the European scale. Hourly discharge data are provided by the Austrian Hydrografische Dienst Zentralbüro (https://www.bmlfuw.gv.at/wasser/wasser-oesterreich/wasserkreislauf/hydrographie_oesterreich.html).

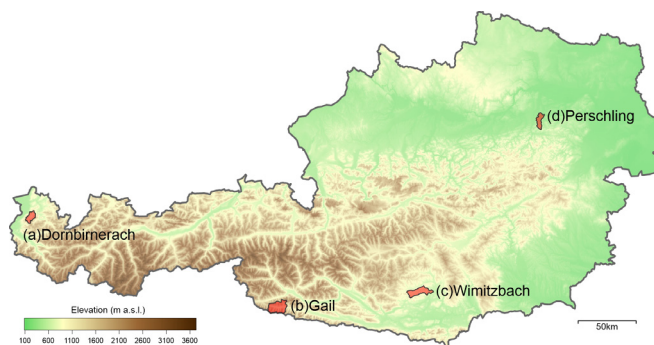


Fig. 1. Location of four study sites in Austria (see Table 1 for an overview of catchment characteristics).

Table 1. Catchment overview. Temporal means are lumped basin averages from 1976–2008.

	Dornbirnerach	Gail	Wimitzbach	Perschling
Hot Spot Region (Gaál et al., 2012)	Bregenzwald (BreWa)	Gail (Gail)	Gurktal (Gurk)	Flysch (Flysch)
catch. size (km ²)	51.1	146.1	106.5	55.3
min-(mean)-max elevation (m a.s.l.)	485-(1118)-1804	1094-(1793)-2622	529-(900)-1309	230-(379)-640
mean annual prec. (mm/y)	2099	1260	892	782
mean annual temp (°C)	6.2	2.8	6.9	9.2
mean potential evaporation (mm/y)	603	477	621	703
mean annual runoff (mm/y)	1743	924	287	256

Data for the years 2000 to 2010 are used in all sites with the exception of Wimitzbach, where overlapping hourly timeseries are available for the period 2004–2009 only.

GEOLOGICAL FIELD-MAPPING OF RUNOFF-GENERATION MECHANISMS

For the four study sites hydrogeologic runoff process maps are derived by Herbert Pirkl, an Austrian geologist, based on the method described in Pirkl (2009, 2012). The maps are obtained by a detailed assessment of geologic maps, hydrogeologic maps, orthophotos and digital terrain models. Based on this information different hydrogeologic response units are defined that discriminate areas dominated by interflow, deep groundwater flow or surface runoff processes. These maps give an idea about the runoff processes in the catchment from a hydrogeologic point of view and highlight areas with high storage potential during flood events. Such maps have successfully been implemented in hydrological studies by Rogger et al. (2012a,b) and proved to be very valuable in understanding the storage properties of a catchment. The geologic conditions and hydrogeologic runoff process maps of the four study sites are described in detail below.

Dornbirnerach

The catchment is part of the Helvetic zone including limestone, sandstone and marl with a small part of flysch in the northern area. A few areas consist of carbonates that have a tendency to karstify, but no fast runoff reaction related to these processes has been observed. The hillslopes are very steep resulting in a high relief energy. The hydrogeologic runoff process map of the catchment is shown in Figure 2a. Large parts of the catchment are characterised by shallow interflow processes. These areas, especially in the upper part of the hillslopes, may get saturated and form surface runoff. The scree areas in the lower parts of the hillslopes have rather large depth and are dominated by deeper interflow processes which may buffer some of the fast surface runoff generated in the upper parts.

Gail

The catchment is part of the Karnic Alps, the Gail crystalline and the Lienzer dolomites. The Karnic Alps are characterised by phyllitic schists, quartzites and metamorphic tuffites, the Gail crystalline by gneiss and mica schist and the Lienzer dolomites by dolomites. The main valley is east-west orientated with rather steep valleys discharging into the Gail from north and shallower valleys from south. The hydrogeologic runoff process map is shown in Figure 2b.

Large areas of the catchment are characterised by surface runoff. There is, however, a potential for runoff retention during strong precipitation events on areas dominated by deep groundwater flow and interflow of different origins. Both in the Karnic Alps as well as in the Gail crystalline deep creeping areas occur (dark green areas) that are characterised by deep groundwater flow (Figure 3a). Scree areas in the lower parts of the hillslopes and valley deposits in the shallower valleys of the Karnic Alps are dominated by deeper interflow. The dolomites in the Lienzer dolomites are strongly weathered forming additional scree areas with deep interflow in the valley bottoms. Runoff retention of the tributaries from the southern and northern valleys may also occur on the large alluvial cone in the valley bottom. During very wet conditions, the alluvial cone may however get saturated so that tributaries can bypass it.

Wimitzbach

The catchment is located in the crystalline series of the Gurktaler Alps characterised by mica schist, phyllites, amphibolites and marble. The hillslopes have a similar structure all over the catchment and are rather plane in the upper parts and steep in the lower parts. The Wimitzbach was not glaciated during the last ice age resulting in a strong weathering of the upper parts and tops of the hillslopes. The hydrogeologic runoff process map is shown in Figure 2c. Due to the strong weathering processes the upper parts and crests of the hillslopes are dominated by deep interflow. The steeper lower parts of the hillslopes on the other hand are characterised by shallow interflow or surface runoff on rocks. The valley bottoms are filled with fine sediments and not very permeable.

Perschling

The catchment is located in the flysch/molasse zone of Austria. The northern parts lay in the molasse zone and are characterised by fine sands and clay marl, while the southern parts are part of the flysch zone and consist of clay marl, marl and sandstone. The hydrogeologic runoff process map is shown in Figure 2d.

The whole catchment is characterised by interflow processes in the weathering zone that has a depth from 2 to 5 m. The valley bottom is filled with sandy gravel and influenced by groundwater. A cross section of the runoff processes on a typical hillslope in the flysch zone is shown in Figure 3b. On the upper parts of the hillslopes water infiltrates into the shallow subsurface while at the slope toes some saturation and surface runoff may occur.

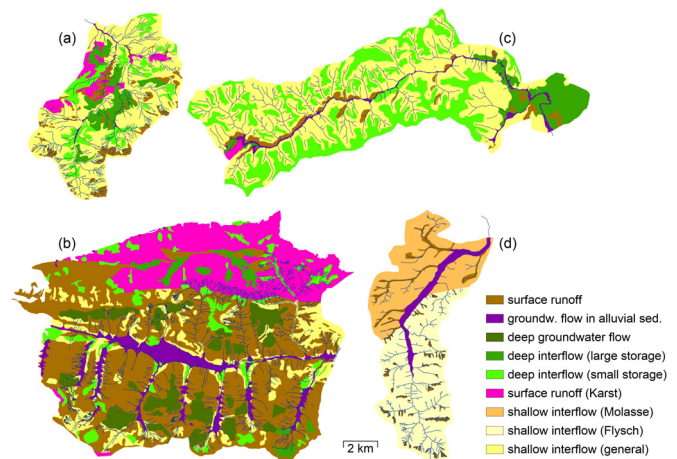


Fig. 2. Hydrogeologic runoff process map of the four Austrian catchments: (a) Dornbirnerach; (b) Gail; (c) Wimitzbach; and (d) Perschling.

MODEL STRUCTURES FROM RUNOFF GENERATION MECHANISMS

The model structure of the four study sites is derived based on the information on hydrogeological processes as explained in the previous section. Simple lumped modelling approaches are chosen with the aim to only represent the dominating runoff processes of the catchments (similarly to Hrachowitz et al., 2014). All models are characterised by a snow-accumulation and snow-melt module. A very simple degree day factor is used with four parameters (ddf , the degree day factor; t_{ss} , the threshold temperature below which precipitation is snow; t_m , thresh-

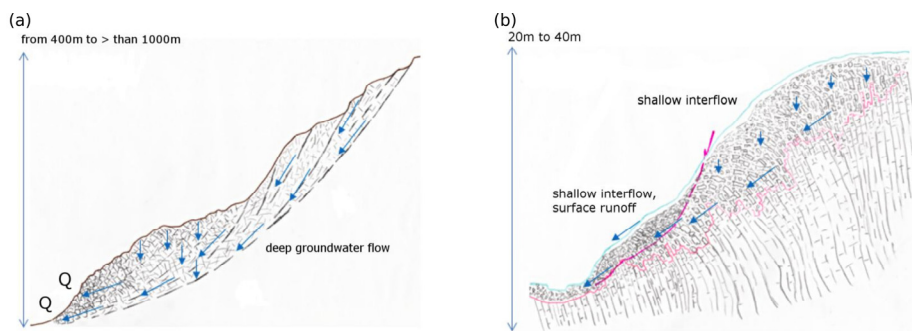


Fig. 3. Examples of cross sections of runoff processes hand-drawn by Herbert Pirkl: (a) deep creeping areas in the Gail catchment; (b) Typical hillslope in Perschling catchment.

old temperature above which melt starts; and SCF, a snow correction factor, see Table 2). All models have a routing module consisting in a simple linear reservoir with response time k_r . For all other model parts, the runoff generation mechanisms identified using the geological information is used and a detailed description of the derivation of the four model structures is given below.

Dornbirnerach

The hydrogeologic runoff process map of the Dornbirnerach looks rather complex (see Figure 2a), but most of the different hydrogeologic runoff response units are directly connected to the river network so that processes occur in parallel rather than in series. For this reason, the different storages representing these processes are arranged in parallel in the model structure (Figure 4a).

Large parts of the Dornbirnerach are characterised by shallow interflow processes. On the upper hillslopes of the catchment very fast interflow occurs (and potentially also surface runoff) which is represented in the model by the fast storage S_s . The remaining interflow areas in the lower parts of the catchment produce a slower interflow component and are modelled by the slower interflow storage S_i . The scree areas that are dominated by deep interflow in the lower parts of the hillslopes produce a slow deep interflow component or baseflow and are represented in the model by a slow storage S_d .

The parameters p_s , p_i and p_d indicate the proportion of input water (rain + snowmelt) that enters the fast storage, the interflow storage and the deep interflow storage respectively. These storages respond linearly with response times k_s , k_i and k_d . The fast storage is characterised by a maximum level S_{smax} above which fast surface runoff occurs. Evaporation happens at potential rate (if the buckets are not empty) and is reparted among the three buckets as specified by parameters e_s , e_i and e_d . These parameters controlling evapotranspiration have not been related to the surface cover or land use since the interest here is in runoff generation by the geological units. Only the fast surface runoff is routed through the linear reservoir with response time k_r . The total runoff is given by the routed runoff plus near surface, interflow and deep interflow runoff. See Table 2 for the description of the parameters and the model equations. Reasonable ranges for the parameters are reported in Table 2.

Gail

Similarly to the case of Dornbirnerach, in the model for the Gail the input rain + snowmelt is partitioned into three components (Figure 4b). One part contributes to the slow storage S_d that represents the deep creeping areas and produces a very

slow baseflow component. The storage is arranged in parallel to the other storages since these areas are directly connected to the river. Outflow of this storage is not expected to contribute significantly to flood events.

Another part of the input contributes to the fast storage S_s that generates a fast near surface runoff component. This runoff component originates from the areas classified as surface runoff areas in the hydrogeologic process that cover large parts of the catchment. It should be noted that even if these areas appear as bare rock on the geologic map, they are actually covered by forest or grassland which means they are more likely to produce near surface than surface runoff component.

In the southern valleys the fast runoff reaction is dampened by the scree areas and alluvial soils in the valley bottoms of the tributaries. Similarly discharges from some of northern tributaries are dampened by the large alluvial cone in the main valley. This is the reason why part of the near surface runoff from the fast storage feeds into an interflow storage S_i that causes a runoff retention. The interflow storage S_i is partially also directly fed by rainfall plus snowmelt representing direct precipitation on these areas.

The same parameters as in the Dornbirnerach model appear here, with the additional o_s parameter, which controls the partitioning of the near surface runoff into the one recharging the interflow storage and the one contributing directly to runoff (see Table 2). The fast surface and (part of) near surface runoff are routed with the linear reservoir. The total runoff is given by the routed runoff plus interflow and groundwater runoff.

Wimitzbach

Due to the homogeneity of the hillslopes all over the catchment, a very simple model structure was chosen for the Wimitzbach (Figure 4c). The upper parts of the hillslopes are deeply weathered and represented by the slow storage S_d , that is fed by water infiltrating from the unsaturated zone. This storage forms a very slow runoff component that mainly contributes to the baseflow in the river. The lower parts of the hillslopes are characterised by the faster storage S_i that form a faster runoff component. Part of the deep interflow from S_d enters S_i as specified by (1 minus) the parameter o_d (see Table 2). The fast surface runoff is routed with the linear reservoir. The total runoff is given by the routed runoff plus the interflows.

Perschling

The whole catchment is dominated by shallow interflow processes, but due to the differences in geologic conditions and land use, the molasse zone and flysch zone are represented in the model by two separate storages (Figure 4d). The molasse

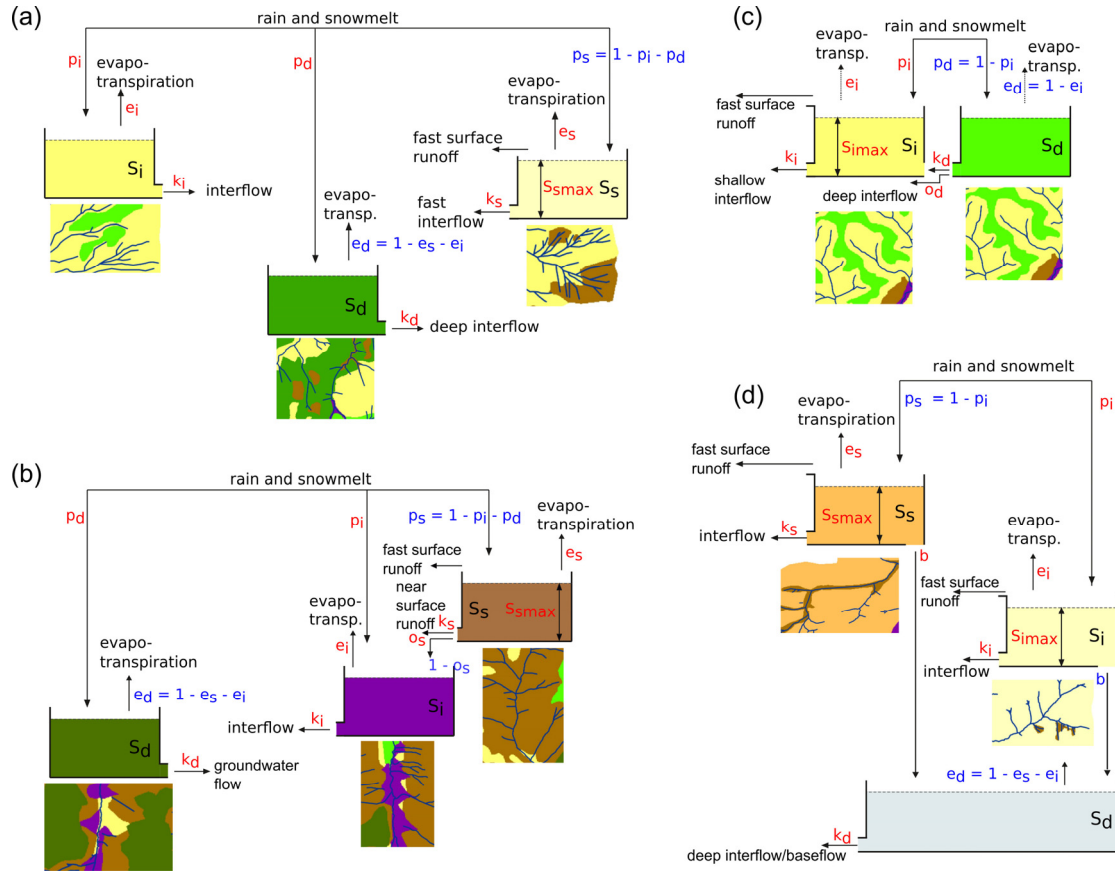


Fig. 4. Model structures for the four austrian catchments based on the hydrogeologic runoff process map of Figure 2. The four catchments are: (a) Dornbirnerach; (b) Gail; (c) Wimitzbach; and (d) Perschling. Outgoing vertical arrows indicate evapotranspiration components. Outgoing horizontal arrows indicate flow components that compose the overall outflow of the models. Model parameters that are set as ‘free’ in calibration are shown in red. Non-free parameters are shown in blue. See Table 2 for the description of the parameters.

Table 2. Model parameters and model equations where they do appear. Other variables are: E_* evaporation from S_* (s = surface, i = interflow, d = deep interflow) (mm h^{-1}); EP potential evaporation (mm h^{-1}); M melt (mm h^{-1}); P precipitation (mm h^{-1}); Q_* runoff from S_* (mm h^{-1}); Q_{*f} fast surface runoff from S_* (mm h^{-1}); S_* storages (s = surface, i = interflow, d = deep interflow) (mm); Sp snow pack (mm); Sr routing storage (mm); t time (h); T temperature ($^{\circ}\text{C}$). The last column shows ranges for the parameters used as calibration ranges when no-apriori is set.

Symbol	Dimension	Description	Equation	Range
ddf	$(\text{mm K}^{-1} \text{h}^{-1})$	degree day factor	$M = \text{ddf} \cdot (T - t_m)$ if $T > t_m$ and $S_p > 0$	0.1
t_s	$(^{\circ}\text{C})$	threshold temperature below which precipitation is snow	if $T > t_s$, $R = P$, else $dS_p/dt = P \cdot \text{SCF}$	0
t_m	$(^{\circ}\text{C})$	threshold temperature above which melt starts	if $T > t_m$, $M = \text{ddf}(T - t_m)$	1
SCF	(-)	snow correction factor	$dS_p/dt = P \cdot \text{SCF}$ if $T < t_s$	1
p_s	(-)	percentage of rain+melt that enters S_s	$dS_s/dt = p_s \cdot (R + M) - E_s - Q_s - Q_{sf}$	$0 \div 1$
p_i	(-)	percentage of rain+melt that enters S_i	$dS_i/dt = p_i \cdot (R + M) - E_i - Q_i - Q_{if}$	$0 \div (1 - p_s)$
p_d	(-)	percentage of rain+melt that enters S_d	$dS_d/dt = p_d \cdot (R + M) - E_d - Q_d$	$1 - p_s - p_i$
e_s	(-)	percentage of evaporation from S_s	$E_s = e_s \cdot \text{EP}$ if $S_s > 0$	$0 \div 1$
e_i	(-)	percentage of evaporation from S_i	$E_i = e_i \cdot \text{EP}$ if $S_i > 0$	$0 \div (1 - e_s)$
e_d	(-)	percentage of evaporation from S_d	$E_d = e_d \cdot \text{EP}$ if $S_d > 0$	$1 - e_s - e_i$
k_s	(h)	response time of the S_s storage	$Q_s = S_s/k_s$	$0 \div 1000$
k_i	(h)	response time of the S_i storage	$Q_i = S_i/k_i$	$k_s + (0 \div 5000)$
k_d	(h)	response time of the S_d storage	$Q_d = S_d/k_d$	$k_i + (0 \div 10000)$
$S_{s\text{max}}$	(mm)	max storage level for the S_s storage	$Q_{sf} = S_s - S_{s\text{max}}$ if $S_s > S_{s\text{max}}$	$0 \div 1000$
$S_{i\text{max}}$	(mm)	max storage level for the S_i storage	$Q_{if} = S_i - S_{i\text{max}}$ if $S_i > S_{i\text{max}}$	$0 \div 1000$
o_s	(-)	percentage of near surface runoff Q_s that doesn't enter the interflow storage S_i	$dS_i/dt = p_i \cdot (R + M) + Q_s \cdot (1 - o_s) - E_i - Q_i$	$0 \div 1$
o_d	(-)	percentage of deep interflow runoff from Q_d that doesn't enter the shallow interflow storage S_i	$dS_i/dt = p_i \cdot (R + M) + Q_d \cdot (1 - o_d) - E_i - Q_i - Q_{if}$	$0 \div 1$
b	(-)	percentage of percolation from Molasse and Flysch storages	$dS_d/dt = b \cdot (S_s + S_i) - E_d - Q_d$	$0 \div 1$
k_r	(h)	response time for the linear routing	$Q_r = S_r/k_r$ where $dS_r/dt = Q_{sf} + \dots + o_s \cdot Q_s - Q_r$	$0 \div 120$

zone is agriculturally used and represented by the molasse storage S_s that is expected to react somewhat faster than the flysch zone S_i which is mainly forested. Both molasse and flysch storages have a maximum level (S_{smax} , S_{imax}) above which fast surface runoff occurs. There is percolation from S_s and S_i to a groundwater storage S_d controlled by the parameter b , the percolation happening instantaneously and proportionally to the storage (see Table 2). Fast surface runoff and interflows from both Molasse and Flysch reservoirs are routed through the linear reservoir with response time kr . The total runoff is given by the routed runoff plus the baseflow.

MODEL PARAMETERS FROM RUNOFF GENERATION MECHANISMS

The information on runoff generation mechanisms is used further to constrain the parameters of the four models described in the previous section.

Two types of information is used: (1) the geographic repartition of the different geological formations is used to specify (a priori) the partition parameters p_s , p_i and p_d for the rain+snowmelt input and the partition parameters e_s , e_i and e_d for the evaporation; (2) an interview with the geologist is conducted to specify the ratios between response times (k_s , k_i and k_d) of the different response units in normal flow situations.

In Table 3 the area percentages of the geological classes obtained from Figure 2 are listed and summarized for all the catchments. These values are used in the model for the partitioning of rain and snowmelt in the different storages as well as for the partitioning of evaporation (parameters p_s , p_i , p_d , e_s , e_i and e_d in Table 2).

Information on the ratios between response times (k_s , k_i and k_d) between response units in normal flow situations is obtained from an interview with the geologist who produced the runoff generation maps. An iterative framework is used. A squared matrix is produced with all response units for all catchments as row and column names. To each element of the matrix a value is assigned that represents the ratio between the response time of the row unit and the response time of the column unit. At the start, the value 1 could be assigned to every element of the

Table 3. Area percentages of the geological classes for the four catchments in Figure 2. The partition parameters p_s , p_i , p_d , e_s , e_i and e_d (Table 2) to be used as a-priori information are derived from these area percentages.

	Dornbirnerach	Gail	Wimitzbach	Persching
surface runoff	9.5%	7.7%	4.0%	
groundwater flow in alluvial sediments	0.5%	8.0%	2.5%	6.0%
deep groundwater flow		12%		
deep interflow (large storage)	11%	0.8%	8.6%	
deep interflow (small storage)	13%	6.4%	29%	
surface runoff (Karst)	6.5%	51%	0.5%	
shallow interflow (Molasse)				41%
shallow interflow (Flysch)				52%
shallow interflow (general)	60%	14%	55%	

matrix, representing zero knowledge about the response times of the different response units. For the ten response units of the four catchments of this paper, we start with ratios which were reasonable from the point of view of the modeller.

With this initial matrix, the interview with the expert starts. The expert (in this case the geologist Herbert Pirkl) is asked whether she/he would suggest changes of the values for particular combinations of response units. She/he will have a perception on the ratio between response times that is different from the proposed values. The elements in the matrix are of course not independent, and changes in one of them will imply changes in the others, which may or may not satisfy the expert. In the second case, the matrix is updated further, based on her/his suggestions. The procedure goes on till the expert is satisfied by the final matrix. The result of our interview with the geologist is shown in Figure 5 where some of the elements are kept empty because they would not add information to the matrix.

In Figure 5, the ratios between response times of response units in the same catchment are shown in the brown square boxes including the diagonal (whose values are 1 for definition). For instance, the response time of the interflow component in the Dornbirnerach and Gail catchments is in the order of 5 times the response time of the respective fast near surface runoff components. Relatively to near surface and interflow

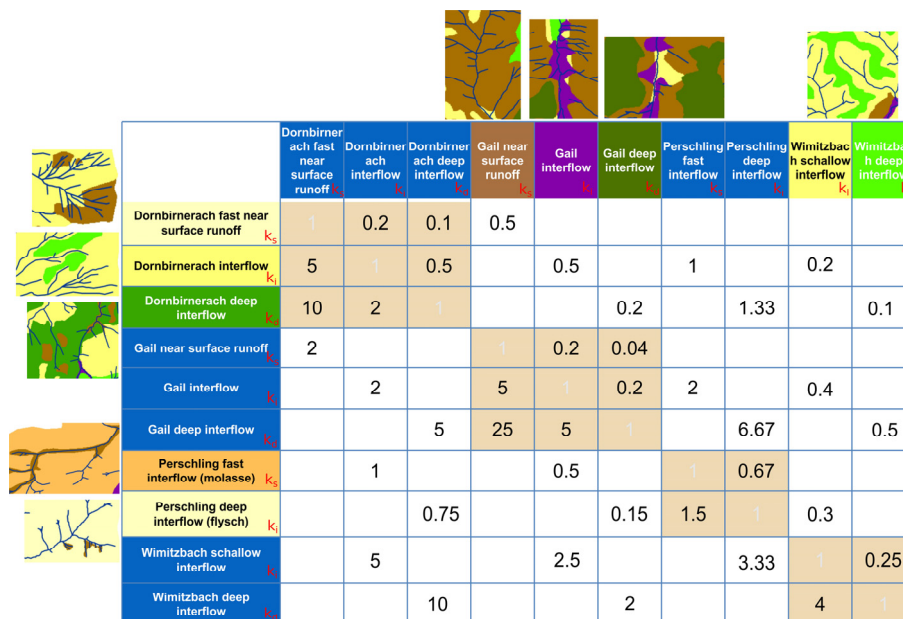


Fig. 5. Relative response times between response units in normal flow situation based on discussions with the geologist. The matrix reads as follows: the response time of the row unit (e.g., Gail interflow) is VALUE times (e.g., 5 times) the response time of the column unit (e.g., Gail near surface runoff).

components, the Gail catchment has a slower deep interflow component than the Dornbirnerach. In the Perschling catchment, the response times of molasse and flysch components are not so different (the flysch response time being expected to be about 3/2 of the molasse one). A larger difference is expected between the shallow and deep interflow components of the Wimitzbach catchment (with a response time ratio of about 4).

We could perform the interview for each catchment separately but, in the spirit of comparative hydrology (Blöschl et al., 2013; Falkenmark and Chapman, 1989), we consider all catchments together and therefore obtain guesses for the response time ratios between response units belonging to different catchments (white boxes in Figure 5). This is also useful in providing arguments for checking the consistency of the table. For example near surface runoff and interflow in the Gail catchment are expected to have longer response times than the analogous components in the Dornbirnerach catchment (with a ratio of 2). The slowest response within the four catchments belong to the Wimitzbach catchment.

EXPERIMENTS

Experiment 1: test model structures and a-priori parameters with no calibration

First, in order to investigate whether the right model structure and parameters allow to obtain reasonable simulation results without calibration, the following experiment is conducted:

- All models are applied to all catchments using mid-range parameters, i.e., parameters selected at the mid point of the

range of values they were developed for (assuming in some cases a logarithmic scale for the range, see Table 4, first 4 columns).

- All models are applied to all catchments using mid-range parameters and information on partition parameters and response time parameters as explained in the previous section (see Table 4, other columns).

- The performances are then compared in terms of ability to simulate the observed runoff.

Figure 6 shows simulated vs. observed discharges for all models in all catchments when the mid range parameters are used (red lines). The figure demonstrates that very different results are obtained with the different model structures even when the parameters corresponding to the model parts representing the same processes are selected equal (see Table 4, first 4 columns).

Figure 7 (top row) shows the results in terms of the Nash Sutcliffe efficiency both for discharges and log-transformed discharges. The efficiencies are low, almost all below the value of 0.5, but surprisingly high if one considers that no calibration at all has been performed. In almost all cases, the model developed explicitly for the catchment (full symbols in Figure 7) outperforms the other models, which seems to confirm our hypothesis that selecting model structures accordingly matters.

Figure 6 also shows simulated discharges for all models in all catchments when the parameters based on runoff generation mechanisms are used (green lines). The figure demonstrates that very different results are obtained with the different model structures even when the parameters are selected in a consistent

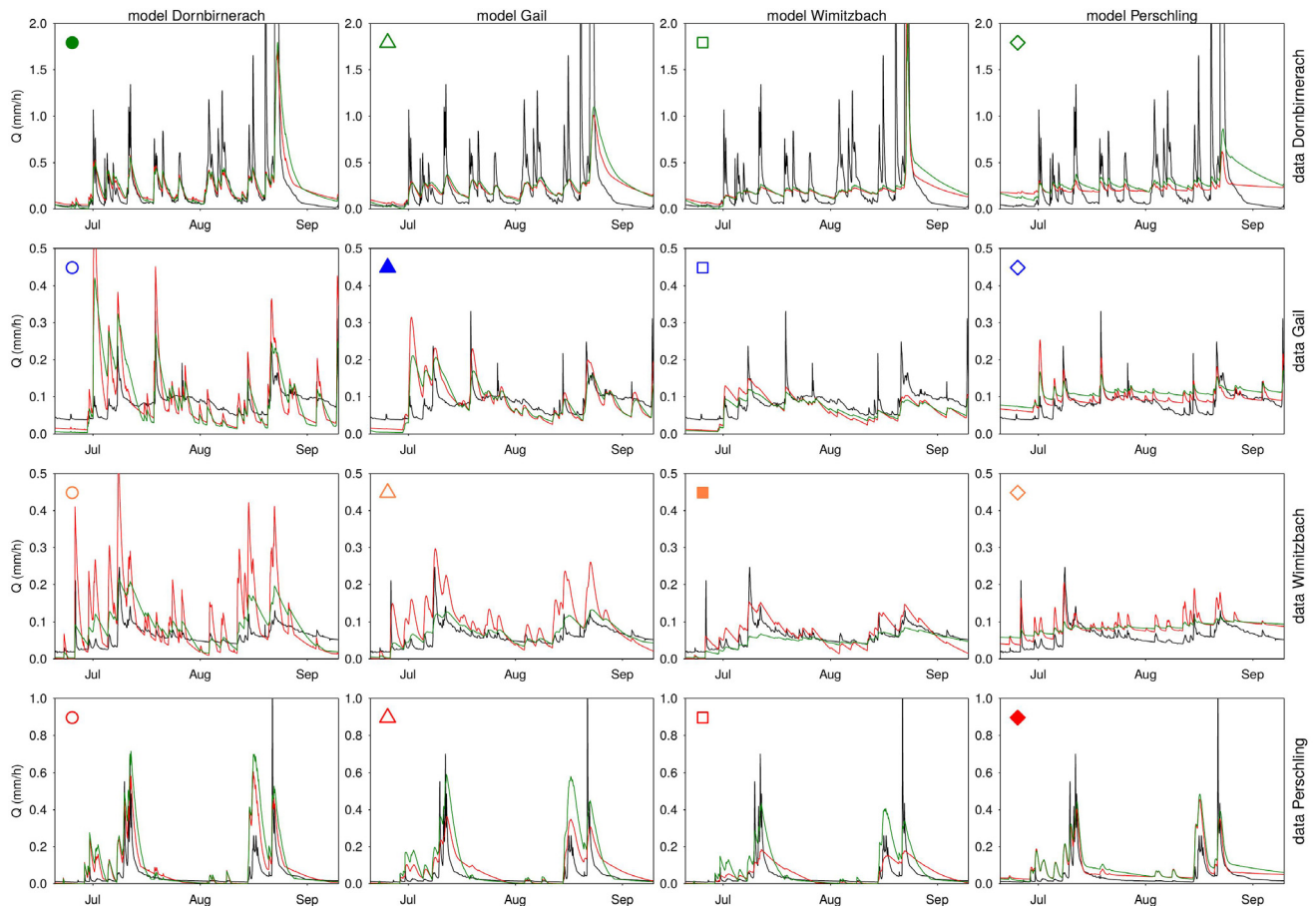
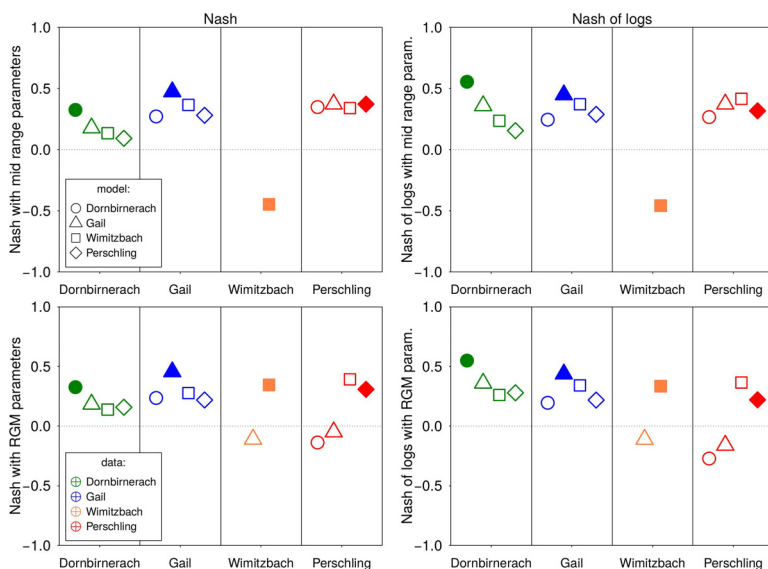


Fig. 6. Observed vs. simulated discharges of summer 2005 in the four catchments with the four models (summer months are shown for which snow accumulation and melt are not relevant). Observed discharges are in black; simulated discharges are in red when the mid-range parameters are used; simulated discharges are in green when the parameters based on runoff generation mechanisms are used (see Table 4).

Table 4. Mid-range parameters and parameters based on runoff generation mechanisms. (D = model for Dornbirnerach; G = model for Gail; W = model for Wimitzbach; P = model for Perschling).

	Mid range				Dornbirnerach				Gail				Wimitzbach				Perschling				
	D	G	W	P	D	G	W	P	D	G	W	P	D	G	W	P	D	G	W	P	
ddf (mm K ⁻¹ h ⁻¹)	0.1	0.1	0.1	0.1	0.1	0.1	0.1	0.1	0.1	0.1	0.1	0.1	0.1	0.1	0.1	0.1	0.1	0.1	0.1	0.1	0.1
t _s (°C)	0	0	0	0	0	0	0	0	0	0	0	0	0	0	0	0	0	0	0	0	0
t _m (°C)	1	1	1	1	1	1	1	1	1	1	1	1	1	1	1	1	1	1	1	1	1
SCF (-)	1	1	1	1	1	1	1	1	1	1	1	1	1	1	1	1	1	1	1	1	1
p _s (-)	1/3	1/3		1/2	0.47	0.47		0.69	0.59	0.59		0.67	0.6	0.6		0.6	0.31	0.31		0.44	
p _i (-)	1/3	1/3	1/2	1/2	0.21	0.21	0.47	0.31	0.29	0.29	0.59	0.33	0.2	0.2	0.6	0.4	0.39	0.39	0.44	0.56	
p _d (-)	1/3	1/3	1/2		0.32	0.32	0.53		0.12	0.12	0.41		9.2	0.2	0.4		0.3	0.3	0.56		
e _s (-)	1/3	1/3		1/2	0.47	0.47		0.69	0.59	0.59		0.67	0.6	0.6		0.6	0.31	0.31		0.44	
e _i (-)	1/3	1/3	1/2	1/2	0.21	0.21	0.47	0.31	0.29	0.29	0.59	0.33	0.2	0.2	0.6	0.4	0.39	0.39	0.44	0.56	
e _d (-)	1/3	1/3	1/2		0.32	0.32	0.53		0.12	0.12	0.41		0.2	0.2	0.4		0.3	0.3	0.56		
k _s (h)	30	30		30	50	50		50	100	100		100	250	250		250	50	50		50	
k _i (h)	300	300	300	300	250	250	250	250	500	500	500	500	1250	1250	1250	1250	75	75	75	75	
k _d (h)	3000	3000	3000	3000	500	500	500	500	2500	2500	2500	2500	5000	5000	5000	5000	1000	1000	1000	1000	
S _{max} (mm)	100	100		100	100	100		100	100	100		100	100	100		100	100	100		100	
S _{imax} (mm)			100	100			100	100			100	100			100	100			100	100	
o _s (-)		0.5				0.5				0.5				0.5				0.5			
o _d (-)			0.5				0.5				0.5				0.5				0.5		
b (-)				0.05				0.05				0.05				0.05				0.05	
k _r (h)	10	10	10	10	10	10	10	10	10	10	10	10	10	10	10	10	10	10	10	10	


Fig. 7. Validation Nash Sutcliffe efficiencies for all models applied on all catchments when all parameters are selected as mid-range parameters (top row) or based on runoff generation mechanisms (bottom row).

way (see Table 4). Looking at the performances in Figure 7 (bottom row), the results are in most cases similar, between mid-range parameters and parameters based on runoff generation mechanisms, with the exception of the Wimitzbach catchment, where the performance of the mid-range parameters is extremely low for all models with the exception of the case when the right model with the a-priori parameters is used. In almost all cases, the model developed explicitly for the catchment (full symbols in Figure 7) outperforms the other models. This is not the case for the Perschling catchment for which the simpler model developed for the Wimitzbach provides better results.

Experiment 2: test model structure with calibration

In order to investigate whether the model structure per-se allows to obtain better simulation results when calibration is involved, the following experiment is conducted:

- For each catchment all models are calibrated on 6 years of data using as objective function a combination (the average) of the Nash-Sutcliffe efficiency measure applied to the hourly discharge data and to their logarithm.

- All parameters are calibrated with the exception of the ones related to snowmelt, which are assumed known and fix for every catchment and every model (see Table 2). The differential evolution optimisation algorithm (DEoptim in R, Mullen et al., 2011) is used and is run 15 times for each combination of model/catchment/calibration period.
- The performances are then compared for two 6 years calibration periods and for two 6 year validation periods (with the exception of the Wimitzbach/Gurk catchment for which shorter input data series are available).

Figure 8 shows the results in terms of the Nash Sutcliffe efficiency. There is no significant difference of the efficiencies in calibration and validation when all the discharge timeseries is considered. For the Wimitzbach catchment, the very simple model explicitly developed for it seems to perform slightly worse than the other models. This is interesting because the model performs very well for the other catchments, for which its efficiency is as good as the one of other models. Looking at the simulated time series (not shown here), very similar results are obtained with the different model structures because the calibration makes sure that the simulated runoff matches at best the observed one.

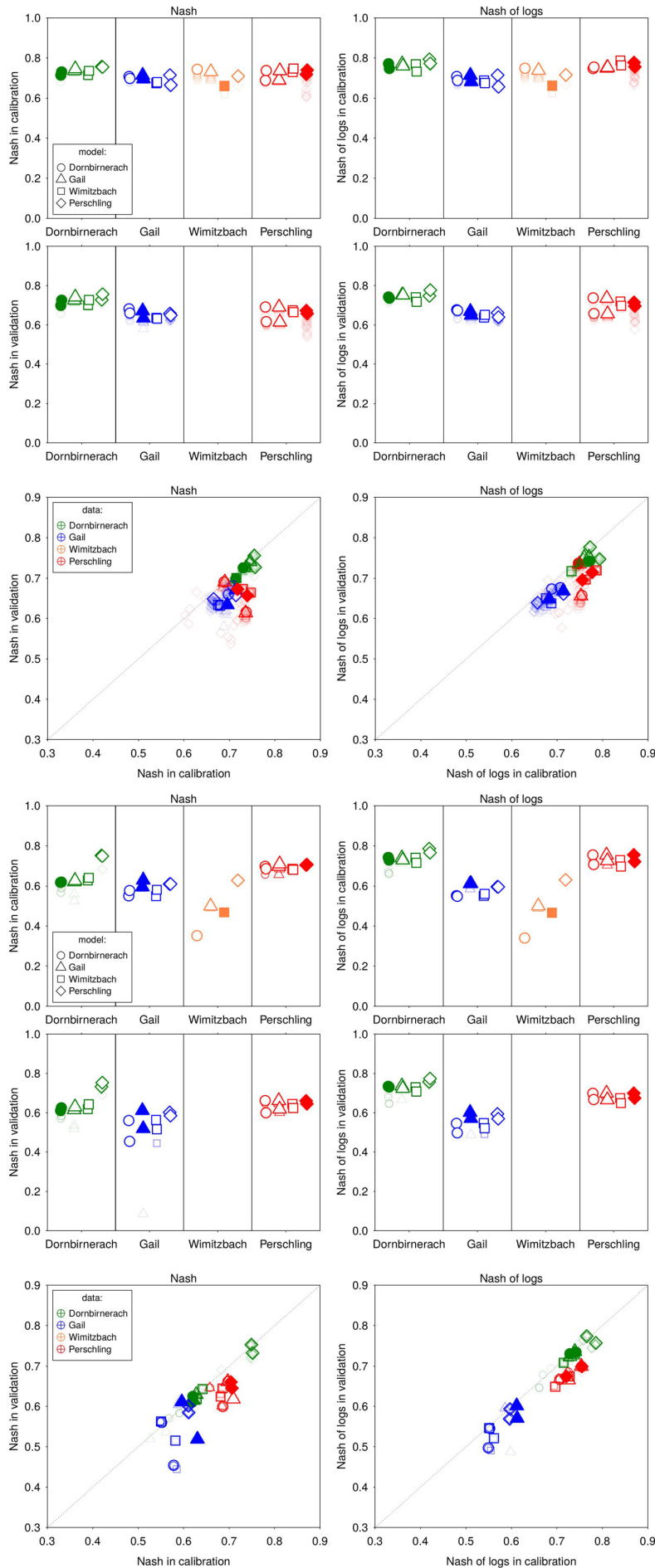


Fig. 8. Calibration and validation Nash Sutcliffe efficiencies for all models applied on all catchments when all parameters are calibrated. The results of the 15 calibrations are shown with light colours, while bold symbols indicate the results for parameters corresponding to maximum efficiencies obtained in calibration (within the 15 runs).

Fig. 9. Calibration and validation Nash Sutcliffe efficiencies for all models applied on all catchments when very few parameters are calibrated (a-priori information is used). The results of the 15 calibrations are shown with light colours, while bold symbols indicate the results for parameters corresponding to maximum efficiencies obtained in calibration (within the 15 runs).

Table 5. Parameters of the model calibrated for the catchments for whom they were developed on two periods, when all parameters are calibrated and when very few parameters are calibrated (a-priori information is used). The non-calibrated parameters are in italic.

	Dornbirnerach		Gail		Wimitzbach	Perschling	
	2000–2005	2005–2010	2000–2005	2005–2010	2004–2009	2000–2005	2005–2010
all parameters calibrated							
p_s	0.80	0.90	0.24	0.31		0.65	0.33
p_l	0.11	0.00	0.56	0.58	0.23	0.35	0.67
p_d	0.09	0.10	0.20	0.11	0.77		
e_s	0.30	0.50	0.10	0.35		0.60	0.19
e_l	0.34	0.42	0.20	0.08	0.08	0.27	0.78
e_d	0.37	0.08	0.70	0.57	0.92	0.13	0.03
k_s	95	64	441	241		4078	2232
k_l	2936	307	561	452	919	7048	2290
k_d	3460	460	7370	5912	6840	7350	4614
S_{smax}	23	23	17	15		870	31
S_{lmax}					38	23	318
o_s			0.03	0.02			
o_d					0.03		
b						0.00	0.00
k_r	5.4	4.9	33.3	23.6	119.5	22.8	11.4
few parameters calibrated							
p_s	0.47	0.47	0.59	0.59		0.44	0.44
p_l	0.21	0.21	0.29	0.29	0.60	0.56	0.56
p_d	0.32	0.32	0.12	0.12	0.40		
e_s	0.47	0.47	0.59	0.59		0.31	0.31
e_l	0.21	0.21	0.29	0.29	0.60	0.39	0.39
e_d	0.32	0.32	0.12	0.12	0.40	0.30	0.30
k_s	24	17	151	88		4990	2650
k_l	118	86	754	440	1859	7485	3974
k_d	236	173	3772	2202	7437	7546	4688
S_{smax}	8	8	17	22		40	41
S_{lmax}					94	618	397
o_s			0.00	0.00			
o_d					1.00		
b						0.00	0.00
k_r	3.1	3.2	118.3	40.8	119.9	26.3	13.9

Experiment 3: test a-priori parameters with calibration

In order to investigate whether a-priori information on model parameters allows to obtain better calibration results than by calibrating all parameters, an experiment similar to Experiment 2 is conducted, with the following differences:

- For each catchment all models are calibrated on 6 years of data using as objective function a combination (the average) of the Nash-Sutcliffe efficiency measure applied to the hourly discharge data and to their logarithm.
- The parameters related to the partitioning of water input in the buckets conceptualising the different geological zones, and those controlling the partitioning of evaporation, are set a priori based on the area percentages in Table 3. When the models have less buckets than what the geology would suggest, aggregations are made.
- The parameters describing the response times of the buckets are calibrated by maintaining the proportions shown in the matrix of model parameter ratios in Figure 5. Ratios of response times within catchment response units are used but not ratios between catchment response units.
- All other parameters are calibrated with the exception of the ones related to snowmelt, which are assumed known and fix for every catchment and every model (see Table 2). The differential evolution optimisation algorithm (DEoptim in R, Mullen et al., 2011) is used and is run 15 times for each combination of model/catchment/calibration period.
- The performances are then compared for two 6 years calibration periods and for two 6 year validation periods (with the exception of the Wimitzbach/Gurk catchment for which shorter input data series are available).

Figure 9 shows the results in terms of the Nash Sutcliffe efficiency and is analogous to Figure 8. There is a decrease in Nash Sutcliffe when going from full calibration to runoff-generation mechanisms based parameters (as would be ex-

pected) but the difference is not huge and the differences between calibration and validation decreases slightly (points are slightly closer to the 1:1 line in the bottom panels of Figure 9 than in Figure 8). Moreover, the parameters to be calibrated are fewer. Table 5 shows the parameters obtained for the catchments for whom they were developed on the two periods (with the exception of Wimitzbach), when all parameters are calibrated and when very few parameters are calibrated. When a-priori information on some of the parameters is used, in most of the cases also the other parameters get closer, between the two periods, than in the case where all parameters are calibrated. When looking at the simulated timeseries (not shown here), very similar results are obtained with the different model structures because the calibration makes sure that the simulated runoff matches at best the observed one, even though there seems to be some more variability than in the case of calibrating all parameters.

DISCUSSION AND CONCLUSIONS

Because of the diversity of hydrologic processes in different catchments, models need to be adjusted to the particular situation to accurately portray the hydrological fluxes. The standard procedure in hydrology is to adjust the model parameters to the local situation but to choose the model structure based on software availability, convenience or other logistic considerations (Holländer et al., 2009). However, because of the wide variety of processes, choosing a suitable model structure for a particular setting may be just as important, if not more important, than choosing suitable model parameters. The main hypothesis we have investigated is that a single model structure cannot capture the wide variety of hydrological processes and ad-hoc model structures are therefore needed. More generally, our aim is to understand the mapping between landscape structure and hy-

drological model structure through the identification of dominant processes.

In this paper we have developed hydrologic models based on field-mapped runoff generation mechanisms as identified by a geologist. For four different catchments in Austria, we have identified four different lumped model structures and constrained their parameters based on the field-mapped information. A repeatable framework for quantifying expert judgement as a-priori information on model parameters has been developed. In order to understand the usefulness of geologic information, we have then tested their capability to predict river discharge without calibration and using the standard split-sample calibration-validation procedure (see e.g., Klemes, 1986). All models have been compared against each other.

Choosing a suitable model structure in a particular catchment may not only help improve model performance, it may also be helpful in estimating the parameters from runoff data. For example, van Werkhoven et al. (2008, 2009) found that an appropriate choice of the model structure simplifies parameter estimation as the plausible parameter range is narrower if the model structure corresponds to the actual controls. Consistently with these studies, our results show that, when no calibration is involved, using the right model structure for the catchment of interest is valuable. This has to do with the fact that the models have been developed in a way that, when reasonable parameter values are used (e.g., mid range values), the catchment response is consistent with what is expected by the modeler (e.g., in terms of smoothness or flashiness of catchment response). A-priori information on model parameters does not always improve the results but allows for more realistic model parameters.

When calibration is performed, the differences between model structures do not result in difference in model performances. This is because calibration compensates for the structural differences (Beven, 2006; Blöschl, 2006). When a-priori information on some of the parameters is used, in most of the cases also the calibrated parameters get closer, between the two calibration periods, as compared to the case where all parameters are calibrated. There seems to be value in estimating the parameters from runoff generation mechanisms, that can be expected to be more realistic and lead to more robust in prediction. However, even when constraining many parameters with a-priori information, the within model results do not differ significantly. This is in contrast with our expectation of finding a stronger difference between results with different model structures when very few parameters are calibrated. Apparently the tuning of these few parameters is able to compensate for other differences. One of the reasons that may have determined this lack of difference between models, when calibration is performed, is the fact that information on runoff generation mechanisms has been used to develop lumped rainfall-runoff models. Since the available information is distributed in space, conceptualising the model in a spatially explicit way may have resulted into a better characterisation of the geology-related processes and in more distinct results between different models, even when calibration is performed (Grayson and Blöschl, 2000).

In this paper, a-priori information on runoff generation mechanisms has been used by selecting some of the model parameters (or parameter ratios) as fixed/exact values. Better performances may have been obtained by constraining these parameters by ranges or distributions. Ideally, a Bayesian framework could be used instead to formally account for a-priori information (see e.g., Kavetski et al., 2006a,b) and fuzzy numbers could be used to account for the imprecision of the information (see e.g., Salinas et al., 2016). The investigation of these hypotheses is left to further studies. Also, we have not

looked here at how strong the input interpolation, the estimation of evapotranspiration and snowmelt modelling have influence the results. Sensitivity analyses will be performed in further studies in order to evaluate this and what are the parameters controlling the runoff goodness-of-fit for the different models.

Even though our results have not shown a significant advantage of selecting ad-hoc models and parameters when calibration is performed, the results obtained without calibration suggest that there is potential of this approach for ungauged catchments, where no calibration is possible and so a priori selection of models and parameters is necessary (Blöschl, 2005; Blöschl et al., 2013). For the same reasons, the modelling framework proposed in this paper has a potential to be suitable for investigating the effects of changes in controls (e.g., land use) in changing runoff regimes in the future (Ehret et al., 2014). Models selected by runoff generation mechanisms are expected to be more robust and more suitable for extrapolation to conditions outside the calibration range than models that are purely based on parameter calibration to runoff data.

Acknowledgements. This work was supported by the Austrian Science Foundation [FWF project P 23723-N21 and Doctoral Program DK-plus W1219-N22], by the German Research Foundation [DFG projekt SPATE, number 278017089] and by the EU project System-Risk [Grant Agreement number: 676027].

REFERENCES

- Abbott, M., Bathurst, J., Cunge, J., O'Connell, P., Rasmussen, J., 1986. An introduction to the European Hydrological System — Systeme Hydrologique Europeen, "SHE", 1: History and philosophy of a physically-based, distributed modelling system. *Journal of Hydrology*, 87, 45–59.
- Bai, Y., Wagener, T., Reed, P.M., 2009. A top-down framework for watershed model evaluation and selection under uncertainty. *Environmental Modelling and Software*, 24, 901–916.
- Beven, K.J., 2001. How far can we go in distributed hydrological modelling? *Hydrology and Earth System Sciences*, 5, 1–12.
- Beven, K.J., 2006. A manifesto for the equifinality thesis. *Journal of Hydrology*, 320, 1–2, 18–36. DOI: 10.1016/j.jhydrol.2005.07.007.
- Blöschl, G., 2005. Rainfall-runoff modeling of ungauged catchments. In: Anderson, M.G. (Ed.): *Encyclopedia of Hydrological Sciences*. John Wiley & Sons, Chichester, pp. 2061–2080.
- Blöschl, G., 2006. Hydrologic synthesis: Across processes, places, and scales. *Water Resources Research*, 42, 3, W03S02. DOI: 10.1029/2005WR004319.
- Blöschl, G., Sivapalan, M., Wagener, T., Viglione, A., Savenije, H.H., 2013. *Runoff Prediction in Ungauged Basins – Synthesis across Processes, Places and Scales*. Cambridge University Press, Cambridge, 484 p.
- Caylor, K.K., D'Odorico, P., Rodriguez-Iturbe, I., 2006. On the ecohydrology of structurally heterogeneous semiarid landscapes. *Water Resources Research*, 42, 7. DOI: 10.1029/2005WR004683.
- Ehret, U., Gupta, H.V., Sivapalan, M., Weijs, S.V., Schymanski, S.J., Blöschl, G., Gelfan, A.N., Harman, C., Kleidon, A., Bogaard, T.A., Wang, D., Wagener, T., Scherer, U., Zehe, E., Bierkens, M.F.P., Di Baldassarre, G., Parajka, J., van Beek, L.P.H., van Griensven, A., Westhoff, M.C., Winsemi-

- us, H.C., 2014. Advancing catchment hydrology to deal with predictions under change. *Hydrology and Earth System Sciences*, 18, 649–671. DOI: 10.5194/hess-18-649-2014.
- Falkenmark, M., Chapman, T., 1989. *Comparative Hydrology: An Ecological Approach to Land and Water Resources*. The Unesco Press, Paris, 479 p.
- Fenicia, F., Kavetski, D., Savenije, H.H., 2011. Elements of a flexible approach for conceptual hydrological modeling: 1. Motivation and theoretical development. *Water Resources Research*, 47, 13. DOI:10.1029/2010WR010174.
- Gaál, L., Szolgay, J., Kohnová, S., Parajka, J., Merz, R., Viglione, A., Blöschl, G., 2012. Flood timescales: Understanding the interplay of climate and catchment processes through comparative hydrology. *Water Resources Research*, 48, W04511. DOI: 10.1029/2011WR011509.
- Grayson, R.B., Blöschl, G. (Eds.) 2000. *Spatial Patterns in Catchment Hydrology: Observation and Modelling*, Cambridge University Press, Cambridge, 404 p.
- Gutknecht, D., Jolánkai, G., Skinner, K., 2008. *Patterns and processes in the catchment*. CAB International, Chapter 2, pp. 18–29.
- He, X., Højberg, A.L., Jørgensen, F., Refsgaard, J.C., 2015. Assessing hydrological model predictive uncertainty using stochastically generated geological models. *Hydrological Processes*, 29, 19, 4293–4311. DOI: 10.1002/hyp.10488.
- Hellebrand, H., Müller, C., Matgen, P., Fenicia, F., Savenije, H., 2011. A process proof test for model concepts: Modelling the meso-scale. *Physics and Chemistry of the Earth*, 36, 42–53.
- Hogue, T.S., Bastidas, L.A., Gupta, H.V., Sorooshian, S., 2006. Evaluating model performance and parameter behavior for varying levels of land surface model complexity. *Water Resources Research*, 42, 8. DOI: 10.1029/2005WR004440.
- Holländer, H.M., Blume, T., Bormann, H., Buytaert, W., Chirico, G.B., Exbrayat, J.-F., Gustafsson, D., Hölzel, H., Kraft, P., Stamm, C., Stoll, S., Blöschl, G., Flühler, H., 2009. Comparative predictions of discharge from an artificial catchment (Chicken Creek) using sparse data. *Hydrology and Earth System Sciences*, 13, 2069–2094. DOI: 10.5194/hess-13-2069-2009.
- Hrachowitz, M., Fovet, O., Ruiz, L., Euser, T., Gharari, S., Nijzink, R., Freer, J.E., Savenije, H.H.G., Gascuel-Oudou, C., 2014. Process consistency in models: The importance of system signatures, expert knowledge, and process complexity. *Water Resources Research*, 50, 9, 7445–7469. DOI: 10.1002/2014WR015484.
- Kavetski, D., Kuczera, G., Franks, S.W., 2006a. Bayesian analysis of input uncertainty in hydrological modeling: 1. Theory. *Water Resources Research*, 42, 3, W03407. DOI: 10.1029/2005WR004368.
- Kavetski, D., Kuczera, G., Franks, S.W., 2006b. Bayesian analysis of input uncertainty in hydrological modeling: 2. Application. *Water Resources Research*, 42, 3, W03408. DOI: 10.1029/2005WR004376.
- Klemes, V., 1986. Operational testing of hydrological simulation models. *Hydrological Sciences Journal - des Sciences Hydrologiques*, 31, 1, 13–24. DOI: 10.1080/02626668609491024.
- Merz, R., Blöschl, G., 2009. A regional analysis of event runoff coefficients with respect to climate and catchment characteristics in Austria. *Water Resources Research*, 45, W01405. DOI: 10.1029/2008WR007163.
- Merz, R., Blöschl, G., Parajka, J., 2006. Spatio-temporal variability of event runoff coefficients. *Journal of Hydrology*, 331, 3–4, 591–604. DOI: 10.1016/j.jhydrol.2006.06.008.
- Milly, P.C.D., Dunne, K.A., 2002. Macroscale water fluxes 2. Water and energy supply control of their interannual variability. *Water Resources Research*, 38, 10, 24–1–24–9. DOI: 10.1029/2001WR000760.
- Mullen, K., Ardia, D., Gil, D., Windover, D., Cline, J., 2011. DEoptim: an R package for global optimization by differential evolution. *Journal of Statistical Software*, 40, 6, 1–26.
- Müller, C., Hellebrand, H., Seeger, M., Schobel, S., 2009. Identification and regionalization of dominant runoff processes – a GIS-based and a statistical approach. *Hydrology and Earth System Sciences*, 13, 779–792.
- Nester, T., Kirnbauer, R., Parajka, J., Blöschl, G., 2012. Evaluating the snow component of a flood forecasting model. *Hydrology Research*, 43, 6, 762–779. DOI: 10.2166/nh.2012.041.
- Nijzink, R.C., Samaniego, L., Mai, J., Kumar, R., Thober, S., Zink, M., Schäfer, D., Savenije, H.H.G., Hrachowitz, M., 2016. The importance of topography-controlled sub-grid process heterogeneity and semi-quantitative prior constraints in distributed hydrological models. *Hydrology and Earth System Sciences*, 20, 1151–1176. DOI: 10.5194/hess-20-1151-2016.
- Parajka, J., Merz, R., Blöschl, G., 2003. Estimation of daily potential evapotranspiration for regional water balance modeling in Austria. In: 11th. International Poster Day Transport of Water, Chemicals and Energy in the Soil - Crop Canopy - Atmosphere System. Slovak Academy of Sciences, Bratislava, pp. 299–306.
- Pirkel, H., 2009. *Hydrogeologische und geohydrologische Grundlagen für die ausgewählten Leiteinzugsgebiete - Unveröffentl. Bericht im Rahmen Projekt Hochwasser Tirol (HOWATI)*. Technical Report, Vienna.
- Pirkel, H., 2012. *Untergrundabhängige Abflussprozesse. Kartierung und Quantifizierung für das Bundesland Tirol. Flächendeckende Aufnahme Osttirols. Endbericht. Unveröffentl. Bericht*, Technical Report, Vienna.
- Rogger, M., Kohl, B., Pirkel, H., Viglione, A., Komma, J., Kirnbauer, R., Merz, R., Blöschl, G., 2012a. Runoff models and flood frequency statistics for design flood estimation in Austria – Do they tell a consistent story? *Journal of Hydrology*, 456–457, 30–43. DOI: 10.1016/j.jhydrol.2012.05.068.
- Rogger, M., Pirkel, H., Viglione, A., Komma, J., Kohl, B., Kirnbauer, R., Merz, R., Blöschl, G., 2012b. Step changes in the flood frequency curve: Process controls. *Water Resources Research*, 48, W05544. DOI: 10.1029/2011WR011187.
- Rosero, E., Yang, Z.-L., Wagener, T., Gulden, L.E., Yatheendradas, S., Niu, G.-Y., 2010. Quantifying parameter sensitivity, interaction, and transferability in hydrologically enhanced versions of the Noah land surface model over transition zones during the warm season. *Journal of Geophysical Research-Atmospheres*, 115, D3. DOI: 10.1029/2009JD012035.
- Salinas, J.L., Kiss, A., Viglione, A., Viertl, R., Blöschl, G., 2016. A fuzzy Bayesian approach to flood frequency estimation with imprecise historical information. *Water Resources Research*, 52, 9, 6730–6750. DOI: 10.1002/2016WR019177.
- Samuel, J.M., Sivapalan, M., Struthers, I., 2008. Diagnostic analysis of water balance variability: A comparative modeling study of catchments in Perth, Newcastle, and Darwin, Australia. *Water Resources Research*, 44, 6. DOI: 10.1029/2007WR006694.
- Savenije, H.H.G., 2009. The art of hydrology. *Hydrology and Earth System Sciences*, 13, 157–161.
- Savenije, H., 2010. Topography driven conceptual modelling (FLEX-Topo), *Hydrology and Earth System Sciences*, 14, 12, 2681–2692. DOI: 10.5194/hess-14-2681-2010, HESS

Opinions.

- Van den Bos, R., Hoffmann, L., Juilleret, J., Matgen, P., Pfister, L., 2006. Regional runoff prediction through aggregation of first-order hydrological process knowledge a case study, *Hydrological Sciences - Journal - des Sciences Hydrologiques*, 51, 1021–1038.
- van Werkhoven, K., Wagener, T., Reed, P., Tang, Y., 2008. Characterization of watershed model behavior across a hydroclimatic gradient. *Water Resources Research*, 44, W01429. DOI: 10.1029/2007WR006271.
- van Werkhoven, K., Wagener, T., Reed, P., Tang, Y., 2009. Sensitivity-guided reduction of parametric dimensionality for multi-objective calibration of watershed models. *Advances in Water Resources*, 32, 8, 1154–1169. DOI: 10.1016/j.advwatres.2009.03.002.
- Wagener, T., Sivapalan, M., Troch, P., Woods, R., 2007. Catchment Classification and Hydrologic Similarity, *Geography Compass*, 1, 4, 901–931. DOI: 10.1111/j.1749-8198.2007.00039.x.
- Winter, T.C., 2001. The concept of hydrologic landscapes. *Journal of the American Water Resources Association*, 37, 2, 335–349. DOI: 10.1111/j.1752-1688.2001.tb00973.x.
- Wolock, D.M., Winter, T.C., McMahon, G., 2004. Delineation and evaluation of hydrologic-landscape regions in the United States using geographic information system tools and multivariate statistical analyses. *Environmental Management*, 34, 1, S71–S88. DOI: 10.1007/s00267-003-5077-9.

Received 7 August 2017
Accepted 10 January 2018

Note: Colour version of Figures can be found in the web version of this article.

Calculation of critical flow depth using method of algebraic inequality

Tiejie Cheng¹, Jun Wang¹, Jueyi Sui^{2*}

¹ School of Civil Engineering, Hefei University of Technology, 193 Tunxi Road, Hefei, Anhui, China. Email: tj-cheng@qq.com

² Environmental Engineering, University of Northern British Columbia, 3333 University Way, Prince George, BC, Canada.

* Corresponding author. E-mail: Jueyi.sui@unbc.ca

Abstract: To calculate the critical depth and the least specific energy of steady non-uniform flows in open channels, one has to solve the polynomial equations. Sometimes, the polynomial equations are too difficult to get them solved. In this study, the theory of algebraic inequality has been used to derive formulas for determining the critical depth and the least specific energy of a steady non-uniform flow in open channel. The proposed method has been assessed using examples. Results using this new method have been compared to those using other conventional methods by engineers and scientists. It is found that the proposed method based on algebraic inequality theory not only makes the calculation process to be easy, but also gives the best calculation results of the critical depth and the least specific energy of a steady non-uniform flow.

Keywords: Critical depth; Mean value inequality; Steady non-uniform flow; Specific energy; Algebraic inequality.

INTRODUCTION

In practice, the critical depth of steady non-uniform flow in open channel is an important variable for engineers to determine optimal cross section (Vatankhah, 2013). Some cross-sectional shapes are often chosen by river engineers in engineering design, such as trapezoidal shape and U-shape, since flow conditions in channels having such cross sections are relatively less complicated in addition to being easily constructed (Liu and Xu, 2016). However, for the steady non-uniform flow in channels having such cross sections, it is not easy to determine the critical depth since either polynomial equations or transcendental equations have to be solved. Normally, either the curve-fitting method or trial-and-error method is used to solve the polynomial equations and transcendental equations. Engineers have to put a lot of efforts to solve polynomial equations or transcendental equations. Also, the calculation processes by means of both curve-fitting method and trial-and-error method are multifarious with relatively low accuracy.

The least specific energy and the critical depth of the steady non-uniform flow in open channel have attracted much attention of researchers. Up to date, some methodologies have been proposed for calculating the least specific energy and the critical depth. By introducing following factors $x = m h_c/b$ and $k = 4mb^{-1}(\alpha Q^2 g^{-1} b^{-2})^{1/3}$, formula have been developed by means of the identical transformation of the basic formula for determining the critical depth in open channels with a trapezoidal cross section (Swamee, 1993; Swamee and Rathie, 2005; Swamee, et al., 1999; Wang, 1998; Zhao, et al., 2009). Li et al. (2010) converted the U-shape cross section into one rectangular part plus two triangular parts. Based on this approach, Li et al. (2010) developed the formula for calculating the critical depth for flow in a channel having an U-shape cross section. By replacing factors in the formulas usually used for calculating the critical depth, Zhang and Li (2012) derived an iterative formula for calculating the critical depth by means of the algebraic transmutation method. Up to date, researchers have improved the calculation accuracy for determining the critical depth by means of different methodologies. However, dimensionless variables have to be solved prior to determining the critical depth. Afterward, based on the calculated dimensionless variables, the critical depth can be determined. Overall, the existing

methods for calculating the critical depth are either cumbersome or inaccurate. In the present study, we introduce a new technique to calculate the critical depth easily and accurately. The theory of algebraic inequality is applied to develop formulas for determining the critical depth for steady non-uniform flow in open channels.

CONVENTIONAL HYDRAULIC CALCULATION METHOD FOR STEADY NON-UNIFORM STEADY FLOW IN OPEN CHANNELS

Chosen the elevation at the channel bed as the reference datum, the hydraulic calculation for steady non-uniform flow in an open channel can proceed. At any individual cross section, the specific energy (defined as the energy per unit weight of fluid) can be determined using the following formula (Wu, 2008),

$$E_s = h \cos \theta + \frac{\alpha v^2}{2g} = h \cos \theta + \frac{\alpha Q^2}{2g A^2} \quad (1)$$

where, E_s is the specific energy of flow at the designated cross section (m); h is flow depth (m); θ is the slope angle of the channel bed (inclined to the horizontal plane); α is the kinematic energy coefficient; v is the average flow velocity (m/s); Q is the flow discharge (m³/s); and A is cross-sectional area of flow (m²). If the specific energy of flow at the designated cross section approaches the minimum, the flow depth corresponding to the least specific energy is defined as the critical depth (h_c). Conventionally, the least specific energy and critical depth of flow at the designated cross section are calculated by neglecting the slope of channel bed and the kinematic energy coefficient, namely, $\cos \theta = 1$ and $\alpha = 1.0$. Then, the first derivative of Eq. (1) with respect to h is as follows,

$$\frac{dE_s}{dh} = \frac{d}{dh} \left(h + \frac{Q^2}{2g A^2} \right) = 1 - \frac{Q^2}{g A^3} \frac{dA}{dh} \quad (2)$$

The width of water surface (B) can be expressed as $dA/dh = B$; for the least specific energy of flow, let $dE_s/dh = 0$, then,

$$\frac{A_k^3}{B_k} = \frac{Q_k^2}{g} \tag{3}$$

Eq. (3) is very important, since it is the basis for many researchers to study the critical depth of a steady non-uniform flow in an open channel having a trapezoidal cross section (as shown in Figure 1 in Table 1). From Eq. (3), the critical depth h_K can be derived. Afterward, the least specific energy of flow in channel (E_{smin}) can be calculated using Eq. (1).

However, the conventional method for calculating the specific energy and critical depth of flow is not perfect. From the first derivative method, the extremum cannot be determined directly. Mathematically, by determining the zero value of the first derivative of a function, one can only get the stationary point of a function. However, the stationary point of a function does not mean that the extremum value exists at this point. To determine the point with extreme value, one has to find the point with zero value of the first derivative of a function in addition to finding the points where the first derivative is absent. In the mean time, the changes of the first derivative besides the stationary points of a function should be assessed, or to determine the extremum by means of the second derivative of a function. The calculation of extreme value of a function needs the assessment of point, which is extremum of each stationary maximum. It is a cumbersome process.

In addition, the conventional methods for calculating the specific energy and critical depth of flow do not consider all factors that affect the specific energy and flow depth. For cross sections having complex shapes, it is really difficult to determine the specific energy and critical depth accurately using the conventional method.

CALCULATION OF THE CRITICAL DEPTH AND THE LEAST SPECIFIC ENERGY BY MEANS OF THE ALGEBRAIC INEQUALITY THEORY
Theory of arithmetic-geometric average inequality

Arithmetic-geometric average inequality (AM–GM inequality) is defined as following, for a list of n non-negative real numbers x_1, x_2, \dots, x_n , the arithmetic mean (A_n) of these non-negative real numbers is greater or equal to the geometric mean (G_n) of the same list, namely, $A_n \geq G_n$ (Garling, 2012).

The arithmetic mean (A_n) can be determined as following

$$A_n = \frac{1}{n} \sum_{i=1}^n x_i = \frac{x_1 + x_2 + \dots + x_n}{n} \tag{4}$$

and the geometric mean (G_n) can be determined as following

$$G_n = \sqrt[n]{\prod_{i=1}^n x_i} = \sqrt[n]{x_1 x_2 \dots x_n} \tag{5}$$

The equal sign in the AM–GM inequality $A_n \geq G_n$ is valid if and only if $x_1 = x_2 = \dots = x_n$.

There are many methodologies for proving the AM–GM inequality (Garling, 2012). The AM–GM inequality is a classical inequality and has been widely used in mathematics. Up to date, much research has been conducted to apply the AM–GM inequality in engineering designs (Sabnis and Agnihothram, 2006).

There is a similar inequality for the weighted arithmetic average mean and weighted geometric average mean (Furuichi, 2011). Specifically, let the non-negative numbers x_1, x_2, \dots, x_n

and the non-negative weights $p_i > 1$ ($i=, 1, 2, 3, \dots, n$) be given.

Set $\sum_{i=1}^n 1/p_i = 1$. Then, the inequality

$$\sum_{i=1}^n \frac{1}{p_i} x_i \geq \prod_{i=1}^n (x_i)^{1/p_i} \tag{6}$$

Inequality (6) holds with equality if and only if $x_1 = x_2 = \dots = x_n$. In the next sections, Inequality (6) will be used to derive formulas for calculating the critical depth and specific energy of flow in channels with some specific cross-sectional shapes.

Equations for critical depth and specific energy derived based on AM–GM inequality

Mathematically, if one equation can be solved through the general arithmetic rules and has at least one solution, this equation can be defined as an equation having an analytical solution. In open channel hydraulics, equations for calculating critical depth have analytical solutions. The relationship between flow cross-sectional area (A) and flow depth (h) can be described as following,

$$A = p(h+q)^r \tag{7}$$

where, p, q and r are constants and have nothing to do with flow depth (h); both q and h have the same dimension of length (m); r is a dimensionless constant; the dimension of p depends on the value of “ r ” (m^{2-r}). Then, the analytical solution for the critical depth can be determined by means of the theory of weighted mean inequality.

Combining Eq. (1) with Eq. (7), Eq. (8) can be derived as,

$$E_s = h \cos \theta + \frac{\alpha Q^2}{2g p^2 (h+q)^{2r}} \tag{8}$$

As shown in Eq. (8), to obtain the least specific energy, the right hand side of Eq. (8) should be transformed. Applying the method of the weighted mean inequality, variable h can be eliminated. Then, under condition of equality holding, the right hand side of Eq. (8) can be split into several parts. After identical transformation, Eq. (8) can be changed as follows,

$$E_s = 2r \left[\frac{(h+q)}{2r} \cos \theta \right] + \frac{\alpha Q^2}{2g p^2 (h+q)^{2r}} - q \cos \theta \tag{9}$$

From the weighted mean inequality (6), we obtain the following,

$$\begin{aligned} & \frac{2r}{2r+1} \left[\frac{(h+q)}{2r} \cos \theta \right] + \frac{1}{2r+1} \left[\frac{\alpha Q^2}{2g p^2 (h+q)^{2r}} \right] \\ & \geq \left[\frac{(h+q)}{2r} \cos \theta \right]^{\frac{2r}{2r+1}} \left[\frac{\alpha Q^2}{2g p^2 (h+q)^{2r}} \right]^{\frac{1}{2r+1}} \\ & = 2r+1 \sqrt{\left[\frac{\cos \theta}{r} \right]^{2r} \frac{\alpha Q^2}{p^2 g}} / 2 \end{aligned} \tag{10}$$

If both sides are multiplied by $(2r+1)$, Eq. (9) can be expressed as follows,

$$2r \left[\frac{(h+q)}{2r} \cos \theta \right] + \frac{\alpha Q^2}{2gp^2(h+q)^{2r}} - q \cos \theta \quad (11)$$

$$\geq \frac{(2r+1)}{2} \sqrt[2r+1]{\left[\frac{\cos \theta}{r} \right]^{2r} \frac{\alpha Q^2}{p^2 g}} - q \cos \theta$$

Thus, the specific energy of flow at the designated cross section can be calculated from the following equation,

$$E_{s \min} = \frac{(2r+1)}{2} \sqrt[2r+1]{\left[\frac{\cos \theta}{r} \right]^{2r} \frac{\alpha Q^2}{p^2 g}} - q \cos \theta \quad (12)$$

Inequality (11) holds with equality if the flow has the least specific energy. Thus, considering the case when weighted mean inequality holds with equality, we obtain the following,

$$\frac{(h+q)}{2r} \cos \theta = \frac{\alpha Q^2}{2gp^2(h+q)^{2r}} \quad (13)$$

Then the equation for the critical depth of flow can be determined as follows,

$$\frac{(h_K+q)}{2r} \cos \theta = \frac{\alpha Q^2}{2gp^2(h_K+q)^{2r}} \quad (14)$$

From Eq. (14), the calculation of the critical depth of flow at a designated cross section (h_K) can be expressed as follows,

$$h_K = 2r+1 \sqrt[2r+1]{\frac{r \alpha Q^2}{g p^2 \cos \theta}} - q \quad (15)$$

Eq. (15) has been derived provided that the relationship between flow cross-sectional area and flow depth can be described by Eq. (7). The calculated critical flow depth at the designated cross section as defined by Eq. (14) is an analytical solution.

Generally, flow cross sections in natural rivers can be approximated by one of the following shapes: rectangular, (quasi-)trapezoidal, (quasi-)U, or a high-order parabolic shape. The relationship between the cross-sectional flow area and flow depth for all above-mentioned cross-sectional shapes can be described as Eq. (7). Namely, there exist analytical solutions for critical flow depth in channels having above-mentioned cross-sectional shapes. In the following sections, equations for determining the critical depth and the least specific energy for natural channels having such typical cross-sectional shapes will be derived.

Solving equations for determining critical depth and specific energy for steady non-uniform flow

Mathematically, the following methodologies can be used to get numerical solutions of equations by means of numerical analysis, iterative method, numerical step-by-step method, and interpolation method. One can calculate the critical depth of flow by means of numerical analysis provided the relationship between flow cross-sectional area and flow depth can be described as follows,

$$A = p \prod_{i=1}^n (h+q_i)^{r_i}, \quad (n \geq 2) \quad (16)$$

where, p , q and r are constants and have nothing to do with flow depth (h); both q_i and h have the same dimension of length (m); r is a dimensionless constant; the dimension of p depends on the value of “ r ” (m^{2-r}).

Then, combining Eq. (1) with Eq. (16), the following equation has been derived for determining the specific energy,

$$E_s = h \cos \theta + \frac{\alpha Q^2}{2g p^2 \prod_{i=1}^n (h+q_i)^{2r_i}} \quad (17)$$

To get the least specific energy from Eq. (17), flow depth (h) is eliminated by means of the method of mean inequality. Then, by holding with equality, the critical depth can be determined. By splitting and identical transforming of the right side of Eq. (17), and through such an inequality minification as Inequality (6), we get following,

$$\sum_{i=1}^n \frac{2r_i}{\left(\sum_{i=1}^n 2r_i + 1 \right)} \left[k_i (h+q_i) \cos \theta \right] + \frac{1}{\left(\sum_{i=1}^n 2r_i + 1 \right)} \left[\frac{\alpha Q^2}{2gp^2 \prod_{i=1}^n (h+q_i)^{2r_i}} \right]$$

$$\geq \prod_{i=1}^n \left[k_i (h+q_i) \cos \theta \right]^{2r_i} \left/ \left(\sum_{i=1}^n 2r_i + 1 \right) \right. \left[\frac{\alpha Q^2}{2gp^2 \prod_{i=1}^n (h+q_i)^{2r_i}} \right]^{1/\left(\sum_{i=1}^n 2r_i + 1 \right)}$$

$$= \sum_{i=1}^n 2r_i + 1 \sqrt[2r_i+1]{\prod_{i=1}^n [k_i \cos \theta]^{2r_i} \frac{\alpha Q^2}{2p^2 g}} \quad (18)$$

When both sides are multiplied by $\sum_{i=1}^n 2r_i + 1$, we get,

$$\sum_{i=1}^n 2r_i \left[k_i (h+q_i) \cos \theta \right] + \frac{\alpha Q^2}{2gp^2 \prod_{i=1}^n (h+q_i)^{2r_i}} \quad (19)$$

$$\geq \left(\sum_{i=1}^n 2r_i + 1 \right) \cdot \sum_{i=1}^n 2r_i + 1 \sqrt[2r_i+1]{\prod_{i=1}^n [k_i \cos \theta]^{2r_i} \frac{\alpha Q^2}{2p^2 g}}$$

Eq. (17) can be modified as following,

$$E_s = \sum_{i=1}^n 2r_i \left[k_i (h+q_i) \cos \theta \right] + \frac{\alpha Q^2}{2g p^2 \prod_{i=1}^n (h+q_i)^{2r_i}}$$

$$- 2 \sum_{i=1}^n q_i r_i k_i \cos \theta \geq \left(\sum_{i=1}^n 2r_i + 1 \right) \sum_{i=1}^n 2r_i + 1 \sqrt[2r_i+1]{\prod_{i=1}^n (k_i \cos \theta)^{2r_i} \frac{\alpha Q^2}{2p^2 g}}$$

$$- 2 \sum_{i=1}^n q_i r_i k_i \cos \theta = E_{s \min} \quad (20)$$

where, k_i ($i = 1, 2, \dots, n$) in inequality (20) are un-determined dimensionless coefficients. Since inequality (20) is the identical transformation of the right hand side of Eq. (17), therefore,

$$2 \sum_{i=1}^n r_i k_i = 1 \quad (21)$$

According to conditions for holding with equality of the weighted mean inequality, the following equation was obtained,

$$k_i(h+q_i)\cos\theta = k_j(h+q_j)\cos\theta = \frac{\alpha Q^2}{2gp^2 \prod_{i=1}^n (h+q_i)^{2r_i}} \quad (22)$$

In Eq. (22), $i \neq j$. Combining Eq. (21) with Eq. (22), coefficients k_i ($i = 1, 2, \dots, n$) can be determined. By holding with equality, $E_s = E_{min}$, and thus, $h = h_k$. Letting the un-determined coefficients k_i ($i = 1, 2, \dots, n$) to be following,

$$k_i = \psi_i(h_K) \quad (23)$$

Considering convergence speed of iterative solution, with $\max_{1 \leq i \leq n} \{r_i\} = r_M$, Eq. (24) was derived,

$$k_M(h_K + q_M)\cos\theta = \frac{\alpha Q^2}{2gp^2 \prod_{i=1}^n (h_K + q_i)^{2r_i}} \quad (24)$$

Combining Eq. (23) with Eq. (24), resulted in Eq. (25),

$$h_K = \sqrt[2r_M+1]{\frac{\alpha Q^2}{2g p^2 \cos\theta \prod_{i \neq M}^n (h_K + q_i)^{2r_i} \psi_M(h_K)}} - q_M \quad (25)$$

$$\text{Let } \varphi(x) = \sqrt[2r_M+1]{\frac{\alpha Q^2}{2g p^2 \cos\theta \prod_{i \neq M}^n (x + q_i)^{2r_i} \psi_M(x)}} - q_M.$$

From Eq. (25), one can see that h_K can be described as $h_K = \varphi(h_K)$. Thus, h_K is the fixed point of this function equation. The fixed point iterative formula for the critical depth is $h_{K,s+1} = \varphi(h_{K,s})$, where s represents the iteration number ($s = 1, 2, \dots$). Thus,

$$h_{K,s+1} = \sqrt[2r_M+1]{\frac{\alpha Q^2}{2g p^2 \cos\theta \prod_{i \neq M}^n (h_{K,s} + q_i)^{2r_i} \psi_M(h_{K,s})}} - q_M \quad (26)$$

After successive iteration of Eq. (26), the $\{h_{K,s}\}$ series will be determined. Then, $\lim_{s \rightarrow \infty} h_{K,s} = h_K$. Thus, the critical depth can be determined using the fixed-point iteration. Afterward, the least specific energy can be calculated using Eq. (1). To speed up the iterative convergence, the iterative method proposed by Kincaid and Cheney (2003) can be used. Critical depth calculated using Eq. (26) is the numerical solution for open channel flows (in these open channel flows, the relationship between cross-sectional area and flow depth can be described by Eq. (16)).

In practice, the cross sections of natural rivers have either trapezoidal or U shapes. The relationship between cross-sectional area and flow depth for channels having both trapezoidal and U-shapes can be described by Eq. (16). For other

complicated cross-sectional shapes, by means of some approximation methods such as interpolation, the relationships between cross-sectional area and flow depth can be also described by Eq. (16). The theory of algebraic inequality can also be used to solve the critical flow depth.

In the following section, we take the trapezoidal cross section shape and derive the hydraulic calculation of the critical depth and the least specific energy of flows by means of algebraic inequality. For flow in channels having other common cross-sectional shapes, a similar calculation method will be used to determine the critical depth and the least specific energy, as shown in Table 1.

Formulas for hydraulic calculation of flow in channel having a trapezoidal cross section

In river engineering, the cross section of natural channels has been often assumed to have a trapezoidal shape. As shown in Figure 1, the width of channel bottom is b ; the width of water surface is B ; m_1 and m_2 represents the left side slope of and right side slope of channel banks, respectively.

The relationship between cross-sectional area and flow depth for the channel having a trapezoidal cross-sectional shape can be written as follows,

$$A = \frac{1}{2}h(B+b) = \frac{(m_1+m_2)}{2}h \left[h + \frac{2b}{(m_1+m_2)} \right] \quad (27)$$

Comparing Eq. (27) to Eq. (16), $p = (m_1+m_2)/2$, $q_1 = 0$; $r_1 = 1$, $q_2 = 2b/(m_1+m_2)$, and $r_2 = 1$. Combining Eq. (21) and Eq. (22) with Eq. (27), then,

$$k_1 = \psi_1(h_K) = \frac{h_K + 2b/(m_1+m_2)}{4\{h_K + b/(m_1+m_2)\}} \quad (28)$$

$$k_2 = \psi_2(h_K) = \frac{h_K}{4\{h_K + b/(m_1+m_2)\}}$$

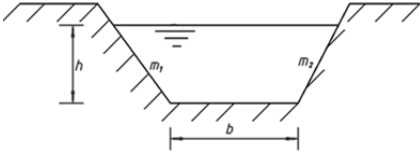
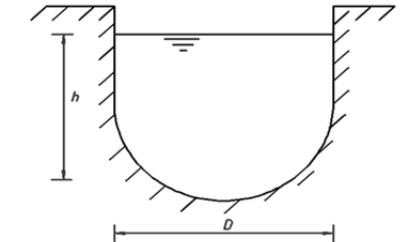
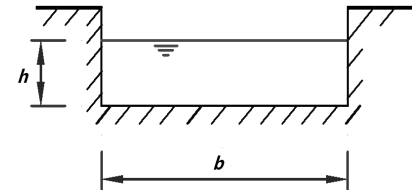
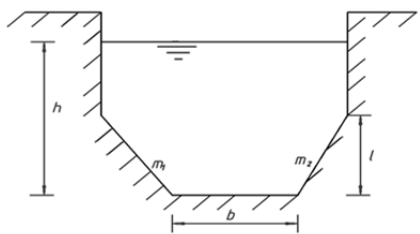
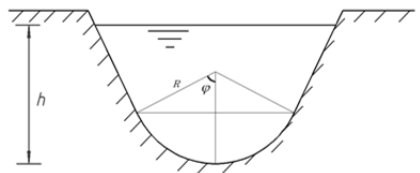
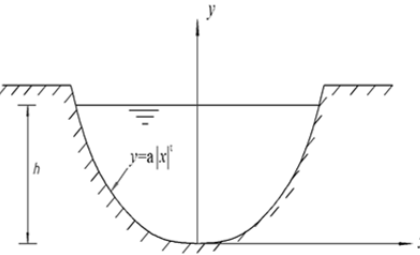
From $\max_{1 \leq i \leq n} \{r_i\} = r_M = r_1 = 1$, $q_M = q_1 = 0$ and Eq. (26), the formula for determining the critical flow depth is derived as following,

$$h_{K,s+1} = \sqrt[3]{\frac{\alpha Q^2 [(m_1+m_2)h_{K,s} + b]}{g \cos\theta}} / \left[\frac{(m_1+m_2)h_{K,s}}{2} + b \right] \quad (29)$$

When $m_1 = m_2 = 0$, the shape of trapezoidal cross section becomes a rectangular cross-sectional shape. When $b = 0$, the trapezoidal cross-sectional shape becomes to a triangular cross-sectional shape. This means, critical flow depths for flows in channels having cross sections of both rectangular and triangular shapes can be calculated using Eq. (29). The derived formulas for specific conditions (such as either " $m_1 = m_2 = 0$ " or " $b = 0$ ") for determining critical flow depths from Eq. (29) are identical to those for flows in channels having cross sections of both rectangular and triangular shapes, respectively (Wu, 2008). This proves the accuracy of Eq. (29).

As summarized in Table 1, formulas for determining the critical depth and the least specific energy of flow in channels having other typical cross-sectional shapes have been also derived.

Table 1. Formulas for calculating critical depth of steady non-uniform flow (h_K) in open channel developed by the method of algebraic inequality.

Typical shapes of channel cross section	Cross-sectional area (A)	Values of p, q, r	Critical flow depth (h_K)
 <p>Fig. 1. Diagram of channel having a trapezoidal cross-sectional shape.</p>	$A = \frac{(m_1 + m_2)}{2} h \left[h + \frac{2b}{(m_1 + m_2)} \right]$	$p = \frac{(m_1 + m_2)}{2}$ $q_1 = 0, \quad r_1 = 1$ $q_2 = \frac{2b}{(m_1 + m_2)}, \quad r_2 = 1$	<p>Numerical solution:</p> $h_{K,s+1} = \sqrt[3]{\frac{\alpha Q^2 [(m_1 + m_2) h_{K,s} + b]}{g \cos \theta}} \left[\frac{(m_1 + m_2) h_{K,s} + b}{2} \right]$
 <p>Fig. 2. Diagram of channel having a U- shape cross-sectional shape.</p>	$A = D \left[h - \frac{D}{8} (4 - \pi) \right]$	$p = D$ $q = -\frac{D}{8} (4 - \pi)$ $r = 1$	<p>Analytical solution:</p> $h_K = \sqrt[3]{\frac{\alpha Q^2}{g D^2 \cos \theta}} + \frac{D(4 - \pi)}{8}$
 <p>Fig. 3. Diagram of channel having a rectangle cross-sectional shape.</p>	$A = bh$	$p = b$ $q = 0$ $r = 1$	<p>Analytical solution:</p> $h_K = \sqrt[3]{\frac{\alpha Q^2}{g \cos \theta b^2}}$
 <p>Fig. 4. Diagram of channel having a quasi trapezoid shape cross-sectional shape.</p>	$A = [b + (m_1 + m_2)l]^* \left\{ h - \frac{(m_1 + m_2)l^2}{2[b + (m_1 + m_2)l]} \right\}$	$p = b + (m_1 + m_2)l$ $q = -\frac{(m_1 + m_2)l^2}{2[b + (m_1 + m_2)l]}$ $r = 1$	<p>Analytical solution:</p> $h_K = \frac{\sqrt[3]{\frac{\alpha Q^2 [b + (m_1 + m_2)l]}{g \cos \theta}} + \frac{(m_1 + m_2)l^2}{2}}{[b + (m_1 + m_2)l]}$
 <p>Fig. 5. Diagram of channel having a quasi-U- shape cross-sectional shape.</p>	$A = \frac{1}{\tan \varphi} [h + R(\lambda - \mu)]^* [h + R(\lambda + \mu)]$ $\lambda = 1/\cos \varphi - 1,$ $\mu = \sqrt{\tan \varphi (\tan \varphi - \varphi)}$	$p = \frac{1}{\tan \varphi}$ $q_1 = R(\lambda - \mu), \quad r_1 = 1$ $q_2 = R(\lambda + \mu), \quad r_2 = 1$	<p>Numerical solution:</p> $h_{K,s+1} = \frac{\sqrt[3]{\frac{2\alpha Q^2 (h_{K,s} + R\lambda) \tan^2 \varphi}{g \cos \theta}}}{h_{K,s} + R(\lambda + \mu)} - R(\lambda - \mu)$
 <p>Fig. 6. Diagram of channel having a high-order parabolic cross-sectional shape.</p>	$A = \frac{2t}{\sqrt[t]{a} \cdot (t+1)} h^{\frac{t+1}{t}}$	$p = \frac{2t}{\sqrt[t]{a} \cdot (t+1)}$ $q = 0$ $r = \frac{t+1}{t}$	<p>Analytical solution:</p> $h_K = \frac{3t+2}{t} \sqrt[t]{\frac{\alpha (\sqrt[t]{a} Q)^2 (t+1)^3}{4gt^3 \cos \theta}}$

Calculation examples

Example 1: In an open channel having a trapezoidal cross section as shown in Figure 1, since the soil in the left bank of the channel is different from that in right bank of the channel, the side slope of the left bank is $m_1 = 1.5$, and the side slope of the right bank is $m_2 = 1.0$, respectively. The width of channel bottom is $b = 6$ m. The designed flow discharge is $Q = 54$ m³/s. The slope of channel bed is $i = 0.008$. The kinematic energy coefficient $\alpha = 1.0$. Determine the critical flow depth (h_K) and the least specific energy (E_{smin}).

Solution: the channel slope is 0.008, thus, $\cos\theta = 1/(1+i)^{0.5}$. For flow in an open channel having a trapezoidal cross section, the critical flow depth can be calculated using Eq. (29),

$$h_{K,s+1} = \sqrt[3]{\frac{1.0 \times 54^2 [(1.5+1.0) h_{K,s} + 6]}{9.8 \times 1 / \sqrt{1+0.008^2}}} / \left[\frac{(1.5+1.0) h_{K,s} + 6}{2} \right]$$

Letting $h_{K,0} = 0$, from Table 1, $h_{K,1} = 2.022$ m, $h_{K,2} = 1.744$ m, $h_{K,3} = 1.779$ m, $h_{K,4} = 1.775$ m, and $h_{K,5} = 1.775$ m.

Thus, the critical flow depth $h_K = 1.775$ m.

Using Eq. (3), the hydraulic calculation can be checked:

$$\frac{A_K^3 \cos\theta}{B_K} = 297.44$$

$$\frac{\alpha Q^2}{g} = 297.55$$

One can see that the relative error using our proposed method is just: $\frac{297.55 - 297.44}{297.55} \times 100\% = 0.037\%$

From the given data, the discharge per unit width is $q = Q/b = 9$ m³/s/m, the average side slope of channel is $m = (m_1+m_2)/2 = 1.25$, the dimensionless factor is

$$k = \frac{4m}{b} \sqrt[3]{\frac{\alpha q^2}{g}} = 1.685 ; \text{ letting } x = \frac{m h_K}{b}$$

In Table 2, the calculated result using our proposed method is compared to five other methods. One can see from Table 2 that the calculation accuracy using our proposed method (0.037%) is much higher than those of others.

After determining the critical flow depth (h_K), the least specific energy (E_{smin}) can be calculated using either Eq. (1) or Eq. (20),

$$E_{smin} = h_K \cos\theta + \frac{\alpha Q^2}{2g \left\{ \frac{(m_1+m_2)}{2} \left[h_K + \frac{2b}{(m_1+m_2)} \right] h_K \right\}^2} = 2.474 \text{ m}$$

Thus, using our formulas, the critical flow depth is $h_K = 1.775$ m, and the least specific energy $E_{smin} = 2.474$ m, respectively.

Example 2: In an open channel having U-shape cross section as shown in Figure 2, the flow has a designed discharge of $Q = 45$ m³/s, $D = 5.0$ m. The channel bed is horizontal. The kinematic energy coefficient $\alpha = 1.1$. Determine the critical flow depth (h_K) and the least specific energy (E_{smin}).

Solution: the channel slope is 0, thus, $\cos\theta = 1$. For the flow in an open channel having U-shape cross section, as shown in Table 1, the critical flow depth (h_K) and the least specific energy (E_{smin}) can be calculated as follows,

$$\begin{cases} E_{smin} = \frac{3}{2} \sqrt[3]{\frac{1.1 \times 45^2}{5^2 \times 9.81}} + \frac{5 \times (4 - \pi)}{8} = 3.666 \text{ m} \\ h_K = \sqrt[3]{\frac{1.1 \times 45^2}{5^2 \times 9.81}} + \frac{5 \times (4 - \pi)}{8} = 2.623 \text{ m} \end{cases}$$

Table 2. Comparison of calculated critical depth of steady non-uniform flow (h_K) in open channel using different formulas proposed by other researchers.

Formulas proposed by	x value	h_K (m)	Relative error (%)
Prabhata	$x = \left[\left(\frac{k}{4} \right)^{-2.1} + \left(\frac{k^3}{32} \right)^{-0.42} \right]^{0.476} = 0.364$	1.746	5.39
Prabhata and Pushpa	$x = \left[\left(\frac{3.1748}{k} \right)^{0.6} + \left(\frac{1.78179}{k} \right)^{1.2} + \left(\frac{0.88341}{k} \right)^{1.8} - \left(\frac{0.68263}{k} \right)^{2.4} - \left(\frac{0.73686}{k} \right)^3 + \left(\frac{0.72866}{k} \right)^{3.6} + \left(\frac{0.77988}{k} \right)^{4.2} - \left(\frac{0.79676}{k} \right)^{4.8} - \left(\frac{0.83631}{k} \right)^{5.4} \right]^{-1} = 0.373$	1.788	2.47
Wang	$x = \frac{\sqrt{1+k(k+1)^{0.2}} - 1}{2} = 0.374$	1.793	3.53
Wu and Patopodis	$x = 0.55k^{0.59} - 0.11 \text{arsh}(9.75k) = 0.364$	1.747	5.21
Zhao	$x = \frac{\sqrt{1+k(k^{1.2}+1)^{1/6}} - 1}{2} = 0.367$	1.763	2.31

The calculated critical flow depth of $h_K = 2.623$ m, and the least specific energy of $E_{smin} = 3.666$ m are the exact solutions.

One can see that, it is a practical method to apply the theory of algebraic inequality for determining the critical depth and the least specific energy of flow. The calculation process is straightforward and convenient. The calculation results using our proposed formula are more accurate than those using other methods.

CONCLUSIONS

In this paper, a new technique based on the theory algebraic inequality has been developed to determine the critical depth and the least specific energy of the steady non-uniform flow in open channel. By means of the theory of weighted arithmetic average mean and weighted geometric average mean, the iterative formulas for calculating the critical flow depth and the least specific energy have been improved. Assessment of the relationships between flow cross-sectional area and flow depth for the typical cross-sectional shapes indicate that there exists analytical solution and numerical solution of equation for determining critical depth. In our proposed new technique for determining the critical depth and the least specific energy of energy, the complicated and cumbersome derivative calculation process of the conventional method has been avoided. Instead of using the time-consuming trail-and-error method, one can calculate the critical flow depth and the least specific energy directly. The calculation process of this new technique is conscious and convenient. Two examples are given to test the calculation results of the critical depth and the least specific energy of flows in channels having the most common cross-sectional shapes, namely, trapezoidal and U-shapes. The comparison of calculation results using this new technique to those using other conventional methods has been conducted. Results show that the proposed new method for determining the critical depth and the least specific energy of a steady non-uniform flow is a straightforward and easy calculation process, giving the best results. The method of algebraic inequality can be used in the hydraulic analysis and calculation, and provide better results in engineering practice.

Acknowledgement. This study is supported by the National Natural Science Foundation of China (Funding Number: 51379054). The authors are grateful for the financial support.

REFERENCES

- Furuichi, S., 2011. On refined Young inequalities and reverse inequalities. *Journal of Mathematical Inequalities*, 5, 21–31.
- Garling, D.J.H., 2012. *Inequalities: A Journey into Linear Analysis*. Beijing World Book Press, Beijing.
- Kincaid D., Cheney W., 2003. *Numerical Analysis*. Beijing Machinery Industry Press, Beijing.
- Li, F., Wen, H., Chen, X., 2010. Explicit formula of hydraulic; calculation of U-shaped channel. *Advances in Science and Technology of Water Resources*, 30, 1, 65–67. (In Chinese.)
- Liu, S., Xue, J., 2016. Theoretical analysis and numerical simulation of mechanical energy loss and wall resistance of steady open channel flow. *Journal of Hydrodynamics*, 28, 3, 489–496.
- Sabnis, S.V., Agnihothram, G., 2006. Application of arithmetic-geometric mean inequality for construction of reliability test plan for parallel systems in the presence of covariates. *Economic Quality Control*, 21, 2, 219–230.
- Swamee, P.K., 1993. Critical depth equations for irrigation canals. *Journal of Irrigation and Drainage Engineering*, ASCE, 119, 2, 400–409.
- Swamee, P.K., Rathie, P.N., 2005. Exact equations for critical depth in a trapezoidal canal. *Journal of Irrigation and Drainage Engineering*, ASCE, 131, 5, 474–476.
- Swamee, P. K., Wu, S., Katopodis, C., 1999. Formula for calculating critical depth of trapezoidal open channel. *Journal of Hydraulic Engineering*, ASCE, 125, 7, 785–786.
- Vatankhah, A.R., 2013. Multiple critical depth occurrence in two-stage cross sections: effect of side slope change. *ASCE Journal of Hydrologic Engineering*, 18, 6, 722–728.
- Wang, Z., 1998. Formula for calculating critical depth of trapezoidal open channel. *Journal of Hydraulic Engineering*, ASCE, 124, 1, 90–92.
- Wu, C., 2008. *Hydraulics (Vol. 1)*. Beijing Higher Education Press, Beijing. (In Chinese.)
- Zhang, Z., Li, R., 2012. Research on critical water depth, Froude Number and hydraulic jump of U-shaped channel. *Journal of Xi'an University of Technology*, 28, 2, 198–202. (In Chinese.)
- Zhao, Y., Zhu, H., Song, S., 2009. Discuss on accurate calculation formula of critical depth of open trapezoidal channel. *Journal of Yangtze River Scientific Research Institute*, 2009, 04, 18-21+47. (In Chinese.)

Received 23 October 2017
Accepted 13 December 2017

Application and comparison of NSGA-II and MOPSO in multi-objective optimization of water resources systems

Ali Hojjati¹, Mohsen Monadi^{2*}, Alireza Faridhosseini¹, Mirali Mohammadi³

¹ Department of Water Engineering, Faculty of Agriculture, The Ferdowsi University of Mashhad, Iran.

² Department of Civil Engineering, Faculty of Engineering, Urmia University, P O Box 165, Urmia 5756115311, Iran.

³ Department of Civil Engineering (Hydraulic Structures & River Mechanics), Faculty of Engineering, Urmia University, Iran.

* Corresponding author. E-mail: mohsen.monadi@gmail.com

Abstract: Optimal operation of reservoir systems is the most important issue in water resources management. It presents a large variety of multi-objective problems that require powerful optimization tools in order to fully characterize the existing trade-offs. Many optimization methods have been applied based on mathematical programming and evolutionary computation (especially heuristic methods) with various degrees of success more recently. This paper presents an implementation and comparison of multi-objective particle swarm optimization (MOPSO) and non-dominated sorting genetic algorithm II (NSGA-II) for the optimal operation of two reservoirs constructed on Ozan River catchment in order to maximize income from power generation and flood control capacity using MATLAB software. The alternative solutions were based on Pareto dominance. The results demonstrated superior capacity of the NSGA-II to optimize the operation of the reservoir system, and it provides better coverage of the true Pareto front than MOPSO.

Keywords: NSGA-II; MOPSO; Multi-objective optimization; Flood control; Hydropower.

INTRODUCTION

Numerous engineering optimization problems are so complex and troublesome; therefore they cannot be solved by traditional optimization techniques. The operation of reservoir system is a multi-objective problem and a difficult task to estimate reservoir operation policies that maximize all the benefits supplied by these reservoirs and also minimize their invisible impacts. The curse of dimensionality is a common problem for classical methods, especially for four reservoir systems and more. Complexity of the optimization model of multi-objective operation systems is the main cause of more interest in the use of heuristic methods among researchers, because these methods are able to find appropriate responses even when functions are non-linear, discontinuous and non-derivable.

Over the past years, several optimization techniques and multi-objective evolutionary algorithms have been developed and applied to optimize reservoir operation. These include Linear Programming (LP add 1 reference); Nonlinear Programming (NLP add 1 reference); Dynamic Programming (DP add 1 reference); Stochastic Dynamic Programming (SDP add 1 reference); Multi-objective differential evolution algorithm (MDEA); and Heuristic Programming such as Genetic Algorithm (GA) and Particle Swarm Optimization (PSO) analyze multi-objective optimization problems and provide useful insight about solutions that are generated using a population-based approach. Schaffer (1985) proposed an extension of the simple GA (SGA) to accommodate vector-valued fitness measures, which he called the Vector Evaluated Genetic Algorithm (VEGA). After him, several researchers have been studying in this field and different methods with different capabilities were developing that many of them were presented in an overview and tutorial by Konak et al. (2006). NSGA-II was developed by Kalyanmoy et al. (2002) and till date several variants and applications for NSGA II have been developed (Chang and Chang, 2009; Ishibuchi et al., 2008; Malekmohammadi et al., 2011). Kalyanmoy and Jain (2012) proposed and applied MO-NSGA-II to a number of many-objective test problems with

three to 10 objectives (constrained and unconstrained) and compared with a recently EMO algorithm (MOEA/D, add reference). The results reveal difficulties of MOEA/D in solving large-sized and differently-scaled problems, whereas MO-NSGA-II was reported to show a desirable performance on all used test-problems. An improved MO-NSGA-II with enhanced mating selection was used for many-objective optimization by Chen and Chiang (2014). Rio et al. (2010) applied an improved NSGA-II based on a novel ranking scheme to the problem of classifying types of leukemia based on microarray data. Results of comparative tests showed that the improved algorithm performs well on large populations.

MOPSO was proposed by Moor and Chapman (1999) to optimize more than one objective functions and till now many variants and applications for MOPSO have been developed. Baltar and Fontane (2006a, 2006b) have been used MOPSO variant to minimize deviations from outflow water quality (targets of: temperature, dissolved oxygen, total dissolved solids and pH). They also presented an application of an evolutionary optimization algorithm for multi-objective analysis for reservoir operations and planning. Reddy and Kumar (2007, 2009) presented and applied Elitist-Mutation operator with MOPSO (EM-MOPSO) to find minimization of the sum of squared deviations for irrigation, maximization of hydropower production and satisfaction level of downstream river water quality requirements. Also, they used an Elitist-Mutated MOPSO (EM-MOPSO) to maximize hydropower production and minimize annual sum of squared of irrigation release from demands. Shuai et al. (2012) applied modified MOPSO to minimize highest water level, releasing peak discharge, difference of water level after flood season and flood control level. Eberhart and Kennedy (1995) introduced a new form of particle swarm optimizer. Ostadrahimi et al. (2011) improved the performance of the standard particle swarm optimization algorithm and incorporated a new strategic mechanism called multi-swarm algorithm and used for multi-objective reservoir operation rules. Fallah-Mehdipour et al. (2011) presented three multi-objective optimization methods based on multi-objective parti-

cle swarm optimization (MOPSO) algorithm. To evaluate these methods, they considered bi-objective mathematical benchmark problems. Results show that all proposed methods are successful in finding near-optimal Pareto fronts. Yang (2012) proposed a new particle swarm optimization algorithm solving hierarchy multi-objective problems and applied it to optimize the operation of hydropower stations. However, some other extensive reviews of different available techniques can be found elsewhere (Adeyemo, 2011; Ajibola and Adewumi, 2014; Bianchi et al., 2009). Kumar and Minz (2014) provided a proper concept of particle swarm optimization and the multi-objective optimization problem in order to build a basic background with which to conduct multi-objective particle swarm optimization. Patil and Dangevar (2014) presented a comprehensive review of a multi-objective particle swarm optimization (MOPSO) reported in the specialized literature. Yusoff et al. (2011) proposed an overview on NSGA-II optimization techniques of machining process parameters. Based on the above techniques, in this paper, application of NSGA-II and MOPSO algorithms in operation of two-reservoir systems to maximize incomes due to the hydropower sale and flood control is proposed.

MATERIALS AND METHODS

Multi-objective optimization is an important part of multiple criteria decision making. It has been applied in many fields of science, including engineering, economics and logistics, where optimal decisions need to be taken in the presence of trade-offs between two or more conflicting objectives. In the optimization problems with incomplete data and information or restricted calculation capacity meta-heuristic is a robust procedure (Blum and Roli, 2003). Meta-heuristics sample a set of solutions which is excessively enormous to be entirely demonstrated. In comparison with another optimization algorithms and iterative methods, meta-heuristics do not guarantee a globally optimal solution on some class of problems (Kennedy and Eberhart, 1995). Many meta-heuristics carry out some forms of stochastic optimization, therefore the solution found is conditional on the set of random variables generated. Meta-heuristics can frequently find excellent solutions with less calculative attempt than optimization algorithms, iterative methods, or simple heuristics by searching over a large set of feasible solutions. So, meta-heuristics are applicable methods for optimization problems. Several books and survey papers have been published on the subject. NSGA-II and MOPSO are the well-known meta-heuristic optimization methods for multi-objective optimization in water resource management. For a nontrivial multi-objective optimization problem, there is not a single solution that simultaneously optimizes each objective. Therefore, the objective functions are mentioned to be contradictory, and there are a number of Pareto optimal solutions. If none of the objective functions can be enhanced in value without humiliating some of the other objective values the solution is called non-dominated Pareto optimal. Without extra subjective precedence information, all Pareto optimal solutions are taken into account equally well. The aim is to find a typical set of Pareto optimal solutions, and/or determine the trade-offs in gratifying the distinctive objectives, and/or finding a single solution that satiates the subjective priorities of a decision maker (DM).

Multi-objective particle swarm optimization

Swarm Intelligence (SI) is mainly defined as the behavior of natural or artificial self-organized, decentralized systems.

Swarms interact locally with each other or with external agents, i.e. environment, and can be in the form of bird flocks, ants, bees etc. Introduced by Srinivas and Kalyanmoy (1994) for optimizing continuous nonlinear functions, Particle Swarm Optimization (PSO) defined a new era in SI. PSO is a population based method for optimization. The population of the potential solution is called as swarm and each individual in the swarm is defined as particle. The particles in the swarm search their best solution based on own experience and the other particles of the same swarm. PSO started to hold the grip amongst many researchers and became the most popular SI technique soon after getting introduced, but due to its limitation of optimization only of single objective, a new concept Multi-Objective PSO (MOPSO) was introduced, by which optimization can be performed for more than one conflicting objectives simultaneously. As mentioned, MOPSO was proposed by Moor and Chapman (1999) to optimize more than one objective functions. In MOPSO instead of a single solution a set of solutions are determined, also called Pareto optimal set. The framework of MOPSO is shown in Figure 1.

Non-dominated sorting genetic algorithm-II

NSGA-II is the latter version of the popular “Non-dominated sorting genetic algorithm” developed in 2002 by Srinivas and Kalyanmoy (1994) to solve non-convex and non-smooth single and multi-objective optimization problems. Compared to NSGA it is a useful algorithm which has an improved mating mechanism dependent upon the crowding distance and performs constraints using an adapted explanation of dominance without the use of penalty functions. The population initialization is done as before. At the beginning, a zero level is allocated to all non-dominated individuals. During elimination of the individuals from the population, the lately non-dominated solutions are allocated level one. This procedure goes on up to the time which all solutions have been allocated a non-domination level. Parents selecting process is carried out using binary tournament selection on the basis of the lesser rank and greater crowding distance. The next step includes off-springs generating from the selected population using crossover and mutation operators, which will be discussed in the following. Finally, the present off-springs and population are sorted another time dependent upon the non-domination and just the best individuals with the number of the population size (P). The flowchart of the NSGA-II is shown in Figure 2.

Case study

The two proposed techniques are applied to find non-dominated solutions for the operation of two reservoirs system in the Ozan catchment. Ostoor and Pirtaqi dams are located in the Ozan catchment with longitude coordinate $48^{\circ} 53' 0.59''$ and $41^{\circ} 13' 51.6''$ eastern and latitude coordinate $37^{\circ} 30' 24.7''$ and $37^{\circ} 28' 4.4''$ northern, respectively. Their locations are shown in Figure 3.

The case study includes two consecutive reservoirs with a hydroelectric power plant in the downstream of each dam. The inflow of Pirtaqi dam is equal to the total discharge from the Senghor Chay River, output water from the turbines and overflow from Ostoor dam. A schematic of the optimization problem is shown in Figure 4.

According to the electricity consumption in different seasons, the selling price of electricity in each season is different. So that, in spring and summer due to greater demand, electricity costs will be higher than autumn and winter. On the other hand,

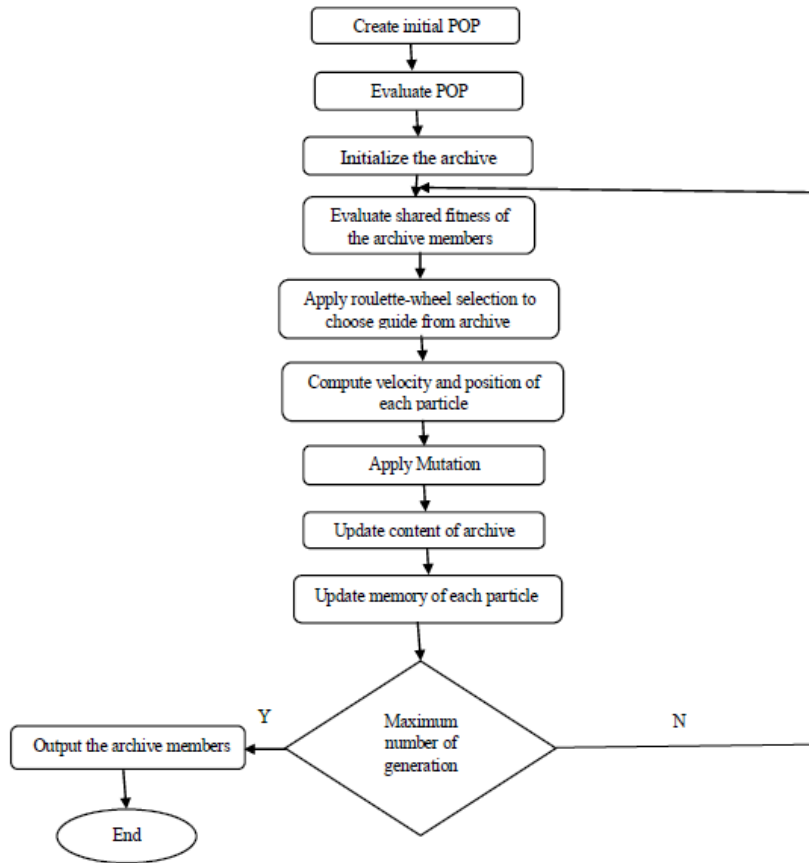


Fig. 1. Flowchart of multi-objective particle swarm optimization.

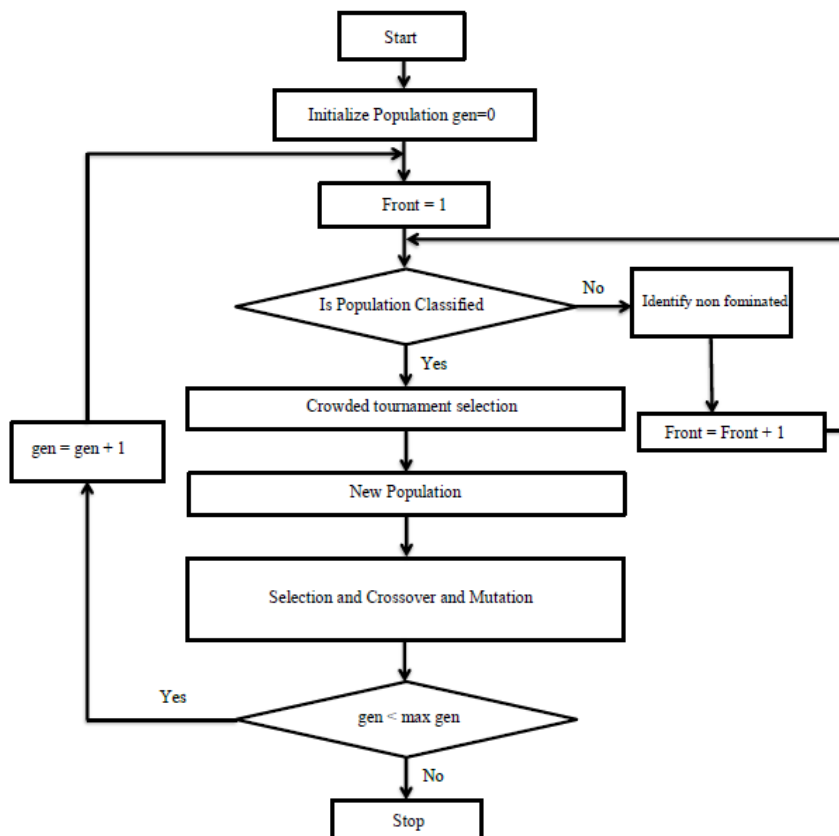


Fig. 2. Flowchart of NSGA-II.

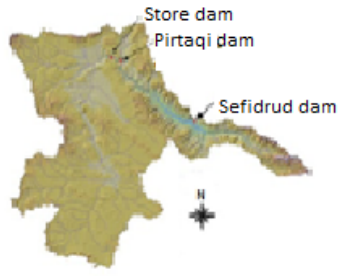


Fig. 3. The position of two reservoirs system.

in February, March, April and May the river inflows into the reservoir have highest discharge so these four months are considered as the flood months. Therefore, because flood control the normal water level should be kept on the lowest level. The objective functions used in the model are as below.

$$f(1) = \text{Maximize} \sum_{i=1}^n \sum_{t=1}^T PWP^t \times PE_i^t \quad (1)$$

$$f(2) = \text{Maximize} \sum_{i=1}^n \sum_{t=1}^T C^t \times (S_i^n - S_i^t) \quad (2)$$

Equations (1) and (2) are for maximization of hydroelectric energy production and flood storage volume, respectively, where T is the time horizon (12 months) of Exploitation model, PWP is proceeds from the sale of a unit of the produced energy in month t in Rial/MWh, C^t is constant coefficient of flood in month t that in the flood months is equal to 1 and in the other months is zero, S_i^n is reservoir volume i at normal level in terms of cubic meters, S_i^t is reservoir volume i in terms of cubic meters in the beginning of the month t , PE_i^t is energy generated in the reservoir i in month t in Watts and n is the number of the under investigation reservoirs.

Constraints used in the model include the following three parts:

a. *Water balance in the reservoir*

$$S_1^{t+1} = S_1^t + I_1^t + P_1^t - E_1^t - R_1^t - Spill_1^t \quad (3)$$

$$S_2^{t+1} = S_2^t + I_2^t + I_3^t + P_2^t - E_2^t - R_2^t - Spill_2^t \quad (4)$$

$$S_{dead} \leq S_t \leq S_{max} \quad (5)$$

where S^t and S^{t+1} are storage of each reservoir at the beginning and end of the time period t , respectively, I_1^t and I_2^t are inflow discharges to the reservoirs, P_1^t and P_2^t are the rainfall over the reservoirs, E_1^t and E_2^t are the evaporation from the reservoirs, R_1^t and R_2^t are the output water of the power plant, $Spill_1^t$ and $Spill_2^t$ are the overflow water from the reservoirs in month t , in reservoir 1 and 2 respectively. Also, I_3^t is the inflow discharge of the SenghorChay River into the reservoir 2 in month t . Equation (5) shows that the storage of the reservoir (S_t) in each time period is limited to the maximum storage (S_{max}) and dead storage (S_{dead}).

b. *Water Release Restrictions*

$$R_{min} \leq R_t \leq R_{max} \quad (6)$$

Equation (6) indicates the restriction on the water releases to the power plants which at R_{min} it is equal to zero and at R_{max} it is equal to 50 m³/s and 40 m³/s for Pirtaqi and Ostor dams, respectively. In this equation, R is water release in m³/s.

c. *Minimum downstream flow to protect the environment*

$$R + Spill \geq MRD \quad (7)$$

Equation (7) indicates the minimum downstream flow to protect the environment where MRD is the minimum requirement of downstream that for each of the reservoir this amount is equal to the highest amount of monthly discharge in the month, that during 42 statistical years, has the lowest average discharge and for Ostor and Pirtaqi reservoirs are 42.85 and 66.96 million cubic meters (MCM), respectively. In this equations (6) and (7) R is water release in m³/s.

Penalty functions

In the restriction of the reservoir balance, the storage of the reservoir (S_t) should not be less than the dead storage of the reservoir (S_{dead}). Also in the restriction of the water releases R_t should be less than R_{min} and in the restriction of the minimum requirements of downstream for environmental issues, the amount should not be less than the minimum flow required for the purpose. If the above conditions are not satisfied the following equations for these restrictions will apply as penalty functions, respectively.

The penalty functions of the storage of water in the reservoirs, water releases to the power plants and the minimum requirements of downstream are as follows.

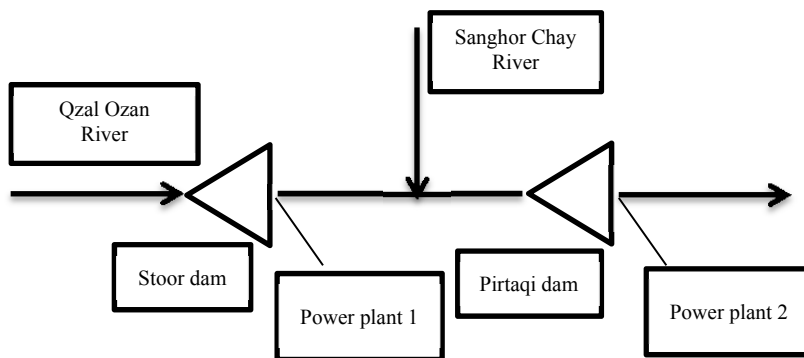


Fig. 4. Schematic of the optimization problem.

$$\text{if } S_t^1 > S_{dead} \rightarrow P_s = I_{t-1}^T \left(1 + K (S_t - S_{dead})^2 \right) \quad (8)$$

$$\text{if } R_t^1 > R_{min} \rightarrow P_R = I_{t-1}^T \left(1 + K (R_t - R_{min})^2 \right) \quad (9)$$

$$\text{if } R_t + Spill_t^1 > MRD \rightarrow P_R = I_{t-1}^T \left(1 + K (R_t - R_{min})^2 \right) \quad (10)$$

where P_s is the penalty function for storage and P_R is the penalty function for release and coefficient K is penalty coefficient and has a large scalar value as $1 \times e^{10}$ which in case of nonconformity of the constraints of the model, and considering that the algorithm is seeking to minimize the objective functions, is added to the objective functions. This amount is large enough that the probability of the member presence in the next generations come down certainly and eliminated practically. All of the variables are explained before.

RESULTS AND DISCUSSION

Non-dominated sorting genetic algorithm II (NSGA-II)

The objective functions for NSGA-II are as equations (11) and (12).

$$f(1) = \text{Minimize} - \left(\sum_{i=1}^n \sum_{t=1}^T PWP^t * PE_i^t \right) \quad (11)$$

$$f(2) = \text{Minimize} - \left(\sum_{i=1}^n \sum_{t=1}^T C^t * (S_i^n - S_i^t) \right) \quad (12)$$

To optimize the objective functions, each chromosome is made of 24 genes, one month time period and planning of the reservoir operation for a year are considered and the population size is equal to 20. At the first, the initial population is simulated and their fitness function determined which is called parent population. Then the parents are placed in case of pair in 15 mating pools. Selection of being pair or the number of mating pools that are often equal to half of the initial population, can be different. In this study tournament selection, with size 2 is used. Then, based on the superiority of rank and fitness between both parents who placed in the pool, crossover and mutation operators are applied on the pair of them. In the NSGA-II a crossover operator called SBC, which is a search engine similar to dual single point crossover, has been used. According to the mentioned crossover and mutation operators, we considered $P_{mutation} = 0.1$, $P_{crossover} = 0.9$, mutation distribution parameter = 50 and crossover parameter = 3. After trial and error, the number of generations produced in the model, which is also considered as stop condition, is equal to 400 generations.

Multi-objective particle swarm optimization (MOPSO)

In this study, maximum number of iteration was considered as stop condition for the MOPSO algorithm. Before setting the parameters of the algorithm, determination of the initial population size is very important to start the algorithm. Therefore, at the first step five different population sizes of 20, 50, 100, 150 and 200 were considered and population size of 200 showed the greatest benefit for objective functions. The input parameters taken for determination of the size of the population are as follows: $C_1 = C_2 = 2$, $w_{damp} = 0.99$, $w = 0.8$, $\gamma = 2$ and $\beta = 2$. Then considering the population size of 200, the inertia coefficient in the range of 0.4 to 0.9 was evaluated, which $w = 0.5$

has been earned the most benefit in the objective functions. With regard to the optimal size of the population and inertia coefficient (w), optimal amount of individual learning coefficient C_1 and global learning coefficient C_2 are equal to 1.5 and 2, respectively. And the other parameters such as inertia weight damping ratio (w_{damp}) and selection pressures (γ and β) were constant according to the past experiences and after applying many changes in the population and parameters and run the algorithm for many times, the best answer was obtained. The appropriate distribution at Pareto front and the maximum value of the objective function are considered as the criteria to determine the optimum solution.

Finally, MOPSO and NSGA-II have been applied with 400 iterations and 400 generations as stop conditions, respectively. The Pareto fronts of both models are shown in Figures 5 and 6 and the solutions for both models are extended as well as in a narrow range of values of the objective functions. In these Figures the reason of the difference between Pareto curves from the two methods is because of the minimization of the objective function multiplied by the negative sign in the NSGA-II model, and as it can be seen from Figure 5 the values are negative.

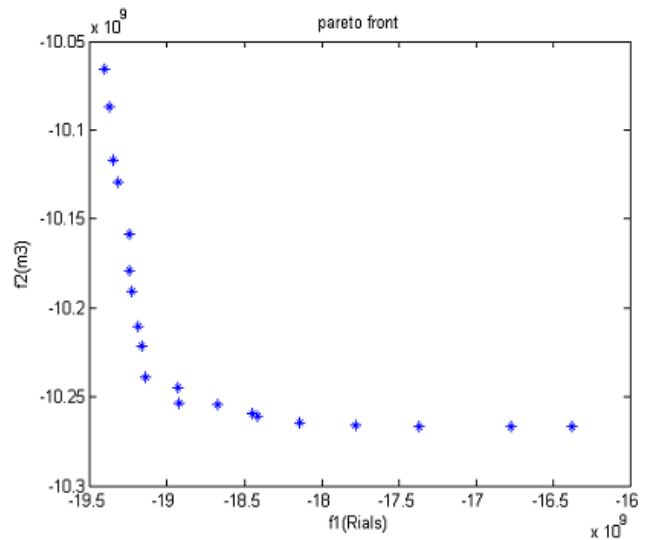


Fig. 5. Pareto optimal points obtained by NSGA-II model.

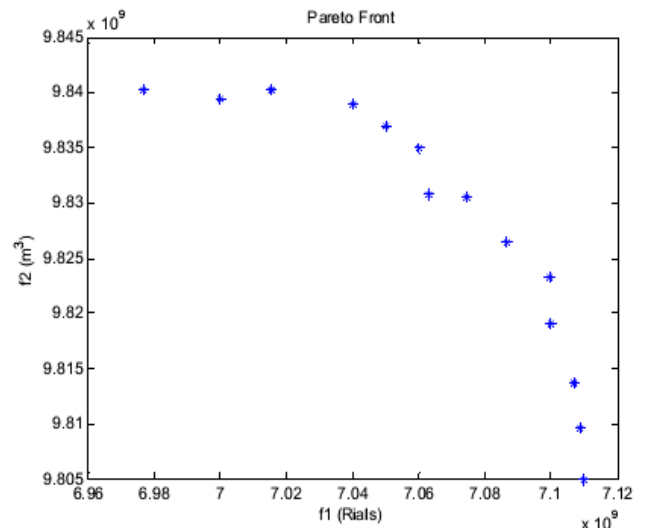


Fig. 6. Pareto optimal points obtained by MOPSO model.

In the NSGA-II model and in power plant of Ostoos (Pirtaqi) reservoir, the highest income and the lowest income are obtained in August and March (February), respectively. In the MOPSO model in Ostoos (Pirtaqi) reservoir, the highest and lowest incomes are obtained in July–August and February–March, respectively. There is more demand for electricity in summer than in winter, thus there is more need to produce energy in summer than in winter. So, the obtained income in both methods in summer is more than in winter. The price of each unit of energy and the total income in each month is pro-

vided in Tables 1 and 2, respectively.

Considering the second objective function that maximizes storage of the reservoir in the flood months, it should be noted that in February to May and in each of Ostoos and Pirtaqi reservoirs, the volume of the reservoir is kept empty in order to control the likely floods (Tables 3 and 4 for both models).

The results of the two algorithms are presented and compared in Table 5, which demonstrated the superior capacity of the NSGA-II for optimizing the operation of the reservoir system than MOPSO algorithm.

Table 1. The price of each unit of energy and the total income of each month in the NSGA-II model.

Total income in Pirtaqi reservoir (MRial)	Total income in Ostoos reservoir (MRial)	Selling price of each MWh of energy (MRial)	Month shift this column to the very right
298.65	105.96	0.046	October
299.86	99.88	0.046	November
370.92	144.26	0.046	December
361.34	103.78	0.044	January
287.30	105.95	0.044	February
268.87	96.99	0.044	March
372.25	130.20	0.049	April
555.29	189.02	0.049	May
594.59	213.45	0.049	June
638.15	248.99	0.057	July
593.51	261.43	0.057	August
519.94	228.86	0.057	September

Table 2. The price of each unit of energy and the total income of each month in the MOPSO model.

Total income in Pirtaqi reservoir (MRial)	Total income in Ostoos reservoir (MRial)	Selling price of each MWh of energy (MRial)	Month same as Table 4
288.67	123.77	0.046	October
269.96	89.14	0.046	November
340.86	174.27	0.046	December
324.34	113.53	0.044	January
267.80	115.33	0.044	February
268.77	97.46	0.044	March
372.55	160.25	0.049	April
535.68	199.36	0.049	May
534.27	213.96	0.049	June
628.44	248.91	0.057	July
563.72	251.22	0.057	August
529.11	248.39	0.057	September

Table 3. Storage of the reservoir for flood control in the NSGA-II method.

Total storage (Mm ³)	Pirtaqi reservoir (Mm ³)	Ostoos reservoir (Mm ³)	Month shift to the very right
3168.13	550.68	2617.45	February
3178.57	481.32	2697.25	March
2742.36	373.69	2368.67	April
1872.88	32.58	1840.30	May

Table 4. Storage of the reservoir to flood control in the MOPSO method.

Total storage (Mm ³)	Pirtaqi reservoir (Mm ³)	Ostoos reservoir (Mm ³)	Month as above
2978.13	560.68	2417.45	February
3058.57	461.32	2597.25	March
2912.36	343.69	2568.67	April
1675.88	35.58	1640.30	May

Table 5. The results of the two presented algorithms.

MOPSO	NSGA-II	
6.9	8.9	Income from electricity (MRial)
10.62	10.96	Storage of flood control (Gm ³)

CONCLUSION

In this paper we applied and compared NSGA-II and MOPSO algorithms for optimization of a system operation with two reservoirs. According to the results, it can be concluded that according to the stop conditions, which is the same for the two algorithms, the NSGA-II is performed better than the MOPSO algorithm. And according to Table 5 it can be seen that the income from electricity and storage of flood control increased by: 22% and 3%, respectively, using NSGA-II.

Some of the most important factors involved in this superiority are mutation operator and appropriate distribution of the population that prevented entrapment of the algorithm in local optimum points. The crowding distance operator for NSGA-II during the selection had a very good performance and the population diversity in different generations was well preserved. It is suggested that the proposed NSGA-II be used to optimize multi-objective system operation with more reservoirs.

REFERENCES

- Adeyemo, J.A., 2011. Reservoir operation using multi-objective evolutionary algorithm – A review. *Asian Journal of Scientific Research*, 4, 1, 16–27. DOI: 10.3923/ajsr.2011.
- Ajibola, A.S., Adewumi, A.O., 2014. Review of population based meta-heuristics in multi-objective optimization problems. *International Journal of Computing, Communications & Instrumentation Engineering (IJCCIE)*, 1, 1, 126–128.
- Baltar, A.M., Fontane, D.G., 2006a. A Multi-objective Particle Swarm Optimization Model for Reservoir Operations and Planning. In: *Proceedings of Joint International Conference on Computing and Decision Making in Civil and Building Engineering*, 14–16 June 2006, Montréal-Canada.
- Baltar, A.M., Fontane, D.G., 2006b. A generalized multi-objective particle swarm optimization solver for spreadsheet models: application to water quality. In: *Proceedings of Hydrology Days*, March 2006, Fort Collins, Colorado, USA, 1–12.
- Bianchi, L., Dorigo, M., Gambardella, L.M., Gutjahr, W.J., 2009. A survey on meta-heuristics for stochastic combinatorial optimization. *Natural Computing: An International Journal*, 8, 2, 239–287.
- Blum, C., Roli, A., 2003. Meta-heuristics in combinatorial optimization: Overview and conceptual comparison. *ACM Computing Surveys*, 35, 3, 268–308.
- Chang, L.C., Chang, F.J., 2009. Multi-objective evolutionary algorithm for operating parallel reservoir system. *Journal of Hydrology*, 377, 12–20.
- Chen, S.W., Chiang, T.C., 2014. Evolutionary many-objective optimization by MO-NSGA-II with enhanced mating selection. In: *Proceedings of IEEE World Congress on Computational Intelligence (WCCI)*, pp. 1397–1404.
- Eberhart, R., Kennedy, J., 1995. A new optimizer using particle swarm theory. In: *Proceedings of IEEE Sixth International Symposium on Micro Machine and Human Science*, 4–6 October 1995, Japan.
- Fallah-Mehdipour, E., Bozorghaddad, O., Marino, M.A., 2011. MOPSO algorithm and its application in multipurpose multireservoir operations. *Journal of Hydroinformatics*, 13, 4, 794–811.
- Ishibuchi, H., Tsukamoto, N., Nojima, Y., 2008. Evolutionary many-objective optimization: A short review. In: *Proceedings of IEEE Congress on Evolutionary Computation*, 1–6 June 2008, Hong Kong.
- Kalyanmoy, D., Jain, H., 2012. Handling many-objective problems using an improved NSGA-II procedure. In: *Proceedings of IEEE Congress on Evolutionary Computation (CEC) 2012*.
- Kalyanmoy, D., Agrawal, S., Pratap, A., Meyarivan, T., 2002. A fast and elitist multi-objective genetic algorithm: NSGA-II. *IEEE Transactions on Evolutionary Computation*, 6, 2, 182–197.
- Kennedy, J., Eberhart, R.C., 1995. Particle swarm optimization. In: *Proceedings of IEEE International Conference on Neural Network*, 27 November to 1 December 1995, Perth, WA.
- Konak, A., Coit, D., Smith, E., 2006. Multi-objective optimization using genetic algorithms, a tutorial. *Reliability Engineering and System Safety*, 91, 9, 92–107.
- Kumar, V., Minz, S., 2014. Multi-objective particle swarm optimization: an introduction. *Smart Computing Review*, 4, 5, 335–353.
- Malekmohammadi, B., Zahraie, B., Kerachian, R., 2011. Ranking solution of multi-objective reservoir operation optimization models using multi-criteria decision analysis. *Expert Systems with Applications*, 38, 7851–7863.
- Moore, J., Chapman, R., 1999. Application of particle swarm to multi-objective optimization. Technical report. Department of Computer Science and Software Engineering, Auburn University, Auburn, Alabama, USA.
- Ostadrahimi, L., Mariño, M.A., Afshar, A., 2011. Multi-reservoir operation rules: Multi-swarm PSO-based optimization approach. *Water Resource Management*, 26, 407–427.
- Patil, D.D., Dangewar, B.D., 2014. Multi-objective particle swarm optimization (MOPSO) based on Pareto dominance approach. *International Journal of Computer Applications*, 107, 4, 13–15.
- Reddy, M.J., Kumar, D.N., 2007. Multi-objective particle swarm optimization for generating optimal trade-offs in reservoir operation. *Hydrological Processes*, 21, 21, 2897–2909.
- Reddy, M.J., Kumar, D.N., 2009. Performance evaluation of elitist-mutated multi-objective particle swarm optimization for integrated water resources management. *Journal of Hydroinformatics*, 11, 1, 79–88.
- Rio, G.L., D'Souza, K., Sekaran, C.H., Kandasamy, A., 2010. Improved NSGA-II based on a novel ranking scheme. *Journal of Computing*, 2, 2, 91–95.
- Schaffer, J.D., 1985. Multiple objective optimization with vector evaluated genetic algorithms. In: *Proceedings of the 1st International Conference on Genetic Algorithm and their applications*, 2 April 1985, Hillsdale, NJ, USA.
- Shuai, W., Xiaohui, L., Xiaomin, H., 2012. Multi-objective optimization of reservoir ood dispatch based on MOPSO algorithm. In: *Proceedings of 8th International Conference on Natural Computation*, 29–31 May 2012, China.
- Srinivas, N., Kalyanmoy, D., 1994. Multi-objective optimization using non-dominated sorting in genetic algorithms. *Evolutionary Computation*, 2, 3, 221–248.
- Yang, J., 2012. A new particle swarm optimization algorithm to hierarchy multi-objective optimization problems and its application in optimal operation of hydropower stations. *Journal of Computers*, 7, 8, 2039–2046.
- Yusoff, Y., Ngadiman, M.S., Zain, A.M., 2011. Overview of NSGA-II for optimizing machining process parameters. *Journal of Procedia Engineering*, 15, 3978–3983.

Received 28 December 2016
Accepted 19 September 2017

Laboratory testing of granular kinetic theory for intense bed load transport

Václav Matoušek*, Štěpán Zrostlík

Czech Technical University in Prague, Department of Civil Engineering, Thákurova 7, 166 29 Prague 6, Czech Republic.

* Corresponding author. E-mail: v.matousek@fsv.cvut.cz

Abstract: Collisional interactions in a sheared granular body are typical for intense bed load transport and they significantly affect behavior of flow carrying bed load grains. Collisional mechanisms are poorly understood and modelling approaches seldom accurately describe reality. One of the used approaches is the kinetic theory of granular flows. It offers constitutive relations for local shear-induced collision-based granular quantities – normal stress, shear stress and fluctuation energy – and relates them with local grain concentration and velocity. Depth distributions of the local granular quantities produced by these constitutive relations have not been sufficiently verified by experiment for the condition of intense bed load transport in open channels and pressurized pipes. In this paper, results from a tilting-flume facility including measured velocity distribution and deduced concentration distribution (approximated as linear profiles) are used to calculate distributions of the collision-based quantities by the constitutive relations and hence to test the ability of the kinetic-theory constitutive relations to predict conditions observed in these collision-dominated flows. This test indicates that the constitutive relations can be successfully applied to model the local collisional transport of solids at positions where the local concentration is not lower than approximately 0.18 and not higher than approximately 0.47.

Keywords: Granular flow; Sheet flow; Sediment transport; Grain collision; Tilting flume experiment.

INTRODUCTION

Coarse granular flows carry grains which tend to intensely interact with each other. Depending on the flow conditions, the interactions take the form of either collisions or sliding contact. Typically, the flows tend to form a layered structure composed of a sliding layer in which grains are in virtually permanent contact and of a collisional transport layer in which conveyed grains suffer intense mutual collisions. Examples are coarse slurry flows near the deposition-limit velocity in pressurized pipes (the sliding layer may dominate) or flows with intense transport of coarse sediment in steep-slope mobile-bed streams (the collisional layer dominates). Appropriate modelling of friction and transport conditions is crucial for models predicting the slope of the energy grade line and solids carrying capacity of such flows. Modelling approaches are based either on an employment of integral quantities of the flow or else based on local quantities associated with the internal structure of the flow. In our earlier work, we followed the integral-quantity approach and made suggestions for modelling of solids transport and bed friction in the upper-plane bed regime in pipes and open channels (Matoušek et al., 2013, 2016a).

The sliding mechanism in a granular body is relatively well understood and successfully applied, for instance, in two-layer models of stratified flows in pressurized pipes. The collisional mechanism, however, is much more complex and requires an analysis of relevant quantities at a local level in the flow. Bagnold's pioneering work (Bagnold, 1954) on local granular rheology of solid-liquid mixtures was carried out for very specific conditions and its results do not seem to be directly applicable to collisional flows transporting grains of density different from the carrier density in open channels (Armanini et al., 2005; Hunt et al., 2002) or pipes. It seems more appropriate to base modelling of flows dominated by granular collisions on kinetic theory of granular flows. Kinetic-theory based models are able to predict a layered pattern of the flow and values of relevant flow quantities (Berzi and Fraccarollo, 2013; Capart and Fraccarollo, 2011). Model predictions include integral flow quantities (discharges of solids and mixture, flow depth) and simpli-

fied distributions of solids concentration and velocity. Typically, a kinetic-theory based model assumes certain granular-rheological related conditions at flow interfaces and quantifies the interfacial stresses, concentration, and velocity. Additional equations (momentum balances) are employed to use the interfacial granular quantities for the prediction of thicknesses of the relevant layers. The discharges of solids and mixture are obtained through integration of the velocities and concentrations over the flow depth. The aim of this paper is to employ results of our previous experiments (which include distributions of velocity and concentration) to shed light on the distribution of granular quantities by the constitutive relations within the collisional layer and its consequences for the application of the constitutive relations in this layer for which a big difference in local concentrations at the top and at the bottom of the layer is typical.

MODELLING OF DISTRIBUTIONS IN A COLLISIONAL LAYER

It is typical for the discussed flows that local concentrations and velocities of the grains span a broad range of values over the thickness of the collisional layer. Associated local granular stresses vary considerably with local position within this collisional layer as well.

Kinetic theory of granular flows

Classical kinetic theory (CKT) considers sheared granular bodies, in which grains are supported exclusively by mutual binary collisions. Constitutive relations are formulated for local grain stresses (both normal and shear stresses) and for a kinetic-theory based balance of grain fluctuation energy in the collisional regime.

CKT covers collision-driven transport of grains at low to moderate local concentrations where the granular motions can be considered as uncorrelated. Recently, the kinetic theory was extended (the extended kinetic theory EKT) to also cover correlated motion of grains at high local concentrations. In principle,

EKT modifies the constitutive relations for the condition of the local concentration $c \rightarrow 1$, which a purely theoretical limit as the local concentration of sediment grains hardly exceeds 0.65. The condition is called the dense limit. So far, most kinetic-theory based models for contact-load transport have only considered the uncorrelated grain condition above the base of the deposit (Armanini et al., 2005; Capart and Fraccarollo, 2011; Jenkins and Hanes, 1998; Spinewine and Capart, 2013), only a few models have employed the dense limit using the EKT principle (Berzi, 2011; Berzi and Fraccarollo, 2013).

Principles of granular rheology in kinetic theory

In the kinetic theory of granular flows, the local shear-induced granular normal stress (also called granular pressure in the literature), σ_s , is related to the local concentration of grains, c , and to the local granular temperature, T . This temperature T expresses a measure of local grain velocity fluctuations due to intergranular collisions. A determination of the local T is one of the main challenges associated with an application of the kinetic theory. The local shear induced granular shear stress, τ_s , is also related to c and T at any vertical position y above the bed. Moreover, τ_s is related to the local strain rate γ , i.e. the distribution of u ($\gamma = du/dy$, u = local longitudinal velocity of grains). The kinetic theory introduces the coefficient of wet restitution, e , as an additional parameter affecting the stresses at the local level. Some kinetic theory based models consider $e = 1$ for convenience. Relations based on CKT do not contain any empirical constants. EKT-relations introduce one empirical constant described below.

Constitutive relations

The general forms of the kinetic theory based relations for the local granular normal stress, σ_s , and the granular shear stress, τ_s , due to intergranular contacts read respectively

$$\sigma_s = 4 \cdot \rho_s \cdot f_\sigma \cdot c \cdot G \cdot T \quad (1)$$

$$\tau_s = \rho_s \cdot f_\tau \cdot c \cdot G \cdot \sqrt{T} \cdot \gamma \cdot d \quad (2)$$

In Equations 1 and 2, ρ_s = density of grains, d = grain size, G , f_σ , f_τ = concentration-related functions. Besides the local concentration c , both stresses depend on the granular temperature T , the shear stress is further dependent on the strain rate γ .

In CKT, the concentration-related function

$$G = c \cdot g_0 = c \cdot \frac{2-c}{2 \cdot (1-c)^3} \quad (3)$$

where g_0 = radial distribution function at contact. Relations for functions f_σ and f_τ take different forms in different models in the literature, the most general being those considering e differing from 1,

$$f_\sigma = \frac{1+e}{2} + \frac{1}{4 \cdot G} \quad (4)$$

$$f_\tau = \frac{8}{5 \cdot \sqrt{\pi}} \cdot \left(\frac{1+e}{2} + \frac{\pi}{32} \cdot \frac{[5+2 \cdot (1+e) \cdot (3 \cdot e-1) \cdot G] \cdot [5+4 \cdot (1+e) \cdot G]}{[24-6 \cdot (1-e)^2-5 \cdot (1-e^2)] \cdot G^2} \right) \quad (5)$$

If the assumption of the dense limit in EKT is taken, then $1/G \rightarrow 0$ at $c \rightarrow 1$ and the functions f_σ and f_τ reduce (for the condition $1/G = 0$) to

$$f_\sigma = \frac{1+e}{2} \quad (6)$$

$$f_\tau = \frac{8}{5 \cdot \sqrt{\pi}} \cdot \left(\frac{1+e}{2} + \frac{\pi}{4} \cdot \frac{(3 \cdot e-1) \cdot (1+e)^2}{24-(1-e) \cdot (11-e)} \right) \quad (7)$$

while the G-function expands (because of the g_0 -function expansion) to

$$G = c \cdot \frac{2-c_f}{2 \cdot (1-c_f)^3} \cdot \frac{c_c-c_f}{c_c-c} \quad (8)$$

for $c_f \leq c \leq c_c$, where c_f = freezing concentration and c_c = random close packing concentration (Torquato, 1995).

Defining the granular viscosity as $\eta_s = \tau_s / \gamma$, a local value of η_s is related to local values of the restitution coefficient e , concentration c , and granular temperature T by, $\eta_s = \rho_s \cdot f_\tau \cdot c \cdot G \cdot \sqrt{T} \cdot d$. Another constitutive relation expresses the balance of the particle collisional fluctuation energy. It requires that the gradient of the vertical component of the flux of particle fluctuation energy, Q , balances the net rate of production of fluctuation energy per unit volume of the mixture (Jenkins and Hanes, 1998),

$$-\frac{\partial Q}{\partial y} + \tau_s \cdot \gamma - \frac{24}{\sqrt{\pi}} \cdot \rho_s \cdot c \cdot G \cdot (1-e) \cdot \frac{\sqrt{T^3}}{d} = 0 \quad (9)$$

The first term on the left-hand side of Equation 9 represents the diffusion of fluctuation energy, the second term the production of energy due to shearing, and the third term represents the rate of collisional dissipation, i.e. the fluctuation energy dissipated by interparticle collisions (Armanini et al., 2005). The flux Q is

$$Q = -\frac{4}{\sqrt{\pi}} \cdot \rho_s \cdot f_Q \cdot c \cdot G \cdot \sqrt{T} \cdot \frac{\partial T}{\partial y} \cdot d \quad (10)$$

in which the function f_Q reads

$$f_Q = 1 + \frac{9 \cdot \pi}{32} \cdot \left(1 + \frac{5 \cdot \pi}{12 \cdot G} \right)^2 \quad (11)$$

and in the dense limit $f_Q = 1 + \frac{9 \cdot \pi}{32}$.

EKT handles the problem of one limiting concentration ($1/G \rightarrow 0$, i.e. $c \rightarrow 1$). This problem is relevant to bed load transport as local concentrations near the top of the bed may reach high values of c , although they tend to the bed concentration c_b ($c \rightarrow c_b$, typically $c_b = 0.6$) rather than $c \rightarrow 1$. The bed concentration is affected by the grain shape for instance and may reach c_c as a limit. EKT also employs the dimensionless correlation length L (e.g. Berzi, 2011) as a parameter quantifying the effect of the presence of correlated motion of grains on the collisional energy dissipation,

$$L = \frac{C \cdot \sqrt[3]{G} \cdot \gamma \cdot d}{2 \cdot \sqrt{T}} \quad (12)$$

in which $C =$ material constant of order unity. At any position y within the collisional layer, $L(y) \leq L_{\max}$ where $L_{\max} = 1$ (Berzi, 2011).

An application of the kinetic theory in the bed load transport also encounters a problem of another limiting concentration, namely $c \rightarrow 0$ typical for the region near the top of the collisional layer. At the top of the layer, $c = 0$ and the granular stresses are zero too. The function $G = 0$ and hence both f_{σ} , f_{τ} tend to infinity at the top of the layer. It follows that there must be some non-zero minimum local concentration required to establish the collisional condition expected by the classical kinetic theory.

Momentum balance equations

Alternative equations relating the distribution of the local concentration with the distributions of the granular stresses are based on the principle of momentum balance. In gravity-driven solid-liquid flow with a free surface, the force balance between the driving force and the resisting force assumes that the total shear stress, τ_e (composed of the granular component, τ_s , and the liquid component, τ_f) at each vertical position y balances the longitudinal component of the weight of overlaying burden of liquid and solids,

$$\tau_e = \tau_s + \tau_f = g \cdot \sin \omega \cdot \int_y^H [\rho_s \cdot c + \rho_f \cdot (1 - c)] \cdot dy \quad (13)$$

in which $\rho_f =$ density of liquid, $g =$ gravitational acceleration, $\omega =$ angle of longitudinal slope, and $H =$ total flow depth. The granular component of the total shear stress

$$\tau_s = \rho_s \cdot g \cdot \sin \omega \cdot \int_y^H c \cdot dy + f_D \quad (14)$$

where $f_D =$ the drag force exerted on the grains by the liquid over the depth ($H-y$), and the liquid component

$$\tau_f = \rho_f \cdot g \cdot \sin \omega \cdot \int_y^H (1 - c) \cdot dy - f_D \quad (15)$$

Furthermore, the granular normal stress balances the normal component of the submerged weight of grains above y ,

$$\sigma_s = (\rho_s - \rho_f) \cdot g \cdot \cos \omega \cdot \int_y^H c \cdot dy \quad (16)$$

EXPERIMENTAL DISTRIBUTIONS IN COLLISIONAL LAYER

Experiments

Bed-load transport experiments were conducted using lightweight granular materials in the laboratory tilting flume at the Czech Technical University in Prague. The flume and its measuring equipment are described elsewhere (Matoušek et al., 2016a). The experiments included detailed measurements of longitudinal velocity profiles over the flow depth using different measuring techniques (Pitot tube for liquid velocity, acoustic methods - Acoustic Doppler Velocity Profiler, Ultrasonic Velocity Profiler - for grain velocity). Furthermore, integral characteristics of the flow (flow depth and longitudinal slope, flow rates of both water and grains) were measured and vertical

positions of interfaces in the layered structure of the flow were visually observed (photographed and filmed). We will consider results for one of the tested lightweight granular materials, the fraction of plastic cylinder-shaped grains (equivalent grain diameter $d = 5.41$ mm, $\rho_s = 1307$ kg/m³, code TLT50).

Observed flow structure

Observed flows were steady-state quasi-uniform flows above the upper stage plane bed. The flows tended to be stratified (Figure 1) and composed of up to three distinct layers (water layer, collisional layer and dense sliding layer). The number of layers changed and the thicknesses of the particular layers varied with flow conditions (Matoušek et al., 2016b) depending on a value of the bed shear stress, τ_b , expressed in a dimensionless form as the bed Shields parameter,

$$\theta = \frac{\tau_b}{(\rho_s - \rho_f) \cdot g \cdot d}$$

In most cases, the collisional layer (a layer of colliding grains with an approximately linear velocity profile, Figure 2) dominated over a dense sliding layer (the layer of grains sliding over each other and being in permanent contact with each other between the top of the stationary bed and the bottom of the collisional layer; note that the sliding velocity of grains was negligible compared to velocities in the collisional layer) and occupied a considerable part of the total flow depth H .

Visual observations and measurements of local velocities, u , allowed the layer interfaces to be identified. In Figure 2, the individual layers are identified thus: bed (deposit at positions $y/H < 0$), DL (dense layer), CL (collisional layer), WL (water layer). Figure 2 also shows how the layered structure varied with the bed Shields parameter θ . No DL was observed in TLT50-flows with θ lower than say 0.9.

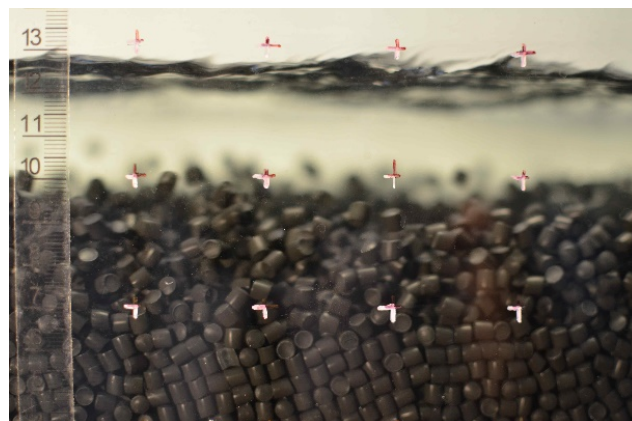


Fig. 1. Layered structure of flow with TLT50-grains (test run TLT50_20150713_3).

An analysis of measured bulk flux of grains and local velocities at the observed interfaces suggested that the local concentration at the bottom of the collisional layer, c_d , was smaller than the bed concentration, c_b , and varied with θ provided that a linear profile was assumed for concentration in CL (Matoušek et al., 2016b). For $\theta < 0.9$, c_d did not exceed approximately 0.47, the condition $c_d = c_b$ was reached at $\theta > 1$.

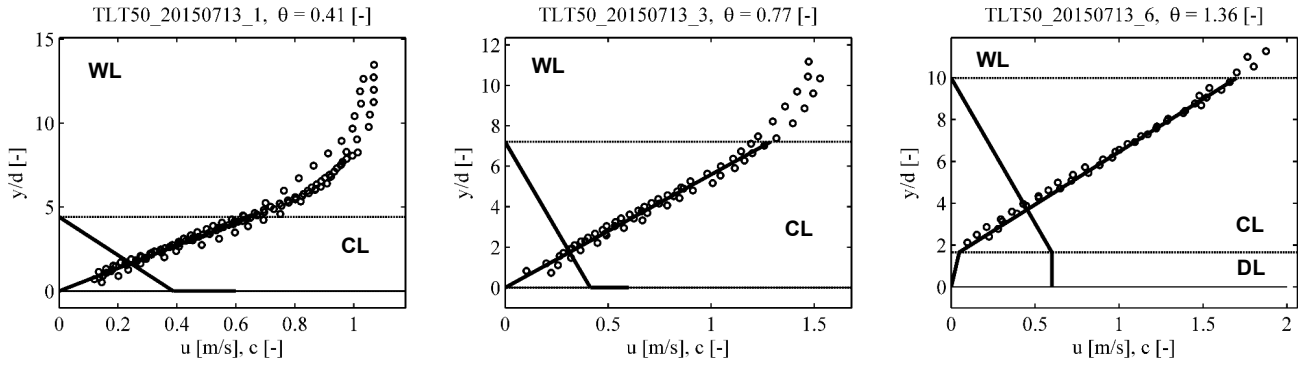


Fig. 2. Observed flow structure in laboratory flume. Legend: \circ = measurements of local velocity u (Pitot tube, Acoustic Doppler Velocity Profiler, Ultrasonic Velocity Profiler); horizontal thin lines = visually observed layer interfaces, DL = dense layer, CL = collisional layer, WL = water layer; thick lines = linear profiles of velocity and concentration based on analysis of experimental data.

DISCUSSION OF DISTRIBUTIONS

An evaluation of a vertical distribution of stresses in CL is pragmatically based on linear distributions of velocities and concentrations across CL. Besides the stress distribution, the evaluation enables stress conditions at the bottom of the collisional layer to be identified, i.e. at the interface with the bed layer, or DL. In this evaluation procedure, we neglect any possible side-wall effect on the stress distribution along a vertical axis of symmetry of the flume cross section.

Relevant information available from experiments

Information on the distribution of concentration (a linear c -profile across CL) enables one to determine the distribution of the total shear stress $\tau_c(y)$ across the entire flow depth H using Equation 13. Also available from the same experimental results is the distribution of the granular normal stress $\sigma_s(y)$ which may be extracted using Equation 16. Direct determination of the granular shear stress $\tau_s(y)$ from the momentum balance is not possible because the experiments provide no information about the local drag force (f_D in Equation 14). Available information on the distributions of c , u , and $\sigma_s(y)$ enable us to evaluate the distribution of local granular shear stress using the constitutive relations (Equations 1 and 2). The use of the momentum-based $\sigma_s(y)$ in Equation 1 produces a corresponding distribution of the granular temperature $T(y)$ and this used as an input to Equation 2 gives $\tau_s(y)$. Furthermore, the processed distributions of $T(y)$ and $\tau_s(y)$ enable evaluation of the distributions of fluctuation energy terms from the third constitutive relation (Equation 9).

Distribution of concentration-related functions

The distributions of G from Equation 3 for CKT and from Equation 8 for EKT are compared in Figure 3. The two distributions diverge considerably at $c > 0.47$, where G by EKT becomes more sensitive to c than G by CKT. In our experiments, the local concentration at the bottom of the collisional layer $c_d > 0.47$ only if the bed Shields parameter was higher than approximately 0.9.

The CKT functions f_σ , f_τ tend to infinity at $c = 0$ and thus their values are extremely sensitive to c in the range of low c values (Figure 4). However, they start converge to the limiting values of f_σ , f_τ given by EKT (i.e. for $c \rightarrow 1$) at c -values much smaller than 1. At the typical value of the bed concentration, $c_b = 0.60$, the difference in f -values between CKT and EKT is negligible and is thus considered negligible at $c = 0.47$ as well.

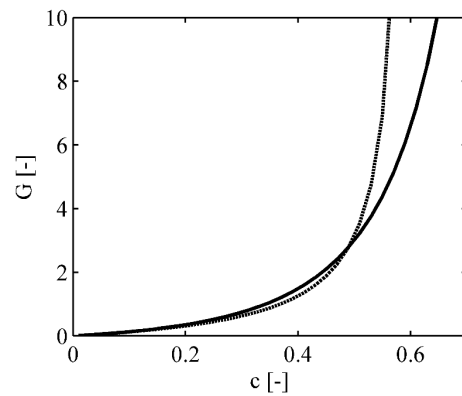


Fig. 3. Concentration-related function for constitutive relations. Legend: solid line = function in CKT (Equation 3); dashed line = function in EKT (Equation 8 for $c_f = 0.49$ and $c_c = c_b = 0.60$).

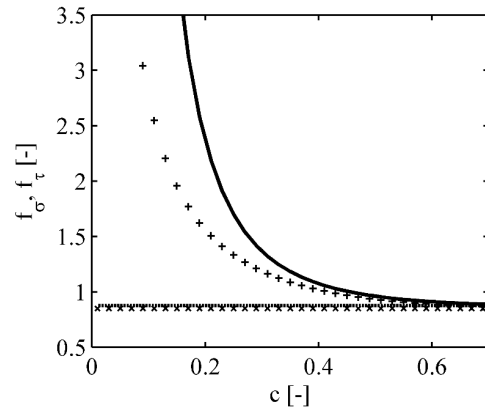


Fig. 4. Concentration-related functions for constitutive relations. Legend: solid line = function for normal stress in CKT (Equations 3–4); dashed line = function for normal stress in EKT (Equation 6 for $e = 0.7$); + = function for shear stress in CKT (Equations 3, 5); x = function for shear stress in EKT (Equation 7 for $e = 0.7$).

To summarize, Figures 3 and 4 show that the G -function is quite sensitive to c in the region of high c values, while f -functions become insensitive to c in the same region. Thus application of the EKT simplifications of the f -functions may not be necessary near the dense limit. On the other hand, the EKT simplification is applicable even if c is smaller than unity and it can simplify calculations at the bottom of CL. The EKT modification of G is essential for our test runs with $c_d > 0.47$, i.e. only for the runs with $\theta > 0.9$.

Distribution of granular temperature

The granular temperature is a key parameter of the kinetic theory as it occurs in all three constitutive relations. However, a direct measurement of the local T is extremely difficult and consequently its measurement is very rare in the literature (Sanvitale and Bowman, 2016).

We determine the distribution of $T(y)$ for the experimentally based linear concentration distribution theoretically using a combination of Equations 1, 3, 4, and 16.

The distribution exhibits a maximum at a position within the collisional layer (Figure 5). T tends to zero at the top of CL and low values at the bottom of CL. In the lower part of CL, damping of T is due to high c which is responsible for a reduction of granular velocity fluctuations. This also explains why the flow of the highest local concentrations (the flow of $\theta = 1.36$) exhibits smaller values of T including the maximum $T(y)$ than the flow of $\theta = 0.77$.

The variation of T with the y within the collisional layer may affect the local coefficient of restitution e and hence local values of granular stresses.

Distribution of shear stress

The procedure described above produces distributions of local granular stresses across the collisional layer. As a result of the CKT-based procedure, the granular component of the total shear stress increases with the depth within CL at the expense of the fluid component of the total shear stress (Figure 6). The fluid component becomes zero at the position where the curve of the total shear stress distribution and the curve of the granular shear stress distribution intersect. Predictions of $\tau_s(y)$ are not

valid at positions below the point of intersection. Figure 6 shows that the position of the point of intersection agrees well with the position of the visually observed bottom of CL provided that c_d does not exceed approximately 0.47 (flows of $\theta = 0.41$ and $\theta = 0.77$). The negligible fluid shear stress is a reasonable assumption for the bottom of the collisional layer and so can be considered reasonable the predictions of the granular stress distributions by the CKT-based formula.

Figure 6 also shows (flow of $\theta = 1.36$) that the curve of predicted granular stresses intersects with the curve of the total shear stress distribution at positions far above the bottom of CL if local concentration in the lower part of CL exceeds 0.47. The point of intersection corresponds with the position at which $c \approx 0.47$, i.e. the value for which the EKT simplifications of the constitutive relations (modifications of functions for G , f_σ , f_τ) are not required. Hence, an application of the modified EKT relations would not improve the results in the sense that it did not provide a position of the point of intersection nearer to the observed bottom of CL.

Distribution of fluctuation energy terms

Distributions of the three terms of the CKT constitutive relation for the collisional fluctuation energy based on earlier determined distributions of c , γ , T , and τ_s are plotted in Figure 7. The distributions suggest that the diffusion term varies very little throughout the collisional layer and although it is important near the top of CL, it is negligible at the lower part of CL if compared to the other two terms. Hence, virtually the entire collisional energy produced by shearing is dissipated in the collision in the lower part of the collisional layer, for the lower Shields-parameter flows.

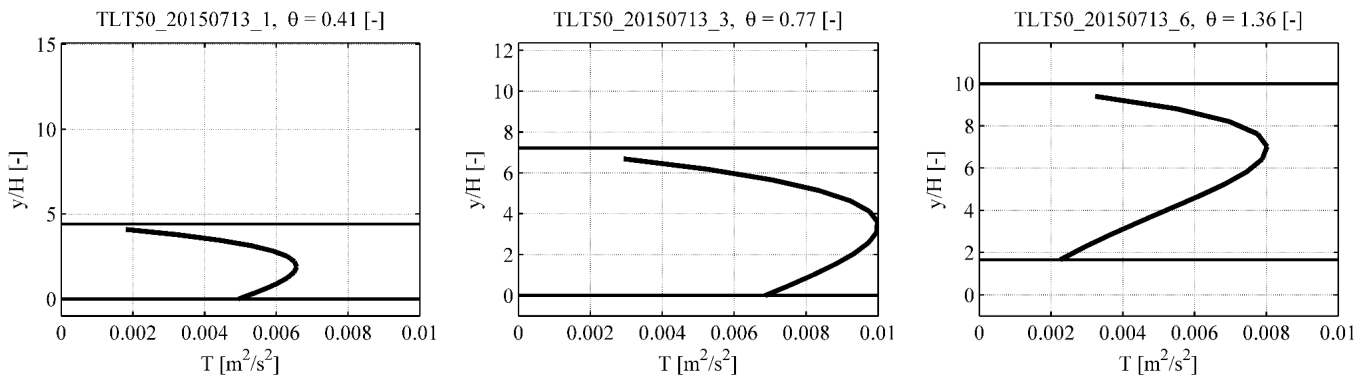


Fig. 5. Distribution of granular temperature in collisional layer. Legend: solid line = T using CKT (Equations 1, 4, 12); horizontal lines = layer interfaces.

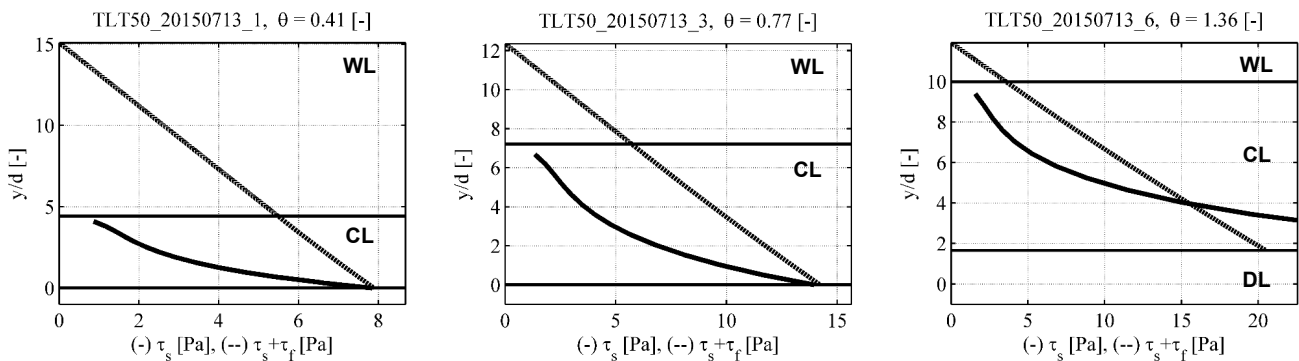


Fig. 6. Distribution of shear stresses in collisional layer. Legend: solid line = granular shear stress using classical kinetic theory (Equations 2, 6, 12); dashed line = total shear stress using momentum balance (Equation 13); horizontal lines = layer interfaces.

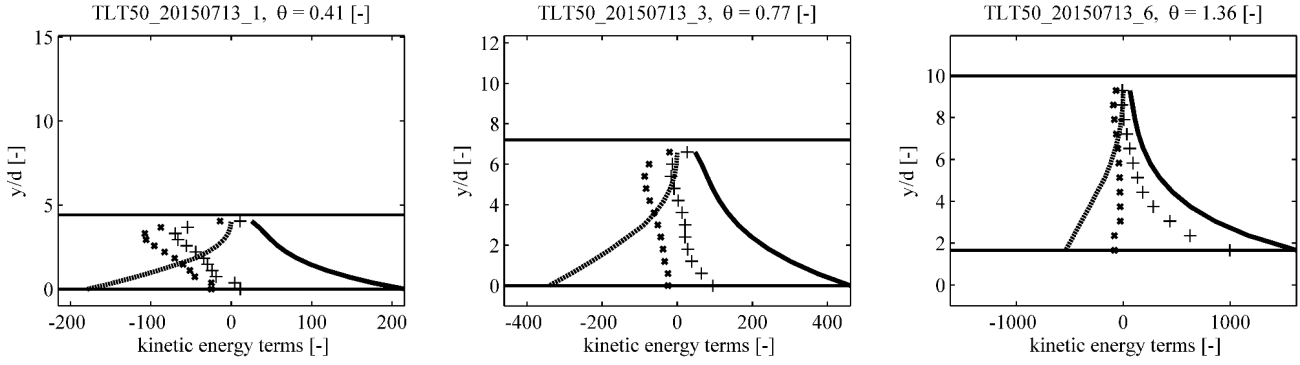


Fig. 7. Distribution of terms of fluctuation energy relation (Equation 9). Legend: solid line = production term (positive values); dashed line = dissipation term (negative values); x = diffusion term; + = sum of three terms; horizontal lines = layer interfaces.

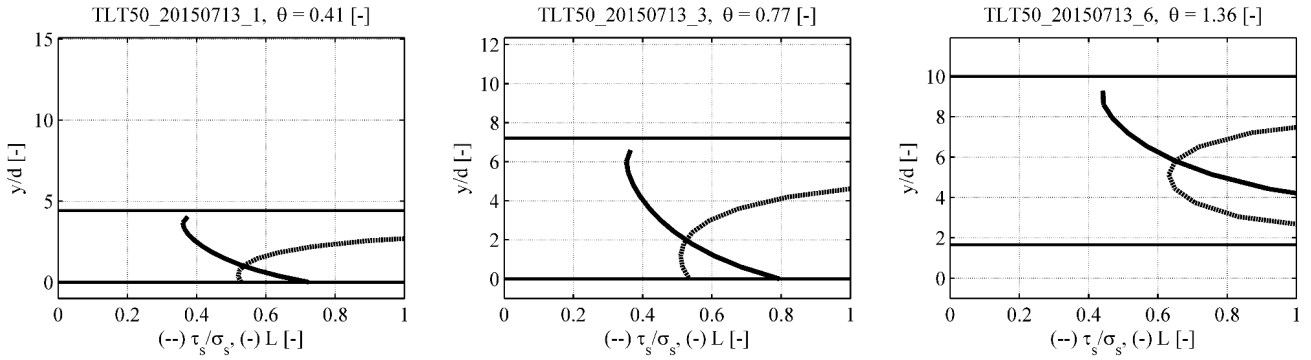


Fig. 8. Distribution of dimensionless correlation length and distribution of granular stress ratio in collisional layer. Legend: solid line = correlation length; dashed line = ratio of granular stresses; horizontal lines = layer interfaces.

However, this does not seem to be the case for the run with the largest Shields parameter ($\theta = 1.36$) where the production is considerably higher than the dissipation at local concentrations exceeding approximately 0.47. Moreover, the relation does not find a balance among the three terms at $c > 0.47$ suggesting that the constitutive relation for CTK is not valid at positions of high c .

Evaluation of criteria/boundaries for application of constitutive relations

In Figure 8, the solid line gives a distribution of L (calculated by Equation 12 for a typical value of $C = 0.7$) across CL showing that L remains below the maximum value of 1 even at the bottom of CL for the two runs with $c_d < 0.47$. For the third run ($\theta = 1.36$, $c_d = c_b$), $L > 1$ in the lower part of CL and L exceeds unity at the virtually same y -position as is the point of intersection of the distributions of the solids shear stress and the total shear stress (Figure 6). The local concentration $c \approx 0.47$ at this y -position.

In order to evaluate the limiting values of c delimiting the concentration range in which the constitutive relations can be applied, it is interesting to evaluate the distribution of the ratio of granular stresses by KT. Equations 1 and 2 give $\frac{\tau_s}{\sigma_s} = \frac{f_\tau}{4 \cdot f_\sigma} \cdot \frac{\gamma \cdot d}{\sqrt{T}}$ which leads to unrealistically high values of

the stress ratio at low c (if $c \rightarrow 0$, then $T \rightarrow 0$ and $f_\tau / f_\sigma \rightarrow \infty$). For the distributions of c and u simplified as linear profiles across the entire CL, the granular stress ratio reaches realistic values smaller than 1 at local c larger than approximately 0.18 only. Hence, this value is considered the minimum c for which

the kinetic theory can be applied (provided that the distributions are assumed linear). At the bottom of CL, the ratio reaches a realistic value corresponding to a value of the Coulombic friction coefficient provided that the local L remains below 1 (i.e. for the two runs with $c_d < 0.47$). For the third run ($\theta = 1.36$, $c_d = c_b$), the stress ratio values are realistic only in the range of y -positions corresponding with the range of c between approximately 0.18 and 0.47.

The correlation length L is related to the granular stress ratio by $L = 2 \cdot C \cdot \frac{f_\sigma}{f_\tau} \cdot \sqrt[3]{G} \cdot \frac{\tau_s}{\sigma_s}$. The term f_σ / f_τ by CTK increases

from zero at $c = 0$ to 0.97 at $c = 0.47$ and remains approximately constant and equal to f_σ / f_τ by EKT at $c > 0.47$. At the y -position with $L = 1$ (and $c \approx 0.47$), the local ratio τ_s / σ_s is still lower than one (see Figure 8 for $\theta = 1.36$). Hence, L exceeds unity due primarily to the extensive increase of G at the lower y -positions with $c > 0.47$. This is another indicator that $c = 0.47$ is a suitable upper limit for an application of the constitutive relations to the conditions considered in this work.

CONCLUSIONS

Constitutive relations of kinetic theory were tested in a collisional layer of intense bed load in a laboratory flume. Kinetic-theory based predictions of depth distributions of grain-related quantities (granular stresses, temperature and collisional energy) were evaluated using results of the bed-load experiments, assuming linear profiles of grain concentration and velocity across the collisional layer. The position of the bottom of the collisional layer resulting from the predicted distributions of shear stress agreed well with the experimentally observed posi-

tion if the local concentration at the bottom of the collisional layer did not exceed approximately 0.47. At positions with the local concentration bigger than 0.47 in the lower part of the collisional layer, the constitutive relations for shear stress and collisional energy failed no matter whether the classical form of the concentration-related functions or the simplified form associated with the extended kinetic theory were used in the constitutive relations. Hence, 0.47 is considered the upper limit of the local concentration of colliding grains to which the constitutive relations can be successfully applied in the conditions given by our experiment. The lower limit of local concentration appears to be approximately 0.18. This limit is based on the obtained distribution of the local ratio of collisional shear and normal stresses by the constitutive relations. The local granular stress ratio must be smaller than 1 and this is not satisfied at positions with $c < 0.18$ in the collisional layers of the observed flows.

Acknowledgement. The research has been supported by the Czech Science Foundation through the grant project No. 16-21421S. An assistance of V. Bareš, J. Hlom, J. Krupička, and T. Pícek with obtaining the experimental results is highly acknowledged.

REFERENCES

- Armanini, A., Capart, H., Fraccarollo, L., Larcher, M., 2005. Rheological stratification in experimental free-surface flows of granular-liquid mixtures. *Journal of Fluid Mechanics*, 532, 269–319.
- Bagnold, R.A., 1954. Experiments on a gravity-free dispersion of large solid spheres in a Newtonian fluid under shear. *Proceedings of Royal Society London, Series A*, 225, 49–63.
- Berzi, D., 2011. Analytical solution of collisional sheet flows. *ASCE Journal of Hydraulic Engineering*, 137, 10, 1200–1207.
- Berzi, D., Fraccarollo, L., 2013. Inclined, collisional sediment transport. *Physics of Fluids*, 25, 106601.
- Capart, H., Fraccarollo, L., 2011. Transport layer structure in intense bed-load. *Geophysical Research Letters*, 38, L20402.
- Hunt, M.L., Zenit, R., Campbell, C.S., Brennen, C.E., 2002. Revisiting the 1954 suspension experiments of R. A. Bagnold. *Journal of Fluid Mechanics*, 452, 1–24.
- Jenkins, J.T., Hanes, D.M., 1998. Collisional sheet flows of sediment driven by a turbulent fluid. *Journal of Fluid Mechanics*, 370, 29–52.
- Matoušek, V., Krupička, J., Pícek, T., 2013. Validation of transport and friction formulae for upper plane bed by experiments in rectangular pipe. *Journal of Hydrology and Hydromechanics*, 61, 2, 120–125.
- Matoušek, V., Bareš, V., Krupička, J., Pícek, T., Zrostlík, Š., 2016a. Experimental evaluation of bed friction and solids transport in steep flume. *Canadian Journal of Chemical Engineering*, 94, 1076–1083.
- Matoušek, V., Bareš, V., Krupička, J., Pícek, T., Zrostlík, Š., 2016b. Structure of flow with intense bed load layer. In: *Proc. Int. Conf. River Flow 2016*, Saint Louis, USA.
- Sanvitale, N., Bowman, E., 2016. Using PIV to measure granular temperature in saturated unsteady polydisperse granular flows. *Granular Matter*, 18, 57.
- Spinewine, B., Capart, H., 2013. Intense bed-load due to a sudden dam-break. *Journal of Fluid Mechanics*, 731, 579–614.
- Torquato, S., 1995. Nearest-neighbor statistics for packings of hard spheres and disks. *Physical Review E*, 51, 4, 3170–3182.

Received 28 December 2017

Accepted 20 February 2018

Assessment of empirical formulae for determining the hydraulic conductivity of glass beads

Jaromír Říha, Lubomír Petrula*, Mario Hala, Zakaraya Alhasan

Faculty of Civil Engineering, Brno University of Technology, Veveří 331/95, 602 00 Brno, Czech Republic.

* Corresponding author. Tel.: +420 541147756. E-mail: petrula.l@fce.vutbr.cz

Abstract: Empirical formulae are often used in practice to quickly and cheaply determine the hydraulic conductivity of soil. Numerous relations based on dimensional analysis and experimental measurements have been published for the determination of hydraulic conductivity since the end of 19th century. In this paper, 20 available empirical formulae are listed, converted and re-arranged into SI units. Experimental research was carried out concerning hydraulic conductivity for three glass bead size (diameters 0.2 mm, 0.5 mm and 1.0 mm) and variable porosity. The series of experiments consisted of 177 separate tests conducted in order to obtain relevant statistical sets. The validity of various published porosity functions and empirical formulae was verified with the use of the experimental data obtained from the glass beads. The best fit was provided by the porosity function $n^3/(1-n)^2$. In the case of the estimation of the hydraulic conductivity of uniform glass beads, the best fit was exhibited by formulae published by Terzaghi, Kozeny, Carman, Zunker and Chapuis et al.

Keywords: Hydraulic conductivity; Empirical formulae; Porosity; Porosity function configuration.

INTRODUCTION

The determination of hydraulic conductivity via field pumping tests may be very costly and time-consuming. At the same time, laboratory testing using permeameters may not be a feasible solution in many cases due to time and cost restrictions. For this reason, in many practical studies, namely in preliminary aquifer assessment (EPG, 2009; Šoltész and Baroková, 2014, etc.), empirical relations appear to be a suitable alternative. However, empirical relations have been derived for specific conditions and have their applicability limits.

The typical form of empirical equations for the determination of hydraulic conductivity comes from dimensional analysis based on the Darcy-Weissbach equation (Kasnow, 2002; Vuković and Soro, 1992). The general problems with the proposed formulae lie in determining the characteristic pore diameter and expressing the effect of soil non-uniformity and the form of the appropriate porosity function which reflects the soil compaction rate.

Probably the first relation was proposed by Hazen (1892). It expresses the simple linear dependence between hydraulic conductivity and soil porosity. In his formula, Hazen did not consider the effect of soil non-uniformity. This is also the case with formulae proposed by Slichter (1899) and Terzaghi (1925). Kozeny (1927) proposed a formula that was modified by Carman (1937, 1939) to become the Kozeny-Carman equation.

Pavchich (VNIIG, 1991), Sauerbrey (1932), Krüger (1918), Kozeny (1953), Zunker (1932), Zamarin (1928), Koenders and Williams (1992), and Chapuis et al. (2005) derived the characteristic pore diameter from the effective grain size d_e and porosity function $\chi(n)$ based on the analysis of typical sphere configurations (VNIIG, 1991). Most authors (Hazen, Slichter, Terzaghi, Beyer, Harleman et al., Chapuis et al., and others) considered d_{10} to be an effective grain diameter, though Sauerbrey and Pavchich preferred d_{17} . Authors like Krüger, Kozeny, Zunker and others calculated the effective grain diameter from the grain size distribution curve. Mallet and Pacquant (1951) published frequently used tables expressing hydraulic conductivity as a function of d_{20} . This dependence was expressed by

the United States Bureau of Reclamation (USBR) engineers via functional dependence.

Other generally less used formulae were proposed by Fair and Hatch (1933), Harleman et al. (1963), Alyamani and Sen (1993) and Chesnaux et al. (2011). The use of these formulae is restricted by their applicability limits.

The aim of the authors was to compare and assess the applicability of selected formulae. Vuković and Soro (1992) and Kasnow (2002) summarized and analysed the most important formulae with the conclusion that even when applying suitable empirical relations to the same soil sample, different resulting hydraulic conductivity values may be obtained. Further research conducted by Odong (2007) was focused on the evaluation and comparison of empirical relations with measured values. Cabalar and Akbulut (2016) measured the hydraulic conductivities of sands of different grain size and shape and compared them with some empirical formulae. Naeef et al. (2017) developed a M5 model tree used to predict hydraulic conductivity based on grain size distribution. An analysis of unconsolidated aquifer materials was performed by Hussain and Nabi (2016). Their aim was to compare seven empirical formulae with experimental data. Rosas et al. (2014) determined hydraulic conductivity from grain size distribution for 400 samples of sediments.

Some of the empirical formulae developed by different authors vaguely define applicability limits via the simple description of material type without any grain size distribution curves or quantification. This often leads to improper use of these equations. In many cases the input parameters (namely the effective grain size) in the empirical formulae need to be expressed in units other than those defined by the SI (e.g. mm, cm), such as hydraulic conductivity in cm/day, m/day, etc.

The objective of this paper is to summarize the most commonly used empirical formulae, convert them strictly into SI units and evaluate their applicability and reliability for glass beads of three different diameters. The assessment of porosity functions is also included in this paper. This analytical approach enables the influence of soil non-uniformity and grain shape to be excluded from the analysis. Moreover, the grain

size is relatively well-defined which is suggested to provide lower uncertainty in resulting hydraulic conductivities when compared with more complex soils.

First, a dimensional analysis was performed, and the dependence between porosity and pore size was established, after which the relation between hydraulic conductivity and porosity was analysed. Second, the determined empirical relations were summarized and converted into SI units. Via laboratory experiments the hydraulic conductivities of glass beads of three different diameters were determined for variable porosity. Finally, the empirical formulae were verified using the results of experimental research.

DIMENSIONAL ANALYSIS

Traditionally, the system of pores was described as the system of parallel tubes oriented in the flow direction, a conception sometimes referred to as the “Hydraulic radius model” (Bear, 1972).

The head loss Δh is defined by the Darcy-Weissbach equation (Vuković and Soro, 1992):

$$\Delta h = \lambda \frac{L}{D} \frac{v^2}{2g}, \quad (1)$$

where L is the tube length, D is the diameter of the tube, v is the cross sectional velocity in the tube, g is the gravitational acceleration, and λ is the coefficient of friction loss, which in the case of laminar flow can be calculated as follows:

$$\lambda = \frac{64}{\text{Re}}, \quad (2)$$

with the Reynolds number Re :

$$\text{Re} = \frac{vD}{\nu}, \quad (3)$$

where ν is the kinematic viscosity.

The hydraulic gradient i along the tube:

$$i = \frac{\Delta h}{L}. \quad (4)$$

After substituting Eqs. (2 to 4) into the Darcy-Weissbach equation (1) and some manipulation, one obtains:

$$i = \frac{32\nu v}{D^2 g}. \quad (5)$$

The average velocity in pores may be expressed using the Darcy law:

$$v = \frac{ki}{n_a}, \quad (6)$$

where n_a is the areal porosity and k is the hydraulic conductivity. Assuming areal porosity n_a is equal to volumetric porosity n (Bear, 1972), and joining Eq. (5) and (6), the hydraulic conductivity may be expressed as:

$$k = \frac{1}{32} \frac{g}{\nu} D^2 n. \quad (7)$$

The tube diameter D has to be substituted by the representative minimum pore diameter $d_0 = D$ (Vuković and Soro, 1992):

$$d_0 = \alpha f(n) d_e, \quad (8)$$

where α is a dimensionless coefficient that depends on the characteristics of the porous medium (structure, grain shape, uniformity, petrographic composition, tortuosity, etc.), $f(n)$ is the porosity function and d_e is the effective grain diameter of the porous medium. Eq. (7) then transforms into:

$$k = \frac{g}{32\nu} \alpha^2 n f^2(n) d_e^2. \quad (9)$$

By introducing $\chi(n) = n f^2(n)$ for the porosity function, Eq. (9) holds:

$$k = \frac{g}{\nu} \beta \chi(n) d_e^2, \quad (10)$$

where β characterizes the properties of the porous medium and includes the constant from Eq. (8). For materials with relatively uniform grain size, such as beads, two theoretical limits to porosity may be identified (Fig. 1) according to the configuration of the grains (Indraratna and Vafai, 1997). The minimum packing corresponds to the void ratio $e_{max} = 0.908$ and maximal achievable porosity $n_{max} = 0.476$ corresponds to the ratios:

$$\frac{d_0}{d_{grain}} = 0.414, \quad \frac{d_{max}}{d_{grain}} = 0.732, \quad (11)$$

where d_{grain} is the diameter of the uniform grain and d_{max} is the maximal pore diameter.

The maximal packing gives $e_{min} = 0.351$, $n_{min} = 0.260$ and the ratios:

$$\frac{d_0}{d_{grain}} = 0.155, \quad \frac{d_{max}}{d_{grain}} = 0.224. \quad (12)$$

Other grain configurations are random and the resulting porosity ranges from 0.260 to 0.476.

For non-uniform materials, Pavchich (VNIIG, 1991) proposed the following relation:

$$d_0 = 0.455 \sqrt{C_U} \frac{n}{1-n} d_{17} \quad (13)$$

where C_U is the coefficient of uniformity, n is porosity and d_{17} is the grain diameter for 17% finer by weight. In the case of a spherical grain material (like glass beads) with $C_U \approx 1$, Eq. (13) can be written as follows:

$$\frac{d_0}{d_{17}} = 0.455 \frac{n}{1-n}. \quad (14)$$

EMPIRICAL FORMULAE

Empirical formulae for the hydraulic conductivity estimate k stem from Eq. (10), while the porosity function is frequently determined from Eq. (13). The following list was assembled via the comparison and critical analysis of the available literature sources. All formulae have been rewritten into dimensional

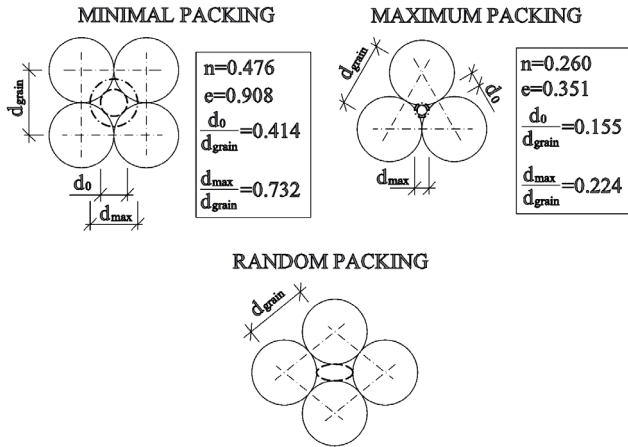


Fig. 1. Schematization of the packing of spherical grains, and possible pore size.

form (10), while the empirical coefficients have been recalculated in order to ensure SI units are used, i.e. grain diameters are expressed in [m] and hydraulic conductivity in [m/s]. The influence of temperature is included in the kinematic viscosity [m²/s].

Hazen (1892)

$$k = \frac{g}{\nu} C_{H,2} [1 + 10(n - 0.26)] d_{10}^2, \quad (15)$$

where d_{10} is the grain diameter for 10% finer by weight and coefficient $C_{H,2} = 6 \times 10^{-4}$. Eq. (15) may be used to estimate the hydraulic conductivity of sand with d_e from 0.1 to 3 mm with the coefficient of uniformity $C_U < 5$.

Slichter's (1899) formula can be used to estimate the hydraulic conductivity of soil with d_e from 0.01 to 5.0 mm:

$$k = \frac{g}{\nu} 0.01 n^{3.287} d_{10}^2. \quad (16)$$

Terzaghi (1925)

$$k = \frac{g}{\nu} C_T \left(\frac{n - 0.13}{\sqrt[3]{1 - n}} \right)^2 d_{10}^2, \quad (17)$$

where C_T depends on the grain shape ($C_T = 10.7 \times 10^{-3}$ for smooth grains and $C_T = 6.1 \times 10^{-3}$ for coarse grains). Eq. (17) may be used for large-grained sands.

Beyer (1964)

$$k = \frac{g}{\nu} C_B d_{10}^2, \quad (18)$$

where C_B is:

$$C_B = 0.0006 \log \frac{500}{C_U}. \quad (19)$$

This formula can be used for soils with $0.06 \leq d_e \leq 0.6$ mm, and with C_U ranging from 1 to 20.

Sauerbrey (1932)

$$k = \frac{g}{\nu} C_Z \frac{n^3}{(1 - n)^2} d_{17}^2, \quad (20)$$

where $C_Z = 3.75 \times 10^{-3}$. Eq. (20) can be used for soils with d_e up to 5.0 mm.

Krüger (1918), Densch et al. (1930), Kasenow (2002)

The Krüger (1918) formula is mentioned in several publications (Densch et al., 1930; Kasenow, 2002; Vuković and Soro, 1992) in a different form. Vuković and Soro (1992) and also Kasenow (2002) mention the following dimensional form:

$$k = \frac{g}{\nu} C_K \frac{n}{(1 - n)^2} d_e^2, \quad (21)$$

where $C_K = 4.35 \times 10^{-3}$, n is porosity and d_e is effective grain defined as follows:

$$\frac{1}{d_e} = \sum_{i=1}^N \frac{2\Delta g_i}{d_i^g + d_i^d}, \quad (22)$$

where Δg_i is the fraction of mass that passes between sieves i and $i+1$ where i is the smaller sieve, and d_i^g and d_i^d are the maximum and minimum grain diameter corresponding to the i -th fraction. Eqs. (21) and (22) can be used for sands of medium grain size with $C_U > 5$, N is the number of fractions.

However, Kasenow (2002) also mentions the form of Eq. (21) with a geometrically justified porosity function corresponding to Eqs. (20), (23), (27) and others. This form exhibits much better agreement with measured values than Eq. (21); see the Discussion section.

Kozeny (1927, 1953)

$$k = \frac{g}{\nu} C_{KO} \frac{n^3}{(1 - n)^2} d_e^2, \quad (23)$$

where $C_{KO} = 8.3 \times 10^{-3}$ and d_e is effective grain size determined as follows:

$$\frac{1}{d_e} = \frac{3\Delta g_1}{2d_1} + \sum_{i=2}^N \Delta g_i \frac{d_i^g + d_i^d}{2d_i^g d_i^d}, \quad (24)$$

with the same notation as in Eq. (22). This formula can be used for coarse-grained sands.

Zunker (1932)

$$k = \frac{g}{\nu} C_{ZU} \left(\frac{n}{1 - n} \right)^2 d_e^2, \quad (25)$$

where C_{ZU} is an empirical coefficient that depends on the porous medium (Table 1), d_e is given by the formula:

$$\frac{1}{d_e} = \sum_{i=1}^N \Delta g_i \frac{d_i^g - d_i^d}{d_i^g d_i^d \ln \frac{d_i^g}{d_i^d}}, \quad (26)$$

Table 1. Empirical coefficient for the Zunker formula (Kasenow, 2002).

Characteristics of the porous medium	$C_{ZU}[-]$
Uniform sand with smooth, rounded grains	2.4×10^{-3}
Uniform composition with coarse grains	1.4×10^{-3}
Nonuniform composition	1.2×10^{-3}
Nonuniform composition, clayey, with grains of irregular shape	0.7×10^{-3}

with the notation from Eq. (22). Eq. (26) can be applied for fine and medium-grained sands.

Zamarin (1928)

$$k = \frac{g}{\nu} C_{ZA} C_n \frac{n^3}{(1-n)^2} d_e^2, \quad (27)$$

where $C_{ZA} = 8.64 \times 10^{-3}$ is the empirical coefficient and C_n is a factor that depends on the porosity:

$$C_n = (1.275 - 1.5n)^2. \quad (28)$$

Effective grain size d_e is given for materials containing grains finer than 0.0025 mm as follows:

$$\frac{1}{d_e} = \frac{3\Delta g_1}{2d_1} + \sum_{i=2}^N \Delta g_i \frac{\ln \frac{d_i^g}{d_i^d}}{d_i^g - d_i^d}, \quad (29)$$

where d_1 is the largest diameter of the finest fraction and Δg_1 is the weight of the finest fraction. For materials that do not contain fractions finer than 0.0025 mm, the effective grain size can be obtained as follows:

$$\frac{1}{d_e} = \sum_{i=1}^N \Delta g_i \frac{\ln \frac{d_i^g}{d_i^d}}{d_i^g - d_i^d}. \quad (30)$$

Eq. (27) can be used for fine and medium-grained sands.

USBR (Mallet and Pacquant, 1951)

$$k = \frac{g}{\nu} C_{US} d_{20}^2, \quad (31)$$

where d_{20} is the diameter of the 20 percentile grain size of the material and C_{US} is:

$$C_{US} = 0.00048(1000d_{20})^{0.3}. \quad (32)$$

The USBR formula, also tabulated by Mallet and Pacquant (1951), is recommended for medium-grained sands with $C_U < 5$.

Pavchich (VNIIG, 1991)

$$k = \frac{0.04}{\nu} \varphi_1 \sqrt[3]{C_U} \frac{n^3}{(1-n)^2} d_{17}^2, \quad (33)$$

where φ_1 is the coefficient depending on the grain size ($\varphi_1 = 1$ for gravel sands, $\varphi_1 = 0.35-0.40$ for gravel), Eq. (33) can be used for grain sizes ranging from 0.06 mm to 1.5 mm.

Seelheim (1880)

$$k = 3570 d_{50}^2, \quad (34)$$

where d_{50} is the diameter of the 50 percentile grain size. The formula was tested on sands, clay and elutriated chalk.

Kozeny-Carman (Carrier, 2003)

The following equation, which depends on the specific surface area of grains, was derived by Kozeny and Carman:

$$k = \frac{g}{\nu} C_{KC} \frac{1}{S_0^2} \frac{n^3}{(1-n)^2}, \quad (35)$$

where $C_{KC} = 480 \pm 30$ is the empirical coefficient, and S_0 is the specific surface of particles (1/m). For uniform spherical grains Eq. (35) can be written as follows:

$$k = \frac{g}{\nu} C_{KC} \frac{6}{d_e} d_e^2 \frac{n^3}{(1-n)^2}, \quad (36)$$

where d_e is the uniform grain diameter (d_{grain}). The formula is not appropriate for clayey soils, but it is applicable for silts, sands and gravel sands.

Harleman et al. (1963)

$$k = 6.54 \times 10^{-4} \frac{g}{\nu} d_{10}^2. \quad (37)$$

Koenders and Williams (1992)

This formula was derived from the Kozeny-Carman equation:

$$k = \frac{1}{\nu} \chi n \left(\frac{n}{1-n} \right)^2 d_{50}^2, \quad (38)$$

where χ is the proportionality coefficient ($\chi = 0.0035 \pm 0.0005$) and d_{50} is the median grain diameter. It is then applicable for silts, sands and gravelly sands.

The following authors used formulae that are rather different in form compared to Eq. (10).

Alyamani and Sen (1993)

$$k = 15046 [I_o + 0.025(d_{50} - d_{10})]^2 \quad (39)$$

where I_o is the intercept point [m] of the line formed by points d_{50} and d_{10} with the grain size axis. The formula can be used for well-distributed samples only.

Chapuis et al. (2005)

$$k = 1219.9 \frac{n^{2.3475}}{(1-n)^{1.565}} d_{10}^{1.565} \quad (40)$$

The formula is applicable for soils with d_{10} ranging from 0.03 to 3 mm.

Fair and Hatch (1933)

$$k = \frac{g}{v} \frac{n^3}{(1-n)^2} \frac{1}{m \left(\frac{\theta}{100} \sum_{i=1}^N \frac{P_i}{d_{mi}} \right)}, \quad (41)$$

where $m = 5$ is the empirically obtained packing factor, θ is the shape factor ranging from 6 to 7.7 (spherical to angular grains), d_{mi} is the geometric mean of the grain fraction, and P_i is the percentage of sand between adjacent sieves determined by the following equation:

$$P_i = 100w_{fi}, \quad (42)$$

where w_{fi} is the weight of the fraction retained on sieve i . For the geometric mean d_{mi} it holds that:

$$d_{mi} = \sqrt{d_{s_i} d_{s_{i+1}}}, \quad (43)$$

where d_{s_i} is the size of the sieve openings for sieve i . This formula is applicable for sands.

NAVFAC DM7 (Chesnaux et al., 2011)

$$k = 0.2272(1.772189 \times 10^{11})^{\frac{n}{1-n}} [d_{10}^{3.31917}]^{\frac{n}{1-n}}. \quad (44)$$

The formula was derived for sands with n ranging from 0.23 to 0.41, C_U ranging from 2 to 12, $d_{10}/d_5 > 1.4$ and d_{10} ranging from 0.1 mm to 2 mm

EXPERIMENTAL RESEARCH

Experiments were carried out in order to verify the porosity function and empirical formulae for uniform material laboratory experiments on glass beads of three different diameters. This experimental research aimed to obtain a sufficient number (at least 50) of hydraulic conductivity measurements for individual glass beads of different diameters with various porosities. The numbers of performed experiments are mentioned in Table 4.

Equipment

The laboratory experiments were performed using a permeameter (plastic cylinder) with upward vertical seepage flow. A permeameter consists of a cylinder containing the sample mounted on a frame. The lower part is connected to a water supply and the upper part is connected to an outlet pipe. Piezometers are located below and above the sample. The seepage flow is generated by a vertically movable water tank that can be adjusted to provide different hydraulic gradients. The movable tank is equipped with a pump that draws water from a storage tank. Water flowing through the permeameter outlet is collected and conveyed back to the storage tank. A schematic diagram of the experimental apparatus is shown in Fig. 2.

Preliminary measurements

A detailed investigation using an electron microscope showed that the sizes of the glass beads did not exactly match the interval declared by the manufacturer. Therefore, bead diameter measurements were conducted using a digital Vernier calliper for each declared (commercial) grain size in order to set up the grain size distribution curves (Fig. 3). The curves pro-

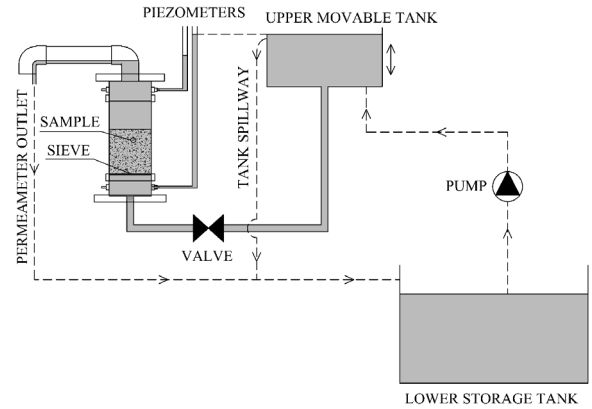


Fig. 2. Schematic diagram of the experimental apparatus.

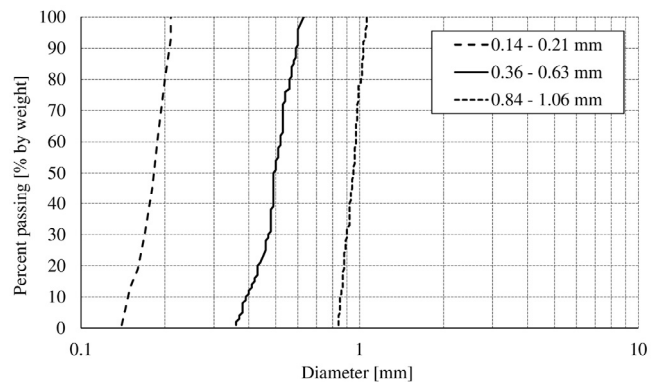


Fig. 3. Grain size distribution curves of the tested glass beads.

vided good fits with the electron microscope and the grain size characteristics were set (Table 3).

Experimental procedure and results

In order to obtain glass bead samples with randomly different porosity, the samples were added to the permeameter via methods involving free fall and compaction by vibration for variable durations. The porosity of each sample was determined by weighing it and then measuring its volume in a Darcy cylinder.

The various piezometric heads (and thus hydraulic gradients) were achieved by gradually raising the upper movable tank (Fig. 2). The seepage discharge was measured each time the tank was raised. In total, 177 laboratory experiments were performed on the glass beads (Table 4).

The dependence of the hydraulic conductivity k on the porosity n was evaluated separately for each bead diameter (Fig. 4). The porosity and hydraulic conductivity ranges are summarized in Table 4. The expected measurement accuracy for individual variables is summarised in Table 5.

COMPARISON OF EXPERIMENTAL RESULTS WITH EMPIRICAL FORMULAE

Comparison of measured porosity with empirical results

First, the porosity functions $\chi(n)$ used in the above-described empirical formulae (Table 2) were analysed. In Fig. 5 the correlation between porosity functions $\chi(n)$ and the ratio between measured hydraulic conductivity and effective grain size (k/d_e^2) is plotted. Only results with a fairly good fit are presented in Fig. 5, those being obtained by Terzaghi (1925), Sauerbrey (1932), Pavchich (VNIIG, 1991) and Chapuis et al. (2005).

Table 2. Summary of empirical formulae.

Number of formula	Author	β	$\chi(n)$	d_e	Use
1	Hazen (1892)	6×10^{-4}	$[1 + 10(n - 0.26)]$	d_{10}	sands, $0.1 \text{ mm} \leq d_{10} \leq 3 \text{ mm}$ $C_U < 5$
2	Slichter (1899)	0.01	$n^{3.287}$	d_{10}	$0.01 \text{ mm} \leq d_{10} \leq 5 \text{ mm}$
3	Terzaghi (1925)	10.7×10^{-3} – smooth grains 6.1×10^{-3} – coarse grains	$\left(\frac{n - 0.13}{\sqrt[3]{1 - n}}\right)^2$	d_{10}	large-grained sands
4	Beyer (1964)	$0.0006 \log \frac{500}{C_U}$		d_{10}	$0.06 \text{ mm} \leq d_{10} \leq 0.6 \text{ mm}$ $1 \leq C_U \leq 20$
5	Sauebrej (1932)	3.75×10^{-3}	$\frac{n^3}{(1 - n)^2}$	d_{17}	$d_{17} \leq 5 \text{ mm}$
6	Krüger (Kasenow, 2002)	4.35×10^{-3}	$\frac{n}{(1 - n)^2}$	Eq. (22)	sands of medium grain size $C_U > 5$
7	Kozeny (1953)	8.3×10^{-3}	$\frac{n^3}{(1 - n)^2}$	Eq. (24)	coarse-grained sands
8	Zunker (1932)	Table 1	$\left(\frac{n}{1 - n}\right)^2$	Eq. (26)	fine and medium-grained sands
9	Zamarin (1928)	8.64×10^{-3}	$\frac{n^3}{(1 - n)^2} (1.275 - 1.5n)^2$	Eq. (29) Eq. (30)	fine and medium-grained sands
10	USBR (Mallet and Pacquant, 1951)	$0.00048(1000d_{20})^{0.3}$		d_{20}	medium-grained sands $C_U < 5$; $T = 15 \text{ }^\circ\text{C}$
11	Pavchich (VNIIG, 1991)	$0.04 \varphi_1 \sqrt[3]{C_U}$	$\frac{n^3}{(1 - n)^2}$	d_{17}	$0.06 \text{ mm} \leq d_{17} \leq 1.5 \text{ mm}$
12	Seelheim (1880)	3570		d_{50}	sands, clay and elutriated chalk
13	Kozeny-Carman (Carrier, 2003)	480 ± 30	$\frac{n^3}{(1 - n)^2}$	d_{grain}	uniform spherical grains
14	Harleman et al. (1963)	6.54×10^{-4}		d_{10}	
15	Koenders and Williams (1992)	0.0035 ± 0.0005	$n \left(\frac{n}{1 - n}\right)^2$	d_{50}	silts, sands and gravelly sands
16	Alyamani and Sen (1993)	15046		I_o, d_{50}, d_{10}	well-distributed sample
17	Chapuis et al. (2005)	1219.9	$\frac{n^{2.3475}}{(1 - n)^{1.565}}$	d_{10}	$0.03 \text{ mm} \leq d_{10} \leq 3 \text{ mm}$
18	Fair and Hatch (1933)	1	$\frac{n^3}{(1 - n)^2}$	$m \left(\frac{\theta}{100} \sum_{i=1}^N \frac{P_i}{d_{mi}}\right)$	sands $m = 5$ $6 \leq \theta \leq 7.7$
19	NAVFAC DM7 (Chesnaux et al., 2011)	0.2272	$(1.772189 \cdot 10^{11})^{\frac{n}{1 - n}}$	d_{10}	$0.23 \leq n \leq 0.41$ $2 \leq C_U \leq 12$ $d_{10}/d_5 > 1.4$ $0.1 \text{ mm} \leq d_{10} \leq 2 \text{ mm}$

Table 3. Grain size characteristics.

Diameter $d_{min} - d_{max}$	d_{10}	d_{17}	d_{20}	d_{60}	$d_{e, Krüger, Zamarin, Zunker}$	$d_{e, Kozeny}$	C_U
	mm	mm	mm	mm			
0.14–0.21	0.16	0.17	0.17	0.19	0.18	0.18	1.19
0.36–0.63	0.39	0.43	0.43	0.52	0.49	0.48	1.33
0.84–1.06	0.85	0.87	0.88	0.97	0.94	0.92	1.14

For each data set a linear relation between the hydraulic conductivity and the porosity function was assumed depending on

Eq. (10). Determination coefficients were evaluated in order to assess the best fit.

Table 4. Summary of performed experiments and the minimum and maximum values of porosity and hydraulic conductivity.

Grain diameter [mm]	Number of experiments	Porosity		Hydraulic conductivity	
		Minimum	Maximum	Minimum	Maximum
0.14–0.21	52	0.377	0.446	0.00416	0.00922
0.36–0.63	53	0.368	0.437	0.00110	0.00220
0.84–1.06	72	0.353	0.416	0.00013	0.00036

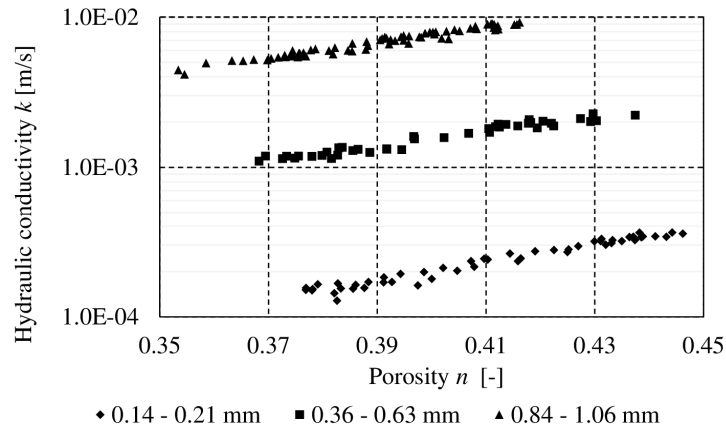
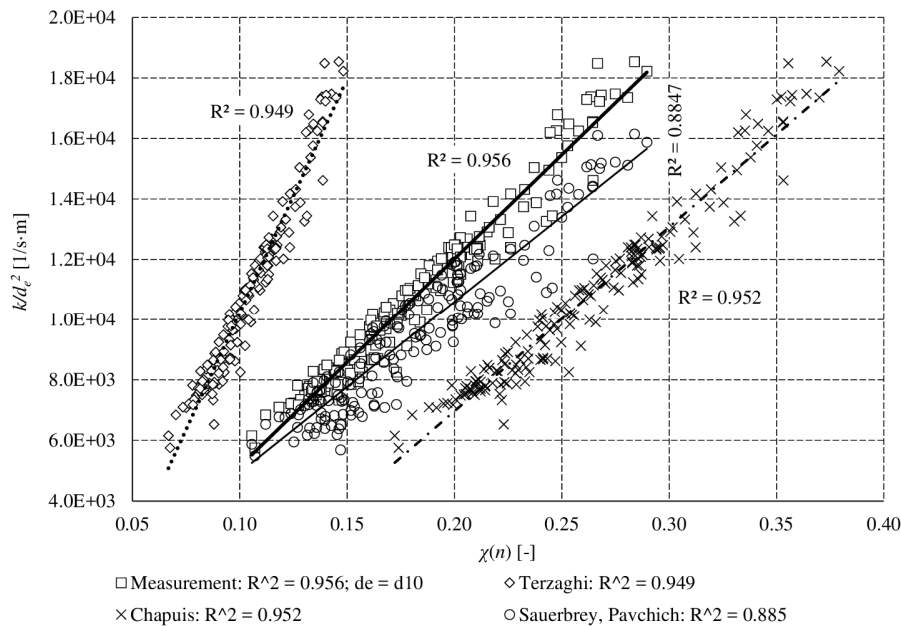

Fig. 4. Dependence of hydraulic conductivity on porosity.

Fig. 5. Correlation between $\chi(n)$ and (k/d_e^2) .

Table 5. Summary of measurement accuracy.

Accuracy of directly measured variables	
Variable	Accuracy
Glass bead diameter	0.01 mm
Weight	0.0001 kg
Permeameter diameter	0.25 mm
Length of sample	0.25 m
Piezometric heights	0.25 mm
Temperature	0.25 °C
Time	0.05 s

The dependence between the most frequently used porosity function from Eq. (10) and the measured hydraulic conductivities and for $d_e = d_{10}$ was added to the graph. This provided the best fit with $R^2 \approx 0.956$. As regards the empirical formulae, the closest values to the measured data were obtained from the Chapuis (2005) and empirical Terzaghi (1925) porosity functions. A relatively good fit was also provided by the geometrically based relation (14) derived by Pavchich (VNIIG, 1991) and Sauerbrey (1932) with $R^2 \approx 0.885$.

Comparison of the measured hydraulic conductivity with the empirical formulae

Figs. 6 to 10 show comparisons of the measured conductivity values with the calculated values gained from the empirical formulas. The ratio k/d_e^2 used in the plots enables the joint comparison of results for all tested bead diameters. This comparison was not performed for formulae that do not meet applicability limits, such as Alyamani and Sen (1993), Fair and Hatch (1933) and Chesnaux et al. (2011).

To quantify the rate of agreement numerically, the sums of the standardised squares of the residuals $\Sigma \varepsilon$ were expressed in Table 6:

$$\Sigma \varepsilon = \sum_{i=1}^N \frac{(k_{i-calculated} - k_{i-measured})^2}{k_{i-measured}^2} \quad (45)$$

where $k_{i-calculated}$ and $k_{i-measured}$ are hydraulic conductivities obtained from empirical formulae and from measurements, respectively, and $N = 177$ is the number of measurements.

DISCUSSION

The analysis of the porosity functions shows that the best fit is provided by a commonly used porosity function based on Eq. (13), or on (14) with the effective grain d_{10} . A quite good fit is also achieved by the dependence proposed by Terzaghi (1925). This is especially true for the measured hydraulic conductivities when $d_e = d_{17}$.

In Figs. 6 to 10 it can be seen that there are considerable differences between the empirical formulae listed above. This is because the individual formulae were derived for specific conditions via different methods. Some are geometrically and physically justified, while others are pure regression dependencies which are not supported by dimensional analysis.

A visual check of Figs. 6 to 10 indicates that for uniform glass beads the best fit with the measured hydraulic conductivities is provided by the formulae published by Terzaghi (Fig. 6), Kozeny-Carman, Zunker (Fig. 8) and Chapuis et al. (Fig. 9). A still reasonable degree of agreement is given by the formulae by Hazen, Zamarin, Sauerbrey and Pavchich.

Table 6. Sums of standardized squared deviations for empirical formulae (ascending order).

Author	Formula number in Table 2	Eq. number	Sum of standardized squared deviations $\Sigma \varepsilon$
Kozeny-Carman (Carrier, 2003)	13	(35)	1.25
Zunker (1932)	8	(25)	1.38
Terzaghi (1925)	3	(17)	1.80
Zamarin (1928)	9	(27)	6.07
Pavchich (VNIIG, 1991)	11	(33)	7.45
Sauerbrey (1932)	5	(20)	7.63
USBR (Mallet and Pacquant, 1951)	10	(31)	16.36
Chapuis et al. (2005)	17	(40)	18.80
Kozeny (1953)	7	(23)	26.47
Harleman et al. (1963)	14	(37)	28.25
Beyer (1964)	4	(18)	30.91
Hazen (1892)	1	(15)	31.60
Seelheim (1880)	12	(34)	46.34
Slichter (1899)	2	(16)	51.29
Koenders and Williams (1992)	15	(38)	145.47
Krüger (Kasenow, 2002)	6	(21)	5284.86

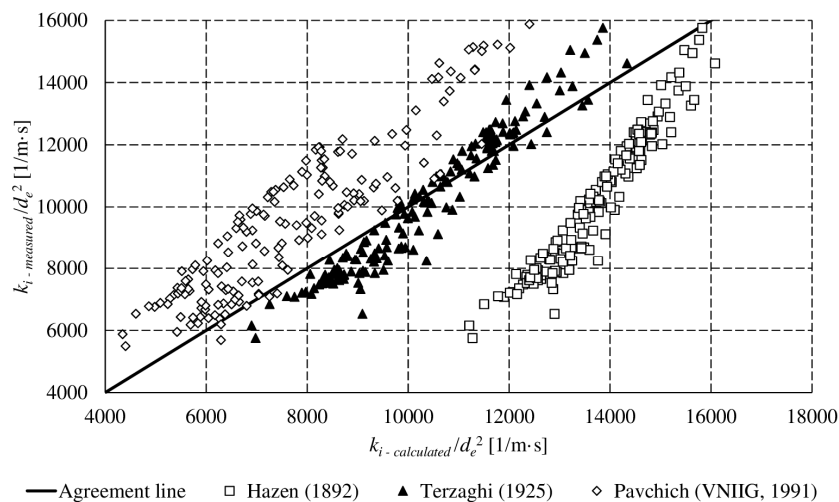


Fig. 6. Comparison of calculated and measured hydraulic conductivity – part 1.

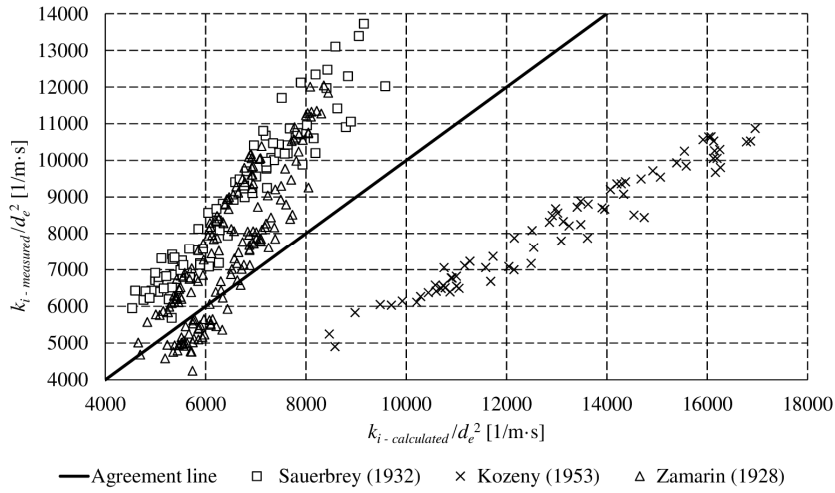


Fig. 7. Comparison of calculated and measured hydraulic conductivity – part 2.

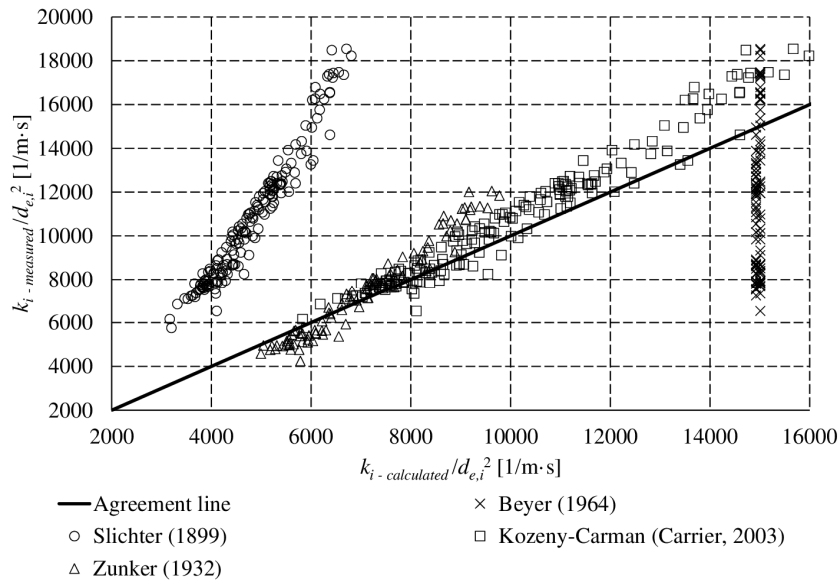


Fig. 8. Comparison of calculated and measured hydraulic conductivity – part 3.

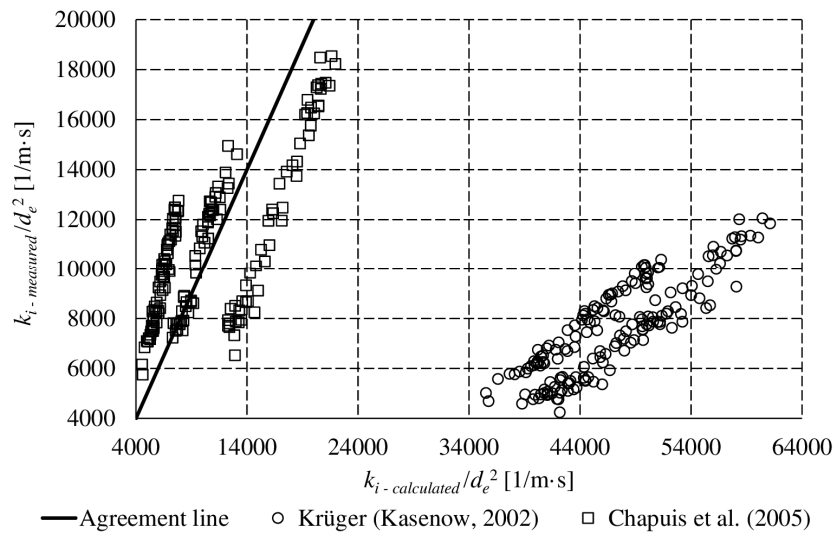


Fig. 9. Comparison of calculated and measured hydraulic conductivity – part 4.

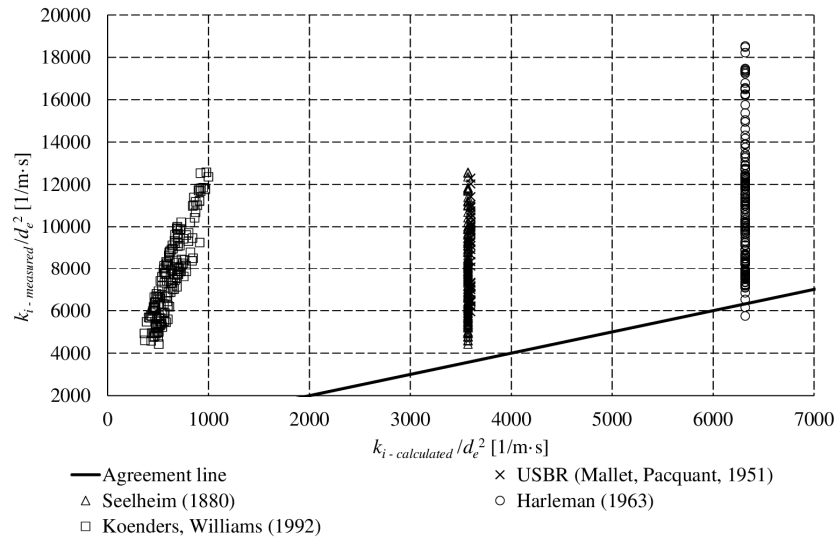


Fig. 10. Comparison of calculated and measured hydraulic conductivity – part 5.

Table 7. – Ratios of calculated and measured values.

Formula number in Table 2	Equation number	Agreement ratio	
		Min. (A_{min})	Max. (A_{max})
1	(15)	0.87	1.98
2	(16)	0.35	0.63
3	(17)	0.78	1.39
4	(18)	0.81	2.30
5	(20)	0.60	0.94
6	(21)	4.85	9.93
7	(23)	1.49	1.75
8	(25)	0.76	1.36
9	(27)	0.67	1.35
10	(31)	0.29	0.60
11	(33)	0.68	1.11
12	(34)	0.28	0.81
13	(35)	0.80	1.24
14	(37)	0.34	1.10
15	(38)	0.07	0.11
17	(40)	0.60	1.98

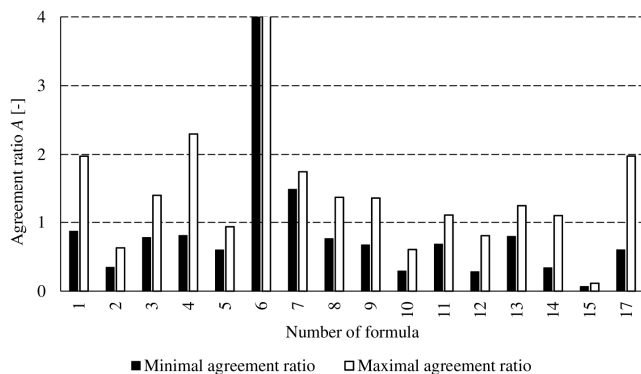


Fig. 11. Minimal and maximal agreement ratios.

In contrast, the worst agreement is provided by the formula derived by Krüger and also formulae which do not take the porosity effect into account, specifically those by Seelheim, USBR, Harleman et al. and Beyer, which show practically no agreement. Interesting results were achieved when the porosity function $n^3/(1-n)^2$ was implemented into the Krüger formula.

The originally poor fit shown in Fig. 9 was significantly improved by this alteration. Other empirical formulae tend to overestimate or underestimate the hydraulic conductivity more significantly in comparison to conducted measurements. To gain an idea about the rate of agreement, the ratios between the calculated and experimentally measured hydraulic conductivity values were computed:

$$A = \frac{k_{emp}}{k_{mea}}, \quad A_{min} = \min(A), \quad A_{max} = \max(A) \quad (46)$$

where A is the agreement ratio, k_{emp} is the hydraulic conductivity obtained from an empirical formula, and k_{mea} is the hydraulic conductivity obtained from measurements. The ratio A was enumerated for all measurements and formulae and its minimum and maximum values were identified for each formula (Table 7, Fig. 11). The best fit is represented by $A = 1.0$.

From the graphs in Figs. 6, 7, 9 two or three slightly different clusters in the term k/d_e^2 may be identified for individual formulae, namely e.g. Hazen (Fig. 6), Zamarin (Fig. 7), Krüger and Chapuis (Fig. 9). This fact may be attributed to the increasing effect of surface tension with decreasing grain size, a factor which is not included in the porosity function. Here, the “effective porosity” (Bear, 1972) should be used instead of “dry” porosity in empirical equations.

CONCLUSION

In the study, empirical formulae for determining hydraulic conductivity were presented and transformed into dimensional form using SI units (m, m/s, etc.). The advisability of using porosity functions in empirical formulae was examined along with their applicability for uniform spherical grains using the results of 177 laboratory tests on glass beads of three different diameters.

The best fit was provided by the geometrically derived porosity function $n^3/(1-n)^2$ based on Eq. (13) when $d_e = d_{10}$ was used. For uniform glass beads the best fit was exhibited by formulae published by Terzaghi (Eq. (17)), Kozeny-Carman (Eq. (36)), Zunker (Eqs. (25, 26)) and Chapuis et al. (Eq. (40)). If applied porosity function $n^3/(1-n)^2$ into the Krüger formula Eq. (21) very good fit with measured values is also achieved.

The comparison shows the increasing effect of surface tension and capillary forces with decreasing grain size. Further research should be focused on this effect and the use of “effective porosity” instead of standard porosity in empirical formulae.

Acknowledgement. This study was conducted as part of the following projects: No. LO1408 AdMaS UP – Advanced Materials, Structures and Technologies; FAST-S-17-4066 The assessment of the filtration instability origin in the soils by the limit state method; and FAST-J-17-4688: Laboratory measurement of internal erosion.

REFERENCES

- Alyamani, M.S., Sen, Z., 1993. Determination of hydraulic conductivity from complete grain-size distribution. *Ground Water*, 31, 4, 551–555.
- Bear, J., 1972. *Dynamics of Fluids in Porous Media*. Elsevier Publishing Company, Amsterdam, 764 p.
- Beyer, W., 1964. On the determination of hydraulic conductivity of gravels and sands from grain-size distribution. *Wasserwirtschaft Wassertechnik*, 14, 165–169. (In German.)
- Cabalar, A.F., Akbulut, N., 2016. Evaluation of actual and estimated hydraulic conductivity of sands with different gradation and shape. *SpringerPlus*, 5, 1, 820.
- Carman, P.C., 1937. Fluid flow through granular beds. *Transactions, Institution of Chemical Engineers*, London, 15, 150–166.
- Carman, P.C., 1939. Permeability of saturated sands, soils and clays. *Journal of Agricultural Science*, 29, 263–273.
- Carrier, W.D., 2003. Goodbye, Hazen; Hello, Kozeny-Carman. *Journal of Geotechnical and Geoenvironmental Engineering*, 129, 11, 1054–1056.
- Chapuis, R.P., Dallaire, V., Marcotte, D., Chouteau, M., Acevedo, N., Gagnon, F., 2005. Evaluating the hydraulic conductivity at three different scales within an unconfined sand aquifer at Lachenaie, Quebec. *Canadian Geotechnical Journal*, 42, 1212–1220.
- Chesnaux, R., Baudement, C., Hay, M., 2011. Assessing and comparing the hydraulic properties of granular aquifers on three different scales. In: *Proceedings of Geohydro 2011*, Quebec City, QC, Canada, 9 p.
- Densch, A., Giesecke, N., Helbig, N., Heß, N., Schubert, N., Zunker, N., 1930. *Die Physikalische Beschaffenheit des Bodens*. Springer Verlag, Berlin. 424 p.
- EPG, 2009. *The sustainable management of groundwater in Canada. Report of the Expert Panel on Groundwater*. ISBN 978-1-926558-11-0. Government of Canada, Ottawa, 254 p.
- Fair, G.M., Hatch, L.P., 1933. Fundamental factors governing the streamline flow of water through sand. *J. Amer. Water Works Assoc.*, 25, 1551–1565.
- Harleman, D.R.F., Melhorn, P.F., Rumer, R.R., 1963. Dispersion-permeability correlation in porous media. *Journal of the Hydraulic Division*, 89, 2, 67–85.
- Hazen, A., 1892. Some physical properties of sand and gravel with special reference to their use in filtration. Rept. Massachusetts. State Board of Health, Boston.
- Hussain, F., Nabi, G., 2016. Empirical formulae evaluation for hydraulic conductivity determination based on grain size analysis. *Int. J. Res. Env. Std.*, 3, 3, 26–32.
- Indraratna, B., Vafai, F., 1997. Analytical model for particle migration within base soil-filter system. *J. Geotech. and Geoenviron. Eng., ASCE*, 123, 2, 100–109.
- Kasenow, M., 2002. *Determination of Hydraulic Conductivity from Grain Size Analysis*. Water Resources Publications, LLC, Highland Ranch, CO, USA, 83 p.
- Koenders, M.A., Williams, A.F., 1992. Flow equations of particle fluid mixtures. *Acta Mechanica*, 92, 91–116.
- Kozeny, J., 1927. Über kapillare Leitung der Wasser in Boden. *Royal Academy of Science, Vienna, Proc. Class I*, 136, pp. 271–306.
- Kozeny, J., 1953. Das Wasser in Boden, Grundwasserbewegung. In: *Kozeny, J. Hydraulik*. Springer, Vienna, pp. 380–445. (In German.)
- Krüger, E., 1918. Die Grundwasserbewegung. *Internat. Mitt. Bodenkunde. Band VIII, Heft 5/6*, pp. 105–122.
- Mallet, C., Pacquant, J., 1951. *Les barrages en terre*. Editions Eyrolles, Paris, 345 p.
- Naeef, M., Naeef, M.R., Salehi, J., Rahimi, R., 2017. Hydraulic conductivity prediction based on grain-size distribution using M5 model tree. *Geomechanics and Geoengineering*, 12, 2, 107–114.
- Odong, J., 2007. Evaluation of empirical formulae for determination of hydraulic conductivity based on grain-size analysis. *The Journal of American Science*, 3, 3, 54–60.
- Rosas, J., Lopez, O., Missimer, T.M., Coulibaly, K.M., Dehwah, A.H.A., Sesler, K., Lujan, L.R., Mantilla, D., 2014. Determination of hydraulic conductivity from grain-size distribution for different depositional environments. *Groundwater*, 52, 3, 399–413.
- Sauerbrey, I.I., 1932. On the Problem and Determination of the Permeability Coefficient. *Proceedings VNIIG, No. 3–5*. (In Russian.)
- Seelheim, F., 1880. Methoden zur Bestimmung der Durchlässigkeit des Bodens. *Analytical and Bioanalytical Chemistry*, 19, 1, 387–418.
- Slichter, C.S., 1899. Theoretical investigation of the motion of ground waters. *U.S. Geological Survey 19th Annual Report, Part 2*. United States Government Printing Office, Washington, DC, USA, 322 p.
- Šoltész, A., Baroková, D., 2014. Analysis of surface and ground water interaction in the Danube river branch system. In: *14th International Multidisciplinary Scientific GeoConference SGEM 2014, Bulgaria, Vol. 1, Issue 3, 2014*, pp. 51–58.
- Terzaghi, C., 1925. *Principles of Soil Mechanics*. Engineering News Record, 95, 832 p.
- VNIIG, 1991. *Recommendations on the Laboratory Methods of Investigation of the Permeability and Filtration Stability of Soils*. P 49-90/VNIIG. The B. E. Vedenev All-Russia Research Institute of Hydraulic Engineering, JSC, Leningrad, 93 p. (In Russian.)
- Vuković, M., Soro, A., 1992. *Determination of Hydraulic Conductivity of Porous Media from Grain-Size Composition*. Water Resources Publications, Littleton, CO, USA, 87 p.
- Zamarin, E.A., 1928. *The Calculus of the Groundwater Flow*. Izd-vo IVCH, Tashkent. (In Russian.)
- Zunker, F., 1932. Fertilization and soil science. *Journal of Plant Nutrition*, A25. (In German.)

Received 20 December 2017

Accepted 12 April 2018

The layering of a mountain podzol can strongly affect the distribution of infiltrated water in the soil profile

Lukáš Jačka^{1*}, Jiří Pavlásek¹, Jana Kalibová², Petr Bašta¹, Martin Kovář¹, Václav Kuráž³

¹ Department of Water Resources and Environmental Modeling, Faculty of Environmental Sciences, Czech University of Life Sciences Prague, Kamýcká 129, Praha 6 - Suchbát, 165 21, Czech Republic.

² Department of Land Use and Improvement, Faculty of Environmental Sciences, Czech University of Life Sciences Prague, Kamýcká 129, Praha 6 - Suchbát, 165 21, Czech Republic.

³ Department of Irrigation, Drainage and Landscape Engineering, Faculty of Civil Engineering, Czech Technical University in Prague, Thákurova 7, Praha 6, 166 29, Czech Republic.

* Corresponding author. Tel.: +420 224 383 827. Fax: +420 234 381 854. E-mail: jacka@fzp.czu.cz

Abstract: The layering of the soil profile can influence the accumulation of infiltrated water and the way in which subsurface runoff is formed. This paper examines a mountain podzol characterized by clearly developed soil horizons. After these horizons had been identified, distinct soil layers were defined (the eluvial horizon, the spodic horizon (undifferentiated), and weathered bedrock). Saturated hydraulic conductivity (K_s), particle size distribution and bulk density were measured in these layers. A visualization of the distribution of infiltrated water in the podzolic profile was performed using a dye tracer experiment. The accumulation of dyed water and a distinct lateral flow were detected in the eluvial layer. Only limited entry of water into the spodic layer was observed. These effects were caused by changes in soil hydraulic properties (SHP) among the investigated layers. For the spodic horizons, the measured K_s value (crucial SHP) was significantly lower than the K_s values for the other tested horizons. The probable reason for the lower K_s was an accumulation of fine particles and various substances in the spodic horizons, and corresponding changes in the porous system. The observed effects of layering indicate that water can be accumulated and subsurface runoff can be formed over the spodic layer during intensive rain or snow melting.

Keywords: Brilliant blue; Guelph permeameter; Field saturated hydraulic conductivity; Infiltration into layered soil; Mountain forest.

INTRODUCTION

The hydrological role of soil for water retention and for transforming precipitation into runoff is pivotal (Kutílek and Nielsen, 1994). Brilliant Blue FCF dye tracer (BB) has become a widely-used and popular tracer for visualizing water flow in a soil profile (e.g. Clark and Zipper, 2016; Kodešová et al., 2012; 2015; Qian et al., 2015; Sander and Gerke, 2007), due to its low toxicity (it is used as a food dye), good colour contrasts in most soils, and its reasonable cost (Laine-Kaulio et al., 2015). Although the dyed soil does not ideally represent the entire flow field, BB provides a useful indication of the preferential flow of the infiltrated water (Leibundgut et al., 2009; Schwen et al., 2014a).

For a physically-based description of soil-water flow, the crucial soil hydraulic parameters (SHP) are saturated hydraulic conductivity (K_s) and the parameters of the retention curve (RETc) (Hillel, 1998; Rezaei et al., 2016). On the basis of knowledge of K_s and RETc, unsaturated hydraulic conductivity can be expressed using an appropriate hydraulic model, e.g. Genuchten – Mualem (van Genuchten, 1980). If this approach is applied, K_s and RETc values enable the water flow in unsaturated soils to be modelled using a numerical solution of the Richards equation (Kutílek and Nielsen, 1994). For sandy soils, pedotransfer functions (indirect methods) based on easily determinable soil properties (texture, bulk density) can be used with sufficient precision for estimating the hydrostatic parameter RETc (Vereecken et al., 2010). For estimates of the dynamic parameter K_s , pedotransfer functions usually exhibit serious errors (see Jarvis et al., 2013), because the value of K_s is very sensitive to specific characteristics of the porous system (e.g.

continuity and tortuosity of the porous system, the occurrence of macropores). Direct measurements of K_s are therefore irreplaceable, although it is a very difficult task to measure K_s properly (Bagarello et al., 2014, 2016; Jačka et al., 2014; Reynolds et al., 2000). The coefficient of variation (CV) of measured K_s within a single soil layer is often higher than 100%, even at the plot scale (Jačka et al., 2016, 2014; Webb et al., 2000). Parameter K_s therefore exhibits high spatial variability (Fodor et al., 2011; Kutílek and Nielsen, 1994), and it is necessary to have a sufficient number of replicates in order to obtain a representative mean value of K_s for each soil layer (Pennock et al., 2008).

Soil layering, which occurs to varying extents in the profiles of most soils, influences the distribution and accumulation of infiltrated water (Huang et al., 2011; Si et al., 2011; Zettl et al., 2011). Knowledge of the SHP of each soil layer is necessary for a correct understanding and for correct modelling of water flow in the layered profile (Shin et al., 2012; Swarowsky et al., 2011). As Schwen et al. (2014b) pointed out, unlike horizontal changes in SHP, vertical changes in SHP have not been sufficiently studied.

For distinctly-layered podzolic soils, possible water accumulation over a less permeable spodic layer is mentioned by Kutílek and Nielsen (1994). This lower permeability arises from an accumulation of fine particles and various substances in the spodic layer, and from a corresponding increase in the tortuosity and decrease in the size of the effective pores (Rezaei et al., 2016; Seuntjens et al., 2001; Wang and McKeague, 1982). However, for mountain podzols, insufficient number of studies (about water flow and accumulation, and changes in the crucial SHP among soil layers) has been reported in the literature.

Moreover, areas dominated by mountain podzols are hydrologically very important, as these areas are characterized by very high average precipitation ($> 1600 \text{ mm year}^{-1}$, Pavlásek et al., 2009). Therefore, these areas have a strong impact on the hydrological situation in lower-located regions during extreme hydrological events (floods and also droughts).

This paper presents a visualization of the distribution of infiltrated water in the profile of a mountain haplic podzol using dye tracer experiments. The results of measurements of the key hydraulic parameter K_s , particle size distribution and bulk density are also presented for identified podzolic layers. The research questions are: 1) Is the flow of infiltrated water affected by the distinct layering of the investigated podzol, and 2) do the values of K_s and related soil properties (texture and bulk density) differ among the identified layers? On the basis of these research questions and the motivation for our study as mentioned above, the following aims of the paper were formulated: 1) Reveal differences in K_s and related soil properties among markedly different podzolic layers. 2) Investigate the effect of this layering on the redistribution of the infiltrated water using dye tracer experiments.

MATERIAL AND METHODS

Study site

The investigation was performed on a study site dominated by a mountain podzol with distinct layers. This site occupies a small part of the Modrava 2 experimental catchment, which is described in Pavlásek et al. (2009, 2010) and in Jačka et al. (2012). The site is located in the high-altitude part of the Šumava National Park, near the Czech-German border (see Figure 1). A description of the site is also given by Jačka et al. (2012, 2014, 2016). The site is covered predominantly with the following plant species: *Calamagrostis villosa*, *Picea abies*, *Avenella flexuosa*, *Vaccinium myrtillus*, *Luzula sylvatica*, *Athyrium distentifolium*.

The study site is an area approx. 60 meters in diameter. The site is characterized by a low slope gradient (mean approx. 4%) with north aspect, and is located in a saddle at an elevation of about 1270 m. The shape of the slope is slightly convex (nearly uniform). Haplic podzol with distinctly differentiated eluvial and illuvial horizons is dominant throughout the site. The soil horizons of the examined podzol are depicted on the vertical cross-section in Figure 2. The mean thicknesses of the soil horizons (determined using boreholes made using a gouge auger close to the Guelph permeameter experiments and on the walls of an excavated pit – see the position in Figure 1) are as follows: organic horizon O, together with humus horizon Ah, 7.5 cm; ash-gray bleached eluvial horizon E 12.5 cm; illuvial spodic horizons Bh_s together with Bs 40 cm. Horizons O and Ah, and also horizons Bh_s and Bs, are not separated by sharp boundaries. The thicknesses and the soil properties are therefore described for these joint horizons as for a single soil layer. The bedrock C, consisting of weathered metamorphic rocks – sillimanite, migmatite and paragneiss, is relatively homogeneous fine-grained material.

Sampling design

Three distinctly different soil layers were defined in the examined podzol: 1) the eluvial horizon, 2) spodic horizons (undifferentiated), and 3) weathered bedrock. In each of these layers, selected soil properties (K_s , particle size distribution and bulk density) were measured. Disturbed soil samples one liter in volume (for determining the particle size distribution) and

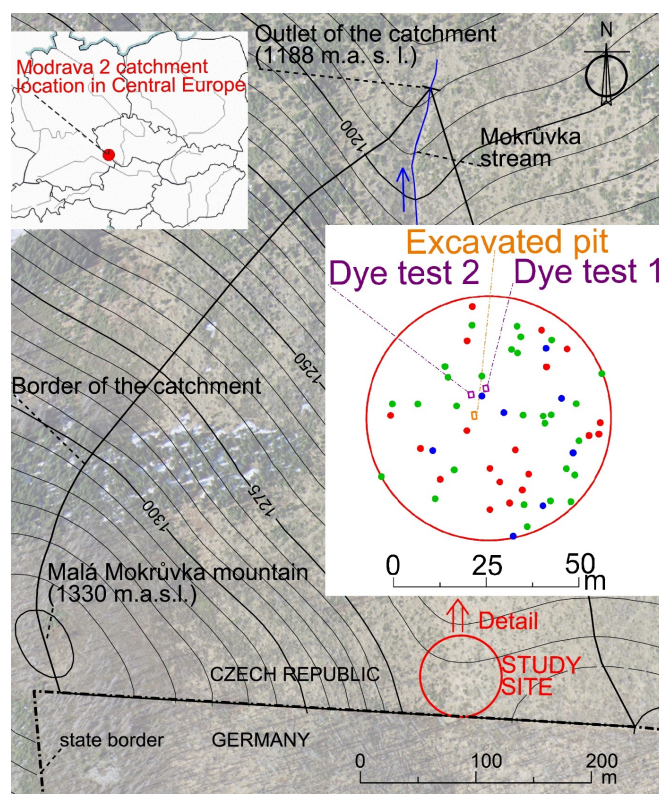


Fig. 1. Location of the study site in the catchment and in Central Europe (modified from Jačka et al. (2012)) and a detail of the sampling positions on the site. The points denote GP tests performed in the eluvial layer (green), the spodic layer (red), and the bedrock (blue).

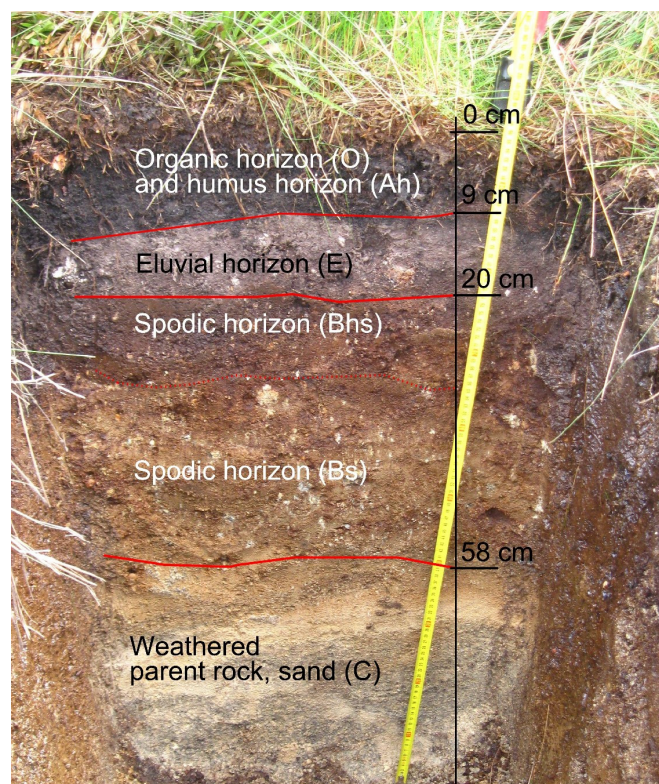


Fig. 2. Podzolic profile with the soil horizons described on the wall of an excavated pit.

undisturbed samples 100 cm³ in volume (for determining the bulk density) were sampled during K_s measurements at the centre of each layer for five replications.

To characterize the soil properties of each layer, measurements were planned to be randomly spatially distributed throughout the site. Random coordinates were generated in the R software environment using the function *runif* (package *stats*, version 3.0.2). These coordinates were used as GPS locations of the sampling positions. Boreholes for the K_s measurements were drilled at these positions (see the points in Figure 1). The random sampling approach was not completely met. Limitations of the random sampling approach included the following: 1) to avoid mutual interference of the experiments, the minimum distance of the sampling points was defined as 1.5 m; 2) it was impossible to drill a borehole to the required depth at some locations, due to stones and roots in the profile and due to the occurrence of young trees and tree stumps on the soil surface. In cases when we were unable to drill a borehole at the randomly generated position, we drilled another borehole as close as possible to this original position. The coordinates of this alternative position were recorded for the further spatial statistical analysis. To characterize K_s of the tested soil layers, a total of 28 Guelph permeameter (GP) infiltration measurements were carried out in the E horizon; 19 experiments in the Bhs and Bs spodic horizons, and 8 measurements in the weathered bedrock (the C horizon). Overall, owing to difficulties that occurred when deep wells were drilled in the stony heterogeneous soil, a smaller number of measurements were performed in deeper boreholes than in shallower boreholes. In addition, some boreholes (usually deeper holes) had to be excluded due to their irregular shape, which is inappropriate for GP measurements. Since the measurements were carried out in August, the measured data represents the growing season, characterized by strong vegetation activity and a high level of evapotranspiration.

Determination of K_s and related soil properties

Field measurements of K_s were performed using a Guelph permeameter (GP), which is a well-documented device (e.g. Bagarello, 1997; Elrick et al., 1989; Reynolds, 2008; Reynolds and Lewis, 2012). The standard measurement method that was applied is described in the operating instructions (Eijkelkamp, 2011). To avoid interference between measurements, an individual borehole was drilled for each GP test. No measurements were made at different depths in the same borehole. The water level (h_g) in the well was kept constant at 16.5 cm. The well (r_g) was 3 cm in radius. Measurements were made until a quasi-steady state (i_{cg}) was reached (from 30 to 60 min). Due to moderate variation, i_{cg} was calculated as the average of the last three measured values. Because the sampling was done in sandy soil containing a small amount of clay particles, no smearing was observed in the wells.

The single constant head approach (Eq. (1)) was used to calculate K_s (Elrick et al., 1989; Reynolds, 2008):

$$K_s = \frac{C_w i_{cg} A_g}{2\pi h_g^2 + C_w \pi r_g^2 + 2\pi h_g / sn} \quad (1)$$

where A_g is the cross-sectional area of the GP water reservoir, C_w is the dimensionless well shape factor, sn is the sorptive number (a value of 0.12 cm⁻¹ was used on the basis of an investigation of the soil texture and structure). The value of C_w was calculated according to Zhang et al. (1998).

To determine the bulk density, undisturbed soil samples were collected into stainless steel sample rings (volume of the sample 100 cm³, 4.1 cm in length and 2.8 cm in inner radius, Eijkelkamp, NL). Subsequently, the samples were oven dried in the laboratory to a constant weight, and the bulk density was calculated (mass of dried soil [g] divided by volume of the sample [cm³]). The particle size analysis was performed using the hydrometer method (CEN ISO/TS 17892-4, 2004). The soil texture was classified according to the textural triangle of the United States Department of Agriculture (USDA).

Statistical analysis

Descriptive statistics were calculated for the three K_s datasets (each representing one of the three defined soil layers). Normality tests (Shapiro and Wilk, 1965) were performed on the measured K_s datasets and normality was rejected. For the decadic logarithms of the K_s datasets, normality was accepted. Therefore, log-normal distributions were found to be suitable for the measured datasets, and one-way analysis of variance (ANOVA) and Tukey's Honestly Significant Difference test (TukeyHSD) were performed on the logarithms. The geometric mean is an appropriate mean for the log-normal distribution, and was used as a representative estimate of the central value of the measured data. The differences in K_s among the soil layers were assessed using ANOVA. When a significant difference in means was indicated, TukeyHSD was carried out for multiple pairwise comparisons. Null hypotheses of ANOVA and TukeyHSD were tested at a significance level of 0.05. The statistical tests were calculated using the Stats package (version 3.0.2), and the descriptive statistics were calculated using the Pastecs package (version 1.3-15) in the R software environment.

For the log-transformed K_s datasets, spatial dependencies were also investigated using an experimental semivariogram. The following theoretical models were fitted to this semivariogram: exponential, Gaussian, linear, nugget. A description of the semivariogram used here and the fitted models is given by Hu et al. (2013); Marin-Castro et al. (2016); Negrete-Yankelevich and Fox (2015). The quality of fit was assessed using the Nash-Sutcliffe (NASH) model efficiency coefficient (Nash and Sutcliffe, 1970). The differences among models were assessed using the Akaike Information Criterion (AIC) (Sakamoto et al., 1986). No spatial dependencies were indicated (no apparent trend in semivariance was observed). The measured K_s values for each soil layer were therefore considered as randomly spatially distributed, and were treated using a classical statistical approach.

Dye tracer tests

The redistribution of the infiltrated water in the podzolic profile was visualized using a dye tracer (Brilliant Blue FCF, referred to here as BB). Two single-ring infiltration tests were performed (see the positions in Figure 1). The mutual distance of the two tests was approx. 4 meters and therefore, the tests represent practically the same position on the slope. A single ring (30 cm in diameter for the first test and 28 cm in diameter for the second test) was inserted to a depth of about 12.5 cm, and the lower sharpened edge of the ring was located in the upper part of the E horizon. The impact of the 2 cm difference in the diameter on the water distribution in the podzolic profile was considered negligible. The slightly different diameters were used as exactly the same rings were not available at the same time (tests were performed during the same day). The soil surface inside the ring was flooded to a depth of approx. 4 cm

using dyed water, and the water level (i.e. the pressure head 4 cm) was kept approximately constant for 2 hours. The amount of water applied (controlled by maintaining the practically constant pressure head for 2 hours) was determined to ensure the quasi-steady infiltration rate conditions and to saturate the soil profile sufficiently (to reveal the effect of the interface of the spodic and the eluvial layer). The undisturbed soil core samples (100 cm³) were collected before the infiltration tests (to define the initial volumetric soil water content) and after the tests during an excavation of the soil profile (to define the volumetric soil water content after the tests). Mean values of the initial water content were 39 Vol.-% for the eluvial layer and 40 Vol.-% for the spodic layer. Mean values of the water content determined after the tests were 45 Vol.-% for the eluvial layer and 42 Vol.-% for the spodic layer. The tracer was applied in a water solution of 5 g l⁻¹ (Schwen et al., 2014a).

The soil profile (a vertical cross-section through the center of the previously flooded area and horizontal cross-sections at various depths from 10 to 40 cm below the surface) was excavated 24 hours after the soil surface inside the ring had been flooded. A visual inspection of the soil was performed on the walls of the cross-sections and photos were taken. The dyed areas in the cross-sections were mapped in the field, and the distances and the sizes of these areas were measured using a measuring tape. Additionally, the sizes and the shapes of the dyed areas were visually inspected using photos depicting the dyed soil and the measuring tape as a scale.

RESULTS AND DISCUSSION

Values of K_s and related properties for the soil layers

A description of the soil texture, bulk density and porosity for the identified podzolic layers is given in Table 1. Particle

size analysis showed that the spodic layer contained a greater amount of clay (+6%) and silt (+12%) than the E horizon. The percentage of gravel (> 2mm) was practically the same for both layers (approx. 30%). According to Wang and McKeague (1982), the increase in content of fine particles can be caused by illuviation of fine particles, which were translocated from the E horizon by infiltrated water together with other substances (humic substances, sesquioxides, chelates), or by synthesis of the new clay minerals from translocated weathering products formed in a strongly acidic environment, which is typical for podzols (e.g. Jankowski, 2014; Waroszewski et al., 2016). Lateral podsolization on the slope (described e.g. in Sommer et al. (2001) or Jankowski (2014)) can also decrease the amount of fine particles contained in the eluvial layer (study site is located in the upper part of the slope in the saddle).

Higher amount of clay in the spodic podzolic layer than in the eluvial layer is a concomitant characteristic of the podzolization process (Sommer et al., 2001), although this characteristic is sometimes not present in podzols due to specific soil conditions (see Waroszewski et al., 2016). The estimated bulk density for the E horizon is 1.4 g cm⁻³, and the calculated porosity is 46% (using the bulk density and mean density of the solid particles). These values are similar for the spodic layer: 1.3 g cm⁻³ and 47%, respectively. The slightly lower bulk density of the spodic layer may be caused by volumetric expansion of accumulated organic matter translocated from the horizons located above (Jersak et al., 1995; Sommer et al., 2001).

Differences in the means, medians, CV, minima and maxima of the measured K_s datasets were noted (see the descriptive statistics in Table 2 and Figure 3). For the tested layers, the ratios of the geometric means of the measured K_s datasets were as follows: C horizon: spodic horizons -5.52, E horizon: spodic horizons -2.87, C horizon: E horizon -1.92. The lowest median,

Table 1. Soil characteristics of the identified podzolic layers (mean \pm SD, n = 5).

Parameters	Units	Identified layer (horizon or group of horizons)		
		Eluvial (E)	Spodic (Bhs and Bs)	Bedrock (C)
Clay ^a (< 2 μ m)	% (weight)	1 \pm 0.5	7 \pm 2.1	8 \pm 1.4
Silt ^a (2-50 μ m)	% (weight)	20 \pm 8.6	32 \pm 4.0	22 \pm 4.0
Sand ^a (0.05-2 mm)	% (weight)	79 \pm 9.2	61 \pm 3.5	70 \pm 2.8
Gravel (> 2mm)	% (weight)	32 \pm 11.0	30 \pm 9.0	25 \pm 10.3
USDA classification		loamy sand	sandy loam	sandy loam
Bulk density	g.cm ⁻³	1.39 \pm 0.09	1.31 \pm 0.07	1.40 \pm 0.04
Porosity ^b	% (volume)	46	48	47

^a Percentages of these soil fractions were calculated from particles < 2mm.

^b Values calculated using the bulk density and pycnometrically determined density of the solid particles.

Table 2. A statistical description of the saturated hydraulic conductivity K_s , measured in different podzolic layers; the different letters following the means indicate significant differences between layers (TukeyHSD test at $\alpha = 0.05$).

Parameters	Units	Depths of boreholes [cm], dominantly sampled layer		
		19–26, Eluvial	30–56, Spodic	68–130, Bedrock
Geometric mean	m.s ⁻¹ \times 10 ⁻⁶	4.415	1.540	8.495
Arithmetic mean	m.s ⁻¹ \times 10 ⁻⁶	6.341	1.863	11.659
Standard deviation	m.s ⁻¹ \times 10 ⁻⁶	5.804	1.284	8.130
Median	m.s ⁻¹ \times 10 ⁻⁶	4.980	1.469	9.633
Minimum	m.s ⁻¹ \times 10 ⁻⁶	0.905	0.618	1.041
Maximum	m.s ⁻¹ \times 10 ⁻⁶	25.800	5.493	25.888
Coefficient of variation	%	92	69	70
Range ^a		1.455	0.949	1.396
Arithmetic mean ^a		-5.355a	-5.812b	-5.071a
Standard deviation ^a		0.390	0.269	0.435
CI mean 0.95 ^{a,b}		0.151	0.130	0.364
Median ^a		-5.303	-5.833	-5.019
No. of experiments		28	19	8

^a Parameters of decadic log-transformed datasets.

^b The confidence interval of the arithmetic mean calculated at the 0.95 significance level.

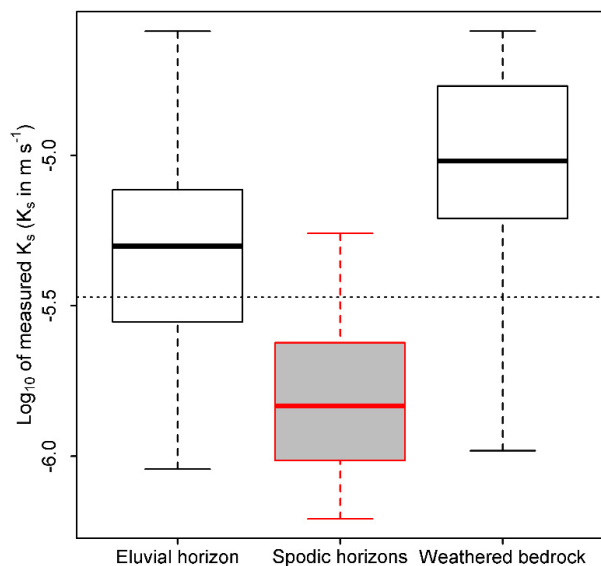


Fig. 3. Boxplots (sample minimum, first quartile, median, third quartile, maximum) of the decadic log-transformed estimates of K_s values [m s^{-1}] for the different podzolic horizons. The dotted line shows the average of all measured data and the red/grey colour of the boxplot illustrates a significantly lower mean.

minimum and maximum of the K_s values were measured for illuvial spodic horizons. The highest CV value was measured for horizon E where its value was more than 20% higher than in the other tested soil layers (see Table 2). The highest CV value may have been caused by greater local heterogeneity in this layer (due to the roots of various plants and remnants of dead wood, which were encountered predominantly in the E horizon). The first quartile, the median, the third quartile, and the maximum of the decadic log-transformed values of K_s measured in the spodic horizons were distinctly lower than for other tested layers (see a graphical comparison with the surrounding layers in Figure 3).

A significant difference between means was found using the ANOVA test applied to the decadic log-transformed K_s datasets, and the null hypothesis was rejected ($p\text{-value} = 7.46 \times 10^{-6}$). According to the subsequent TukeyHSD test, significant differences in the means of the log-transformed K_s values were found for the following pairs: E horizon and spodic horizons ($p\text{-value} = 2.38 \times 10^{-4}$), and C horizon and spodic horizons ($p\text{-value} = 3.00 \times 10^{-5}$). For the pair of K_s datasets collected in the E horizon and in the C horizon, the means of the log-transformed values were not different according to the Tukey HSD test ($p\text{-value} = 0.130$).

The lower K_s values measured for the spodic horizons are obviously related to changes in the porous system. These changes in the porous system can be caused by the different content of fine particles (see the above-mentioned increase in clay and silt content in the spodic layer in comparison with the eluvial layer). Another reason for these changes can be an accumulation of various substances (organic matter, Al and Fe oxides and complexes of these oxides with organic acids - chelates) in the spodic horizon. Translocation of these substances from the upper E horizon to spodic horizons by intensive water infiltration in acidic soil conditions is a characteristic of the podzolization process (Lundström et al., 2000; Sommer et al., 2001; Waroszewski et al., 2016). Illuviated substances form coatings inside the pores (Jankowski, 2014). These coatings, together with translocated fine particles, can

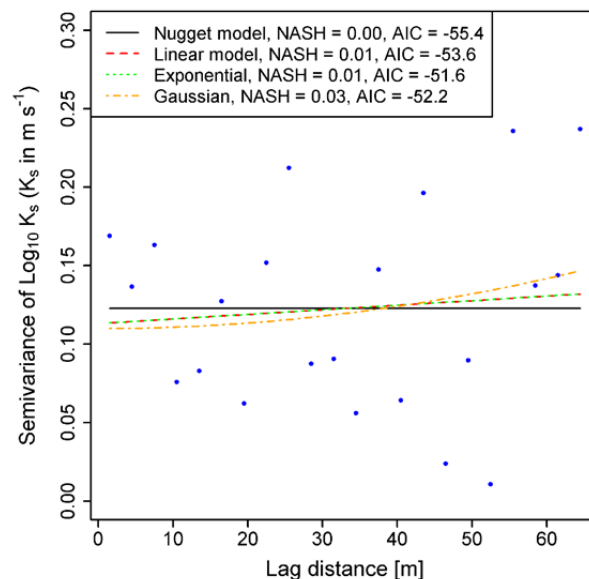


Fig. 4. Spatial dependency of K_s values measured in the E horizon tested using an experimental semivariogram and fitted models. The black solid horizontal line shows the nugget model.

cause clogging or partial blocking of effective pores, reduce the cross-sectional area of the effective pores, increase tortuosity and, as a consequence, slow down the water flow and reduce K_s .

For an illuvial cemented layer of an agriculturally-managed lowland arenic podzol, Rezaei et al. (2016) also found lower mean K_s values than for the layer below and the layer above, using two different methods. Rezaei et al. (2016) pointed out that lower K_s of the illuvial (spodic) layer located at a depth of 47–52 cm could be also partially caused by compaction by heavy machinery. Seuntjens et al. (2001) measured K_s using a pressure infiltrometer in horizons of two different lowland podzols, i.e., a drier podzol, characterized by a lower situated groundwater level and a sharply-defined spodic horizon; and a wetter podzol with a diffuse spodic horizon located in an old land dune landscape covered with spots of vegetation of various types. For the spodic illuvial horizons of the two podzols, considerably lower mean K_s values were also noted than for the surrounding horizons.

K_s spatial dependencies were also investigated. See a representative example in Figure 4. The experimental semivariogram represents a cloud of points, and the fitting quality of all theoretical models is therefore low. See the NASH values in Figure 4. Moreover, the lowest value of AIC was indicated for the nugget model (Figure 4). All of these findings indicate no obvious trend in semivariance and no apparent spatial dependencies. The K_s values for each podzolic layer can therefore be treated as a randomly horizontally distributed variable, and the best estimate for the entire site is the appropriate mean (the geometric mean, due to the log-normal distribution of the datasets).

The following reasons can be offered why no spatial dependencies were detected on a plot scale. 1) High local heterogeneity of the tested mountain forest soil (due to the occurrence of rocks, decaying dead wood and the roots of various plants in the profile) and the corresponding occurrence of preferential flow and other irregularities in the geometry of the flow field. 2) Subjective variability arising from the use of the GP method (a relatively small sampling volume, and possible influence of the soil during drilling). The local heterogeneity, together with the subjective variability, can introduce “noise” into measured

data, can increase the overall variability of K_s , and can mask the spatial patterns. Marin-Castro et al. (2016) also did not find the expected spatial dependencies at the plot scale, probably for the reasons mentioned above.

The representativeness of the GP method was tested for the specific conditions of the investigated podzol by Jačka et al. (2014). For the E horizon, the GP method yielded a non-significantly different mean of K_s in comparison with the single ring infiltrometer method (field estimate K_s), and a slightly lower mean value (1.6 times lower) than a laboratory permeameter applied to the undisturbed soil cores.

Dye tracer visualisation of water flow

The redistribution of the BB dyed water (which infiltrated through the surface inside the single ring infiltrometer) indicated that most of the infiltrated water was accumulated in the E horizon, and just a small portion of this water was distributed into the spodic layer (see dyed area in Table 3). Distinct lateral flow of the dyed water was detected in the E horizon. The distribution of the dyed water at different depths of the podzolic profile beneath the infiltrometer is shown in Figures 5 and 6. In Figure 5, the cross-section at a vertical depth of 20 cm shows that the predominant part of the dyed water is located in the E horizon. The cross-section at a vertical depth of 30 cm shows only a few small colored areas, which are located in the spodic layer. The distinct effect of the layer interface (eluvial and spodic) is shown in a vertical cross section (Figure 5a). In the lower left corner of Figure 5b, there is a blue dye staining located in the upper part of the spodic layer close to the large rock. Possible explanation is that this rock blocked a lateral flow on the layer interface (see Figure 5a) and redirected the water flow to the deeper spodic layer.

In Figure 6, dyed areas can be detected in the E horizon, even at a horizontal distance greater than 30 cm from the centre of the infiltrometer (an indication of distinct lateral flow), and the cross-section in the spodic layer again shows only a few small colored areas.

The observed dyed patterns in the layered profile correspond to the measured significant decrease in K_s in the spodic layer. However, it should be mentioned here that the dyed soil patterns do not match the water flow patterns exactly, because dissolved BB exhibits problematic sorption effects and lower mobility than untreated water in smaller-sized pores (Fér et al., 2016; Nobles et al., 2010; Wang and Zhang, 2011). Nevertheless, the areas dyed by BB usefully visualize the major flow field in the soil profile (Jiang et al., 2017; Leibundgut et al.,

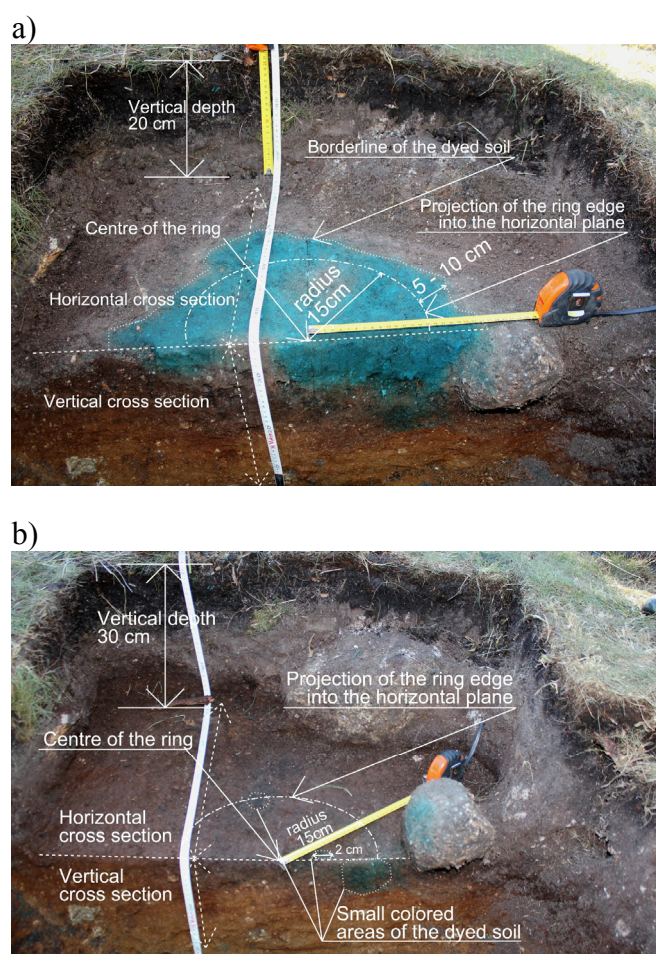


Fig. 5. Distribution of the infiltrated water below single ring infiltration test No. 1, visualized using a BB tracer – (a) the horizontal cross-section at a vertical depth of 20 cm (above), and (b) the horizontal cross-section at a vertical depth of 30 cm (below).

2009). For the examined profile, the BB experiments revealed distinct differences among the soil layers in hydrologically important pores (macropores and upper size capillary pores, where the preferential flow occurs). According to the flow field of the dyed water, the major interconnected part of these pores is located in the E horizon, and the vertical connection of these pores in the soil profile is interrupted in the spodic layer.

Table 3. Horizontal and vertical spread of the BB dye tracer in the examined soil layers.

BB test	Layer (horizon or group of horizons)	Thickness of the layer [cm]	Thickness of the dyed soil [cm] ^a	Shape of the dyed patterns	Vertical depth [cm] ^b	Horizontal distance [cm] ^c	Dyed area [cm ²] ^d
1	Horizon E	from 9 to 20	16	Large interconnected dyed area with undyed soil patterns	20	30	1500
	Spodic layer (horizon Bhs together with Bs)	approx. 39	7	A few separate stains of small size (max. 6 cm)	30	27	100
2	Horizon E	from 11 to 21	18	Large interconnected dyed area with undyed soil patterns	18	48	1100
	Spodic layer (horizon Bhs together with Bs)	approx. 42	2	A few separate stains of small size (max. 3 cm)	30	29	50

^a Maximum vertical thickness.

^b Vertical depth (from the surface) of the horizontal cross-section with the maximum horizontal spread of the dye.

^c Distance of the maximum horizontal spread of the dye measured from the vertical axis of the ring.

^d Estimated size of the dyed area in the horizontal cross-section with the largest spread of the dye.

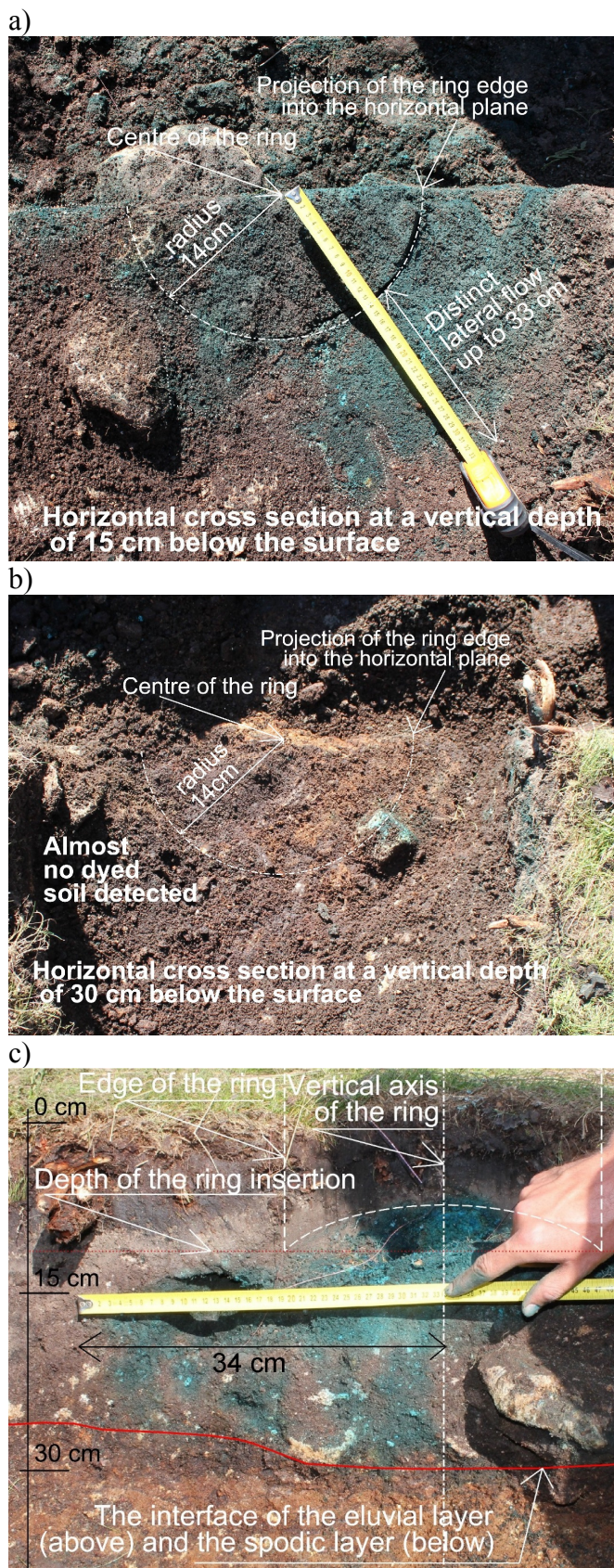


Fig. 6. Distribution of the infiltrated water below single ring infiltration test No. 2, visualized using a BB tracer – (a) the horizontal cross-section at a vertical depth of 15 cm, (b) the horizontal cross-section at a vertical depth of 30 cm, (c) corresponding detail on the vertical cross section through the centre of the ring.

Limitations of the research

For an investigation of the hydrological effects of the podzolic profile, we selected a small area of the site, rather than selecting the entire catchment area. The described hydrological behavior may therefore not be valid for podzolic profiles with less distinct layers that occur in lower parts of the catchment. The small area of the site was selected due to 1) the occurrence of a distinctly layered haplic podzol throughout the site, and 2) the time-demanding nature of direct field measurements of K_s in a rather inaccessible heterogeneous podzol. Parameter K_s is the key soil property affecting soil water flow, and is unfortunately very difficult to measure properly (see Fodor et al., 2011). We have decided for a detailed characterization of K_s including higher number of collected samples on a small site in well-developed soil layers.

For the infiltration measurement, we have used well-established field methods which sample small volume of the soil. We have selected these small-scale methods because they require relatively small soil disturbances, are easy to operate and exhibit low water consumption which is a very important aspect for hardly this accessible site without water supply. The examined site is located in the valuable central part of the Šumava National Park, where excavations and other soil disturbances should be minimized. Larger volume sampling methods such as for a rainfall simulator or large infiltrometer are theoretically more suitable for the examined heterogeneous soil but are also impracticable in this specific case due to the reasons mentioned above. To account for large stones (see their sizes in Figures 5 and 6) for particle size and bulk density measurements, large excavations would also be required. Therefore, these stones were not included in the analysis.

Engineering implications

After heavy rainfalls, water filling of empty shallow boreholes (formed during the GP tests) was observed. Some of these boreholes were flooded to a few centimetres below the surface of the soil. Dye tracer tests also indicated an accumulation of infiltrated water and lateral flow on the layer interface in the E horizon over the spodic layer (see Figures 5 and 6 and Table 3). Significantly lower K_s was measured in the spodic layer (see Table 2 and Figure 3), and this corresponds to the findings mentioned above. Therefore, the spodic layer can probably form a hydraulic barrier under field-saturated conditions as it is indicated by the two different infiltration methods (GP and dye tracer tests) and by the observations of the water-level in the shallow boreholes after the heavy rainfalls.

As Si et al. (2011) pointed out, shallow subsurface runoff (lateral flow) on the layer interface can be formed when hydraulically different layers occur on a slope. According to Sommer et al. (2001), about 30% of the discharge is formed by this lateral flow denoted here as interflow in a sandstone podzolic catchment. For mountain podzols, waterlogging in the E horizon and water flow at the layer interface (E and spodic layer) were observed by Waroszewski et al. (2016). The results of our study also clearly show the important role of layering on lateral flow and water accumulation in mountain podzols. For correct hydrological modelling, the effect of layering should be implemented for the examined soil. Using the measured K_s values and RETC estimated indirectly from pedotransfer functions based on the measured soil texture and bulk density for identified layers, the water flow in the layered podzol investigated here can be modelled using specialized software, e.g. DRUeS (Kuráž et al., 2015), Hydrus (Šimůnek et al., 2016), and others.

CONCLUSION

The findings presented here are a contribution to knowledge about the hydrological behaviour of mountain haplic podzols. For this hydrologically important soil, vertical changes in the crucial hydraulic parameter K_s among identified soil layers have been quantified, and the effect of the layering of the soil profile on the redistribution of infiltrated water has been assessed using dye tracer tests. A relatively large number of point-scale well-infiltration experiments showed significantly lower mean K_s values for the spodic illuvial horizons than for the surrounding horizons. Reasons for the lower K_s were probably an accumulation of fine particles and various substances in the spodic horizons, which were translocated from the above-located eluvial horizon during the podzolization process. The translocated substances and fine particles can form coatings on the soil solid phase and partially block the effective pores.

A strong effect of the interface between the eluvial layer and the spodic layer on the distribution of the infiltrated water was detected by dye tracer experiments, and this finding corresponds with the measured decrease in K_s in the spodic layer. During heavy rainfall, the observed distinct lateral flow and water accumulation on the interface of these layers can cause water accumulation and the subsequent formation of shallow subsurface runoff if the interface is located on a slope. The predictions of hydrological models for areas dominated by mountain haplic podzols can be made more accurate by applying quantifications of K_s and by using information about water flow directions from the dye tracer tests presented here. Due to the differently layered podzolic profiles that usually occur in mountain catchments (different thicknesses of the layers and different intensity of podzolization), further infiltration experiments and runoff observations in other sites are needed in order to provide an accurate description of the impact of podzolic layers on water flow on a larger scale.

Acknowledgements. We gratefully acknowledge support from the Internal Grant Agency of the Faculty of Environmental Sciences, Czech University of Life Sciences Prague, within the framework of Projects Nos. 20124252, 2011422003143, 20174223. We would also like to express our gratitude to the anonymous reviewers for their helpful comments.

REFERENCES

- Bagarello, V., 1997. Influence of well preparation on field-saturated hydraulic conductivity measured with the Guelph Permeameter. *Geoderma*, 80, 169–180.
- Bagarello, V., Baiamonte, G., Castellini, M., Di Prima, S., Iovino, M., 2014. A comparison between the single ring pressure infiltrometer and simplified falling head techniques. *Hydrol. Process.*, 28, 4843–4853.
- Bagarello, V., Iovino, M., Lai, J., 2016. Testing steady-state analysis of single-ring and square pressure infiltrometer data. *Geoderma*, 261, 101–109.
- CEN ISO/TS 17892-4, 2004. Geotechnical Investigation and Testing – Laboratory Testing of Soil – Part 4: Determination of Particle Size Distribution. Inštitut za standardizacijo, Ljubljana, Slovenija.
- Clark, E.V., Zipper, C.E., 2016. Vegetation influences near-surface hydrological characteristics on a surface coal mine in eastern USA. *Catena*, 139, 241–249.
- Eijkelkamp, 2011. Operating instructions. 09.07 Guelph permeameter. <https://www.eijkelkamp.com/download.php?file=b2082939>, 11/2011, accessed: 22/06/2016.
- Elrick, D.E.; Reynolds, W.D., Tan, K.A., 1989. Hydraulic conductivity measurements in the unsaturated zone using improved well analyses. *Ground Water Monit. Rev.*, 9, 184–193.
- Fér, M., Leue, M., Kodešová, R., Gerke, H.H., Ellerbrock, R.H., 2016. Droplet infiltration dynamics and soil wettability related to soil organic matter of soil aggregate coatings. *J. Hydrol. Hydromech.*, 64, 111–120.
- Fodor, N., Sándor, R., Orfanus, T., Lichner, L., Rajkai, K., 2011. Evaluation method dependency of measured saturated hydraulic conductivity. *Geoderma*, 165, 60–68.
- Hillel, D., 1998. *Environmental Soil Physics*. Academic Press, San Diego, USA, 771 p.
- Hu, W., Shao, M., Wang, Q., She, D., 2013. Effects of measurement method, scale, and landscape features on variability of saturated hydraulic conductivity. *J. Hydrol. Eng.*, 18, 4, 378–386.
- Huang, M., Barbour, S.L., Elshorbagy, A., Zettl, J.D., Si, B.C., 2011. Water availability and forest growth in coarse-textured soils. *Can. J. Soil Sci.*, 91, 199–210.
- Jačka, L., Pavlásek, J., Jindrová, M., Bašta, P., Černý, M., Balvín, A., Pech, P., 2012. Steady infiltration rates estimated for a mountain forest catchment based on the distribution of plant species. *J. For. Sci.*, 58, 536–544.
- Jačka, L., Pavlásek, J., Kuráž, V., Pech, P., 2014. A comparison of three measuring methods for estimating the saturated hydraulic conductivity in the shallow subsurface layer of mountain podzols. *Geoderma*, 219–220, 82–88.
- Jačka, L., Pavlásek, J., Pech, P., Kuráž, V., 2016. Assessment of evaluation methods using infiltration data measured in heterogeneous mountain soils. *Geoderma*, 276, 74–83.
- Jankowski, M., 2014. The evidence of lateral podzolization in sandy soils of northern Poland. *Catena*, 112, 139–147.
- Jarvis, N., Koestel, J., Messing, I., Moeys, J., Lindahl, A., 2013. Influence of soil, land use and climatic factors on hydraulic conductivity of soil. *Hydrol. Earth Syst. Sci.*, 17, 5185–5195.
- Jersak, J., Amundson, R.G., Brimhall Jr., G., 1995. A mass balance analysis of podzolization: examples from the north-eastern United States. *Geoderma*, 66, 15–42.
- Jiang, X.J., Liu, S., Zhang, H., 2017. Effects of different management practices on vertical soil water flow patterns in the Loess Plateau. *Soil and Tillage Research*, 166, 33–42.
- Kodešová, R., Němeček, K., Kodeš, V., Žigová, A., 2012. Using dye tracer for visualization of preferential flow at macro- and microscales. *Vadose Zone Journal*, 11, 1–10.
- Kodešová, R., Němeček, K., Žigová, A., Nikodem, A., Fér, M., 2015. Using dye tracer for visualizing roots impact on soil structure and soil porous system. *Biologia*, 70, 1439–1443.
- Kuráž, M., Mayer, P., Pech, P., 2015. Solving the nonlinear and nonstationary Richards equation with two-level adaptive domain decomposition (dd-adaptivity). *Applied Mathematics and Computation*, 267, 207–222.
- Kutílek, M., Nielsen, D.R., 1994. *Soil Hydrology*. Catena Verlag, Cremlingen - Destedt, Germany, 370 p.
- Laine-Kaulio, H., Backnäs, S., Koivusalo, H., Laurén, A., 2015. Dye tracer visualization of flow patterns and pathways in glacial sandy till at a boreal forest hillslope. *Geoderma*, 259, 23–34.
- Leibundgut, C., Maloszewski, P., Kulls, C., 2009. *Tracers in Hydrology*. John Wiley & Sons, Chichester, UK, 415 p.
- Lundström, U.S., van Breemen, N., Bain, D., 2000. The podzolization process. A review. *Geoderma*, 94, 91–107.
- Marín-Castro, B.E., Geissert, D., Negrete-Yankelevich, S., Gómez-Tagle Chávez, A., 2016. Spatial distribution of

- hydraulic conductivity in soils of secondary tropical montane cloud forests and shade coffee agroecosystems. *Geoderma*, 283, 57–67.
- Nash, J., Sutcliffe, J., 1970. River flow forecasting through conceptual models part i — a discussion of principles. *J. Hydrol.*, 10, 282–290.
- Negrete-Yankelevich, S., Fox, G.A., 2015. Spatial variation and linear modeling of ecological data. In: Fox, G.A., Negrete-Yankelevich, S., Sosa, J.V. (Eds.): *Ecological Statistics: Contemporary Theory and Application*. University Press, Oxford, pp. 228–260.
- Nobles, M.M., Wilding, L.P., Lin, H.S., 2010. Flow pathways of bromide and Brilliant Blue FCF tracers in caliche soils. *J. Hydrol.*, 393, 114–122.
- Pavlásek, J., Ředinová, J., Skalská, P., 2009. Evaluation of monitoring on Modrava catchments. *Soil Water Res.*, 4 (Special Issue 2), 66–74.
- Pavlásek, J., Tesař, M., Máca, P., Hanková, R., Hudečková, K., Jačka, L., Klose, Z., Ředinová, J., 2010. Ten years of hydrological monitoring in upland microcatchments in the Bohemian Forest, Czech Republic. In: Herrmann, A., Schumann, S. (Eds.): *Status and Perspectives of Hydrology in Small Basins*. Red Book IAHS No. 336. IAHS Press, Wallingford, pp. 213–218.
- Pennock, D., Yates, C., Braidek, J., 2008. Soil sampling designs. In: Carter M.R., Gregorich, E.G. (Eds.): *Soil Sampling and Methods of Analysis*. 2nd ed. CRC Press Taylor & Francis, Boca Raton, USA, pp. 1–14.
- Qian, J., Wu, Y., Zhang, Y., Liu, Y., Lu, Y., Yu, Z., 2015. Evaluating differences in transport behavior of sodium chloride and Brilliant Blue FCF in sand columns. *Transport in Porous Media*, 109, 765–779.
- Reynolds, W.D., 2008. Saturated hydraulic properties: Well permeameter. In: Carter M.R., Gregorich, E.G. (Eds.): *Soil Sampling and Methods of Analysis*. 2nd ed. CRC Press Taylor & Francis, Boca Raton, USA, pp. 1025–1042.
- Reynolds, W.D., Bowman, B.T., Brunke, R.R., Drury, C.F., Tan, C.S., 2000. Comparison of tension infiltrometer, pressure infiltrometer, and soil core estimates of saturated hydraulic conductivity. *Soil Sci. Soc. Am. J.*, 64, 478–484.
- Reynolds, W.D., Lewis, K.L., 2012. A drive point application of the Guelph permeameter method for coarse-textured soils. *Geoderma*, 187–188, 59–66.
- Rezaei, M., Seuntjens, P., Shahidi, R., Joris, I., Boëne, W., Al-Barri, B., Cornelis, W., 2016. The relevance of in-situ and laboratory characterization of sandy soil hydraulic properties for soil water simulations. *J. Hydrol.*, 534, 251–265.
- Sander, T., Gerke, H.H., 2007. Preferential flow patterns in paddy fields using a dye tracer. *Vadose Zone J.*, 6, 105–115.
- Sakamoto, Y., Ishiguro, M., Kitagawa G., 1986. *Akaike Information Criterion Statistics*. D. Reidel Publishing Company, Springer, Netherlands, 290 p.
- Schwen, A., Backus, J., Yang, Y., Wendroth, O., 2014a. Characterizing land use impact on multi-tracer displacement and soil structure. *J. Hydrol.*, 519, 1752–1768.
- Schwen, A., Zimmermann, M., Bodner, G., 2014b. Vertical variations of soil hydraulic properties within two soil profiles and its relevance for soil water simulations. *J. Hydrol.*, 516, 169–181.
- Seuntjens, P., Mallants, D., Toride, N., Cornelis, C., Geuzens, P., 2001. Grid lysimeter study of steady state chloride transport in two Spodosol types using TDR and wick samplers. *J. Contam. Hydrol.*, 51, 13–39.
- Shapiro, S.S., Wilk, M.B., 1965. Analysis of variance test for normality (complete samples). *Biometrika*, 52, 591–611.
- Shin, Y., Mohanty, B.P., Ines, A.V.M., 2012. Soil hydraulic properties in one-dimensional layered soil profile using layer-specific soil moisture assimilation scheme. *Water Resour. Res.*, 48, W06529.
- Si, B.C., M. Dyck, Parkin, G., 2011. Flow and transport in layered soils. *Can. J. Soil Sci.*, 91, 127–132.
- Swarowsky, A., Dahlgren, R.A., Tate, K.W., Hopmans, J.W., O'Geen, A.T., 2011. Catchment-scale soil water dynamics in a Mediterranean-type oak woodland. *Vadose Zone J.*, 10, 800–815.
- Šimůnek, J., van Genuchten, M.T., Šejna, M., 2016. Recent developments and applications of the HYDRUS computer software packages. *Vadose Zone Journal*, 15, 1–25.
- Sommer, M., Halm, D., Geisinger, C., Andruschkewitsch, I., Zarei, M., Stahr, K., 2001. Lateral podzolization in a sandstone catchment. *Geoderma*, 103, 231–247.
- van Genuchten, M.T., 1980. A closed form equation for predicting the hydraulic conductivity of unsaturated soils. *Soil Sci. Soc. Am. J.*, 44, 892–898.
- Vereecken, H., Weynants, M., Javaux, M., Pachepsky, Y., Schaap, M.G., van Genuchten, M.T., 2010. Using pedotransfer functions to estimate the van Genuchten-Mualem soil hydraulic properties: a review. *Vadose Zone J.*, 9, 795–820.
- Wang, C., McKeague, J.A., 1982. Illuviated clay in sandy podzolic soils of New Brunswick. *Can. J. Soil Sci.*, 62, 79–89.
- Wang, K., Zhang, R., 2011. Heterogeneous soil water flow and macropores described with combined tracers of dye and iodine. *J. Hydrol.*, 397, 105–117.
- Waroszewski, J., Egli, M., Kabała, C., Kierczak, J., Brandova, D., 2016. Mass fluxes and clay mineral formation in soils developed on slope deposits of the Kowarski Grzbiet (Karkonosze Mountains, Czech Republic/Poland). *Geoderma*, 264, 363–378.
- Webb, T.H., Claydon, J.J., Harris, S.R., 2000. Quantifying variability of soil physical properties within soil series to address modern land-use issues on the Canterbury Plains, New Zealand. *Aust. J. Soil Res.*, 38, 1115–1129.
- Zettl, J.D., Barbour, S.L., Huang, M., Si, B.C., Leskiw, L.A., 2011. Influence of textural layering on field capacity of coarse soils. *Can. J. Soil Sci.*, 91, 133–147.
- Zhang, Z.F., Groenevelt, P.H., Parkin, G.W., 1998. The well shape factor for the measurement of soil hydraulic properties using the Guelph permeameter. *Soil Till. Res.*, 49, 219–221.

Received 3 July 2017
Accepted 22 January 2018

Note: Colour version of Figures can be found in the web version of this article.